UNIVERSIDAD TÉCNICA FEDERICO SANTA MARÍA
DEPARTAMENTO DE ELECTRONICA
VALPARAÍSO - CHILE

MATHEMATICAL MODELING OF PHYSICAL LAYER IMPAIRMENTS IN SPATIAL DIVISION MULTIPLEXING (SDM) OPTICAL FIBER NETWORKS BASED ON FEW-MODE FIBERS (FMF)

ASTRID ADRIANA LOZADA VERGARA

Thesis submitted to the
Universidad Técnica Federico Santa María
as a partial requirement for the degree of
DOCTOR IN ELECTRONIC ENGINEERING

Supervised by : Dr. RICARDO OLIVARES

January 2025

To my parents, Zuleima and Hernan.

ACKNOWLEDGEMENTS

The following acknowledgments are addressed to all the people who have contributed with their support and collaboration to the success of this work.

Firstly, I would like to express my sincere gratitude to the Universidad Técnica Federico Santa María and the Agencia Nacional de Investigación y Desarrollo (ANID) for providing me with the opportunity and financial support to pursue postgraduate studies. To my supervisor, Dr. Ricardo Olivares Veliz, for his support, encouragement, and availability, as well as for the careful scientific review of my work. To Dr. Alejandra Beghelli and Dr. Filipe Marques Ferreira, for giving me the invaluable opportunity to do a research stay at the Optical Network Group in UCL. To all members of IRO research group, for their availability, support, and attention to detail in reviewing my work.

I would like to especially thank my husband and daughter for their love, unconditional support, patience and sacrifices during these years of postgraduate studies. I would also like to thank my parents, sisters, family, and friends, you have always shown me how proud you are of my achievements.

MATHEMATICAL MODELING OF PHYSICAL LAYER IMPAIRMENTS IN SPATIAL DIVISION MULTIPLEXING (SDM) OPTICAL FIBER NETWORKS BASED ON FEW-MODE FIBERS (FMF)

Thesis presented by **Astrid Adriana Lozada Vergara** for the degree of **Doctor in Electronic Engineering**.

Thesis advisor: **Dr. Ricardo Olivares**

ABSTRACT

Space division multiplexing (SDM) has emerged as a long-term solution to overcome the capacity limitations of current wavelength division multiplexing (WDM) networks. Due to the increase in data traffic demand, the theoretical capacity limits of standard single-mode fibers are insufficient to meet the requirements of future networks, hence the importance of developing new technologies that increase this capacity. In the context of this thesis, SDM systems are studied addressing aspects from signal propagation and amplification to the resource allocation problem.

This research specifically investigates the performance of SDM networks based on Few-Mode Fiber (FMF) with a focus on how physical layer impairments (PLI) impact transmission quality. SDM-FMF networks experience several linear and nonlinear PLI. These impairments were mathematically modeled under weak and intermediate coupling regimes to analyze their impact on the signal-to-noise ratio (SNR) along FMF links.

To analyze optical amplification within SDM-FMF networks, two amplification strategies were studied: lumped amplification using Few-Mode Erbium-Doped Fiber Amplifiers (FM-EDFA) and distributed amplification using Few-Mode Distributed Raman Amplifiers (FM-DRA). Genetic algorithms were employed to optimize the pump configurations of these amplifiers, minimizing Differential Modal Gain (DMG) and Differential Spectral Gain (DSG) to improve system performance.

A novel Joint DMG-DSG Minimization Methodology was proposed to optimize the performance of two-stage FM-EDFA, ensuring high mean gain and low DMG and minimal DSG. This methodology involves the design of pumping profile and gain flattening filter. Simulation results show that the two-stage FM-EDFA achieves enough gain to compensate for fiber losses in spans of 100 km. Additionally, optimization of FM-DRA was also performed. The optimization process aims to minimize gain ripple and DMG. Performance under three configurations in the pumping direction-backward, forward, and bi-directional-was compared for signals in the conventional C-band. In terms of the on-off gain, the three configurations achieved a similar value. The main difference between these three configurations is regarding the noise. Finding that, bidirectional pumping provides the optimal balance between on-off gain and noise. To extend operation to the C + L optical bands, FM-DRA optimization was done. In this case, the number of pump wavelengths and the pumping power budget was increased compared to operation in the C-band alone. Resulting in higher gains and greater ASE noise power, at the expense of larger DMG and gain ripple.

Within the context of solving the resource allocation problem, a novel Routing, Spatial Mode, and Spectrum Allocation (RSSA) algorithm, named BANG, was developed. BANG's mode group selection strategy demonstrated a significant reduction in blocking probability compared to existing algorithms.

The findings of this work—optimized amplification profiles using FM-EDFA and FM-DRA, and BANG algorithm—are promising solutions for implementation in next-generation SDM-FMF systems to address the limited capacity of existing wavelength division multiplexing networks. Finally, the thesis outlines future research directions, including hybrid amplification techniques and the application of elastic optical networks for improved resource assignment.

Keywords. Spatial Division Multiplexing; Few-Mode Fiber; Few-Mode Erbium-Doped Fiber Amplifier; Few-Mode Distributed Raman Amplifier; Mode-Group Division Multiplexing; Routing, Spatial mode, and Spectrum Allocation.

MODELAMIENTO MATEMÁTICO DE LAS RESTRICCIONES DE CAPA FÌSICA EN REDES DE FIBRA ÓPTICA CON MULTIPLEXACIÓN POR DIVISIÓN ESPACIAL BASADAS EN FIBRAS DE POCOS MODOS

Tesis de grado presentada por **Astrid Adriana Lozada Vergara** como requisito parcial para optar al grado de **Doctor en Ingeniería Elecrónica**.

Supervisor de tesis: **Dr. Ricardo Olivares**

RESUMEN

La multiplexación por división espacial (SDM), ha surgido como una solución de largo plazo para superar las limitaciones por capacidad de las actuales redes de comunicaciones por fibra óptica con multiplexación por longitud de onda (WDM). Debido al aumento en la demanda de tráfico de datos, los límites teóricos de capacidad de las fibras monomodo estándar se muestran insuficientes para responder a los requerimientos de las redes futuras, por ello la importancia de que se desarrollen nuevas tecnologías que permitan aumentar esta capacidad. En esta tesis, se estudian sistemas SDM, considerando aspectos asociados a la propagación, amplificación y el problema de asignación de recursos.

Específicamente, se investiga el desempeño de redes de fibra de pocos modos (FMF) considerando las restricciones de capa física que afectan la calidad de transmisión. Las redes SDM-FMF experimentan diversas restricciones de capa física tanto lineales como no lineales. Estas restricciones, se modelaron matemáticamente bajo regímenes de acoplamiento modal débil e intermedio para determinar su impacto en la relación señal-a-ruido a lo largo de enlaces SDM-FMF.

La amplificación óptica en los sistemas SDM-FMF se estudió considerando dos estrategias de amplificación: amplificadores concentrados de fibra dopada con erbio de pocos modos (FM-EDFA) y amplificadores Raman distribuidos de pocos modos (FM-DRA). Se emplearon algoritmos genéticos para optimizar los perfiles de bombeo de estos amplificadores, minimizando la ganancia modal diferencial (DMG) y la ganancia espectral diferencial (DSG) para mejorar el rendimiento del sistema.

Se propuso la metodología *Joint DMG-DSG Minimization* para optimizar FM-EDFA de dos etapas, asegurando una alta ganancia media, DMG y DSG bajos. Esta metodología implica el diseño del perfil de bombeo y el diseño del filtro aplanador de ganancias. Los resultados de simulación muestran que el FM-EDFA de dos etapas ofrece ganancia suficiente para compensar las pérdidas de fibra en tramos de 100 km, con señales que se propagan en la banda C. Adicionalmente, se realizó la optimización de FM-DRA. El proceso de optimización tuvo como objetivo minimizar la dispersión de ganancia y la DMG a través de simulaciones numéricas. Se comparó el rendimiento, trabajando en la banda C, usando tres configuraciones en la dirección de bombeo: co-propagante, contra-propagante y bidireccional. En términos de ganancia on-off se alcanza un valor similar con las tres configuraciones. La principal diferencia entre estas tres configuraciones está relacionada con el ruido. El bombeo bidireccional ofrece el equilibrio óptimo entre ganancia on-off y ruido. Con el fin de extender la operación a las bandas ópticas C y L, se realizó una optimización adicional del FM-DRA. En este caso, se aumentó el número de longitudes de onda así como el presupuesto de potencias para el bombeo, en comparación con el perfil de bombeo diseñado con operación en banda C únicamente. Dando como resultado, mayores ganancias y potencia de ruido ASE, a expensas de un mayor DMG y una menor planicidad espectral.

En el contexto del problema de asignación de recursos, se desarrolló un nuevo algoritmo de asignación de ruta, modo espacial y espectro, denominado *BANG*. La estrategia de selección de grupo de modos de BANG demostró una reducción significativa en la probabilidad de bloqueo en comparación con los algoritmos existentes.

Los resultados de este trabajo- perfiles de amplificación optimizados utilizando FM-EDFA y FM-DRA, y el algoritmo BANG- son soluciones prometedoras para su implementación en sistemas SDM-FMF de próxima generación, para abordar la capacidad limitada de las redes de multiplexación por división de longitud de onda existentes. Por último, la tesis describe las futuras direcciones de investigación, incluidas las técnicas de amplificación híbrida y la aplicación de redes ópticas elásticas para una mejor asignación de recursos.

Palabras Clave. Multiplexción por División Espacial, Fibra de Pocos Modos, Amplificadores Dopados con Erbio de Fibra de Pocos Modos, Amplicador Raman de Fibra de Pocos Modos, Multiplexación por División de Grupos de Modos, Asignación de Ruta, Modos Espacial y Espectro.

Contents

List of Tables

List of Figures

List of Acronyms

ASE	Amplified Spontaneous Emission
BANG	Balanced AllocatioN of Mode Groups
BDM	Band Division Multiplexing
BER	Bit Error Rate
CAGR	Compound Annual Growth Rate
CD	Chromatic Dispersion
CNLSE	Coupled Nonlinear Schrödinger Equation
DCF	Dispersion Compensation Fiber
DMD	Differential Mode Delay
DMG	Differential Modal Gain
DRA	Distributed Raman Amplifier
DSG	Differential Spectral Gain
DSP	Digital Signal Processing
EDFA	Erbium-Doped Fiber Amplifier
ED-FMF	Erbium-Doped Few-Mode Fiber
EON	Elastic Optical Networks
FM-DRA	Few-Mode Distributed Raman Amplifier
FM-EDFA	Few-Mode Erbium-Doped Fiber Amplifier
FM-MCF	Few-Mode Multicore Fiber
FMF	Few-Mode Fiber
FWM	Four-Wave Mixing
GA	Genetic Algorithm
GFF	Gain Flattening Filter
GI	Graded Index
GVD	Group-Velocity Dispersion
HCF	Hollow-Core Fiber
IM-FWM	Inter-modal Four Wave Mixing
IM-XPM	Inter-modal Cross Phase Modulation
IM-SRS	Inter-modal Stimulated Raman Scattering
IoT	Internet of Things
ISO	Optical Isolator
ISRS	Inter-channel Stimulated Raman Scattering
LP	Linearly Polarized
MCF	Multi-Core Fiber
MDL	Mode-Dependent Loss
MDM	Mode-Division Multiplexing
MDMUX	Multi-mode Demultiplexer
MG DEMUX	Mode-Group Demultiplexer
MG MUX	Mode-Group Multiplexer
MGDM	Mode-Group Division Multiplexing
MGDM-LT	MDGM solution using light trail

MIMO	Multiple-Input Multiple-Output
MMF	Multi-Mode Fiber
MMUX	Multi-mode Multiplexer
NF	Noise Figure
NLI	Nonlinear Impairnment
NLSE	Nonlinear Schrödinger Equation
OSA	Optical Spectrum Analizer
OSNR	Optical Signal-to-Noise Ratio
PDM	Polarization Division Multiplexing
PL	Photonic lantern
PLI	Physical Layer Impairments
PMD	Polarization Mode Dispersion
PSK	Phase Shift Keying
QAM	Quadrature Amplitude Modulation
QoT	Quality-of-Transmission
QPSK	Quaternary Phase-Shift Keying
RMMSA	Routing, Modulation format, Mode-group, and Spectrum Allocation
ROADM	Reconfigurable Optical Add/Drop Multiplexer
RSCA	Routing, Spectrum, and Core Allocation
RSSA	Routing, Spatial mode, and Spectrum Allocation
SI	Step-Index
SDM	Spatial Division Multiplexing
SM-EDFA	Single Mode Erbium-Doped Fiber Amplifier
SMF	Single Mode Fiber
SMF-B	Single-Mode Fiber Bundles
SNR	Signal-to-Noise Ratio
SPM	Self-Phase Modulation
SRS	Stimulated Raman Scattering
TDM	Time Division Multiplexing
TE	Transverse Electric
TM	Transverse Magnetic
WDM	Wavelength Division Multiplexing
WSC	Wavelength Selective WDM Coupler
XPM	Cross-Phase Modulation
XT	Crosstalk

1

Introduction

1.1 Problem Statement and Motivation

Technological advances have enabled new services such as cloud gaming, cloud computing, high-definition video streaming, virtual reality, smart cities, self-driving vehicles, and others involving the Internet of Things (IoT). Many of these services demand greater bandwidth from the networks serving end users. At the same time, a large number of smartphones, tablets, personal and desktop computers, smart watches, machine-to-machine devices, all labeled as “smart” to indicate that they are connected to the Internet, contribute to growing global traffic demands. Klaus *et al*. [6] report that every 1.5 to 2 years the network traffic is doubling. Additionally, studies such as the *Regional Overview Latin America Market Trends* by TeleGeography [1] predicted that used international bandwidth in Latin America will grow to almost 700 Tbps by 2026 at a compound annual growth rate (CAGR) of 36%, as is showed in Figure 1.1. Given these trends, it is possible that soon current transport networks will collapse upon reaching their maximum capacity, a phenomenon known in the literature as the capacity crunch [7].

Given the importance of connectivity for governments, institutions, industries, and society in general, maintaining data transport networks that support current and future requirements is mandatory, many resources are invested worldwide in the study and development of new technologies in this area. The core of transport networks is based on optical fiber. From its beginning in 1975, fiber optic communication systems have been evolving to meet bandwidth demands, where the multiplexing of resources has been one of the main protagonists, developing various multiplexing formats over six generations of fiber optic communication systems [8]. Initially time division multiplexing (TDM), later wavelength division multiplexing (WDM), then polarization division multiplexing (PDM), and more recently, spatial division multiplexing (SDM) and band division multiplexing (BDM) [8].

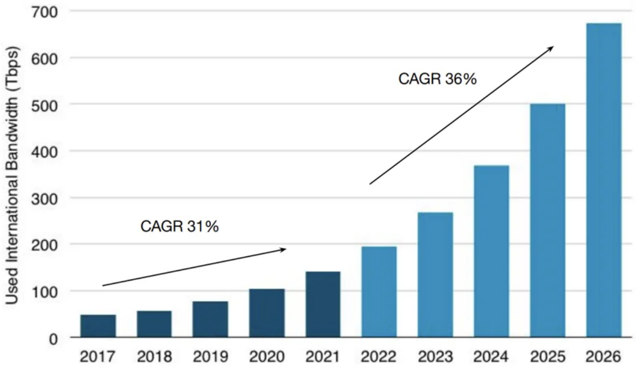

Figure 1.1: Used International Bandwidth in Latin America, 2017 - 2026 [1].

Current long-haul optical networks are based on WDM with standard single-mode fiber (SMF) infrastructure [9] using PDM and modulation formats such as m-phase shift keying (m-PSK) and m-quadrature amplitude modulation (m-QAM). Figure 1.2 shows the evolution of research demonstrations reported in [2], with data rate records in WDM systems using SMF from 1996 to 2021. Data rates of WDM systems have been mostly limited to around 100 Tbps, making it difficult to cope with the growing demand for bandwidth [9]. However, with the adoption of new transmission bands, the data rate could double [2].

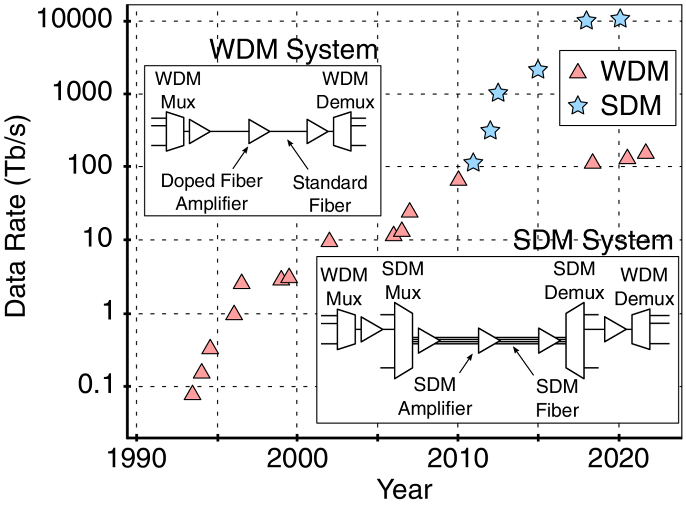

Figure 1.2: Evolution of data rate records for WDM systems and SDM systems. Top inset: Generalized WDM system. Bottom inset: Generalized SDM transmission system. [2]

One short-term solution to address the *capacity crunch* is the adoption of a flexible frequency grid [9], which gives rise to the new paradigm of elastic optical networks (EON); the use of the L band [9] and, the use of complex technology based on digital signal processing [9]. EON proposes the division of the optical spectrum into frequency ranges of 12.5 GHz [10], called *slots*, which are grouped to respond to the transmission requirements of users. For a long-term solution, the alternatives that seem to be the most effective way to increase the capacity per fiber are to use fibers that support multiple spatial modes or multiple bands of the optical spectrum [6]. Figure 1.2 also shows the evolution of data rate records in SDM systems from 2011 to 2021, reported in [2]. Those SDM studies have been shown to achieve data rates nearly 2 orders of magnitude greater than WDM. Virgillito *et al.* [11] presented a comparative study regarding the increase in capacity offered by SDM and BDM technologies, concluding that whenever SDM is an alternative from a techno-economic point of view, it is preferable over BDM.

A basic WDM and SDM transmission system are plotted in the upper and lower inset of Figure 1.2, respectively. The main components are the optical fiber, the MUX/DEMUX, and the optical amplifiers, in this case, the doped fiber type is represented. The main difference between both schemes is the requirement for additional MUX/DEMUX in the spatial domain to direct optical signals in and out of spatial channels in the SDM system.

The basic concept of SDM is based on placing numerous spatial channels in an optical fiber structure or array [12]. Figure 1.3 shows the different types of SDM fibers that have been developed [2], such as single-mode fiber bundles (SMF-B), multi-core fibers (MCF), few-mode or multi-mode fibers (FMF or MMF), or combinations of these such as few-mode multi-core fibers (FM-MCF). One parameter that characterizes an SDM fiber is spatial efficiency defined as the number of spatial channels per unit area of the optical fiber [13].

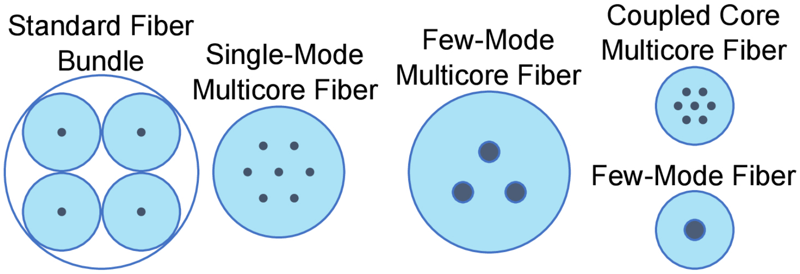

Figure 1.3: Types of SDM fibers [2].

In an SMF-B many conventional single-mode fibers are packed together to create a thick fiber bundle or flat cable [12], of large dimension, where crosstalk between cores does not occur [3]. SMF-B offers up to hundreds of parallel links, at the expense of its large dimension, thus having low spatial efficiency [12]. This form of SDM is commercially available and has been adopted in current optical infrastructure [12].

MCFs can be classified into two categories according to the separation distance between the cores. The first category corresponds to weakly-coupled MCFs, where the distance between neighboring cores, known as core pitch, is designed large enough to reduce the coupling between cores [13], this distance must be greater than 30 μm [14]. In this case, no multiple-input multiple-output (MIMO) digital signal processing (DSP) is required at the receiver side to recover the signal. The second category is strongly-coupled MCFs, where the core pitch is less than 30μm and strong inter-core crosstalk occurs [14]. In this case, MIMO-DSP is required at the receiver side to recover the signal [12]. The most important restriction in MCFs is the crosstalk between cores [12, 15]. Different core arrangements have been proposed in the literature such as single-ring and double-ring structures, linear array, two-pass structure, and hexagonal structure [12]; however, the combination of 7 cores with a hexagonal array is the most widely used in research [10].

MMFs support tens of guided transverse modes for a given optical frequency and polarization, operating efficiently over short distances [12]. As a simpler alternative, FMFs use a small number of linearly polarized (LP) modes as spatial channels [16], typically between 2 and 10-20 modes [17]. In the particular case of FMF, SDM is known as mode-division multiplexing (MDM). FMFs have a greater potential to reduce the cost per bit, because they carry more data per unit area, achieving greater spatial efficiency compared to MCFs, and unlike MMFs they allow long-distance communication [12]. The main limitations of MMF and FMF fibers include mode coupling and differential modal group delay [12, 18, 15].

In FM-MCFs, several modes are multiplexed in each fiber core [16]. It is a combination of MCF and FMF, which increases the capacity by a factor multiple of the number of cores and the number of modes ($\#\, cores \times \#\, modes$) [12]. FM-MCFs must simultaneously overcome the problems of both MCF and FMF, however, the most critical aspect of FM-MCFs is the crosstalk between cores [12].

To fully capitalize on the benefits offered by SDM transmission networks, including improved spatial efficiency and reduced power consumption, a rigorous design of all optical components within the network is necessary. This includes elements such as optical amplifiers, switches, filters, multiplexers and demultiplexers, isolators, pump combiners, and various other components, ensuring a feasible system.

From the above analysis, the importance of the study and development of SDM networks for future fiber optic communication networks is evident. This thesis will study SDM-FMF systems, specifically the aspects related to propagation and optical amplification since they are the main elements in achieving long-haul transmission systems. Mathematical models for propagation and optical amplification will be studied and implemented on a computer, modeling the physical layer impairments affecting SDM-FMF systems. The design of the optical amplifiers will also be optimized. This modeling and optimization will provide insights into the quality of transmission in an FMF link to solve the problem of resource allocation.

1.2 Hypothesis

This thesis aims to answer the following research question:

Research question

How can the physical layer impairments of amplified SDM-FMF optical networks be effectively managed to mitigate their impact on transmission quality and resource allocation within these networks?

To answer the research question, it is essential to characterize and model in terms of mathematical expressions, the physical layer impairments (PLI) present in an optical path, to represent, evaluate, and predict the quality of transmission (QoT) of FMF links. Properly estimating the quality of received signals allows for the design of networks that can meet current and future bandwidth requirements. Consequently, the hypothesis of this thesis is formulated as follows:

Hypothesis

Accurate and rigorous characterization and modeling of physical layer impairments in few-mode fiber links enable the optimization, evaluation, and prediction of the quality of transmission in SDM-FMF optical networks. By optimizing optical amplifier configurations and employing integrated physical layer models, resources in these networks can be managed more effectively, enhancing performance and meeting bandwidth requirements.

The performance of the FMF links considered in this work will be measured, mainly, in terms of the signal-to-noise ratio (SNR) or the optical signal-to-noise ratio (OSNR), which are limited by the amplified spontaneous emission (ASE) noise generated by amplifiers; and by the crosstalk (XT) between propagation modes generated by the modal coupling present in SDM-FMF transmission. The ASE noise power is determined by the amplification scheme used; this thesis will address lumped amplification employing few-mode erbium-doped fiber amplifiers (FM-EDFA), and distributed amplification using few-mode distributed Raman amplifiers (FM-DRA). The crosstalk (XT) between propagation modes depends on the mode coupling regime. This work focuses on two coupling regimes: the weak-coupling regime, representing the ideal scenario, and the intermediate coupling regime, reflecting practical conditions. Both regimes account for linear and nonlinear PLI, which must be accurately characterized to evaluate the QoT of FMF links.

The use of FMF amplifiers involves challenges related to the non-flatness -modal and spectral- of the amplifier gain profiles; therefore, optimization is necessary to achieve the lowest differential modal gain (DMG) in the spatial domain and the lowest gain ripple in the spectral domain. In this work, genetic algorithms will be used to design optimized pumping profiles for FM-EDFA and FM-DRA.

Efficient management of available resources is essential to avoid the potential capacity crunch of data transport networks. Inefficient utilization of spectral and modal resources can lead to fragmentation in both dimensions, ultimately degrading network performance. This poor performance can be measured in a reduced number of served users in networks with static operation, or high blocking probability rates in networks with dynamic operation.

Applying an integrated physical layer model and optimizing amplifier configurations to estimate the transmission quality in FMF links allows the design of algorithms that solve the resource allocation problem considering the limitations imposed by the physical layer. For network operators, it is important to estimate the transmission quality of the links in a rigorous manner, since this way the overestimation or underestimation of the effect of the PLI is avoided. Overestimation results in inefficient resource usage, while underestimation can lead to non-compliance with service level agreements, both cases are unfavorable for the operation of the network.

The assignment of routes, spatial modes, and spectrum in the SDM-FMF is solved with routing, spatial mode, and spectrum allocation (RSSA) algorithms; these are usually heuristics in which the route is selected first, then the spatial mode is selected, and finally, the portion of the spectrum to attend the request is assigned. In this work, transparent networks are considered; this implies that there is no opto-electrical-optical regeneration of the signals, so there are continuity restrictions -modal and spectral- in the assignment of resources.

1.3 Summary of Contributions

The contribution to the state-of-the-art of this work is summarized as follows:

- Signal propagation through SDM-FMF was studied under two coupling regimes: weak-coupling and intermediate coupling. Both regimes include linear and nonlinear physical layer impairments (PLI). Attenuation, dispersion, crosstalk, mode-dependent loss, and differential mode delay are the main linear PLIs. While, self-phase modulation, cross-phase modulation, and four-wave mixing are the main nonlinear PLIs. The performance of an FMF system was evaluated by comparing the signal-to-noise ratio (SNR) under these two coupling regimes.
- A new methodology, named Joint DMG-DSG Minimization, was applied to design SDM-WDM networks based on optimized FM-EDFA of two-stages. This approach minimizes differential modal gain (DMG) and differential spectral gain (DSG) per LP mode, which are the main limitations of optical amplification in SDM-WDM systems. The methodology integrates gain flattening filters (GFF) with a multi-pump profile design obtained using a genetic algorithm (GA). For the first time, it was designed a two-stage 6M-EDFA supporting a dense number of wavelengths in the conventional C-band. Additionally, this thesis presents the first study of a full-load link composed of a cascade of two-stage FM-EDFAs.
- It was studied the performance of FM-DRA with a more rigorous mathematical model incorporating noise contributions often neglected in prior studies. This approach provides a more accurate analysis of FM-DRA performance. Furthermore, the pumping profile for a 6M-DRA was optimized by using a genetic algorithm to minimize gain variations in both the modal and wavelength domains. For the first time, was characterized the performance of a 6M-DRA in terms of on-off gain, effective noise figure, OSNR, and pumping efficiency.
- For the first time, a dynamic mode-group division multiplexing (MGDM) network was studied using optical amplification based on FM-EDFA. A novel algorithm, BANG (**B**alanced **A**llocatio**N** of Mode **G**roups) was proposed for dynamic network provisioning in SDM-FMF systems under MGDM. It was compared the blocking probability of BANG against a baseline based on a state-of-the-art algorithm in various scenarios, using optical reach values that considered not only the propagation impairments in SDM-FMF networks, but also few-mode amplification. Simulation results showed that BANG algorithm outperforms the state-of-the-art in well-connected networks by up to 100%.

1.4 Summary of Publications

This thesis is supported by the following articles in journals and conferences, where the author of this work is the main author.

Journal Publications

1. **A. Lozada**, F. Calderón, J. Núñez, D. Bórquez-Paredes, R. Olivares, A.Beghelli, N. Jara, A. Leiva, and G. Saavedra, “Impact of Amplification and Regeneration Schemes on the Blocking Performance and Energy Consumption of Wide-Area Elastic Optical Networks”. IEEE Access, vol. 9, pp. 134355-134368). [19]
2. **A. Lozada**, R. Olivares, N. Jara, P. Morales, B. D. Feris, A. Leiva, G. Saavedra, and D. Bórquez-Paredes, “Performance evaluation of a two-stage few-mode EDFA for high-capacity SDM systems,” Optics Express, vol. 32, no. 23, pp. 41 417–41 432, 2024. [20]
3. **A. Lozada**, R. Olivares, A. Leiva, G. Saavedra, N. Jara, P. Morales, B. Dumas and D. Bórquez-Paredes, “Optimized Backward Pumping Design for a 6-Mode Distributed Raman Amplifier for SDM Systems,” IEEE Photonics Technology Letters, 2024. (Submitted)

Conference Publications

4. **A. Lozada** and R. Olivares, “Optimized Two-Stage Few-Mode Erbium Doped Fiber Amplifier,” in 2023 SBMO/IEEE MTT-S International Microwave and Optoelectronics Conference (IMOC), 2023, pp. 316–318. [21]
5. **A. Lozada**, R. Olivares, D. Bórquez-Paredes, F. M. Ferreira, and A. Beghelli, “Few-Mode Amplification-Aware Resource Allocation in Mode-Group Division Multiplexing Systems,” in IEEE Latin-American Conference on Communications, 2024. [22]

Additional Journal Publications

6. F. I. Calderón, **A. Lozada**, D. Bórquez-Paredes, R. Olivares, E. J. Davalos, G. Saavedra, N. Jara, and A. Leiva, “BER-Adaptive RMLSA Algorithm for Wide-Area Flexible Optical Networks,” IEEE Access, vol. 8, pp. 128 018–128 031, 2020. [23]
7. P. Morales, **A. Lozada**, D. Bórquez-Paredes, R. Olivares, G. Saavedra, A. Leiva, A. Beghelli, and N. Jara, “Improving the Performance of SDM-EON Through Demand Prioritization: A Comprehensive Analysis,” IEEE Access, vol. 9, pp. 63 475–63 490, 2021. [24]
8. F. Calderón, **A. Lozada**, P. Morales, D. Bórquez-Paredes, N. Jara, R. Olivares, G. Saavedra, A. Beghelli, and A. Leiva, “Heuristic Approaches for Dynamic Provisioning in Multi-Band Elastic Optical Networks,” IEEE Communications Letters, vol. 26, no. 2, pp. 379–383, 2022. [25]
9. D. Bórquez-Paredes, A. Beghelli, A. Leiva, N. Jara, **A. Lozada**, P. Morales, G. Saavedra, and R. Olivares, “Agent-based distributed protocol for resource discovery and allocation of virtual networks over elastic optical networks,” Journal of Optical Communications and Networking, vol. 14, no. 8, pp. 667–679, 2022. [26]

10. J. Pinto-Ríos, F. Calderón, A. Leiva, G. Hermosilla, A. Beghelli, D. Bórquez-Paredes, **A. Lozada**, N. Jara, R. Olivares, and G. Saavedra, "Resource allocation in multi-core elastic optical networks: a deep reinforcement learning approach," Complexity, vol. 2023, no. 1, p. 4140594, 2023. [27]

Additional Conference Publications

11. D. Bórquez-Paredes, F. Calderón, N. Jara, A. Leiva, **A. Lozada**, R. Olivares, and G. Saavedra, "3R Regeneration in Elastic Optical Networks and its Impact on the Network Quality of Service," in 2020 22nd International Conference on Transparent Optical Networks (ICTON), 2020, pp. 1–4. [28]
12. J. Bermúdez, **A. Lozada**, R. Olivares, and N. Jara, "Fragmentation-aware spectrum assignment strategies for elastic optical networks with static operation," in 2020 39th International Conference of the Chilean Computer Science Society (SCCC), 2020, pp. 1–8. [29]
13. D. Hernández, P. Morales, **A. Lozada**, R. Olivares, and N. Jara, "On sorting transmission demands in Elastic Optical Networks with Spatial-Division Multiplexing," in 2020 39th International Conference of the Chilean Computer Science Society (SCCC), 2020, pp. 1–8.[30]
14. P. Morales, P. Franco, **A. Lozada**, N. Jara, F. Calderón, J. Pinto-Ríos, and A. Leiva, "Multi-band Environments for Optical Reinforcement Learning Gym for Resource Allocation in Elastic Optical Networks," in 2021 International Conference on Optical Network Design and Modeling (ONDM), 2021, pp. 1–6. [31]

1.5 Thesis Structure

The remainder of this thesis is structured as follows:

- Chapter 2 introduces the fundamental aspects of SDM systems, including SDM optical fibers, optical amplification solutions, optical switching technologies, and the principles of the resource allocation problem.
- Chapter 3 introduces the fundamental aspects of SDM-FMF propagation, including basic FMF concepts, as well as the linear and nonlinear PLI that affect signal transmission. The principles of the weak and intermediate coupling regimes are discussed, along with the mathematical models to numerically simulate these coupling regimes. Simulation results are also presented.
- Chapter 4 focuses on optical amplification based on FM-EDFAs. It begins with a review of the relevant literature, followed by a detailed description of the two-stage FM-EDFA design methodology joint DMG-DSG minimization. The chapter includes simulation results of the designed pumping and gain flattening filter (GFF) profiles, and the characterization of the two-stage FM-EDFA using forward, backward and bidireccional pumps. Additionally, an analysis of the simulation results of a link composed of a cascade of the designed amplifier with forward pumping is also presented.
- Chapter 5 focuses on optical amplification using FM-DRAs. It starts with a review

of the relevant literature and then describes the mathematical model of FM-DRAs, including the use of a genetic algorithm to optimize the pumping profile. The chapter then presents the theoretical characterization of FM-DRAs with backward, forward, and bidirectional pumping.

- Chapter 6 introduces the BANG algorithm, a PLI-aware heuristic designed to solve the RSSA problem. The chapter begins with a literature review of resource allocation in SDM-FMF networks using mode-group division multiplexing technology. Then, the description of the network models, including the physical layer, network, and traffic models is provided. The BANG algorithm is then presented in detail, as well as the simulation results.
- Chapter 7 presents final remarks and future work.

2

SDM Technology

2.1 Introduction

To set the basis for a detailed study of SDM-FMF systems, this chapter begins with an overview of the fundamental components of an SDM system and the physical layer impairments that influence their performance. The following sections will review key elements such as SDM fibers, optical amplification techniques, optical switching solutions, and resource allocation principles. A basic schematic of an SDM link is shown in Figure 2.1. Transmitters (Tx) and Receivers (Rx) can operate with conventional single-mode fiber (SMF), each carrying WDM signals, while all intermediate elements - such as optical fiber, multiplexers/demultiplexers, optical amplifiers, switches, and reconfigurable optical add/drop multiplexers (ROADM)- operate with SDM technology. Additionally, Figure 2.1 shows the physical layer restrictions introduced by each element. SDM multiplexers/demultiplexers and ROADM introduce crosstalk and insertion losses, while optical amplifiers, including EDFAs and Raman, add ASE noise, crosstalk, and mode-dependent gain. Besides, the SDM fiber introduces linear and nonlinear phenomena that further impact signal propagation.

Some physical layer impairments that affect SDM have been identified in the literature, and their significance varies depending on the network extension (long-haul, metro/region, data center). In general, the propagation of light in the p mode of an optical fiber can be represented by a linear part ($\widetilde{D_p}$) and a nonlinear part ($\widetilde{N_p}$) [32]. The linear part depends on parameters such as the fiber attenuation coefficient, dispersion, group velocity, mode propagation constant, and crosstalk between spatial modes. On the other hand, the nonlinear component depends on phenomena such as self-phase modulation, cross-phase modulation, and four-wave mixing [32]. These impairments are simultaneously classified into intramodal restrictions, when they occur within a spatial mode, either a core in an MCF or an LP mode in an FMF; and intermodal restrictions, when they occur between

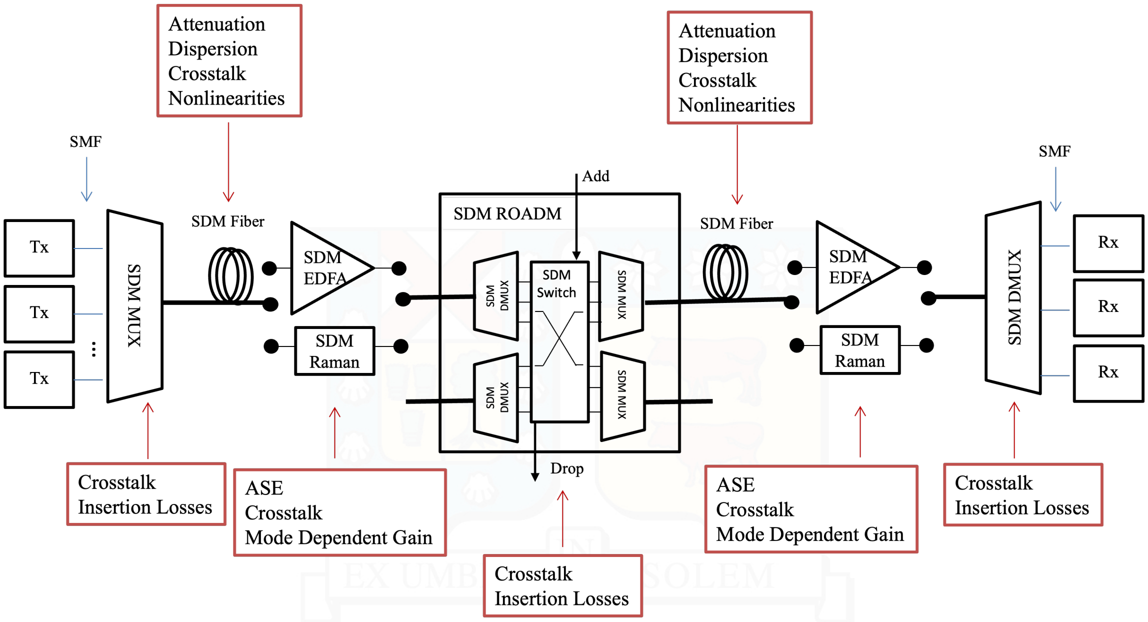

Figure 2.1: Basic schematic of a SDM link.

spatial modes.

Including linear and nonlinear effects in the mathematical modeling of optical signal propagation in SDM fibers, as well as the impairments introduced by amplifiers and optical nodes, is a fundamental task, as it allows for representing the physical layer phenomena that limit the performance of the transmission system and to determine the maximum transmission rate or maximum transmission reach for a network.

This chapter presents a review of the basic elements of an SDM system. It is structured as follows: Section 2.2 starts by describing SDM fibers; Section 2.3 presents a review of optical amplification solutions for SDM systems; Section 2.4 describe some optical switching solutions for SDM systems. Finally, in Section 2.5 the principles of resource allocation are presented.

2.2 SDM Optical Fiber

Figure 2.2 summarizes the main types of SDM fiber: SMF-B, MCF, FMF or MMF, and FM-MCF, which will be described next.

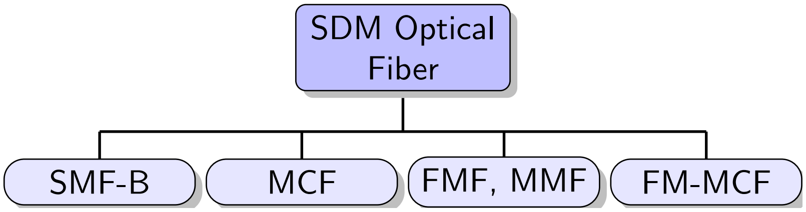

Figure 2.2: Classification of SDM optical fibers.

- **Single-Mode Fiber Bundles (SMF-B)**

  In an SMF-B, many conventional single-mode fibers are packed together to create a larger cable [12], where no crosstalk between cores occurs [3]. SMF-B offers up to hundreds of parallel links at the expense of its large dimension, thus having low spatial efficiency [12]. For the same diameter or cross-sectional area, they offer fewer spatial channels. However, this type of optical SDM fiber has been introduced as the first generation of SDM technology [33]. Nowadays, a reduced number of submarine optical cables are using this type of technology. The Dunant cable, was the first submarine cable using SDM fiber [33], with 12 fiber pairs, covering 6600 km between the United States and France, crossing the Atlantic, operating since January 2019. For 2025, 18 SDM submarine fiber cables will be ready for service, with 24 the maximum number of fiber pairs in one SMF-B [33].

- **Multi-Core Fiber (MCF)**

  MCFs can be classified into two categories according to the core pitch. The first category corresponds to weakly-coupled MCFs, where the core pitch is designed large enough to reduce the inter-core crosstalk. The second category corresponds to strongly-coupled MCFs, where strong crosstalk between cores occurs [14]. At first glance, using MCFs with more cores is advantageous due to the higher resource availability [10]. However, the most important physical impairment in MCFs is the inter-core crosstalk [12] which increases with transmission distance. Therefore, long-haul networks are especially sensitive to this physical impairment [3]. Consequently, the inter-core crosstalk limits the distance that optical signals can travel while preserving a certain transmission quality [34]. Thresholds associated with crosstalk have been established in the literature for different modulation formats. The estimation of this threshold is related to the maximum distance that a signal with a certain modulation format can travel while preserving a certain transmission quality. In this way, lower-level modulation formats, such as BPSK, can tolerate greater crosstalk than higher-level modulation formats, such as 64-QAM [27].

  Studies have been performed on how to minimize crosstalk in MCF structures, and it has been shown that it can be successfully addressed by using trench-assisted cores with step [12] and graded [13] refractive index profiles. Other studies have used well-spaced cores to minimize the inter-core crosstalk [12]. Another proposed solution is to use cores with different refractive indices resulting in an MCF with heterogeneous cores, or even to allocate bidirectional optical signals on adjacent cores to avoid long co-propagation in the same direction and thus reduce crosstalk [12].

- **Few-Mode Fiber (FMF) and Multi-Mode Fiber (MMF)**

  MMFs can support hundreds of guided transverse modes for a given optical frequency and polarization, operating efficiently over short distances, typically over tens of meters [12]. The main constraints with MMFs, especially when many modes co-propagate, are modal dispersion, inter-mode crosstalk, and differential mode delay [12]. Addressing these issues requires compensation through MIMO-DSP at the receiver [12]. As a simpler alternative with reduced DSP complexity, FMFs use a limited number of LP modes as spatial channels [16], ranging from 2 to 20 modes [17], and unlike MMFs, allow long-distance communication [12]. FMFs also have greater potential to reduce the cost per bit compared to MCFs, as they carry more data per unit area, achieving greater spatial efficiency [17]. However, major limitations in FMF fibers include crosstalk between modes and the differential mode delay [12, 18, 15].

Linear crosstalk between LP modes degrades the quality of optical signals in FMF and MMF fibers. Its origin lies in fiber imperfections, splices, mode multiplexers, and mode demultiplexers [17, 35]. Additionally, the differential mode delay arises due to the different propagation velocities of guided modes [17], it corresponds to the time difference between the fastest mode and the slowest mode in a core [36]. Consequently, fractions of the same light pulse traveling in different modes arrive at the receiver at different instants, leading to pulse broadening [17]. Successful demultiplexing in FMF systems without high-order MIMO-DSP equalization requires a limited amount of differential mode delay and inter-mode crosstalk [17], which is typically the case for short distances; in long-haul systems, the use of high-order MIMO-DSP is required to compensate for the differential mode delay and crosstalk effects [17].

- **Few-Mode Multicore Fiber (FM-MCF)**

  In FM-MCFs, multiple modes are multiplexed onto each fiber core [16]. It is a combination of MCF and FMF, which increases the capacity by a factor of the number of cores in the MCF times the number of modes in the FMF [12]. FM-MCFs must simultaneously overcome the physical impairments of both MCF and FMF, however, the most critical aspect in FM-MCFs has been identified as the crosstalk between cores [12]. Increasing the number of LP modes per core in FM-MCF increases inter-core crosstalk because higher-order modes extend further into the cladding area [2]. Therefore, well-spaced and trench-assisted cores have been used to reduce inter-core crosstalk.

2.3 SDM Optical Amplifiers

Several solutions have been proposed for optical amplification for SDM systems based on MCF or FMF, including conventional EDFAs, i.e., with single-mode operation; FM-EDFA; MC-EDFA and distributed Raman amplifiers (DRA) [37, 38]. Regardless of the type of amplifier used, it must be able to uniformly amplify both cores/modes and wavelengths over the optical band used [37].

In a transmission system using conventional single-mode EDFAs, modal multiplexer/demultiplexer devices can be used to demultiplex the spatial channels [18]. Each channel is amplified by a different single-mode EDFA and then multiplexed back onto the FMF or MCF transmission line. The advantage of this scheme lies in the gain control of each spatial channel. However, this is achieved at the expense of high amplification cost [18].

To reduce the cost and power consumption compared to parallel single-mode EDFA, channels must share the pump. Considering this, two pumping schemes have been developed: core-pumping and cladding-pumping [38]. Core-pumping implies that, the original signal after co-propagation with the pump signals in each core, is amplified, just as in classical EDFA systems [12]. In cladding pumping, a single pump source, pumps simultaneously all the cores coupled in the cladding [12]; additionally, cores are co-doped with ytterbium to increase the pump absorption [39].

SDM amplification schemes, such as MC-EDFA, FM-EDFA, or FM-DRA, are more attractive as they offer cost-effectiveness through the integration of amplifiers [18]. The major challenge regarding the implementation of such systems is to ensure uniform gain in both the spatial and spectral domains [18]. However, this is complicated by the presence of crosstalk between spatial modes and mode-dependent losses. As a result, the most important design parameters for SDM amplifiers are the differential modal gain (DMG) and the gain ripple.

In FM-EDFA and FM-DRA, lower-order modes experience lower propagation loss in the fibers and lower insertion loss in the optical components. These modes also tend to be significantly amplified compared to higher-order modes [40]. When the number of modes increases, MDG control becomes increasingly difficult [17]. To address DMG and gain ripple minimization, different strategies have been proposed in the literature. These strategies include doping profile optimization [37, 41, 42], refractive index profile optimization [43], and pump signal optimization in terms of the number of modes, wavelengths, and power levels [37, 41, 42, 44].

Regarding MC-EDFAs, these can be pumped in the core or the cladding. Pumping each core separately in an MC-EDFA using single-mode pumping, although it implies a higher cost, has the advantage of allowing independent control of the gain in each core by adjusting the power of the pump signal [39]. Pumping in the cladding, on the other hand, requires fewer optical components and has the potential to use low-cost multimode diodes [39], in this case, the cores are co-doped with ytterbium to increase the pump absorption [39, 45].

DRA amplification also can be used in combination with MC-EDFAs or FM-EDFAs to form hybrid schemes [46, 47].

2.4 SDM Reconfigurable Optical Add/Drop Multiplexer (ROADM)

ROADM optical switching hardware enables wavelength channels to be added or dropped across fiber optic networks, either by routing channels at network nodes to their final destination or by simply replacing them with new channels at intermediate nodes. However, signal degradation occurs at crossing nodes due to losses and crosstalk.

Switching strategies for SDM are classified by the switching granularity, i.e., by the smallest switched element [48, 3, 49]. Figure 2.3 summarizes the paradigms of optical switching for SDM systems.

The highest switching granularity is offered by independent spatial-spectral switching [3], where each spatial mode and wavelength channel can be switched individually to any output port of the ROADM, as shown in Figure 2.3.a, at the expense of high implementation complexity [3].

Less complex schemes than independent switching offer either spatial or spectral granularity. In the former case, spatial switching is performed in the spatial domain across

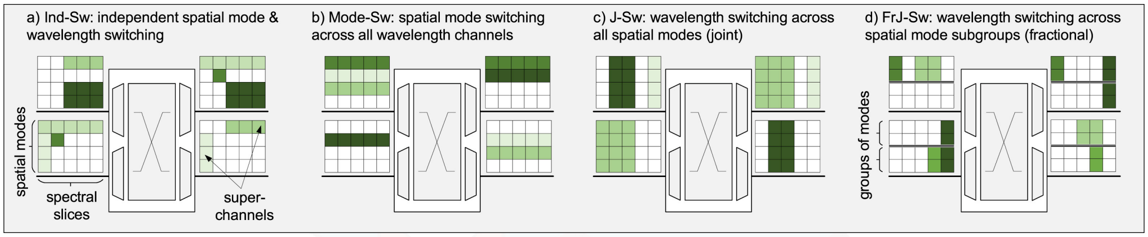

Figure 2.3: Spectral-spatial switching paradigms [3].

the entire optical communication band (all WDM channels), as shown in Figure 2.3.b, losing any wavelength flexibility [48, 3]. Spectral switching, also called wavelength switching, shown in Figure 2.3.c, sacrifices the spatial domain to simplify the switching hardware. The latter case is the only applicable one when all spatial modes are strongly coupled since they must stay together throughout the network [48, 3].

Another proposed switching scheme under the SDM scenario offers full-wavelength and fractional spatial granularity, this switching scheme is called mode-group division multiplexing [49]. This scheme is appropriate for fibers where the coupling between modes is limited within spatial subgroups. This strategy adopts a wavelength granularity approach for subgroups, and each subgroup can be switched independently based on wavelength, shown in Figure 2.3.d. The attractive features of this strategy are intermediate routing flexibility and moderate implementation complexity [48, 49].

The choice of switching granularity directly affects the specific SDM-ROADM architecture, resource assignment provisioning, and overall network performance [48].

2.5 Resource Allocation in SDM

The resource allocation problem in SDM networks consists of finding a route - an optical connection between two network nodes-, a spatial mode (core, mode, or a mode-core pair), and a portion of the spectrum - a wavelength using the fixed grid approach or a group of frequency slot units using the flexible grid approach - available in the route to serve a connection request from a user in the SDM network. This problem is often referred to as the RSSA (routing, spatial mode, and spectrum allocation) problem [3, 50]. From a resource allocation point of view, the main challenge in establishing optical connections is the efficient usage of spectrum resources [3, 24].

The methodologies implemented in the literature to solve the RSSA problem have been optimization using mathematical programming, heuristics, and metaheuristics [3]. Optimization using integer linear programming for networks with static operation has the disadvantage that these solutions are not scalable to real network topologies due to their high computational cost [3]. Heuristics and metaheuristics, although they do not guarantee an optimal result, have no applicability limitation in terms of the network topology or the type of assignment (static or dynamic). Recently, machine learning techniques have been used to complement traditional techniques to solve the RSSA problem [51, 52, 27].

Heuristic solutions for the RSSA problem are usually solved in sequential stages [24], as shown in Figure 2.4. First, a route is assigned, often based on the shortest path. Next, a suitable spatial mode is chosen, which can include the previous selection of a modulation format. This means that an adaptive selection of the most efficient modulation format is performed. Resulting in the Routing, Modulation Level, Spatial mode, and Spectrum Allocation (RMLSSA) problem [24], also shown in Figure 2.4. Finally, the spectrum on each link is assigned, typically, using the first available slot [24].

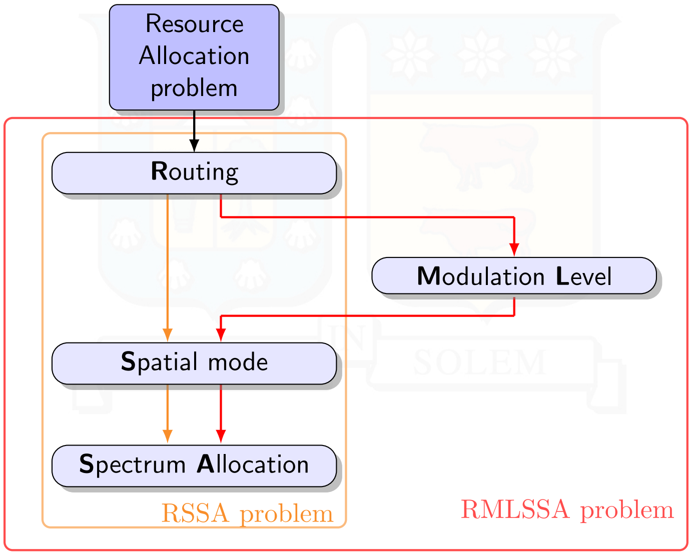

Figure 2.4: Diagram of the sequential stages in the solution of the RSSA (or RMLSSA) problem.

As a consequence of the sequential approach used to solve the RSSA or RMLSSA problem, it is usual to find unallocated spectral resources. This situation, known as fragmentation, is undesirable because it might prevent attending to additional demands due to inefficient capacity usage. Therefore, a common goal of RSSA and RMLSSA solutions is to decrease fragmentation to maximize capacity utilization [53]. In static operation, it has been shown that the order in which demands are served affects network fragmentation and, therefore, network capacity requirements [24].

For transparent optical communications (without wavelength conversion), RSSA and RMLSSA algorithms must comply with the following constraints: first, each wavelength can host only one demand; second, the assigned wavelength must be maintained along the entire origin-destination route and spatial mode, known as the continuity and spatial mode constraints, respectively.

In solving the RSSA and RMLSSA problems, the physical layer impairments imposed when signals propagate along optical links must be considered for each SDM system scenario (MCF, FMF, and FM-MCF). In this context, provisioning algorithms are required for network operators to assign resources considering the physical layer restrictions that degrade link performance. For example, resource allocation algorithms for an SDM network based on MCF must account for inter-core crosstalk [54, 27], while those based on FMF must consider crosstalk between LP modes [49]. These constraints are mentioned as an example, the rigor with which physical layer constraints are aware will depend largely on the associated computational cost and the focus of the solution.

Typically, maximum optical reach tables are pre-calculated offline under specific network configurations or scenarios [49, 55, 54, 24, 27]. These tables are then used as input data for RSSA or RMLSSA solutions. Considering physical layer restrictions for provisioning allows efficient use of resources by adapting them to real operating scenarios. Inefficient use of spectral and spatial resources will generate fragmentation in both spatial and spectral dimensions, leading to poor network performance.

2.6 Conslusions

In an SDM system, several WDM signals are launched into spatial channels of an SDM optical fiber structure. These spatial channels can be cores in an MCF, LP modes in an FMF, or combinations of these in FM-MCF fibers. To implement SDM technology, it is necessary to have elements such as optical fiber, amplifiers, switches, and multiplexers/demultiplexers, that operate under this technology. In this chapter, the main aspects regarding SDM optical fiber, SDM amplifiers, SDM ROADM, as well as the resource allocation problem for this technology, were described.

Among the SDM optical fiber solutions are SMF-B, MCF, MMF, FMF and FM-MCF. Ordered from the lowest to the highest spatial efficiency. The first generation of SDM has been based on the deployment of SMF-B, which, while increasing network capacity, has low spatial efficiency, as it offers fewer spatial channels for the same diameter or cross-sectional area. FMFs have a greater potential to reduce the cost per bit, because they carry more data per unit area, achieving greater spatial efficiency compared to SMF-B and MCFs.

Regarding amplification schemes for SDM systems, solutions based on EDFAs and DRAs have been proposed for both MCF and FMF. One of the main challenges is to obtain a uniform gain profile both at the spatial and spectral domains.

SDM ROADMs offer different levels of granularity for signal switching. The highest granularity would allow each wavelength to be addressed in each mode independently, however, this fine granularity has a very high complexity. Therefore, switching with spatial or spectral granularity is also an option. Additionally, switching by mode groups presents the best balance between the granularity and flexibility offered with the complexity of implementation.

Another important aspect of deploying SDM technology is the solution of the RSSA problem, which must consider the physical layer impairments imposed by each SDM system scenario. In this sense, resource allocation is carried out considering real conditions of the optical links. Therefore, they can be based on restrictions such as maximum optical reach or minimum signal-to-noise level required considering a certain modulation format, or using thresholds for crosstalk between spatial modes produced by the type of SDM fiber used as a propagation medium, all while preserving certain transmission quality. When allocating resources, the spectral and spatial continuity constraints in transparent networks must also be respected. Inefficient use of spectral and spatial resources will generate fragmentation in both dimensions, which leads to poor network performance.

From the analysis presented, it is evident the importance of the study and development of SDM networks for future fiber optic networks, in particular, it is necessary to have mathematical models that adequately integrate all the phenomena that occur in the physical layer, for the design, planning, and administration of optical networks, with the objective of making efficient use of resources. Consequently, in this work, the mathematical modeling of physical layer restrictions and the optimization of optical amplification for SDM networks based on FMF is deepened.

The next chapter will start by addressing the physical layer impairments and their mathematical modeling during propagation.

3

Few-Mode Propagation

3.1 Introduction

In the transition from current WDM systems to WDM-SDM networks, FMFs emerge as a promising solution due to their enhanced spatial efficiency compared to MCFs. Additionally, the deployment of MMF in short-reach links provides an opportunity to facilitate this transition with minimal infrastructure changes. By transforming existing MMF links into FMF links and replacing only intermediate network nodes, significant cost savings can be achieved while leveraging the benefits of spatial multiplexing. For these reasons, this work addresses the study and optimization of SDM-FMF systems.

This chapter presents a review of optical signal propagation in SDM-FMF systems. Physical layer impairments (PLI) are the main source of limitation in SDM-FMF system capacity and its maximum transmission reach. PLI related to the multimode nature of the optical fiber can be classified into inter-modal linear and nonlinear categories.

The inter-modal linear impairments are the differential mode delay (DMD), linear mode crosstalk (XT), and mode-dependent loss (MDL). The inter-modal nonlinearities are the cross-phase modulation (IM-XPM), inter-modal four-wave mixing (IM-FWM), and inter-modal stimulated Raman scattering (IM-SRS). Besides the linear and nonlinear impairments, components such as mode-multiplexers (de) (MMUXs/MDMUXs) can introduce additional insertion losses and optical amplifiers can introduce mode-dependent gain and amplified spontaneous emission (ASE) noise.

This chapter is structured as follows: Section 3.2 starts by reviewing the FMF modal theory, introducing key concepts regarding the spatial modes inside an FMF. Then, in Section 3.3, the linear and nonlinear physical layer impairments are identified. Next, in Section 3.4, the mathematical models to numerically simulate propagation with different levels of inter-modal coupling in an FMF, are presented. Subsequently, Section 3.5 presents the simulation results under two types of inter-modal coupling regimes. Finally, Section 3.6 summarizes this chapter.

3.2 Few-Mode Fiber

Optical fibers transmit light by confining the optical wave to a microscopic cylindrical glass core with a high refractive index surrounded by a low refractive index cladding, a phenomenon known as total internal reflection. Based on the refractive index profile, there are two main types of optical fiber: step-index (SI) and graded-index (GI), as shown in Figure 3.1. In SI fibers, there is an abrupt change between the refractive index of the core, n_1, and the refractive index of the cladding, n_2. In GI fibers, there is a gradual change from the refractive index of the core to the cladding, it can follow different types of shapes as a function of the radial coordinate. The most common type of GI fibers have a parabolic shape.

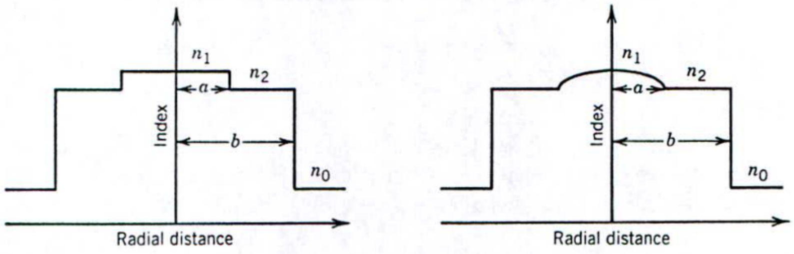

Figure 3.1: Cross section and refractive-index profile for step-index (left) and graded-index (right) fibers [4].

The total electric field propagating in FMFs can be written in the spectral domain as a sum of M distinct spatial modes in the fiber, as follows [35, 56]:

$$\widetilde{\mathbf{E}}(x, y, z, \omega) = \sum_{p=1}^{M} e^{j\beta_p(\omega)z}\widetilde{\mathbf{A}}_p(z, \omega)\frac{\mathbf{F}_p(x, y)}{\sqrt{N_p}}, \tag{3.1}$$

where $\widetilde{\mathbf{A}}_p(z, \omega) = [\widetilde{\mathbf{A}}_{p,x}(z, \omega), \widetilde{\mathbf{A}}_{p,y}(z, \omega)]^T$ is the slowly varying field envelope of mode p with propagation constant $\beta_p(\omega)$, spatial distribution $\mathbf{F}_p(x, y)$ and power carried N_p. The tilde in Eq. 3.1 indicates a frequency domain variable while the superscript ^{T} denotes the transpose operation. The mode field is considered to be linearly polarized in the transverse plane on the weakly guiding approximation [56], where $F_p(x, y)$ is real and the phase of the optical wave is contained in the complex amplitude $\widetilde{\mathbf{A}}$ [56].

The propagation constant for any guided mode p, β_p, is given by $\beta_p = \bar{n}_p k_0$ and bounded by $(n_1 k_0; n_2 k_0)$, where $\bar{n}_p$ is the effective index of mode p and k_0 is the propagation constant of light in vacuum. Therefore, any mode p can be characterized by its $\bar{n}_p$ and the mode field distribution, $\mathbf{F}_p(x, y)$; both are obtained by solving the wave equation under appropriate boundary conditions [4].

The mode field distribution $\mathbf{F}_p(x, y)$ has the property that does not change with propagation [4]. It is composed of a combination of transverse electric (TE) modes with no electric field along the longitudinal axis, transverse magnetic (TM) modes with no magnetic field along the longitudinal axis, and hybrid modes for which neither the electric nor the magnetic field are zero along the longitudinal axis, denoted by HE or EH, depending on whether longitudinal magnetic or electric field dominates [17]. This led to the linearly polarized (LP) modes, a simplified notation used under the weakly guiding approach (the relative refractive index difference between core and cladding is << 1) [17]. LP modes are denoted using two indexes that describe the mode field distribution, $\mathrm{LP}_{\mathrm{lm}}$, where indexes l and m are defined as follows:

- l: represents the periodicity of the azimuthal distribution. When $l = 0$ the amplitude is unchanged by a 2π rotation at constant radial coordinate (ρ). For any other value of l, there are $2l$ intensity field maxima along a 2π rotation at constant ρ.
- m: represents the periodicity of the radial distribution. For any m value, there are m intensity field maxima along the radial coordinate.

The following rules are applied to composition of the LP modes [17]: (a) each $\mathrm{LP}_{0\mathrm{m}}$ is composed of a $\mathrm{HE}_{1\mathrm{m}}$; (b) each $\mathrm{LP}_{1\mathrm{m}}$ is composed of a linear combination of modes $\mathrm{TE}_{0\mathrm{m}}$, $\mathrm{TM}_{0\mathrm{m}}$ and $\mathrm{HE}_{2\mathrm{m}}$; (c) each $\mathrm{LP}_{\mathrm{lm}}$ ($l \geq 2$) is composed of a linear combination of $\mathrm{HE}_{\mathrm{l+1,m}}$ and $\mathrm{EH}_{\mathrm{l-1,m}}$. Figure 3.2 shows the intensity mode field distribution of the first 6 LP modes: LP_{01}, LP_{11_a}, LP_{11_b}, LP_{02}, LP_{21_a} and LP_{21_b}. This plot was obtained using the solver published by [57] for step-index FMF. All these LP modes are degenerate, with a factor of 2, given the two orthogonal polarizations x and y. Besides, for $\mathrm{LP}_{\mathrm{lm}}$ modes with $l \geq 1$, two orthogonal field distributions are achieved by a $\pi/(2l)$ rad rotation, this is typically denoted by the extra sub-index a or b, as shown in figure 3.2 for LP_{11_a} and LP_{11_b}, and LP_{21_a} and LP_{21_b}.

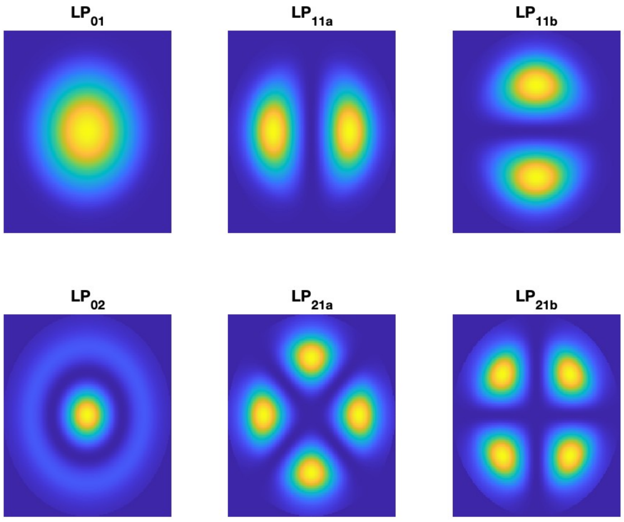

Figure 3.2: Intensity mode field distribution for the first 6 LP modes in a step-index FMF.

3.3 Physical layer impairments in FMF

In the literature, some PLI have been identified and take greater or lesser importance considering the scope of the network (core, metro/region, data center). In [15], PLI introduced by SDM fibers are classified into two groups: intra-modal and inter-modal impairments. At the same time, both can be classified as linear or nonlinear. A summary of all these physical impairments is shown in Figure 3.3. Intra-modal impairments occur inside a mode, they are associated with the PLIs known in SMFs, such as power losses and dispersion in the case of linear restrictions; and phenomena such as self-phase modulation (SPM), cross-phase modulation (XPM), four-wave mixing (FWM), and inter-channel stimulated Raman scattering (ISRS) for the case of nonlinear constraints [58, 59]. Inter-modal impairments occur between LP modes, these are the differential mode delay (DMD), linear mode crosstalk (XT), and mode-dependent loss (MDL) in the case of linear constraints. The inter-modal nonlinearities are the cross-phase modulation (IM-XPM) [17], inter-modal four-wave mixing (IM-FWM) [17], and inter-modal stimulated Raman scattering (IM-SRS) [60].

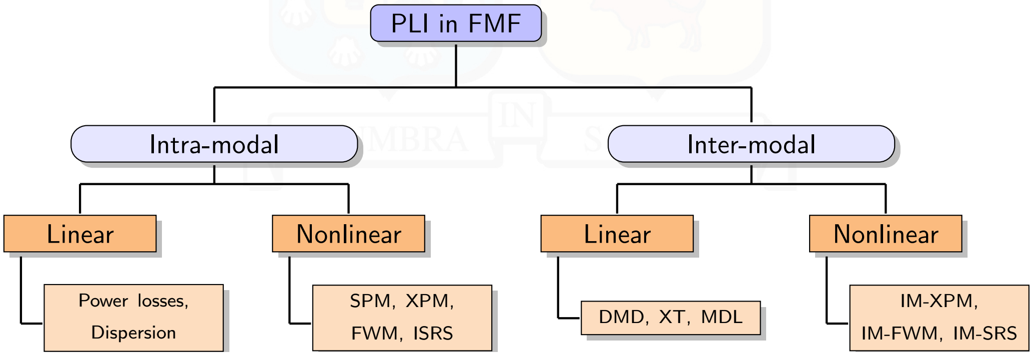

Figure 3.3: Summary of PLI in few-mode fibers.

The above-mentioned linear impairments can be compensated using digital signal processing (DSP). However, compensation increases transceivers complexity and their power consumption. On the other hand, in the nonlinear regime, nonlinear impairments cannot be compensated, resulting in a degradation of the performance of the system.

In the following subsections, the main PLI that degrade the performance of SDM-FMF systems are reviewed.

3.3.1 Intra-modal Impairments

3.3.1 Linear

- **Power losses**

  Power losses in optical communication systems refer to the accumulated losses from source to destination along a fiber optic link. These are mainly due to material absorption, Rayleigh scattering, and waveguide imperfections [4]. Material absorption can be divided into two categories: intrinsic and extrinsic absorption [4]. Intrinsic absorption losses correspond to absorption by fused silica (the material used to make fibers), whereas extrinsic absorption is related to losses caused by impurities within silica [4]. Rayleigh scattering is a mechanism that arises from local microscopic fluctuations in material density, generating random fluctuations of the refractive index on a scale smaller than the optical wavelength [4]. Additionally, imperfections at the core-cladding interface and fiber bends can lead to additional losses that contribute to the net fiber loss [4].

Power losses are measured by the attenuation coefficient (α) of the optical fiber, which has a value of the order of 0.2 dB/km at 1550 nm. The output power (P_{out}) at the end of a fiber of length L, is given by [4]:

$$P_{out} = P_{in} \exp(-\alpha L) \tag{3.2}$$

where P_{in} is the power launched at the input of the fiber. This relationship does not consider the splice and bend losses present in a real optical fiber.

Figure 3.4 shows the close relationship between the attenuation coefficient of optical fiber and wavelength and the relative contribution of the material absorption and Rayleigh scattering to the attenuation coefficient. This figure is the result of measurements made on a single-mode silica fiber in a study conducted in 1979, the first time that a loss of 0.2 dB/km in the wavelength region near 1.55 μm was reported.

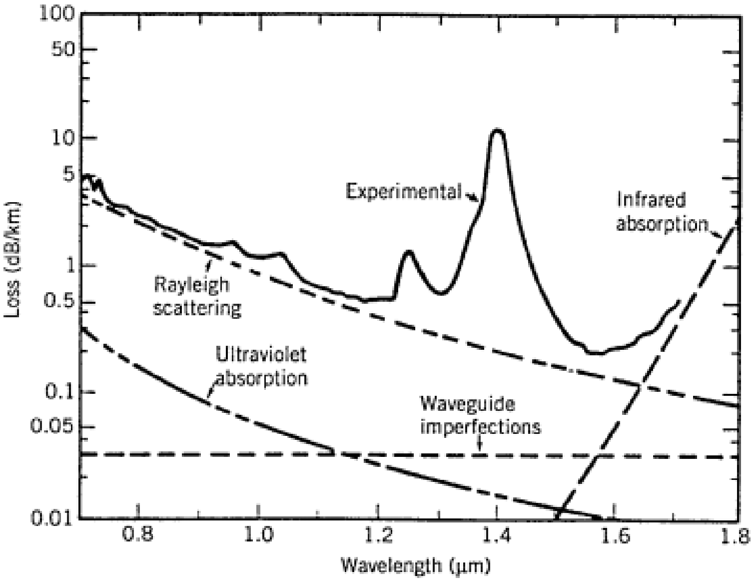

Figure 3.4: Loss spectrum of a single-mode fiber. Wavelength dependence of several fundamental loss mechanisms is also shown [4].

Long-haul optical communications systems are limited by fiber attenuation. To compensate for fiber attenuation, optical amplifiers are used. However, the use of optical amplification degrades the signal transmission quality as it adds ASE noise to the signals.

- **Dispersion**

  Intra-modal dispersion can be classified into chromatic dispersion (CD) and polarization mode dispersion (PMD). The effect of dispersion is the broadening of optical pulses so that they spread into the time slots of adjacent pulses, causing inter-symbol interference [61].

  Chromatic dispersion is also known as group velocity dispersion (GVD), intra-modal dispersion, or simply fiber dispersion. It is governed by the GVD coefficient denoted by D, and measured in ps/(km − nm) [4]. The CD in a fiber is given by the sum of the material dispersion and the waveguide dispersion (D_W) [61]. Dispersion of the material occurs because the refractive index of silica changes with the optical frequency [4]. Waveguide dispersion occurs because the effective propagation constant, related to the waveguide nature of the fiber, depends on wavelength [61].

Figure 3.5 shows the D parameter and their components, material dispersion (D_M) and waveguide dispersion (D_W), for a typical single-mode fiber. The zero-dispersion wavelength (λ_{ZD}) is also shown, point where the total dispersion is zero. Typical values of D parameter range from 15 to 18 ps/(km − nm) near 1.55 μm.

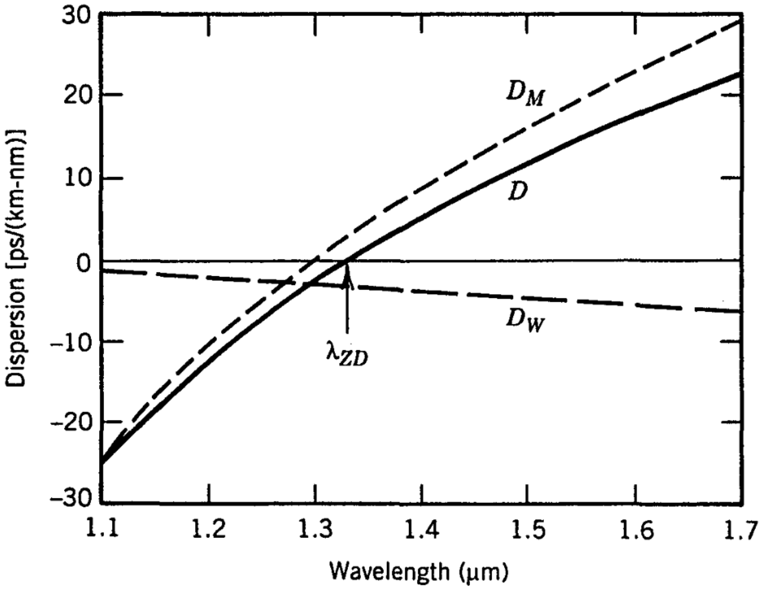

Figure 3.5: Total dispersion (D) and relative contributions of material dispersion (D_M) and waveguide dispersion (D_W) for a conventional single-mode fiber [4].

The dispersion due to the polarization mode, PMD, is related to the birefringent nature of the fiber and the two polarizations of light that propagate, generating a single broadened pulse at the receiver [61]. The PMD parameter of the fiber is measured in ps/$\sqrt{km}$.

Because it is a linear phenomenon, dispersion can be completely compensated; for example, using dispersion compensation fiber (DCF) modules or DSP modules in the receiver [4].

3.3.1 Nonlinear

- **Self-Phase Modulation** (SPM)

SPM is a nonlinear intra-channel effect that occurs due to the intensity dependence of the optical pulse with changes in the refractive index of the fiber. This change, in the refractive index, results in a phase shift that leads to frequency modulation of the optical pulse [62]. Because the modulation effect is proportional to the power of the transmitted signal, SPM effects are stronger in systems with high transmitted power.

The effects produced by SPM and linear dispersion are opposite in nature [62].

Depending on the dispersion region in which SPM and GVD interact, the pulse may broaden or narrow. For example, for fibers with a GVD coefficient $D < 0$ ps/(km − nm) (normal dispersion region), the main effect of SPM is to broaden the pulse in the frequency domain. By properly choosing the pulse shape and input power, one effect will compensate for the other, leading to an undistorted pulse in the time and frequency domains [62]; such a pulse is called soliton.

- **Cross-Phase Modulation** (XPM)

  XPM is a nonlinear inter-channel effect, it refers to the nonlinear phase modulation of an optical pulse caused by fluctuations in the intensity of other optical pulses [62]. XPM occurs when two optical fields propagate at the same time and affect each other through the intensity dependence of the refractive index [58]. The result of XPM can be asymmetric spectral broadening and pulse shape distortion. In WDM systems the combined power of the signals from all the channels can increase the phase shift induced by XPM.

- **Four-Wave Mixing** (FWM)

  The FWM phenomenon is a parametric process. This means that the propagation of light is affected by some parameters of the medium, such as the refractive index of the optical fiber. If three optical signals with carrier frequencies f_i, f_j and f_k, propagate simultaneously within a fiber, FWM products are generated at new frequencies such as $f_i + f_j - f_k$ [62].

  The performance degradation due to FWM occurs in two ways: the first is because the generation of new components at different frequencies represents a loss of signal energy; the second is because, in WDM systems with equally spaced channels, new components fall on the frequencies assigned to other channels, causing crosstalk [61].

- **Inter-channel Stimulated Raman Scattering** (ISRS)

  The Kerr nonlinearities such as SPM, XPM and FWM, are the prevailing nonlinear effects for optical bandwidths within the conventional C-band, limiting the achievable data rates in optical communication systems [59]. However, when ultra-wideband transmission is available, inter-channel stimulated Raman scattering (ISRS) must be taken into account [59, 63].

  Inter-channel stimulated Raman scattering is a non-parametric nonlinear process that transfers power from high frequencies to lower frequencies components during propagation, causing signal distortions [59]. In modern optical communications that use coherent technology in combination with dispersion-uncompensated fiber links, ISRS effectively introduces a different power profile for each frequency component [63].

  For C-band transmission (approximately 5 THz), ISRS is not significant and its impact is negligible in most cases [63]. However, for systems that occupy the entire C + L band (approximately 5 THz + 10 THz), ISRS becomes significant [63], due to it scales exponentially with optical bandwidth [59].

3.3.2 Inter-modal Impairments

3.3.2 Linear

- **Differential Mode Delay** (DMD)

  Besides chromatic dispersion, another type of dispersion occurs only when more than one mode is propagated through the optical fiber. This is called inter-modal dispersion or DMD [17]. It is defined as the variation of the group velocities, that cause different group delays per unit length between modes [17]. It is defined as [17]:

  $$\mathrm{DMD}_{m,m_0} = \frac{1}{v_{g,m}} - \frac{1}{v_{g,m_0}} \tag{3.3}$$

  where $v_{g,m}$ is the group velocity of mode m. The subindex m_0 is representing the reference mode, LP_{01}.

  In FMF the pulse distortion is determined mainly by the inter-mode dispersion measured by DMD [58]. Modal dispersion in these systems results in a larger group delay spread than that caused by CD [58]; this means a higher broadening of signal pulses.

  FMFs require the usage of DSP equalization to compensate for DMD, increasing the complexity, cost, and power consumption of the system [17]. An alternative to reduce DSP complexity is to mitigate the accumulation of DMD [18] by using dispersion compensation schemes (FMFs with positive DMD followed by FMFs with negative DMD) or by tailoring the refractive index profiles [17], with shapes such as air-trench-assisted [64], graded-core cladding-trench [65, 17], and multilevel step-index [17]. However, the manufacturing process is more complex compared with step-index and graded-index profiles. Therefore, the trade-off between complexity, cost, and desired performance is not something trivial for these systems.

- **Linear crosstalk** (XT)

  Due to the orthogonality condition, no coupling will occur among the guided modes in an ideal FMF. However, in real FMF mode coupling will occur due to bends, refractive index imperfections during the fabrication process, fiber splices imperfections, and imperfections in optical devices, such as MMUX/MDMUX [17, 58]. All these imperfections cause the orthogonality condition to break and an exchange of energy between modes occurs, this phenomenon is known as linear XT [17] or mode coupling [58]. The accumulated distributed XT in mode m along an FMF introduced by imperfections and fiber bends, as well as the discrete XT introduced by optical devices, can be calculated by [66]:

  $$XT_m = \sum_{n \neq m} \frac{P_n}{P_m}, \tag{3.4}$$

  where P_n is the power of mode n, after a segment of fiber under test when only the m mode was launched.

  Given a pair of modes (m and n), the coupling strength among them depends on the difference between the propagation constant ($\beta_m - \beta_n$) and the overlap integral of the modes field distribution [17]. If m and n are a pair of degenerate modes, such as LP_{11_a} and LP_{11_b}, the mode coupling will be strong; i.e., a high amount of power will be transferred between the modes within a few hundred meters [17]. Otherwise, if m and n are a pair of non-degenerate modes, such as LP_{01} and LP_{11_a}, the mode coupling will be weak; i.e. a negligible amount of power will be transferred between the modes within a few hundred meters, however, a significant amount of power will be transferred between modes after tens of kilometers [17].

The mode coupling has been classified as weak, intermediate, or strong [58, 35, 66]. When the transmission distance is hundreds to thousands of kilometers, FMF systems usually operate in the weak or intermediate coupling regime [66], positioning those approaches for cases relevant to optical communication systems. The mathematical models to study propagation through FMF under those approaches are presented in Section 3.4.

- **Mode-dependent loss** (MDL)

  Fiber imperfections, splices, MMUX/MDMUX, and optical amplifiers can introduce losses that are dependent on the mode [17], these are named MDL. Different losses will cause unequal variations in the power of signals propagating in different modes and impose a mode-dependent limitation in the optical reach of signals. The main source of MDL is the mode-dependent gain in multimode optical amplifiers [17] measured by the performance parameter differential modal gain (DMG). Chapters 4 and 5 present more details of the optical amplification process in FMF systems.

3.3.2 Nonlinear

- **Inter-Mode Four Wave Mixing** (IM-FWM)

  The interaction of three wavelengths λ_1, λ_2 and λ_3, propagating in different spatial modes denoted by m, n and p, generate a new spectral component at the frequency $\omega_{\lambda_4} = \omega_{\lambda_1} + \omega_{\lambda_2} - \omega_{\lambda_3}$ in the spatial mode q, as a consequence of IM-FWM [67, 15]. Only interactions between pairs of spatial modes are significant, the other interactions give rise to long-distance unstable FWM processes, which leads to an insignificant generation of new spectral components [60, 32, 15]. The significant interactions are named FWM processes in the literature [17, 32, 68]. The frequency of the FWM process 1 fulfills the condition $\omega_{\lambda_4} = \omega_{\lambda_1} + \omega_{\lambda_2} - \omega_{\lambda_3}$ and for the FWM process 2 the condition changes to $\omega_{\lambda_4} = \omega_{\lambda_1} - \omega_{\lambda_2} + \omega_{\lambda_3}$.

  IM-FWM occurs when two frequency components in one fiber mode create a beating component that modulates a third spectral component that propagates in another mode, creating a new frequency component that fulfills the frequency condition [32]. The strength of the newly created spectral components depends on the phase-matching condition [32]:

$$\Delta\beta_{mmpp} = (\beta_{1,p} - \beta_{1,m})(\omega_{\lambda_2} - \omega_{\lambda_0}) - \beta_{2,p}(\omega_{\lambda_1} - \omega_{\lambda_0})(\omega_{\lambda_2} - \omega_{\lambda_0}), \tag{3.5}$$

  where $\beta_{1,m(p)}$ and $\beta_{2,m(p)}$ are the group-delay and the dispersion parameters of $m(p)$ mode, respectively; and ω_{λ_i} are angular frequencies with sub-index 0 denoting a reference frequency, and sub-indexes 1 and 2 are frequency components in different modes. The maximum IM-FWM interaction occurs when ω_{λ_1} and ω_{λ_2} are related as follows [32, 68]:

$$\omega_{\lambda_1} - \omega_{\lambda_2} = \frac{\beta_{1,m} - \beta_{1,p}}{2\pi\beta_{2,m}}. \tag{3.6}$$

The numerator of (3.6) represents the DMD between m, p modes, therefore, highlighting the important relationship between DMD and IM-FWM.

- **Inter-Mode Cross-Phase Modulation** (IM-XPM)

  The IM-XPM process induced spectral broadening of optical signals, it can be treated as a special type of FWM process. In [69], the IM-XPM was experimentally observed using a data-modulated pump and an unmodulated probe in FMFs with low DMD between spatial modes. In that work, it was demonstrated that the IM-XPM magnitude is comparable to intra-modal XPM.

  As with IM-FWM, there are mode and phase-matching conditions for significant IM-XPM. The IM-XPM mode matching condition involves the interaction between two different modes (m and p), while the phase-matching condition is defined as follows:

$$\Delta\beta_{mpmp} = (\beta_{1,m} - \beta_{1,p})(\omega_{\lambda_1} - \omega_{\lambda_0}) - \beta_{2,m}(\omega_{\lambda_1} - \omega_{\lambda_0})(\omega_{\lambda_2} - \omega_{\lambda_0}), \tag{3.7}$$

  where the same definitions of Eq. (3.5) are used.

- **Inter-mode Stimulated Raman Scattering** (IM-SRS)

  Stimulated Raman scattering (SRS) is an important nonlinear process that can convert optical fibers into broadband Raman amplifiers [70]. At the same time, it can also severely limit the performance of WDM systems because the short-wavelength channels can act as a pump for longer-wavelength channels and thus transfer part of the pulse energy to neighboring channels [70]. This leads to the ISRS described in Section 3.3.1, which can affect the system performance considerably.

  Raman scattering is a dissipative process where a phonon from the fiber medium interacts with the electric field, causing a spectral redshift [71]. It can cause energy transfer between LP modes [60, 71], revealing the existence of IM-SRS. SRS between LP modes is mathematically modeled using the Raman response of the fiber medium and the fraction of the Raman contribution to the total Kerr effect, as well as the nonlinear coupling coefficients for the Raman effect [71].

3.4 Mathematical Modeling of the Physical Layer

The mathematical modeling of the physical layer allows us to represent, predict, and quantify, all the physical layer impairments described in Section 3.3, to guarantee the quality of the transmission. In the absence of appropriate physical layer models, the effects of PLIs may be either overestimated or underestimated, resulting in inefficient resource allocation or non-compliance with service level agreements; both cases are unfavorable for the operation of the network.

Light propagation in mode m through an FMF can be represented by a linear part ($\widetilde{D}$) and a nonlinear part ($\widetilde{N}$), as follows [32]:

$$\frac{\partial \vec{A}^{(m)}(z,t)}{\partial z} = \widetilde{D} + \widetilde{N}, \tag{3.8}$$

where $\vec{A}^{(m)}(z,t) = [A_x^{(m)}(z,t), A_y^{(m)}(z,t)]^T$, is the field envelope of the fiber mode m, considering polarization in x and y, propagating along z direction. The linear part depends on parameters such as fiber attenuation, dispersion, group velocity, and XT. Conversely, the nonlinear component depends on the nonlinear phenomena [32]. Accurate modeling of nonlinear propagation in SDM fibers is a fundamental task to determine the upper limit of the achievable transmission rate, established by the nonlinearity of the fiber [60].

Nonlinear propagation in multimode optical fibers has been modeled by the coupled nonlinear Schrödinger equations (NLSE), but their complexity, and in particular the large number of nonlinear coefficients they imply, makes their numerical implementation quite cumbersome [60]. These difficulties are resolved when unique properties of multimode fiber structures with lengths relevant to optical communications are taken into account. The most important of these properties is the presence of random linear coupling between modes, which is caused by manufacturing imperfections and installation-related problems, and which often occurs on a length scale that is much shorter than the length scale of length that characterizes nonlinear phenomena [60]. The existence of this random coupling leads to a considerable simplification of the propagation equations, which reduces to the generalized form of the Manakov equation [60] or the coupled NLSE (CNLSE) [17].

The simplifications of the NLSE cited above allow the modeling of different coupling regimes between propagation modes. The Manakov equation has been used for weak and strong coupling regimes [35, 60, 15], while the CNLSE has been used for weak and intermediate coupling regimes [17, 66]. FMF systems with lengths between 100 and 1000 km operate in the weak or intermediate coupling regime [66]. The intermediate coupling regime arises because, although strong mode coupling can be assumed within groups of degenerate modes (e.g., LP_{11_a} and LP_{11_b}), mode coupling between non-degenerate modes (e.g., LP_{01} and LP_{11}) cannot be considered insignificant or strong [66].

In this work, the mathematical models for propagation in FMF under weak and intermediate coupling regimes will be studied, since these represent the cases of interest to model SDM-FMF systems for practical scenarios. These coupling regimes will be described in the following subsections.

3.4.1 Weak Coupling Regime

Manakov equations have been used for modeling propagation through both FMF and MCF fibers [35, 60, 15]. Mumtaz et al. [35] investigated theoretically nonlinear transmission in SDM systems, using MMF and MCF fiber, generalizing the Manakov equations for the cases of weak coupling and strong coupling between spatial modes. Similarly, Antonelli et al. [60] generalized the Manakov equations to take into account the Raman contribution to the nonlinear response of the fiber, applicable to MCF and MMF. Shariati et al. [15], also starting from the Manakov equations considering a weak coupling regime between spatial modes, developed an analytical model to estimate the transmission quality in SDM networks based on FMF and MCF.

Additionally, analytical or semi-analytical models have been developed based on the Manakov equations, such as the case of the study carried out by Rademacher et al. [32], where the Gaussian noise model of nonlinear interference for fibers is presented for MMF and FMF, analyzing nonlinear interference between intra-modal and inter-modal signals. Rademacher et al. [72] experimentally observed intra-modal and inter-modal nonlinear impairments and compared them with the Gaussian noise model presented in [32]. They found a correspondence between the two, validating the model as a tool for the design of transmission systems based on FMF.

The generalized Manakov equation in the weak coupling regime is given by [35, 60, 15]:

$$\begin{aligned}\frac{\partial \vec{A}^{(m)}(z,t)}{\partial z} + \frac{\alpha}{2}\vec{A}^{(m)}(z,t) + j(\beta_0^{(m)} + \beta_0)\vec{A}^{(m)}(z,t) + (\beta_1^{(m)} - \beta_1)\frac{\partial \vec{A}^{(m)}(z,t)}{\partial t} + ..\\ j\frac{\beta_2^{(m)}}{2}\frac{\partial^2 \vec{A}^{(m)}(z,t)}{\partial t^2} = j\gamma\left(f_{mmmm}\frac{8}{9}\left|\vec{A}^{(m)}\right|^2 + \sum_{p\neq m} f_{mmpp}\frac{4}{3}\left|\vec{A}^{(p)}\right|^2\right)\vec{A}^{(m)}\end{aligned} \tag{3.9}$$

where $\vec{A}^{(m)}(z,t)$ is the slowly varying envelope of mode m (p) considering polarization in x and y; α is the attenuation coefficient of the fiber considered to be equal for all fiber modes; $\beta_0^{(m)}$, $\beta_1^{(m)}$ and $\beta_2^{(m)}$ are the propagation constant, the inverse group velocity and the group-velocity dispersion of mode m, respectively; γ is the nonlinear coefficient considered to be equal for all fiber modes; and f_{mmpp} is the intensity overlap integral between modes m and p. β_0 and β_1 are parameters related to the fundamental mode LP_{01}. The first and second lines in Eq. 3.9 correspond to the linear and nonlinear parts in Eq. 3.8, respectively. The first nonlinear term represents the intra-modal nonlinear effects, present as well in SMF (e.g. SPM, XPM, FWM). The second nonlinear term represents the inter-modal nonlinearities among various modes (i.e. IM-XPM, IM-FWM).

To include the Raman contributions into the generalized Manakov equation, the nonlinear part of Eq. (3.9) must be modified, as demonstrated by Antonelli et al. [60]. Two additional terms are introduced. The first term accounts for phase modulation in the corresponding modulating mode, which, unlike standard SPM and XPM terms, is proportional to the time derivative of the signal power in the modulating mode [60]. This term does not produce any net gain or loss for the propagating modes; however, it reshapes the overall signal power spectrum [60]. The second term allows the transfer of energy between mode [60]. Both terms are multiplied by the Raman time constant and involve auxiliary nonlinear coefficients defined using the parameter f_R, which represent the fraction of the Raman contribution to the total nonlinear susceptibility.

The nonlinear coupling between spatial modes is governed by the parameter f_{mmpp}, defined as follows [73]:

$$f_{mmpp} = A_{eff_0}\frac{\iint |F_m|^2 |F_p|^2 dxdy}{\iint |F_m|^2 dxdy \cdot \iint |F_m|^2 dxdy} \tag{3.10}$$

where A_{eff_0} is the effective area of the fundamental mode and has a normalization proposed in Eq. (3.10); and F_m (F_p) is the mode field distribution of mode m (p). The parameter

f_{mmpp}, is the inverse of the effective modal area, consequently, two notations are available: the intra-modal effective area ($A_{eff}^{(mmmm)} = f_{mmmm}{}^{-1}$) referring to the traditional concept of the effective area of an optical fiber [32], and the inter-modal effective area ($A_{eff}^{(mmpp)} = f_{mmpp}{}^{-1}$) that can be understood as a value describing the amount of fiber cross-section shared by different modes. The nonlinear coefficient, γ, is defined as $\gamma = \frac{n_2\omega_0}{cA_{eff}}$, where n_2 is the nonlinear coefficient approximately equal to $2.6 \cdot 10^{-20}$ m^2/W; ω_0 is the angular frequency; c is the speed of light in vacuum approximately equal to $3 \cdot 10^8$ m/s; and A_{eff} is the effective modal area.

For cases where γ is not equal for all modes, it is used the nonlinear intra-modal ($\widetilde{\gamma}_{mmmm}$) and inter-modal ($\widetilde{\gamma}_{mmpp}$) coefficients in the Manakov equations; these coefficients have been studied in [60]. Under the weak coupling regime, these coefficients are given by [60, 58]:

$$\widetilde{\gamma}_{mmmm} = \frac{4}{3}\frac{2M}{2M+1}\frac{n_2\omega_0}{cA_{eff}^{(mmmm)}}, \tag{3.11}$$

$$\widetilde{\gamma}_{ppqq} = \frac{4}{3}\frac{n_2\omega_0}{cA_{eff}^{(mmpp)}}, \tag{3.12}$$

where M is the number of spatial modes in the FMF. The intra- and inter-modal averaging factors given in Eq. 3.11 and 3.12 are $\frac{4}{3}\frac{2M}{2M-1}$ and $\frac{4}{3}$, respectively. Note that when $M = 1$, the averaging factor is equal to 8/9, the same coefficient in SMF systems [74]. However, averaging over random birefringence fluctuations reduces the coefficient to 4/3 for the inter-modal case.

The generalized Manakov equation (Eq.(3.9)) is an extension of the standard Manakov equation for multimode fibers, which evaluates the overall effect of random birefringence after a significant distance of propagation within each mode. To solve this equation, numerical techniques, such as the split-step Fourier method [70], must be applied.

3.4.2 Intermediate Coupling Regime

To model FMF systems operating in the intermediate coupling regime, coupling matrices, representing misaligned fiber splices in small fiber sections, are required. Ferreira et al. [66, 75] have presented a semi-analytical model to describe the linear and nonlinear mode coupling for fibers operating in the intermediate coupling regime. To do it, a model was proposed introducing a random amount of crosstalk per fiber section that approximates a desired level on average. Most FMFs with step-index or graded-index profiles range from −50 dB/100 m to −40 dB/100 m as the average XT [66].

Considering both linear and nonlinear contributions to the field envelope, the generalized CNLSE is expressed as [66, 75]:

$$\frac{\partial \vec{A}^{(m_e)}}{\partial z} + \frac{\alpha}{2}\vec{A}^{(m_e)} + \beta_1^{(m_e)}\frac{\partial \vec{A}^{(m_e)}}{\partial t} - j\frac{\beta_2^{(m_e)}}{2}\frac{\partial^2 \vec{A}^{(m_e)}}{\partial t^2} = -j\sum_{p\neq m}\sum_{d} C_{m_e,p_d}\vec{A}^{(p_d)}e^{j(\beta_0^{(m_e)}-\beta_0^{(p_d)})z} \,.. \tag{3.13}$$
$$-j\left(\gamma_{m_e}\left|\vec{A}^{(m_e)}\right|^2 + 2\sum_{p_e\neq m_e}\gamma_{m_e p_e}\left|\vec{A}^{(p_e)}\right|^2 + \frac{2}{3}\sum_{p_d}\gamma_{m_e p_d}\left|\vec{A}^{(p_d)}\right|^2\right)\vec{A}^{(m_e)}$$

where $\vec{A}^{(m_e)}(z,t)$ is the slowly varying field envelope of mode m (p) and state of polarization e (d); α, β_1, β_2, and β_0 have the same meaning than in Eq. (3.9) i.e. attenuation coefficient, group velocity parameter, GVD parameter and, propagation constant, respectively; C_{m_e,p_d} are the coupling coefficients between modes m and p; and $\gamma_{m_e p_d}$ is the nonlinear coupling parameter between the e polarization of mode m and the d polarization of mode p, which depends on the nonlinear refractive index n_2 and on the intermodal effective area $A_{eff}^{(mmpp)}$, given by: $\gamma = \frac{n_2\omega_0}{cA_{eff}^{(mmpp)}}$, similar to Eq. (3.12).

The first and second lines in Eq. 3.13 correspond to the linear and nonlinear parts in Eq. 3.8, respectively. The linear XT is represented by the first term after the equal sign. Ferreira et al. [66] have proposed a semi-analytical solution method for computing the coupling matrix C_{m_e,p_d} with proven accuracy for transmission lengths from 10 m to 10000 km, in any coupling regime from -50 dB/100 m to 0 dB/100 m. The coupling coefficients are given by the area integral of the dot product of the electrical fields between two spatial modes. The first nonlinear term represents the intramodal SPM of the polarization e of the mode m. The second nonlinear term represents the XPM from the same polarization (e) of different modes ($p \neq m$). The third nonlinear term also results in XPM but comes from the orthogonal polarization (d) of the same ($m = p$) or different modes ($p \neq m$).

The main difference between Eq. (3.9) and (3.13) is the inclusion of the linear XT through a modal coupling matrix, which can be combined with methods such as the split-step Fourier for the resolution of Eq. (3.13), without computational time constraints using the methodology presented in [66].

3.5 Simulation Results

In this section, the models presented in Section 3.4 were solved by applying the split-step Fourier method [59]. The physical configuration used in this chapter is presented in Figure 3.6. One span combines 100 km of FMF and one bundle of single-mode EDFAs (SM-EDFA) compensating for the losses per spatial mode in the previous span. Although this configuration requires additional multiplexing and demultiplexing at each amplification step, it is the most common in the literature when studying signal propagation in an FMF [35, 73, 15]. In the simulations executed to show the results of this chapter, the SDM MUX and DEMUX were considered ideal, thus adding no penalty to the system performance.

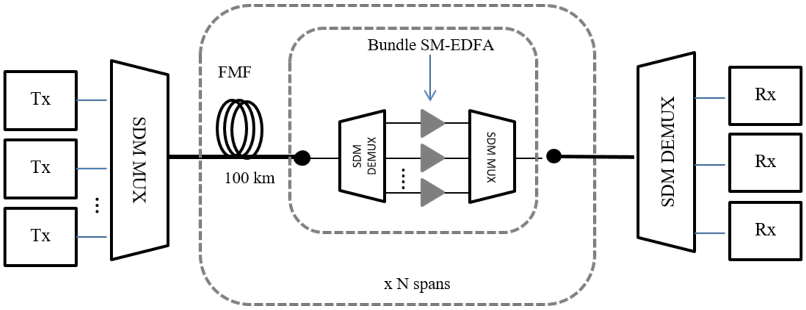

Figure 3.6: Schematic of an FMF system using bundle SM-EDFA.

An FMF supporting six co-propagating signal modes (LP_{01}, LP_{11_a}, LP_{11b}, LP_{02},

LP_{21_a}, and LP_{21b}), with the fiber parameters summarized in Table 3.1 was considered. n_1 and NA in Table 3.1 are the core refractive index, and the numerical aperture, respectively. The step size was set to 100 m and the fiber length to 100 km.

Table 3.1: Step-index FMF parameters.

LP mode	**DMD** [ns/km]	**D** [ps/(km – nm)]	A_{eff} [μm^2]	α [dB/km]	γ [(W.km)$^{-1}$]	**Radius** [μm]	$\mathbf{n_1}$ [-]	**NA** [-]
LP_{01}	0	25	80	0.2	1.4	6.25	1.45	0.2
$LP_{11_{a,b}}$	6.5	27.3	76					
LP_{02}	9.9	−2.3	83					
$LP_{21_{a,b}}$	12	20.8	86					

In the following simulations, one channel per polarization, per spatial mode, was assumed at a bit rate of 100 Gbps using QPSK (Quadrature Phase Shift Keying) modulation format and symbol rate of 28.5 Gbaud. Each QPSK signal is made up of 2^{15} modulated symbols with 2^{17} samples per polarization.

The f_{mmpp} values used for modeling propagation in the weak coupling regime are shown in Table 3.2. Those values were obtained using the step-index fiber parameters reported in [35, 73], and resumed in Table 3.1.

Table 3.2: Calculated values of $\mathbf{f_{mmpp}}$ for the six LP spatial modes.

	LP_{01}	LP_{11_a}	LP_{11_b}	LP_{02}	LP_{21_a}	LP_{21_b}
LP_{01}	1	0.661	0.661	0.734	0.455	0.455
LP_{11_a}	0.661	1.053	0.249	0.369	0.608	0.608
LP_{11_b}	0.661	0.249	1.053	0.369	0.608	0.608
LP_{02}	0.731	0.369	0.369	0.964	0.335	0.335
LP_{21_a}	0.455	0.608	0.608	0.335	0.930	0.190
LP_{21_b}	0.455	0.608	0.608	0.335	0.190	0.930

3.5.1 Weak Coupling Regime

This section presents the results of two case studies. The first examines a single-channel system, where the configuration depicted in Figure 3.6 includes only one transmitter (Tx) and one receiver (Rx), representing a single wavelength. The second case study explores a multi-channel system, as illustrated in Figure 3.6, representing multiple wavelengths transmitted simultaneously.

Figure 3.7 shows the signal-to-noise ratio (SNR) as a function of input power per wavelength per LP mode in the range between −7 dBm to 7 dBm for the first case of study (1 channel is copropagating in 6 spatial modes through 10 spans) in the weak-coupling regime. The SNR is degraded due to linear effects, dominated by ASE noise – in this case, it is the same for all spatial modes – and nonlinear effects, dominated by intra-channel intra-modal phenomena, such as SPM. The best performance is achieved in the channel at LP_{01}, which is the fundamental mode. As the number of modes increases, the SNR performance decreases. The worst performance is achieved in the channel at LP_{02}, the considered higher order mode. From Figure 3.7, it is observed that there is an optimal input power per spatial mode, after that value, the performance degrades due to nonlinear impairments (NLIs).

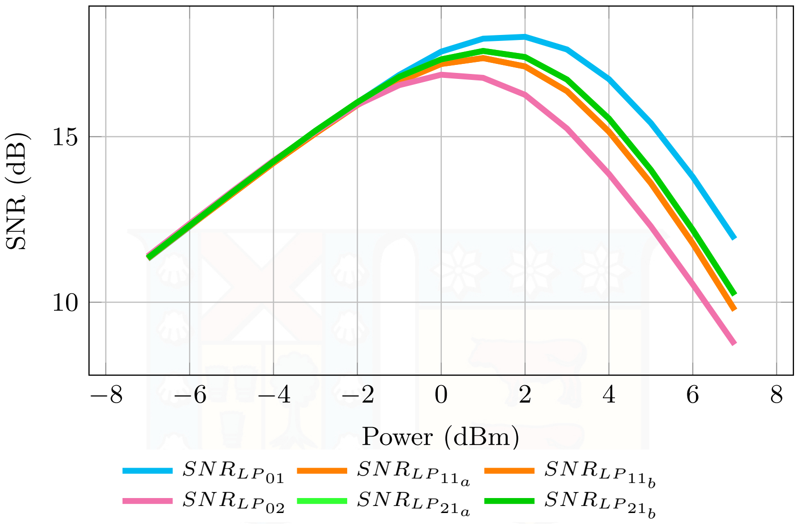

Figure 3.7: SNR versus launch power per mode in an FMF system under the weak-coupling regime, using SM-EDFA for amplifying signals per mode. The FMF system carries one wavelength channel per spatial mode, using spans of 100 km each and a total of 10 spans.

Figure 3.8 shows the SNR of the central channel as a function of its input power for the second case of study (9 WDM channels copropagate in 6 spatial modes through 10 spans). As the number of channels per mode increases, the SNR degrades as can be observed in Figure 3.8 where the number of wavelengths was increased to 9 per LP mode. The shift to a lower optimal input power is explained by inter-modal inter-channel NLIs in this scenario. For practical systems operating in a full C-band occupancy scenario, identifying the optimal launch power is a mandatory task to achieve the best possible performance.

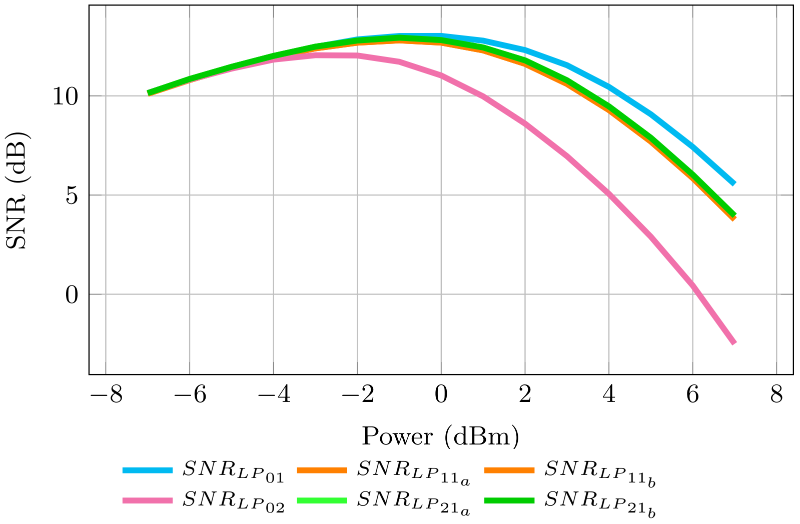

Figure 3.8: SNR of the central channel versus launch power per wavelength per LP mode in an FMF system under the weak-coupling regime, using SM-EDFA for amplifying signals per mode. The FMF system carries 9 wavelengths per spatial mode, using spans of 100 km each and a total of 10 spans.

3.5.2 Intermediate Coupling Regime

Figure 3.9 shows the span coupling matrix in the intermediate coupling regime for the step-index FMF fiber with parameters reported in Table 3.1. This matrix was obtained using the method presented in [66], using a mean average XT of −35 dB/km, and a step size of 1 km. This matrix represents the accumulated XT after one span with random coupling between modes due to waveguide imperfections, present in real FMF transmission distances of hundreds of kilometers in length. The diagonal of the matrix has the highest values because it represents the linear coupling of the same mode with a strong coupling between polarizations x and y, in the rest of the matrix it shows lower coupling between non-degenerate modes.

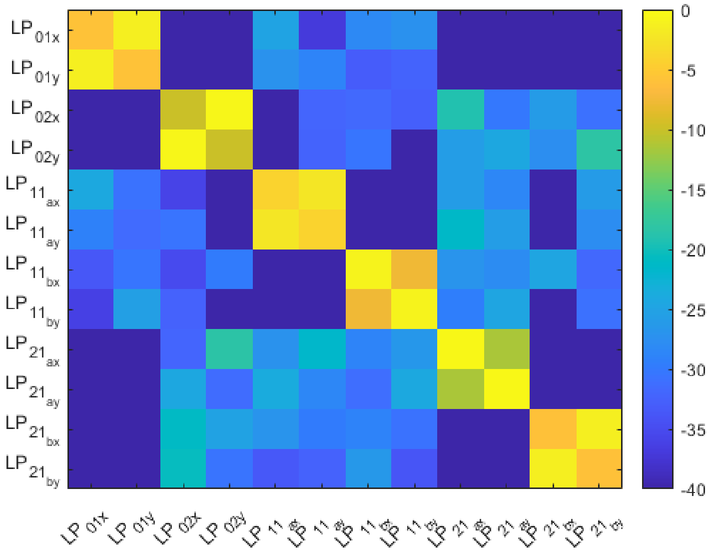

Figure 3.9: Span coupling matrix in the intermediate coupling regime with average fiber XT of −35 dB/km, values represent the accumulated XT ([dB]) after one span of 100 km.

Under the intermediate coupling regime, single-channel and multi-channel case studies are also presented, as presented for the weak coupling regime case. The SNR after 10 spans for single channel transmission in the intermediate coupling regime is shown in Figure 3.10. The SNR is degraded by both linear and nonlinear effects, showing the presence of an optimal value of launch power to the fiber to obtain the maximum SNR value. In the linear part, the modes do not have the same performance, as it happens under the weak-coupling regime because there is now a linear XT between modes, described by the coupling matrix. This XT has a random nature since it models imperfections in the fiber, so it is necessary to set a fixed seed for the execution of the numerical simulations and avoid generating a new coupling matrix for each execution. A comparison of SNR performance under the two coupling regimes described in this chapter, shows that in the intermediate coupling regime there is a greater penalty in SNR reaching values below 15 dB for all modes, this is also reflected in a shift, towards a lower value, of the optimal input power.

Figure 3.11 shows the SNR of the central channel after four spans, when 9 WDM channels propagate in each LP mode. It is observed that as the number of channels per

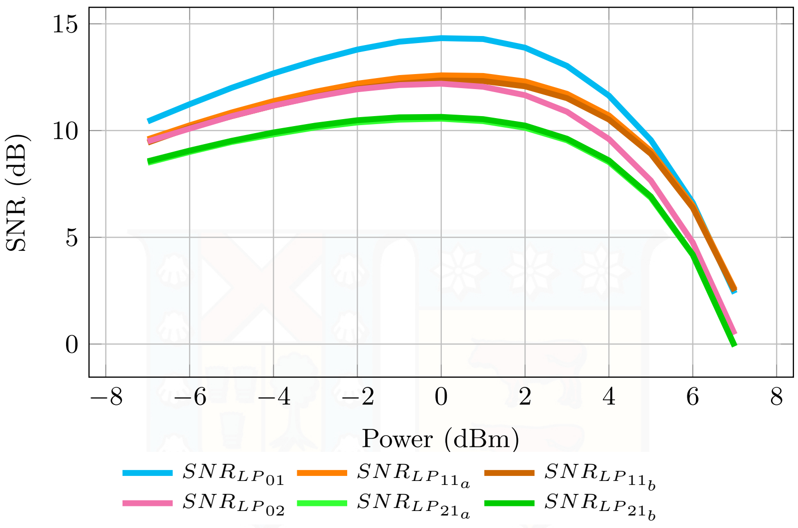

Figure 3.10: SNR versus launch power per mode in an FMF system under the intermediate coupling regime, using SM-EDFA for amplifying signals per mode. The FMF system carries one wavelength channel per spatial mode, using spans of 100 km each and a total of 10 spans.

mode increases, the SNR degrades due to the presence of inter-modal inter-channel NLIs. The number of spans and the range of input power were reduced, compared to previous figures, because above these ranges, the SNR degradation was excessive.

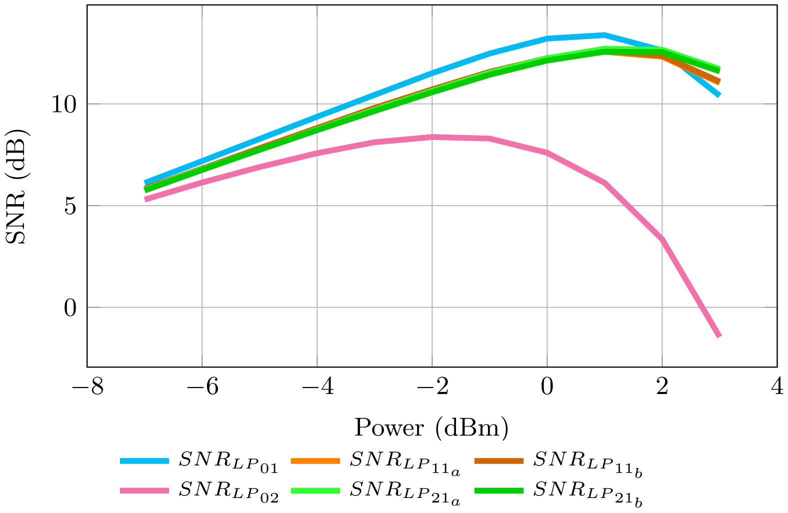

Figure 3.11: SNR of central channel versus launch power per mode in an FMF system under the intermediate coupling regime, using SM-EDFA for amplifying signals per mode. The FMF system carries nine channels per spatial mode, using spans of 100 km each and a total of 4 spans.

3.6 Conclusions

This chapter has presented the physical layer constraints that degrade signal quality in space division multiplexing systems based on FMF. All optical systems are degraded by both linear and nonlinear PLIs; however, the degree to which system performance is degraded by these phenomena depends largely on the multiplexing scheme and the detection and equalization scheme employed at the receiver.

Attenuation, dispersion, crosstalk, mode-dependent loss, and the differential mode delay are the main linear PLIs. On the other hand, self-phase modulation, cross-phase modulation, four-wave mixing, and stimulated Raman scattering are the main nonlinear PLIs. At the same time, these PLIs can be classified as intramodal or intermodal interactions, according to the signal interactions to produce these phenomena.

Attenuation can be compensated by optical amplification; however, all amplifiers degrade the SNR by adding ASE noise to the signal. Dispersion effects can be reduced by employing dispersion management techniques such as alternating compensation schemes or DSP techniques at the receiver.

Nonlinear PLIs are caused by high optical powers incident on the optical fiber. If the channels are well-spaced and the average power per channel is below a power level threshold, nonlinear effects can be neglected. This assumption is valid when operating within the conventional C-band. However, inter-channel stimulated Raman scattering in ultra-wideband systems becomes an important PLI that degrades system performance.

Propagation in SDM-FMF systems was modeled using two coupling regimes: weak coupling [35] and intermediate coupling [66, 75]. Both models were implemented and solved numerically using the split-step Fourier method. The SNR was analyzed for two case studies under these coupling regimes: a single-channel system and a multi-channel system. In both cases, the transmission link was constituted by several FMF fiber spans with a single-mode amplification scheme. Simulation results showed a potential SNR penalty of up to 6.8 dB under the intermediate coupling regime compared to the weak coupling regime, in the single-channel propagation scenario with an input power of 0 dBm to the FMF fiber.

The following chapters describe optical amplification solutions for SDM-FMF systems.

4

Few-Mode Erbium-Doped Fiber Amplifiers

4.1 Introduction

SDM technology is a promising alternative to face the potential capacity crunch of existing SMF [6]. In particular, SDM-FMF offers enhanced spatial efficiency and reduced power consumption compared to SMF, as discussed in the previous chapter. Long-haul SDM-FMF transmission requires optical amplification to compensate for fiber losses. Two main types of optical amplifiers have been used for these systems: few-mode erbium-doped fiber amplifiers (FM-EDFA) and few-mode distributed Raman amplifiers (FM-DRA). Along Chapters 4 and 5 an extensive review of the two main types of optical amplification for SDM-FMF systems will be presented. This chapter specifically focuses on FM-EDFA.

Designing and fabricating either FM-EDFAs or FM-DRA is a challenging task. The main goal is to achieve high gain and low differential modal gain (DMG) between spatial modes [76]. Low DMG means similar gain for all spatial modes available at a specific wavelength [37]. Besides that, it is also required to achieve a flat gain shape among all wavelengths per spatial mode, this metric, known as the differential spectral gain (DSG) [37], is referred to as the gain ripple in the context of single-mode systems. Furthermore, it is essential to maintain a low noise figure and high power efficiency.

This chapter is structured as follows: Section 4.2 presents a review of the literature. Then, Section 4.3 outlines the two-stage FM-EDFA design methodology joint DMG-DSG minimization. Subsequently, Section 4.4 presents the simulation results of the designed FM-EDFA. Finally, Section 4.5 summarizes this chapter.

The work presented in this chapter is based on works published in:

[21] **A. Lozada** and R. Olivares, “Optimized Two Stage Few-Mode Erbium Doped Fiber Amplifier,” in *2023 SBMO/IEEE MTT-S International Microwave and Optoelectronics Conference (IMOC)*, 2023, pp. 316–318.
[20] **A. Lozada**, R. Olivares, N. Jara, P. Morales, B. D. Feris, A. Leiva, G. Saavedra, and D. Bórquez-Paredes, “Performance evaluation of a two-stage few-mode EDFA for high-capacity SDM systems,” Optics Express, vol. 32, no. 23, pp. 41 417–41 432, 2024. (Appendix A)

4.2 Literature Review

FM-EDFAs have been studied in the context of optical amplification for SDM-FMF systems [77, 76, 37, 38]. Due to optical amplification performance depends on the fiber structure and the doping profile, researchers have focused on three approaches to improve FM-EDFA performance: tailoring the rare-earth doping profile [77, 78, 79, 80, 81, 82, 83, 84]; tailoring the refractive-index profile [76, 85, 84]; and tailoring the pumping profile [86, 87, 21]. Another technique that improves the performance of FM-EDFA in terms of reducing DSG involves the use of gain flattening filters [85, 21, 88, 89, 90]. To fabricate GFF for SDM-FMF systems three approaches have been published in literature, including free-space optical modules using spatial light modulators [88], long-period fiber gratings [89], and mode-selective couplers [90].

All these techniques to improve FM-EDFA have been used individually or in combination to achieve the desired amplification performance as can be seen in Table 4.1 which summarizes characteristics and performance metrics for a variety of FM-EDFA works. To be comparable, Table 4.1 include works that have reported C-band operation in the range of 1530 to 1565 nm for signals over six LP modes (LP_{01}, $LP_{11_{a,b}}$, LP_{02}, and $LP_{21_{a,b}}$). From this table, some trends can be identified. The fiber refractive index profile has taken some configurations: step-index [78, 87, 77, 21], double-cladding step-index [89], trench-assisted [76], and staircase index [84]. The pumping profile covers some degrees of freedom, for example, the pump can be injected into the core [79, 80, 89, 87, 76, 21] or the cladding [78, 84, 77]; the pump can be launched into one or more spatial modes [79, 80, 89, 87, 76, 21] with equal or different power and directions; and the optical fiber can be uniformly [80, 89, 87, 21] or non-uniformly doped [78, 79, 80, 81, 76, 84].

From Table 4.1, it can be observed that in terms of DMG, the best value is reported in [84], where it is proposed an optimization method to reduce DMG in FM-cladding pumped EDFAs. Regarding DSG, three works have reported results in the range between 0.38 to 0.6 dB [21, 90, 89]. These works have in common that they use GFF to obtain a low DSG. In [90], it is proposed an FM-GFF based on mode selective couplers, in this case, the FM-GFF follows the FM-EDFA device. Finally, in [89], it is proposed an FM-GFF based on cascaded long-period fiber grating using double cladding FMF, in this case, the FM-GFF is placed at the end of the FM-EDFA. A dash in Table 4.1 represents that the information about the parameter presented in the column was not provided in the referenced study.

Table 4.1: FM-EDFA papers reported over six-signal modes and C-band (1530-1565 nm) operation.

FM-EDFA	Index profile	WDM channels	Pumping profile				DMG	DSG	Mean Gain	NF
			Type	Direction	Power	Doping				
6M-EDFA [78]	Step-index	15	Cladding	Forward	2.5 W	Multilayered	< 1 dB	–	24.8 dB	5.3 dB
6M-EDFA [79]	–	4	Core	–	LP_{01} (100 mW), LP_{02} (100 mW)	Micro-structure	2.3 dB	2.3 dB	18.8 dB	–
6M-EDFA [80]	–	–	Core	–	LP_{01}(264.94 mW), LP_{02} (500 mW), and LP_{21} (500 mW)	Uniform	2 dB	–	–	–
	–	–	Core	–	LP_{01} (600 mW)	Multi-well ion	2.5 dB	–	–	–
6M-EDFA [89]	Double-cladding	–	Core	–	LP_{02} (200 mW)	Uniform	0.6 dB	0.6 dB	20 dB	–
6M-EDFA [87]	Step-index	8	Core	–	LP_{01} (400 mW or 800 mW)	Uniform	10 dB	2.5 dB	–	–
			Core	–	LP_{01} and LP_{11} (400 mW or 800 mW)	Uniform	10 dB	5 dB	–	–
6M-EDFA [76]	Trench-assisted	8	Core	Forward	LP_{01} (400 mW)	Multilayer	1.945 dB	2.562 dB	25 dB	4 dB
6M-EDFA [84]	Staircase index	36	Cladding	-	20 W	Double-ring	0.18 dB	< 4 dB	23.7 dB	4.08 dB
6M-EYDFA [77]	Step-index	7	Cladding	Forward (1st stage) and Backward (2nd stage)	0.8 W (1st stage) and 8 W (2nd stage)	Ytterbium co-doping	3 dB	4 dB	40 dB	7 dB
6M-EDFA [90]	Step-index	–	Core	Forward	LP_{01} (600 mW)	Uniform	0.38	0.38	21	–

Most of the studies presented in Table 4.1 introduce methodologies for optimizing amplifier design. In references [78, 80, 76, 84], either the refractive index or the doping profile of the fiber has been optimized to minimize DMG. Additionally, in [79], the doping profile was optimized to maximize gain and minimize the maximum DMG or DSG. Notably, few previous works [89, 21, 90] have jointly minimized DMG and DSG. In [89] and [90], the design of the GFF was optimized based on a cascade of 15 long-period fiber gratings for a double cladding FMF, and a cascade of 5 mode selective couplers, respectively.

The studies outlined in Table 4.1 limited the number of WDM channels between 4 [79] to 36 [84]. However, conventional C-band has the potential to allow until 320 WDM channels, using a separation between adjacent channels of 12.5 GHz [91]. To harness the full capabilities of SDM-FMF systems for practical applications, and to meet the demands of increased data capacity while ensuring the reliability and efficiency of FMF networks, it becomes necessary to explore the entire spectrum of the C-band. Consequently, FM-EDFA must exhibit robust performance under these conditions.

The contributions of this work were published in [21] and [20]. In [21], the performance of a two-stage FM-EDFA was characterized, with the pumping profile and the profile of a single GFF, placed in the middle of the amplifier, optimized to flatten the gain spectrum across 6 LP modes and 9 wavelengths per spatial mode. In [20], the adaptability of the design presented in [21] was validated to accommodate a larger number of WDM channels and its use in an SDM-FMF link. None of the other studies presented in Table 4.1 have performed this validation.

4.3 Joint DMG-DSG Minimization Methodology

Figure 4.1 presents a diagram of the proposed methodology named, joint DMG-DSG minimization. This methodology begins by defining the physical configuration of the two-stage FM-EDFA, including the pump direction which can be forward, backward, or bidirectional. An example of a physical configuration using forward pumping is presented in subsection 4.3.1. Next, a genetic algorithm (GA) is applied to design the pumping profile (subsection 4.3.2) in conjunction with an iterative algorithm to design the GFF profile (subsection 4.3.4). The output is a pumping and GFF profile that jointly minimizes DMG and DSG. Joint minimization of DMG and DSG is accomplished in two steps: DMG is minimized by tailoring the pumping profile using a GA, and DSG is minimized by adjusting the GFF profile using an iterative algorithm.

The following subsections detail each step in the joint DMG-DSG minimization methodology.

4.3.1 Two-Stage FM-EDFA Configuration

The two-stage FM-EDFA using forward pumping, which will later be extended to include backward and bidirectional pumping, is illustrated in Figure 4.2. This configuration involves injecting WDM channels into the first erbium-doped few-mode fiber (ED-FMF) stage through a Wavelength-Selective WDM Coupler (WSC_1). Signal amplification is achieved using 980 *nm* forward multimode pumping. WSCs are considered to have high isolation between the signal and pump ports, so that any unwanted interference between

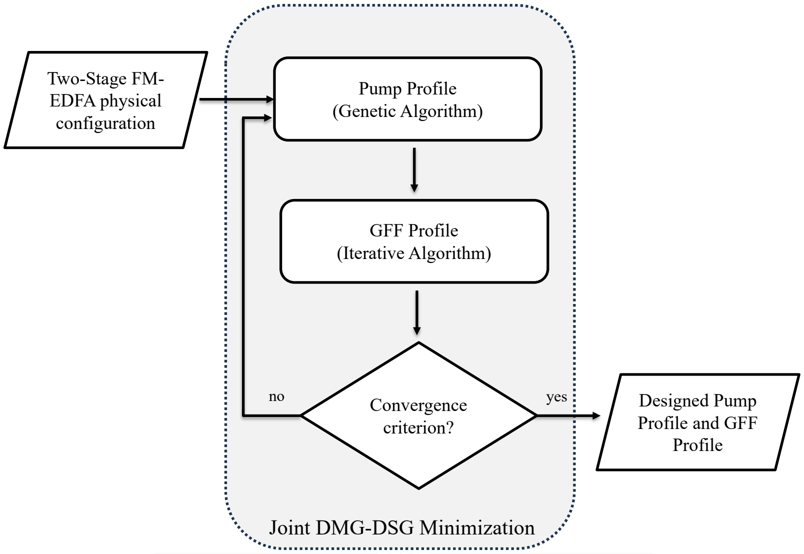

Figure 4.1: Schematic of the Joint DMG-DSG Minimization methodology

the signals and the pumps can be neglected. A GFF, an ASE filter, and an optical isolator (ISO) are strategically positioned between two ED-FMF equal sections, as in [21, 85, 92], referred to as *Stage 1* and *Stage 2*. *Stage 1* has the major contribution to the total gain and noise figure of the two-stage FM-EDFA, while *Stage 2* provides the additional gain necessary to achieve an output gain profile as flat as possible. The GFF is designed to flatten the gain curve across the wavelength range for each spatial mode, consequently, the bandwidth of the filter is around 4 THz. The ASE filter, which is a bandpass filter, is introduced to only pass the wavelengths of interest and eliminate the propagation of the forward-traveling ASE noise. In practice, the ASE filter and the GFF can be implemented in a single filter. The ISO is incorporated to suppress backward-traveling ASE originating in *Stage 2* of the amplifier. *Stage 2* is then fed by the flattened WDM signals and residual pumping from the first stage, facilitated through a third WSC_3.

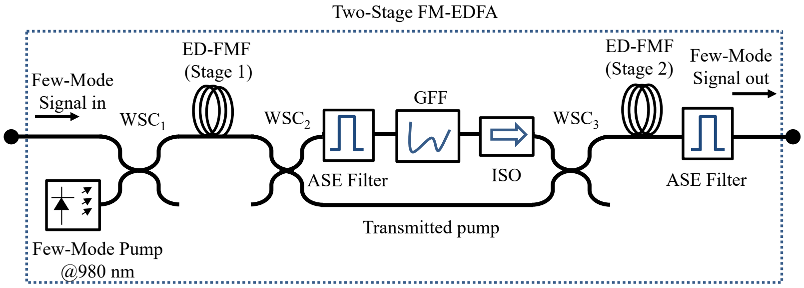

Figure 4.2: Configuration of the two-stage FM-EDFA.

4.3.2 Pumping Profile Design

The pumping profile for an FM-EDFA should define the type, pump direction, pump wavelength(s), pump mode(s), pump power(s), and doping profile. In this section, it is assumed a core pumping type in forward direction at 980 nm with uniform doping profile. This wavelength and pump direction were selected based on the performance it has shown for amplifying the first LP modes [85, 86]. As is also the case in single-mode EDFAs, where higher pumping efficiency is shown due to a larger absorption cross-section at 980 nm compared to 1480 nm, and low noise figure with forward pumping [93]. To complete the design of the pumping profile, which involves the selection of the pumping mode(s) and its power, a GA was employed. GAs have demonstrated effectiveness in improving various aspects of FM-EDFA designs, including the selection of parameters such as the doping profile in a multilayer configuration [78, 79, 82, 76], the refractive index profile in a trench-assisted configuration [85], and the pumping profile itself [21]. The GA originally introduced in [21] was refined in [20] to design the pumping profile for the specific demands of C-band full-channel occupation. The fitness function (FF) employed to evaluate individuals within each population is defined as follows:

$$FF = \sum_{\lambda_s=1530\text{nm}}^{1565\text{nm}} \frac{G_{ave}(\lambda_s)}{DMG(\lambda_s)}, \tag{4.1}$$

where G_{ave} denotes the average modal gain at λ_s and $DMG(\lambda_s)$ is the maximum DMG at wavelength λ_s. The objective of the GA presented in Algorithm 1 is to maximize the fitness function, selecting a proper combination between pumping modes and pumping powers. In the GA, each individual is represented by a vector $\mathbf{g}$ of size $2p$, where p denotes the number of pumping modes. Each pair of genes within this vector represents a specific pumping mode along with its corresponding power. As an example, for 3 pumping modes, $\mathbf{g} = [0, 100, 1, 100, 2, 100]$. This individual represents a pumping profile composed of 3 LP modes, identified with different integer numbers $(0, 1, 2)$, each one with equal power of 100 mW.

The GA operation, described in Algorithm 1, can be summarized in the next four steps:

- Step 1: To generate a starting population of size I
  The first step of the GA is to build a starting population of size I, which is composed of a number I of individuals $\mathbf{g}$. Each $\mathbf{g}$ is generated by randomly selecting p pumping modes and p pumping powers from a predefined set of searching ranges for each variable. This step is represented in line 3 of Algorithm 1.

- Step 2: Individual evaluation
  The second step of the GA performs the following actions for each individual in the population: (1) Determine the GFF profile using Algorithm 2; (2) To solve the set of coupled Eq. (4.2)-Eq. (4.4) with the GFF at the midstage of the amplifier, refereed as function $EDFA_{calc}$ in Algorithm 1; (3) To calculate the fitness function. Once all individuals in the population have been evaluated, the best individual, characterized by the maximum fitness value, is saved as a potential solution. This step is represented from lines 1 to 9 in Algorithm 1.

- Step 3: Generation of new populations
  The third step of the GA is to construct a new population based on the previous one, in this step the processes of selection ($\mathbb{S}$) using the tournament approach, crossover ($\mathbb{X}$) with probability p_c, and mutation ($\mathbb{M}$) with probability p_m are applied. Then, the individuals' evaluation is repeated over this new population. Lines 12 to 19 in

Algorithm 1 are representing this step.

- Step 4: Termination condition
  The fourth step of the GA is to check if the termination condition is met, this is either when the number of populations (P) reaches the predefined maximum value ($MaxP$)-condition of the while loop of step 3- or when, after 25 successive populations, the best individual is the same, this is the convergence condition verified in line 15 of Algorithm 1. The GA returns the best pumping profile based on the constructed populations.

Algorithm 1 Genetic Algorithm

```
Require: $I$, $p$, mode and power range, $MaxP$, $p_c$, $p_m$, $P = 0$.
 1: if $P == 0$ then
 2:     for $i = 0 : i++ : I - 1$ do
 3:         Create $\mathbf{g}_i$ of size $2p$
 4:         $[GFF] = GFF\ Algorithm$
 5:         $[Gain, DMG] = EDFA_{calc}(\mathbf{g}_i, GFF)$
 6:         $FF_i(Gain, DMG)$
 7:     end for
 8:     Save the best $\mathbf{g}$ (max($FF$))
 9: end if
10: $P = P + 1$
11: while $P <= MaxP - 1$ do
12:     $[New\ population] = \mathbb{S} \rightarrow \mathbb{X}(p_c) \rightarrow \mathbb{M}(p_m)$
13:     Repeat 4 to 6 $\forall\ \mathbf{g} \in New\ population$
14:     Save the best $\mathbf{g}$ (max($FF$)) and compare it with the previous best max($FF$)
15:     if best max($FF$) $\rightarrow$ converges then
16:         break
17:     end if
18:     $P = P + 1$
19: end while
        return Pumping profile: $\mathbf{g}$(max($FF$))
```

The algorithmic complexity is determined by the population size I, i.e., the number of individuals per generation, the maximum number of generations $MaxP$, the number of signaling and pumping wavelengths Λ_s and Λ_p, respectively, and the number of LP modes M. For each individual per generation, the mathematical model for the two-stage FM-EDFA is solved going through all Λ_s and Λ_p for all M modes to compute de fitness function of that individual. Consequently, the algorithmic complexity is $O(I \cdot MaxP \cdot \Lambda_s \cdot \Lambda_p \cdot M)$. The fitness function evaluations dominate the overall complexity and scales with the product of population size and number of generations.

4.3.3 Mathematical Model of FM-EDFA

The behavior of an FM-EDFA can be described through a set of coupled differential equations. These equations model the dynamics of optical power propagation for the signal, pump, and ASE noise within the amplifier [37]. It is also required to model the Erbium population densities between energy levels to describe the amplification process. The mathematical model used here, is the multimode case of the model suggested by Giles and Desurvire [94], which has been extensively used to describe the optical amplification process in single mode EDFA. This model has the following assumptions [87]: (1) At 980 nm pump wavelength, the model is approximately a quasi-three-level system, and the excited state absorption is ignored; (2) The concentration of Erbium ions is uniformly distributed along the longitudinal direction of the fiber.

The coupled equations representing power on spatial signal mode ($P_{s,i}$), spatial pump mode ($P_{p,j}$), and ASE ($P_{ASE,i}$) are mathematically expressed as follows [85, 38, 37]:

$$\frac{dP_{s,i}}{dz} = P_{s,i} \iint \Gamma_{s,i}(r,\phi)[N_2(r,\phi)\sigma_{es,i} - N_1(r,\phi)\sigma_{as,i}]dA - \sum_{k=1}^{m_s} d_{s,i\to k}[P_{s,i} - P_{s,k}], \tag{4.2}$$

$$\frac{dP^{\pm}_{p,j}}{dz} = P^{\pm}_{p,j} \iint \Gamma_{p,j}(r,\phi)\, N_1(r,\phi)\sigma_{ap,j}\, dA - \sum_{k=1}^{m_p} d_{p,j\to k}[P^{\pm}_{p,j} - P^{\pm}_{p,k}], \tag{4.3}$$

$$\frac{dP^{\pm}_{ASE,i}}{dz} = P^{\pm}_{ASE,i} \iint \Gamma_{ASE,i}(r,\phi)[N_2(r,\phi)\sigma_{eASE,i} + N_1(r,\phi)\sigma_{aASE,i}]dA \tag{4.4}$$

$$\ldots + 2\sigma_{eASE,i} h\nu_{ASE,i}\Delta\nu_{ASE,i} \iint N_2(r,\phi)\Gamma_{ASE,i}(r,\phi)dA - \sum_{k=1}^{m_s} d_{s,i\to k}[P^{\pm}_{ASE,i} - P^{\pm}_{ASE,k}],$$

where subscripts s and p indicate the signal and pump wavelengths, respectively. ASE refers to the central wavelength of a spectral slot of width $\Delta\nu_{ASE}$ (noise bin) that result from decomposing the total spectrum of frequencies of interest of the amplifier. The ASE subscript will run through all the spectral positions of the amplifier bandwidth, while s will only refer to those where the signals are located. Therefore, ASE and s may or may not assume the same values, depending on whether or not they refer to the same spectral position. Subscripts i, and j indicate the i-th signal mode and j-th pump mode. $\Gamma_{s/p}(r,\phi)$ is the normalized intensity profile of the i-th signal or j-th pump mode; $N_1(r,\phi)$ and $N_2(r,\phi)$ are the population densities of Erbium atoms in the lower and upper levels; $\sigma_{es(p),i}$ and $\sigma_{as(p),i}$ are the emission and absorption cross sections at the i-th signal (pump) mode at the wavelength of the signal (pump) $\lambda_{s(p)}$; h is the Planck's constant; $\nu_{s,i}$ is the frequency of the i-th signal mode at the wavelength λ_s; $\Delta\nu_{s,i}$ is the equivalent amplifying bandwidth; and $d_{s(p),i\to k}$'s [95] are coupling coefficients between signal modes i and k at wavelength $s(p)$ and computed as a function of the difference between the propagation constants of modes i and k. $d_{s(p),i\to k}$ represents a fraction of the i-th mode power scattered into the k-th mode [95].

The total doping concentration N_0, is given by [38]: $N_0(r,\phi) = N_1(r,\phi) + N_2(r,\phi)$. The rate equations for the population densities are as follows:

$$N_1(r,\phi) = \frac{\frac{1}{\tau} + W^{e}_{(s,ASE)}}{\frac{1}{\tau} + W^{(e,a)}_{(s,ASE)} + W^{a}_{p}} N_0(r,\phi), \tag{4.5}$$

$$N_2(r,\phi) = \frac{W^{a}_{(s,ASE)} + W^{a}_{p}}{\frac{1}{\tau} + W^{(e,a)}_{(s,ASE)} + W^{a}_{p}} N_0(r,\phi), \tag{4.6}$$

the auxiliary variables $W^{e(a)}_{(s,ASE)}$, $W^{(e,a)}_{(s,ASE)}$, and W^{a}_{p} to calculate $N_1(r,\phi)$ and $N_2(r,\phi)$ are defined as follows:

$$W^{e(a)}_{(s,ASE)} = \sum_{s=\lambda_{s_1}}^{\lambda_s} \sum_{i=1}^{m_s} \frac{[P_{s,i} + P_{ASE,i}]\sigma_{e(a)s,i}\Gamma_{s,i}(r,\phi)}{h\nu_{s,i}}, \tag{4.7}$$

$$W^{(e,a)}_{(s,ASE)} = \sum_{s=\lambda_{s_1}}^{\lambda_s} \sum_{i=1}^{m_s} \frac{[P_{s,i} + P_{ASE,i}](\sigma_{es,i} + \sigma_{as,i})\Gamma_{s,i}(r,\phi)}{h\nu_{s,i}}, \tag{4.8}$$

$$W^{a}_{p} = \sum_{p=\lambda_{p_1}}^{\lambda_p} \sum_{j=1}^{m_p} \frac{P_{p,j}\sigma_{ap,j}\Gamma_{p,j}(r,\phi)}{h\nu_{p,i}}, \tag{4.9}$$

where τ is the spontaneous emission lifetime for the excited state, $m_{s(p)}$ is the total number of guided modes for signal (pump), and $\lambda_{s(p)}$ is the total number of wavelengths for signal (pump). With the initial conditions at $z = 0$, i.e. input signal and pump power, backward and forward ASE power, Eq. (4.2) - (4.4) can be solved numerically using the standard fourth-order Runge-Kutta method to calculate the gain and noise figure of the FM-EDFA.

4.3.4 Gain-Flattening Filter (GFF)

To design the GFF profile, an iterative algorithm based on the gradient-descent optimization approach [79, 96] was programmed. The pseudo-code is presented in Algorithm 2. This algorithm requires the following inputs: $Filter_{in}$ which is related to the signal and noise power obtained by solving Eq. (4.2) and Eq. (4.4) in the midstage of the EDFA, the filter adaptation step (ΔFit), the power variation goal (ΔP_{target}), and the maximum number of iterations ($MaxIt$). Parameters ΔFit, ΔP_{target}, and $MaxIt$ should be selected according to the target performance and the computation constraints. The output of the algorithm is the GFF profile, represented by a set of coefficients ranging from 0 to 1 associated with the signal wavelengths.

Algorithm 2 Gain Flattening Filter Algorithm

```
Require: $Filter_{in}, \Delta Fit, \Delta P_{target}, MaxIt.$
$i = 1;$
$GFF(i)$ initialized with ones
while ($\Delta P > \Delta P_{target}$) or ($i <= MaxIt$) do
    $Filter_{out} = Filter_{in} * GFF(i)$
    $EDFA_{out}(i) = EDFA_{calc}(Filter_{out})$
    $GFF(i+1) = GFF(i) - \Delta Fit(EDFA_{out}(i) - \min(EDFA_{out}(i)))$
    $\Delta P = \max(EDFA_{out}(i)) - \min(EDFA_{out}(i))$
    $i = i + 1$
end while
return GFF profile: $GFF(i-1)$
```

In the first iteration ($i = 1$), the GFF profile is initialized with ones, this way it does not have a flattening effect over the output signals of the first stage of the FM-EDFA. To determine the new set of coefficients ($GFF(i + 1)$), the input signal and the average output signal of the second stage of the FM-EDFA are required, these are represented by $Filter_{out}$ and $EDFA_{out}$ in Algorithm 2. The function $EDFA_{calc}$ solves the set of differential coupled Eq. (4.2) to Eq. (4.4) and returns the mean power of the output signal. The coefficients of the GFF profile for the next iteration are adjusted using the product between ΔFit and the difference between the mean signal output and its minimum value. This relationship allows the adaptation of the filter transfer function, aiming to achieve reduced power variations (ΔP) and the desired flattening effect, consequently decreasing DSG per mode.

The parameter ΔFit is fixed to a constant value within the range of $[0-1]$. On one hand, a value closer to 0 results in gradual changes to the GFF profile in each iteration, requiring a higher iteration count to meet the $\Delta Ptarget$ condition. On the other hand, a value closer to 1 induces rapid changes to the GFF profile, potentially compromising the achievement of $\Delta Ptarget$. Therefore, selecting an optimal ΔFit requires a sensitivity analysis to evaluate its impact on the overall process. The iterative algorithm ends either when the current ΔP is lower than ΔP_{target} or when the iteration count reaches $MaxIt$.

4.3.5 Performance Metrics

To evaluate the performance of the two-stage FM-EDFA, various key metrics were employed to provide a comprehensive analysis. The chosen performance metrics verify the effectiveness of the amplifier in maintaining low noise and flat gain distribution, in the spectral and spatial domains, handling multiple WDM signals. These metrics are crucial for optimal performance in practical applications. These metrics are defined as follows:

- The **gain** in the signal at wavelength s and at a mode i is:

  $$G(s,i) = \frac{P_{s,i}(z)}{P_{s,i}(0)}, \tag{4.10}$$

  where $P_{s,i}(z)$ is obtained using Eq. (4.2) at any position z.

- Although the **total NF** strongly depends on NF of the first stage, it is also degraded by the GFF and the second stage of the amplifier. Total NF in the signal at wavelength s and at a mode i is [97, 98]:

  $$NF_{s,i}^{total} = NF_{s,i}^{stage_1} + \frac{NF_s^{GFF} - 1}{G_{s,i}^{stage_1}} + \frac{NF_{s,i}^{stage_2} - 1}{G_s^{GFF}.G_{s,i}^{stage_1}}, \tag{4.11}$$

  where $NF_{s,i}^{stage_1}$ is the noise figure of the first stage of the amplifier; NF_s^{GFF} is the noise figure of the GFF computed as the inverse of the gain flattening filter coefficients; $NF_{s,i}^{stage_2}$ is the noise figure of the second stage of the amplifier; and $G_{s,i}^{stage_x}$ is the gain of the stage of the amplifier indicated by the superscript $stage_x$. Subscripts s and i indicate the wavelength and the LP mode, respectively.

- The **DMG** parameter is the differential gain in the modal domain for a fixed wavelength s, it is defined as [37]:

  $$DMG(s) = \max\{|G(s,i) - G(s,j)|\}, \tag{4.12}$$

  where at wavelength s, $i \neq j$ for all i and j spatial modes.

- The **DSG** parameter is the differential gain in the wavelength domain for one spatial mode i, it is defined as [37]:

  $$DSG(i) = \max\{G(s,i)\} - \min\{G(s',i)\}, \tag{4.13}$$

  where $s \neq s'$ for the spatial mode i.

4.4 Simulation Results

This section provides a comprehensive evaluation of the joint DMG-DSG minimization methodology employed for designing the pumping profile and the GFF profile, along with a detailed characterization of the two-stage FM-EDFA. Numerical techniques were applied to solve Eq. (4.2) - Eq. (4.4) to simulate the amplification process within the FM-EDFA. Six co-propagating signal modes (LP_{01}, LP_{11_a}, LP_{11b}, LP_{02}, LP_{21_a}, and LP_{21b}) were considered, with input parameters resumed in Table 4.2. The total length of the amplifier was optimized by numerical simulation to achieve the highest possible gain, taking into account the available pump power levels. The length of the doped fiber of *Stage 1* and *Stage 2* is half of the value reported in Table 4.2. The emission and absorption coefficients for the Erbium-doped fiber were obtained from the software VPItransmissionMaker™ [99]. A coupling coefficient, $d_{s(p),i\rightarrow k}$, with a mean value of the order of μm^{-1} was assumed, consequently, its impact on amplifier performance is small.

Table 4.2: Simulation parameters for FM-EDFA.

Step-index ED-FMF		**Signal**		**Pump**	
Parameter	**Value**	**Parameter**	**Value**	**Parameter**	**Value**
Radius [μm]	6.25	Wavelength range operation [nm]	1530 – 1565 (C-band)	Pump wavelength [nm]	980
Core refractive index (n_1)	1.45	Number of wavelengths	9 or 81	Pump direction	Forward, Backward or Bidirectional
Numerical aperture	0.2	Input power (per wavelength) [dBm]	-25		
Uniform doping concentration [$(N)\ m^{-3}$]	$1 \cdot 10^{24}$			Power range [mW]	200 – 300
Length [m]	30				
Photon lifetime [ms]	10				

4.4.1 Forward Pumping and GFF Profiles

The GA described in Algorithm 1 was programmed to design the pumping profile, aiming to select the most effective combination of LP modes and their corresponding powers for injecting forward pumping into the first stage of the amplifier. For the pumping mode search range, it was limited to the first eight LP modes that best match the intensity profile distribution of the signal modes (LP_{01}, $LP_{11_{a,b}}$, LP_{02}, $LP_{21_{a,b}}$, and $LP_{12a,b}$). Additionally, the pumping power search range was set between 200 mW and 300 mW. Each population consisted of 80 individuals, and for subsequent populations, the tournament method for selection was used, and crossover and mutation probabilities were set to 0.90 and 0.10, respectively. Numerical simulations were programmed in C++ and run on an Apple M1 Pro, with time costs of 432000 s. The fitness function preserves the individuals with high gain average and lower DMG.

Two optimization scenarios were conducted with 9 and 81 WDM signals equally distributed across the conventional C-band. In the case where 9 WDM signals propagate in each spatial mode, 40 populations were required for the GA to converge. The designed pumping profile in this case was: LP_{02} (200 mW), LP_{21_a} (225 mW), and LP_{21_b} (235 mW). While, when 81 WDM signals propagate in each spatial mode, after 21 populations the fitness function value does not experience a significant change. Figure 4.3 shows the evolution of the fitness value for 60 populations for the case of 81 WDM signals propagating in each spatial mode. The optimal individual, extracted from the 46-th population, is composed of the pumping profile: LP_{02}(295 mW), LP_{21a}(295 mW) and, LP_{21b}(285 mW). The resultant optimized pumping profiles are explained by the mode field distribution of each mode and its capabilities to amplify the LP signal modes. The two-stage FM-EDFA with this pumping profile, exhibits the best combination between high mean gain and low DMG.

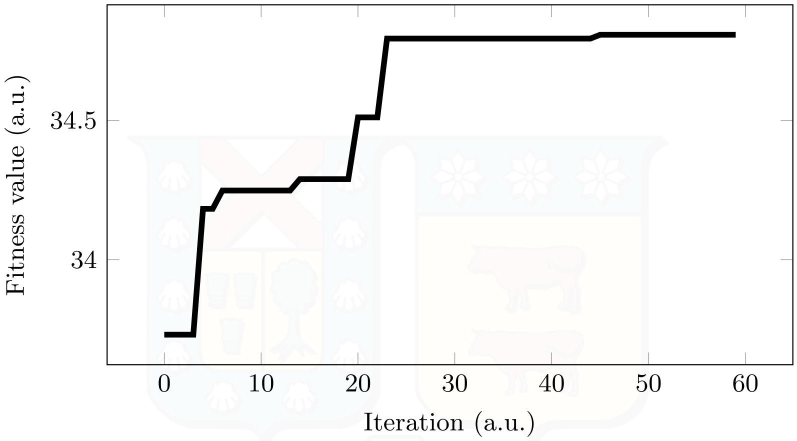

Figure 4.3: Genetic algorithm fitness function evolution for 60 populations for the two-stage FM-EDFA forward pumping profile design when 81 WDM signals propagate per spatial mode.

The predefined parameters required for designing the GFF were set to 0.6 for the filter adaptation step (ΔFit) and 0.3 dB for the power variation goal (ΔP_{target}). These specific values were carefully chosen to obtain the lowest DSG when the optimized pumping profile was used. The resulting GFF profile is illustrated in Figure 4.4. Lower coefficients are allocated to wavelengths requiring a more pronounced flattening effect, while higher coefficients correspond to wavelengths where a lower flattening effect is necessary. This tailored profile grants the efficiency of the GFF in achieving the flattened gain profile across the wavelength spectrum.

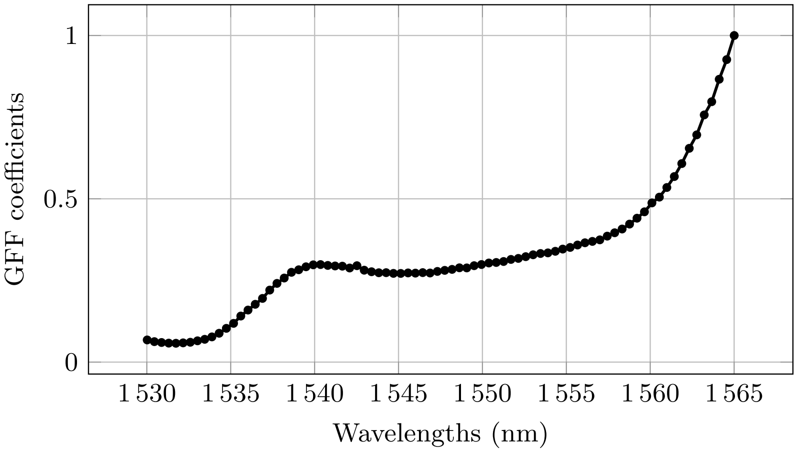

Figure 4.4: GFF profile for gain flattening in a 6M-EDFA with 81 WDM signals per spatial mode.

With the pump profile and GFF design established, the characterization of the two-stage FM-EDFA will be explored in more detail. Figure 4.5 illustrates two cases of study for 9 WDM signals propagating in each spatial mode: one without using the gain flattening filter (w/o GFF - dotted lines) and the other with its application (wGFF - solid lines). The comparison is drawn for both the best (LP_{01}) and the worst (LP_{02}) spatial modes, with similar trends observed across other modes. The effectiveness of the GFF is measured by

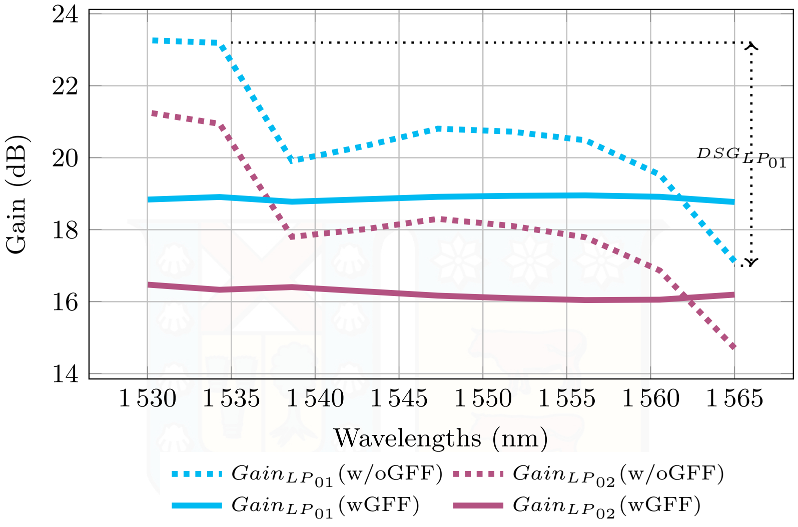

Figure 4.5: Gain for modes LP_{01} and LP_{02} using the GFF (wGFF - solid lines) and without using it (w/oGFF - dotted lines) when 9 WDM signals propagate in each spatial mode.

the parameter DSG (Eq. (4.13)), where a lower DSG means a flatter gain profile. In the absence of the GFF, the maximum DSG reaches 6.55 dB for the LP_{01} mode. Conversely, with the implementation of the GFF, the DSG is improved, reaching a value of 0.53 dB. There is an unavoidable cost in terms of gain reduction when the GFF is applied. For this cost not to impact communication efficiency in practical applications, it must be included in the power budget of the initial design of the amplifier, to compensate for link losses adequately. Despite this, the loss in modal mean gain is only 2.2 dB, which is offset by a substantial improvement in flatness, reducing from 6.55 dB to 0.53 dB.

Figure 4.6 shows the cases w/o GFF and wGFF for 81 WDM signals propagating in each spatial mode, showing a higher granularity in the gain curve compared to Figure 4.5. When the GFF was not used, the worst scenario was for LP_{02} with a DSG value of 9.17 dB. However, when the GFF was used, the DSG value was reduced to 0.54 dB. Figures 4.6 and 4.6 highlight the substantial benefit of applying the GFF, resulting in a flat gain profile. When comparing the gain curves without GFF for 9 and 81 WDM signals, a peak in gain is observed in the range of 1530 – 1535 nm, which does not appear when 9 WDM signals are used. This results in a 2.62 dB higher DSG for the case with 81 WDM signals. Furthermore, DSG results obtained in Figures 4.5 and 4.6, have around 2 dB difference in the achieved mean gain per mode, showing that both pumping profile design and GFF design are required when the system capacity change.

4.4.2 FM-EDFA Gain Characterization using Forward Pumping

Using the designed forward pumping profile and the GFF from the preceding subsection for 9 WDM signals per spatial mode, the gain and DMG as a function of wavelengths in the two-stage FM-EDFA, are presented in Figure 4.7. The calculations for gain and DMG were obtained from Eq. (4.10) and Eq. (4.12), respectively. The FM-EDFA demonstrates a mean gain exceeding 17 dB per mode across the entire C-band, with the maximum DMG reaching 3 dB at 1530 nm.

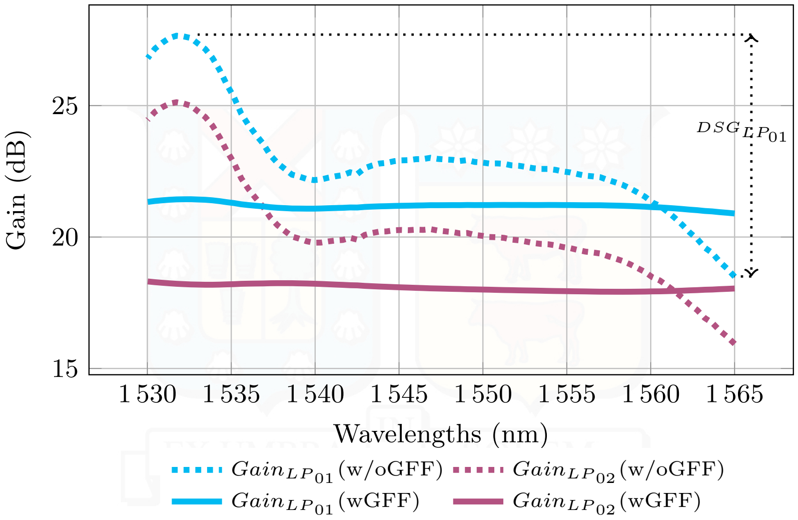

Figure 4.6: Gain for modes LP_{01} and LP_{02} using the GFF (wGFF - solid lines) and without using it (w/oGFF - dotted lines) when 81 WDM signals propagate in each spatial mode.

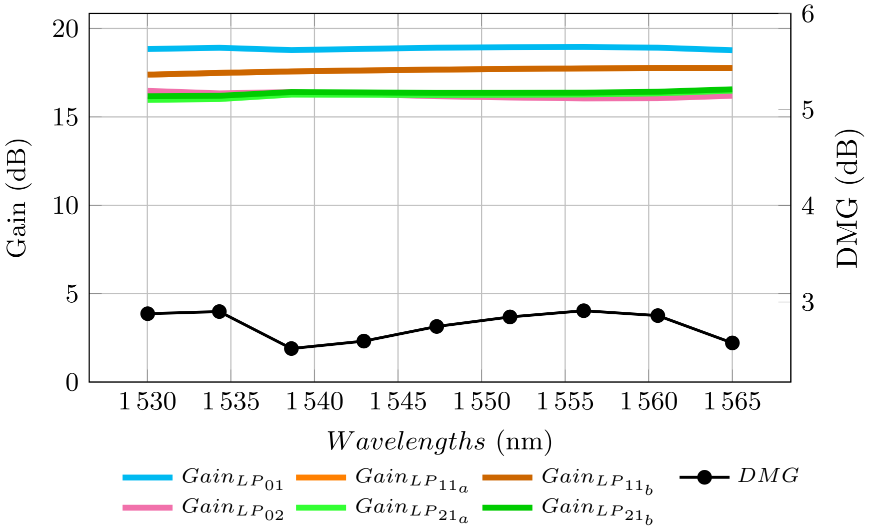

Figure 4.7: Gain per mode and maximum DMG for a two-stage 6M-EDFA using a GFF and the designed forward pumping profile for 9 WDM signals per spatial mode.

Regarding the noise, NF was computed using Eq. (4.11), and the results are shown in Figure 4.8. The highest NF is observed at 1530 nm reaching 4.6 dB for LP_{21a}, while the lowest value, 3.5 dB, is observed at 1560 nm for LP_{01}. This represents a noise figure variation of 1.1 dB for the worst case scenario. Nonetheless, the resultant mean NF produced by the two-stage FM-EDFA remains below 5 dB, aligning with the desirable noise performance across the entire C-band spectrum for EDFA amplifiers.

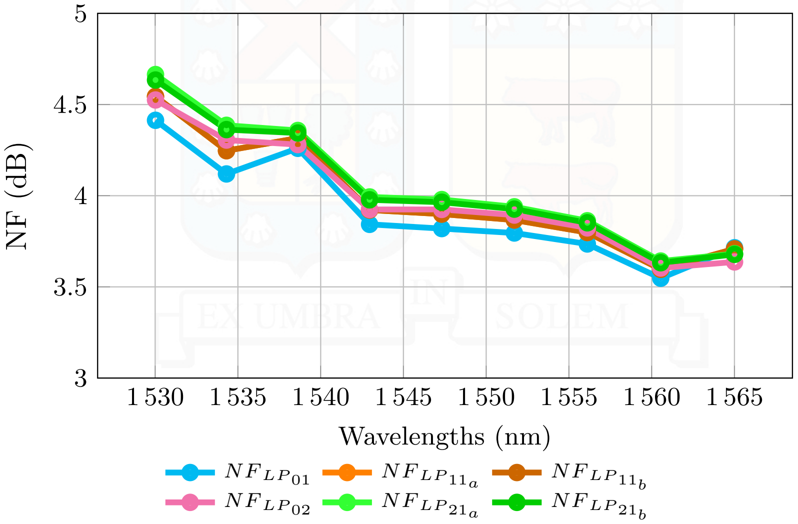

Figure 4.8: Noise figure per mode for a two-stage 6M-EDFA using a GFF and the designed forward pumping for 9 WDM signals per spatial mode.

When propagating 81 WDM signals in each of the 6 LP modes, DMG and DSG were below 3.58 dB and 0.54 dB, respectively, with an average gain of 18 dB and NF below 5.83 dB, as can be seen in Figures 4.9 and 4.10, respectively. Considering the DMG values reported in Table 4.1 for FM-EDFA configurations with the same conditions of refractive index, pumping type, and doping profile, this amplifier has better performance than [89], in addition to being the only one tested under the full channel load scenario. Only works with refractive indices and/or doping profiles more complex and, consequently, more expensive, obtain better results in terms of DMG.

The results reported in Figures 4.7 and 4.8 are close to those reported in Figures 4.9 and 4.10, respectively, but in the former case, the system has a reduced capacity by a factor of 9 and a notable lack of granularity in the NF curve. The pumping profile and GFF design were performed for both case studies. The difference is reflected in different pumping budgets; for the case of 9-WDM signals, it is 660 mW, and for the case of 81-WDM signals the pumping budget is 1.33 times higher. Additionally, the computation time increased by a factor of 2.5 by increasing the system capacity by 9. Thanks to the designed pumping profile using the joint DMG-DSG minimization methodology, the increase in the number of WDM signals carried by each mode does not translate into a significantly worse performance in terms of DMG, DSG, average gain, and NF.

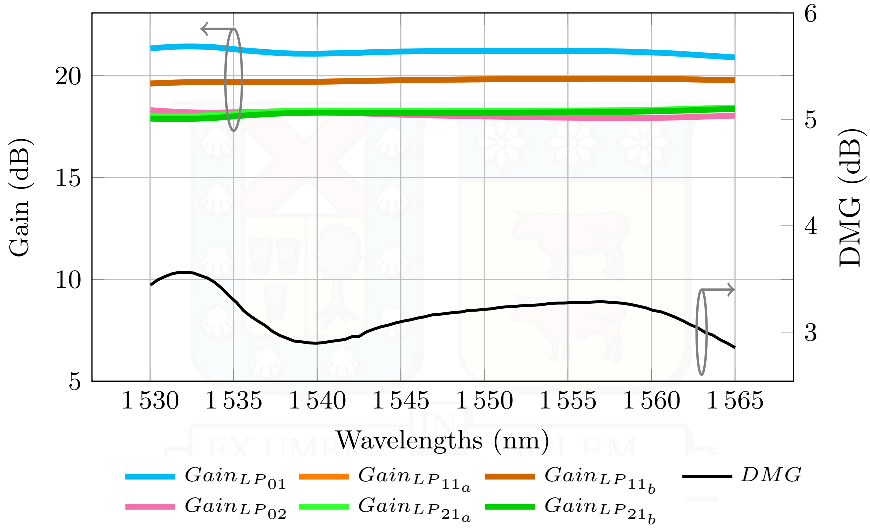

Figure 4.9: Gain per mode and maximum DMG for a two-stage 6M-EDFA using a GFF and the designed pumping scheme for 81 WDM signals per spatial mode.

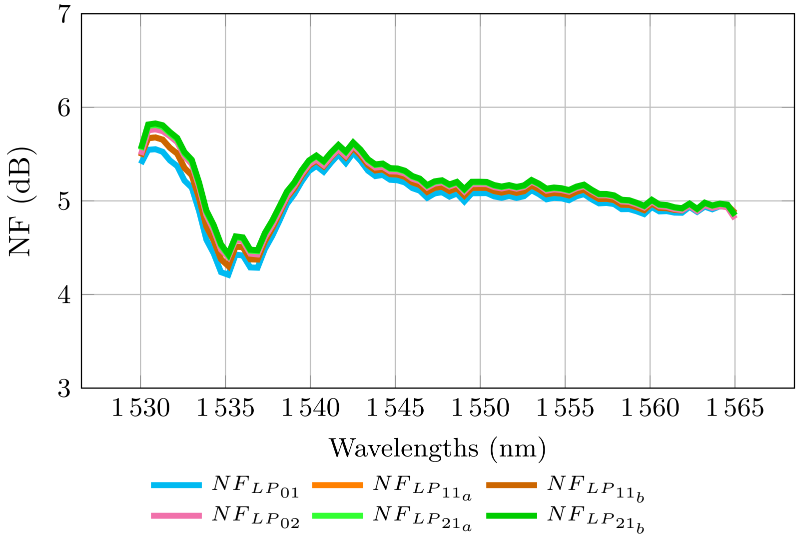

Figure 4.10: Noise figure per mode for a two-stage 6M-EDFA using a GFF and the designed pumping scheme for 81 WDM signals per spatial mode.

4.4.3 FM-EDFA Gain Characterization using Backward Pumping

One of the degrees of freedom in the design of EDFA amplifiers is the pump direction, which can be forward, backward or bidirectional [100]. The forward pumping configuration has been the most commonly used [21, 76, 78], as it offers good performance in terms of gain and noise figure, as shown in the previous section (4.4.2). To the best of our knowledge, backward pumping configuration for FM-EDFA has been explored in only one study [100]. That study reported similar performance to forward pumping in terms of gain and DMG using a single-channel configuration per LP mode. However, no results were provided regarding DSG or noise performance. In this subsection, the gain characterization of a two-stage FM-EDFA using backward pumping is presented.

The two-stage FM-EDFA configuration uses backward pumping, as shown in Figure 4.11. Comparing this configuration to the previous one (Figure 4.2), there are many similarities as well as some differences. The configuration involves injecting 9 WDM channels into the first ED-FMF stage through WSC$_1$. WSC_4 allows multimode pumping to be injected at 980 *nm* in the backward direction. The GFF, ASE filter, and ISO are inserted between *Stage 1* and *Stage 2* of the FM-EDFA, as in subsection 4.3.1. *Stage 1* has the major contribution to the total gain and noise figure of the two-stage FM-EDFA, while *Stage 2* provides the additional gain necessary to achieve an output gain profile as flat as possible. The GFF is designed to flatten the gain curve across the wavelength range for each spatial mode. The ASE filter and the ISO have the same function described in subsection 4.3.1. *Stage 1* is fed by the WDM signals and the residual backward pumping from the second stage. Besides, *Stage 2* is fed by the flattened WDM signals and the backward pumping.

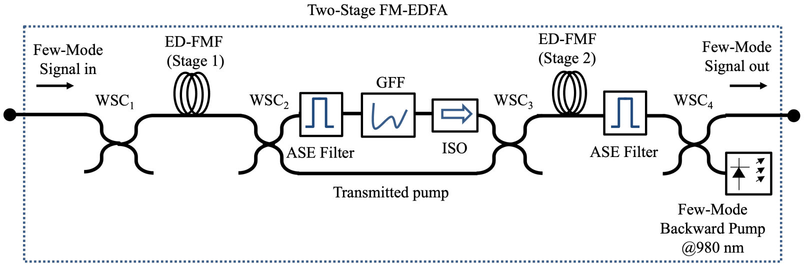

Figure 4.11: Configuration of the two-stage FM-EDFA with backward pumping.

The Joint DMG-DSG Minimization methodology proposed in Section 4.3 was applied to design the backward pumping profile and the GFF filter profile. Using Algorithm 1, the optimized backward pumping profile was determined as follows: LP_{02} (183.45 mW), LP_{21_a} (224.63 mW), and LP_{21b} (224.84 mW). This represent a pumping power budget reduction of 27.08 dB compared to the forward pumping designed for 9 WDM signals per LP mode.

Using the designed backward pumping profile and GFF, the gain and DMG as a function of wavelengths in the two-stage FM-EDFA with backward pumping, are presented in Figure 4.12. The gain and DMG were obtained using Eq. (4.10) and Eq. (4.12), respectively. The FM-EDFA demonstrates a modal mean gain exceeding 17 dB across the entire C-band, with maximum DMG of 2.95 dB at 1530 nm and 1534.3 nm. Compared to the forward pumping design shown in Figure 4.7, the backward pumping profile achieves the same modal mean gain of 17 dB despite the reduction of 4.1% in the pump power budget. DMG shows a minor variation of 0.5 dB. However, DSG degrades from 0.53 dB in the forward pumping case to 0.98 dB with the backward pumping design.

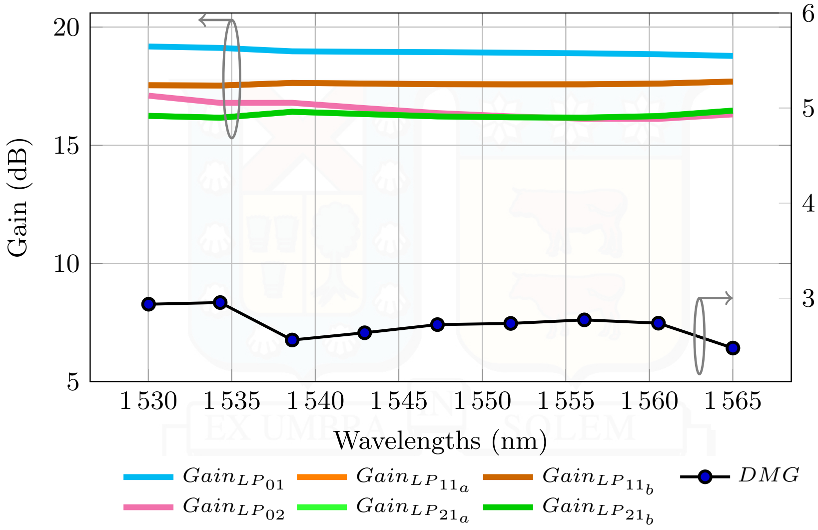

Figure 4.12: Gain per mode and maximum DMG for a two-stage 6M-EDFA using a GFF and the designed backward pumping profile for 9 WDM signals per spatial mode.

The NF was computed using Eq. (4.11), and the results are shown in Figure 4.13. The highest NF is observed at 1534.3 nm reaching 7.30 dB and the lowest value (5.31 dB) at 1565 nm. This represents a noise figure variation of 1.99 dB for the worst case. Compared to the forward pumping design shown in Figure 4.8, with the backward pumping profile, an increase of 2.7 dB is achieved in the maximum noise figure, due to a higher ASE noise generated in the backward direction.

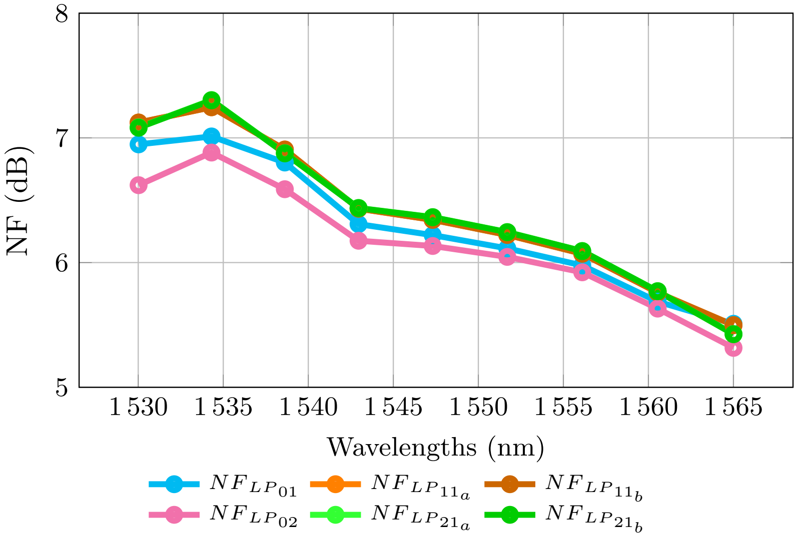

Figure 4.13: Noise figure per mode for a two-stage 6M-EDFA using a GFF and the designed backward pumping profile for 9 WDM signals per spatial mode.

4.4.4 FM-EDFA Gain Characterization using Bidirectional Pumping

Expanding the analysis of pump direction in EDFA amplifiers to cover all three configurations —forward, backward, and bidirectional—, the bidirectional pump configuration is studied. Bidirectional pumping could offer the best trade-off between gain and noise figure [93], using a larger pump power budget, without significantly increasing noise, DMG, and DSG. In this subsection, the gain characterization of a two-stage FM-EDFA using bidirectional pumping is presented.

The two-stage FM-EDFA configuration now includes forward and backward pumping, as shown in Figure 4.14. This configuration is a combination of the previous ones (Figures 4.2 and 4.11). The configuration involves injecting 9 WDM channels into the first ED-FMF stage through WSC_1. The latter allows multimode pumping to be injected at 980 *nm* in the forward direction, while WSC_4 allows multimode pumping to be injected at 980 *nm* in the backward direction. The GFF, ASE filter, and ISO are inserted between *Stage 1* and *Stage 2* of FM-EDFA, as in subsection 4.3.1. The GFF is designed to flatten the gain curve across the wavelength range for each spatial mode. The ASE filter and the ISO have the same function described in subsection 4.3.1. *Stage 1* is fed by the WDM signals, the forward pumping, and the residual backward pumping from the second stage. Besides, *Stage 2* is fed by the flattened WDM signals, the residual forward pumping from the first stage, and the backward pumping.

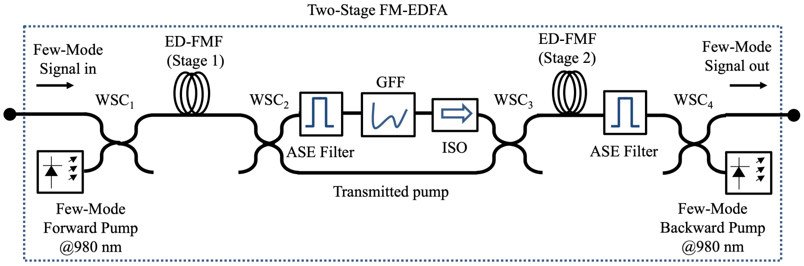

Figure 4.14: Configuration of the two-stage FM-EDFA with forward and backward pump.

The methodology of Joint DMG-DSG minimization, proposed in the Section 4.3, was used to design the backward pumping profile and the GFF filter profile for the bidirectional pumping case. The previously designed pumping profile in the forward direction, where 9 WDM signals propagate through spatial modes, was used, i.e., the configuration for forward pumping was [21]: LP_{02} (200 mW), LP_{21_a} (225 mW), and LP_{21_b} (235 mW). Therefore, Algorithm 1 was applied for the design of the pumping profile in the backward direction and the GFF profile. It was decided to do it this way, in order to reduce the computation time. Table 4.3 presents the designed bidirectional pumping profile, both pumping directions were injected at 980 nm.

Using the designed bidirectional pumping profile and GFF, the gain and DMG as a function of wavelengths in the two-stage FM-EDFA with bidirectional pumping, are presented in Figure 4.15. The calculations for gain and DMG were obtained from Eq. (4.10) and Eq. (4.12), respectively. The FM-EDFA demonstrates a mean gain exceeding 19.3 dB per mode across the entire C-band, with the maximum DMG reaching 3.5 dB at 1530 nm.

Table 4.3: Bidirectional pumping profile for a two-stage FM-EDFA.

Mode	Forward	Backward
LP_{02}	200mW	143mW
LP_{21_a}	225mW	69mW
LP_{21_b}	235mW	60mW

Compared to Figure 4.7, with bidirectional pumping 2 dB more in mean gain is achieved, with a mere increase in DMG of 0.5 dB. While, DSG degrades from 0.53 dB in the forward pumping case to 0.67 dB with the bidirectional pumping design. In the forward direction the pumping power budget was 660 mW, while for bidirectional pumping this budget increases to 932 mW, that is, 40% more to obtain an average gain 2 dB greater than the case of pumping in the forward direction.

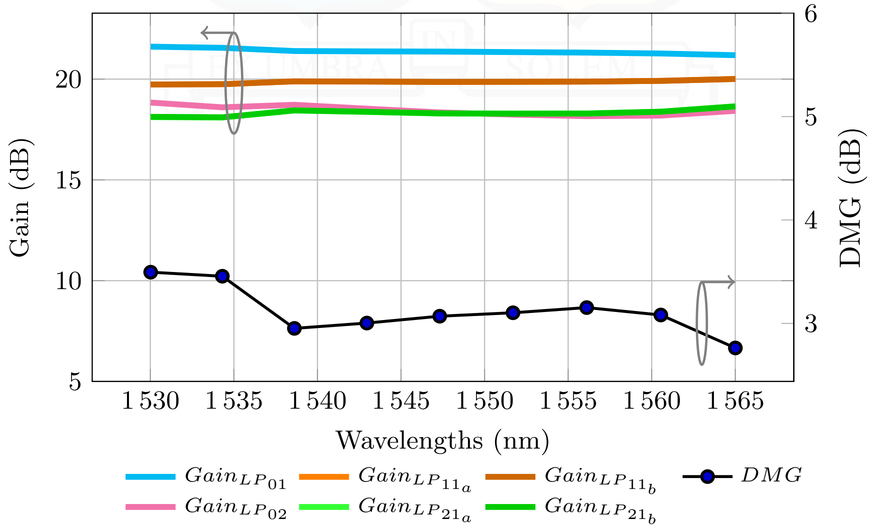

Figure 4.15: Gain per mode and maximum DMG for a two-stage 6M-EDFA using a GFF and the designed bidirectional pumping profile for 9 WDM signals per spatial mode.

The NF was computed using Eq. (4.11), and the results are shown in Figure 4.16. The highest NF is observed at 1530 nm reaching 6.2 dB and the lowest value (5.07 dB) at 1560 nm for LP_{01}. This represents a noise figure variation of 1.13 dB for the worst case. Compared to Figure 4.8, with bidirectional pumping, an increase of 1.6 dB is achieved in the maximum noise figure, due to ASE noise generated in the backward direction. Bidirectional pumping offers an increased gain compared to forward pumping with a 40% increase in pump power budget and without an excessive increase in noise figure.

4.4.5 Cascade of FM-EDFA in an FMF Link

Once an individually optimized amplifier is obtained, it is pertinent to study an FMF link to verify that the amplifier design is robust and can be applied to amplifier chains. In this subsection, the two-stage FM-EDFA designed in subsection 4.4.1 is used for the propagation of 81 WDM signals in each spatial mode in an FMF link using forward pumping, schematized in Figure 4.17. The link is composed of a cascade of 4 spans, each consisting of a section of FMF fiber and a two-stage FM-EDFA. Designing the amplifier

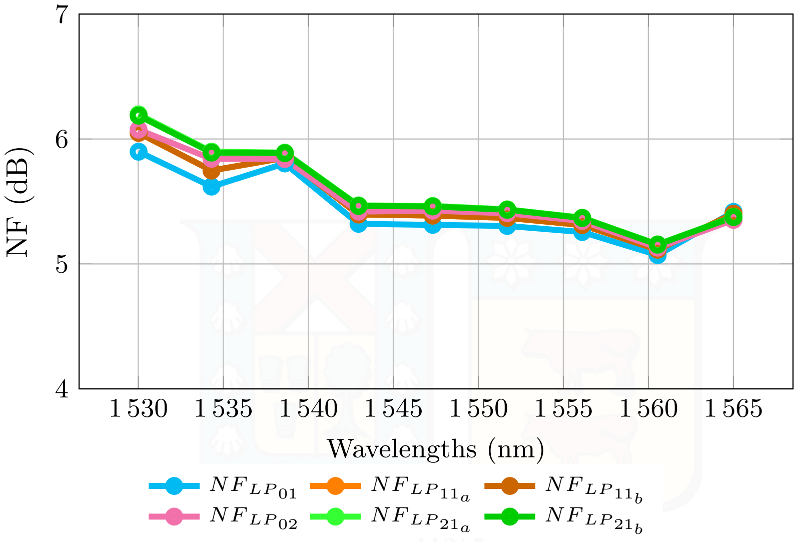

Figure 4.16: Noise figure per mode for a two-stage 6M-EDFA using a GFF and the designed bidirectional pumping profile for 9 WDM signals per spatial mode.

across a broad spectrum of wavelengths enables simulation and analysis of its behavior under the transmission scenario with a full channel load in the conventional C-band.

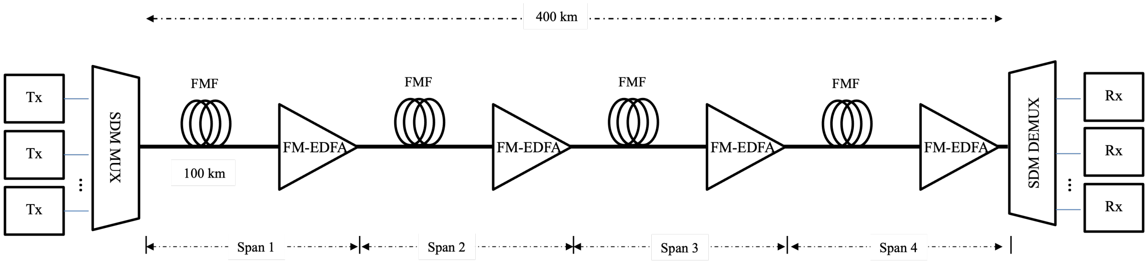

Figure 4.17: Schematic of an FMF link with amplification based on FM-EDFA.

The SDM-FMF system is composed of 4 spans of 100 km each. Following each span, a two-stage FM-EDFA is placed. For the transmission modeling part the Manakov equation for FMF in the weak-coupling regime [35] (Eq. (3.9)) was solved numerically with the split-step Fourier method. The parameters used in this part of the simulation are equal to those used in Chapter 3 and shown in Table 3.1. The injected power per wavelength per mode is equal to −5 dBm.

Figure 4.18 presents the output signal power of each FM-EDFA throughout the FMF link. The input signal at the first amplifier is uniform for all LP modes and wavelengths, equal to −25 dBm, as we assumed that the attenuation coefficient is the same for all LP modes in the wavelength range of signals. The first amplifier satisfies the input power condition for the designed FM-EDFA, resulting in amplified signals with the gains reported in Figure 4.9 and the corresponding DMG. However, as signals progress through successive spans, the signal power becomes non-uniform due to DMG, leading to power dispersion for each subsequent FM-EDFA.

On one hand, mode LP_{01} achieves the highest gain, with a mean value of 21.24 dB

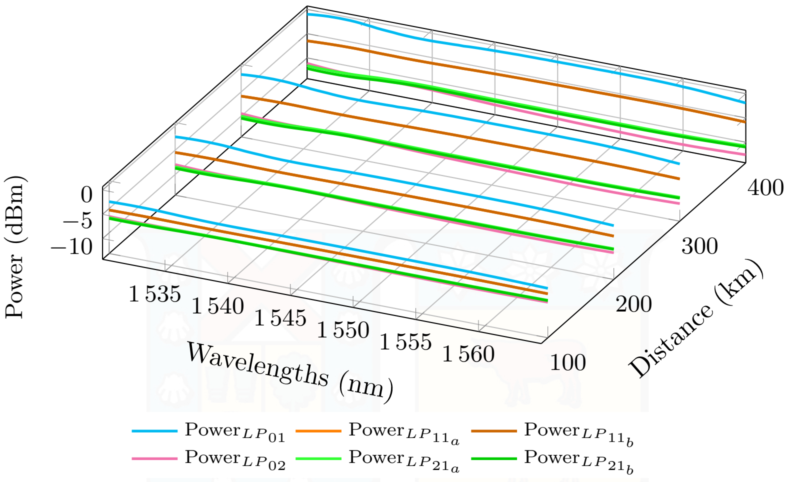

Figure 4.18: Output signal power of successive FM-EDFAs in an SDM-FMF system composed of 4 spans.

in the first span, over compensating for all losses due to the attenuation coefficient of the fiber, estimated to be 20 dB per span, resulting in higher input power to the successive amplifiers in the link and a maximum mean gain variation of 0.65 dB along the link. On the other hand, LP_{02} achieves a mean gain of 18.12 dB in the first span, failing to fully compensate for losses associated with the attenuation coefficient of the fiber, resulting in lower input power to the following amplifiers in the link. This is also valid for mode $LP_{21_{a,b}}$, with a mean gain of 18.25 dB in the first span. The maximum mean gain variation for LP modes LP_{02} and $LP_{21_{a,b}}$ is 0.20 dB and 0.24 dB, respectively. The mean gain achieved by the signal over modes $LP_{11_{a,b}}$ is close to 20 dB span after span, resulting in minimal power variations and a maximum mean gain variation of 0.3 dB.

The signal power for modes LP_{01}, LP_{02}, and $LP_{21_{a,b}}$ at the output of the FM-EDFAs deviates from the initial value of −5 dBm. However, there are ways to control this range of variation in the output power. For example, the powers of the input signals to the amplifier could be corrected periodically or the pumping profile could be adapted periodically.

Figure 4.19 presents the DMG evolution throughout the FMF link. The upper line in the plot is equal to the one presented in Figure 4.9, as the first FM-EDFA satisfies the input power condition for the designed FM-EDFA. Note that, as the signal progresses through the spans DMG decreases while signal power dispersion at the FM-EDFA output increases. This inverse relationship can be explained by the gain definition and the power evolutions shown in Figure 4.18. The gain is a relation between output and input power to the amplifier, the maximum difference between output and input powers (maximum gain) occurs in the first amplifier because of the uniform launched powers. As the signal power evolves along the link, the power variations between spans become smaller. Consequently, the gain variation compared to the previous span also decreases, leading to a lower DMG.

In Figure 4.19 it is also observed a shift of the maximum DMG from lower wavelengths in the first span to higher wavelengths in the last span. This phenomenon is due to the GFF, lower wavelengths are more attenuated than higher wavelengths (Figure 4.4). If LP_{01} and LP_{02} are looked at in detail -as these LP modes dictate the DMG- after the first span, the signal power is relatively higher for lower wavelengths than for the higher ones.

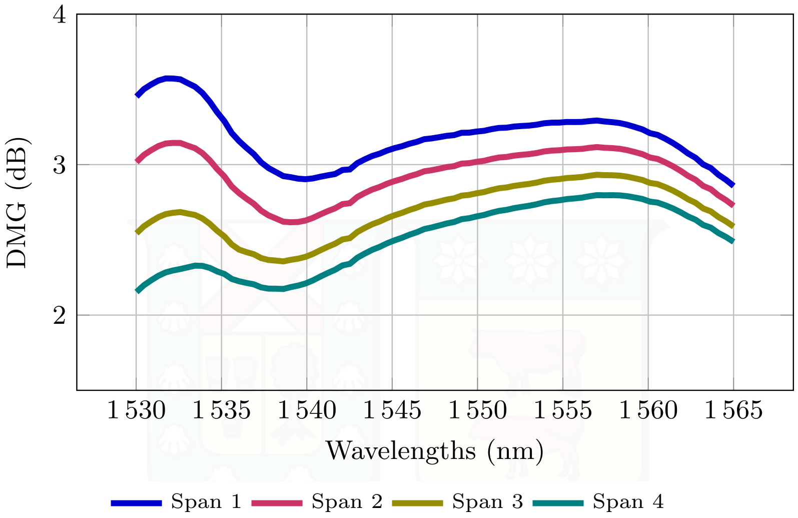

Figure 4.19: DMG per span in an SDM-FMF system composed of 4 spans.

After successive spans, this trend is preserved but reduced for LP_{01} and pronounced for LP_{02}, this leads to a shift in DMG from 1530 nm in the initial span to 1557 nm after the fourth span.

Figure 4.20 presents the DSG evolution throughout the FMF link. The first amplifier reaches the highest DSG value for mode LP_{01}. The designed GFF demonstrates effectiveness in maintaining DSG values below 0.6 dB after successive spans, thanks to the fact that the GFF coefficients were designed from the average modal gain, which remains close to 19 dB for the entire link.

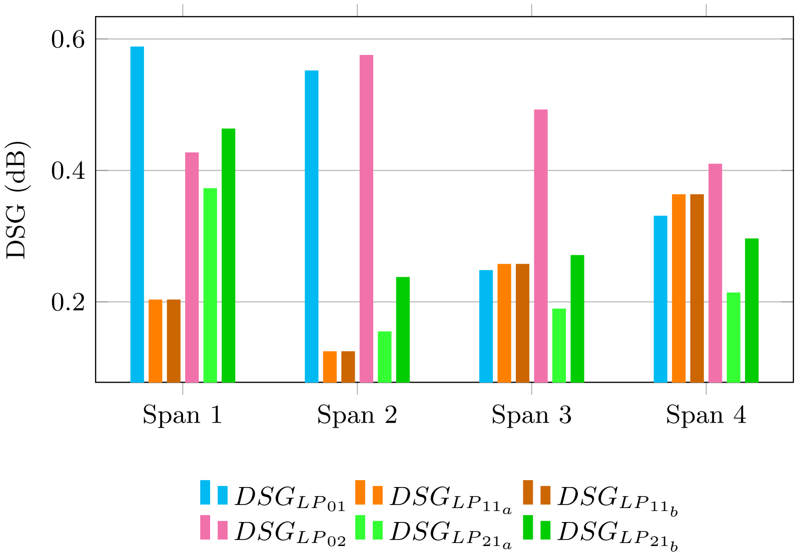

Figure 4.20: DSG per span in an SDM-FMF system composed of 4 spans.

The last FM-EDFA exhibits the gain presented in Figure 4.21, with a mean gain of 19 dB and achieving a maximum DMG of 2.8 dB at 1557 nm. These are better results compared to the ones obtained for the first amplifier, this is due to the gain reduction of the mode LP_{01}. In terms of DSG, it is not degraded after 4 spans, in fact, it is improved, and the final value is under 0.42 dB.

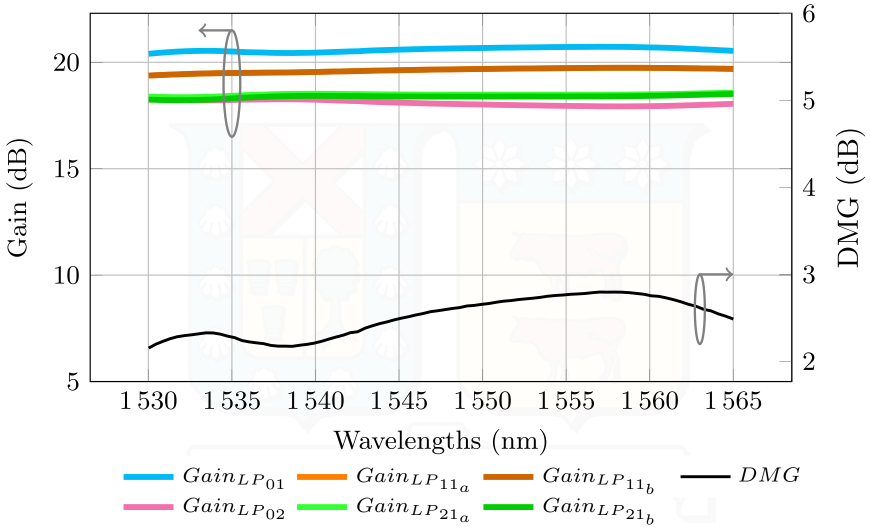

Figure 4.21: Gain per mode and DMG achieved by the last FM-EDFA in a 400 km FMF link.

The performance of the SDM-FMF system in terms of the Optical Signal-to-Noise Ratio (OSNR) [101] was also evaluated. In this particular case, input power is within the linear regime, where the OSNR is primarily limited by ASE noise, while nonlinear effects are negligible. The OSNR at the output of the last FM-EDFA is shown in Figure 4.22. The highest OSNR is achieved by mode LP_{01} and the lowest by LP_{02}, aligning with the gain performance reported in Figure 4.21. The differential OSNR between the best and worst LP modes reaches a maximum of 5.5 dB at 1533 nm. Nevertheless, in the wavelength range of 1535 to 1565 nm, the OSNR is close to or higher than 20 dB with a differential OSNR of 5 dB. Furthermore, spectral variations of OSNR are observed for each LP mode, with the highest value for LP_{21_b} with 1.90 dB and the lowest for LP_{01} with 0.71 dB. This variability is related with the use of the GFF over the signals and noise power for reducing the DSG. These results verify the effectiveness of the proposed two-stage FM-EDFA to meet the compensation of losses in spans of 100 km length, preserving low DMG and DSG for SDM-FMF systems. At the same time, the OSNR values obtained at the end of the FMF link fulfill the requirements for bit rates of 100 Gbps [102], which would allow a system capacity of 48.6 Tbps.

4.5 Conclusions

SDM networks with hundreds to thousands of kilometers in length, such as metro and long-haul networks, require amplification systems that compensate for losses in the optical fiber. Among the optical amplification solutions for SDM systems based on FMF, FM-EDFAs are a promising solution. EDFAs are the most widely used amplification scheme in single-mode long-haul systems, thanks to high gains adding acceptable noise levels. This chapter has presented the theory of FM-EDFA.

FM-EDFA amplification is achieved through population inversion, which occurs

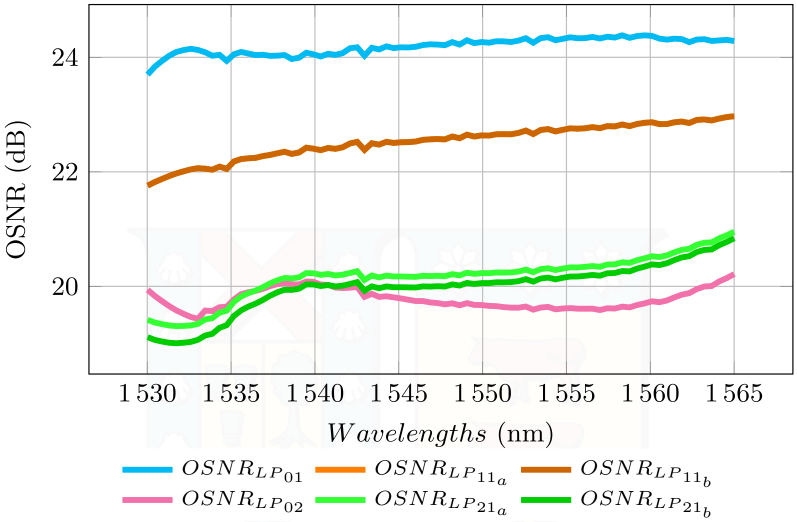

Figure 4.22: OSNR out per mode, achieved by the last FM-EDFA in a 400 km FMF link.

when the amplifier is pumped optically, at 980 or 1480 nm. The main limitation of FM-EDFA amplifiers is the non-uniformity of the gain profile at both the spectral (DSG) and modal (DMG) domains, which causes different WDM channels to be amplified with different gains in both dimensions. In the search to minimize these two limitations, this chapter presented the Joint DMG-DSG Minimization Methodology to design two-stage FM-EDFA amplifiers, with the purpose of jointly minimizing DMG and DSG by optimizing the pumping profile and designing the profile of a GFF.

Joint DMG-DSG Minimization methodology is based on a genetic algorithm whose objective function includes the DMG and mean gain metrics. To determine these metrics, the fourth-order Runge Kutta method was applied to solve the mathematical model of FM-EDFA, composed of three differential equations that represent the power evolution of signals, pump, and ASE noise. The total gain and noise achieved by the FM-EDFA depends, among other parameters, on the pumping profile. The latter is composed of at least one pumping mode at 980 nm, injected with a certain power. With the proposed methodology, a multi-pumping profile was designed for WDM signals propagating in modes LP_{01}, $LP_{11_{a,b}}$, LP_{02}, and $LP_{21_{a,b}}$, minimizing the DMG. The flatness in the gain spectrum per LP mode was achieved with a GFF filter inserted between the two amplifier stages.

Joint DMG-DSG Minimization Methodology was applied to design the pumping profile and GFF profile for a two-stage FM-EDFA with uniform doping profile and the transmission of: (a) 9 WDM channels per LP mode using forward, backward, and bidirectional pumping; and (b) 81 WDM channels per LP mode using forward pumping. Using this methodology, it was determined that the pumping modes that contribute to minimizing DMG- when signals propagate in modes LP_{01}, $LP_{11_{a,b}}$, LP_{02}, and $LP_{21_{a,b}}$- are the LP_{02} and $LP_{21_{a,b}}$. This is due to the mode field distribution of these modes and their capabilities to amplify the LP signal modes.

Simulation results showed that, for 9 WDM channels per LP mode using 3 pumping modes in the forward direction, DMG and DSG were kept below 3 dB and 0.6 dB, respectively; with a mean gain of 17 dB and NF below 5 dB, along the conventional C-band. In the case of backward pumping, the designed configuration used a total power budget 5% lower than that of the forward configuration. In this case, the mean gain and DMG, were similar to those obtained in the forward configuration; however, DSG and NF increased to 0.98 dB and 7.31 dB, respectively. Additionally, by applying bidirectional pumping with a total pumping power budget 40% higher than applied in the forward case, the mean gain increases to 19.3 dB and the noise figure remains below 6.2 dB.

Simulations results for 81 WDM channels per LP modes and using 3 pumping modes in the forward direction, exhibits a mean gain of 18 dB, DMG below 4 dB, DSG lower than 0.6 dB, and a NF under 6 dB. This performance is similar to the 9 WDM channel case; however, the capacity has increased by 9 in this case. The pumping profile and the GFF filter designed for this case of the study were used to simulate a 4-span FMF link, 100 km each. DMG and DSG along the cascade of FM-EDFA within the link are not degraded compared to the results of the designed amplifier. A modal OSNR higher than 19.2 dB for the wavelength range between 1530 to 1565 nm, corresponding to a potential system capacity of 48.6 Tbps.

The union of strategies such as the use of GFF and the design of the multipumping profile put in evidence the potential of the proposed two-stage FM-EDFA for next-generation optical communication networks. The performance obtained position the amplifier as highly promising for the implementation in long-haul SDM-FMF systems.

The next chapter will explain the optical amplification solution for SDM-FMF systems based on distributed Raman amplifiers.

5

Few-Mode Distributed Raman Amplifiers

5.1 Introduction

SDM technology is a promising alternative to face the potential capacity crunch of existing SMF [6]. Especially, MDM systems based on FMF have attracted significant attention due to their enhanced spatial efficiency and reduced power consumption compared to SMF. Long-haul SDM-FMF transmission requires optical amplification to compensate for fiber losses. Two main types of optical amplifiers have been used for these systems: few-mode erbium-doped fiber amplifiers (FM-EDFA) and few-mode distributed Raman amplifiers (FM-DRA). Along Chapter 4 an extensive review of FM-EDFA was presented. In this chapter, the review will be made on FM-DRA. One key advantage of FM-DRAs over FM-EDFAs is that the optical fiber itself acts as the Raman amplifier, as spontaneous Raman scattering (SRS) does not require a special dopant to provide gain [5]. Raman gain is also flexible in the spectral domain, offering an ultra-wide gain bandwidth and low noise. However, FM-DRAs require higher pump powers compared to FM-EDFAs to achieve the same level of gain.

Low gain ripple, minimal DMG, and low effective NF are highly desired for any SDM-FMF system. Unequal gain among the different wavelengths (resulting in gain ripple) or modes (resulting in DMG) leads to penalties at the receiver due to uneven OSNR [103]. The pump profile should be optimized to achieve flat gains in the wavelength and spatial modal domains with FM-DRA, this means tailoring the power at different wavelengths and modes. Another highly desired characteristic in any optical amplifier is high pump efficiency, which is the capability to convert each watt of pump power into signal optical gain.

This chapter addresses FM-DRA and is structured as follows: Section 5.2 presents the literature review. Then, Section 5.3 outlines the FM-DRA mathematical modeling and the optimization process. Subsequently, Section 5.4 presents the simulations results with the theoretical characterization of the FM-DRA.

The work presented in this chapter is based on work reported in:

A. Lozada, R. Olivares, A. Leiva, G. Saavedra, N. Jara, P. Morales, B. Dumas, and D. Bórquez-Paredes, "Optimized Backward Pumping Design for a 6-Mode Distributed Raman Amplifier for SDM Systems," IEEE Photonics Technology Letters, 2024. (Submitted)

5.2 Literature Review

FM-DRA offers advantages over FM-EDFA, including a wide gain bandwidth and low noise, traits well established in DRA for SMF systems. Experimental demonstrations of FM-DRA supporting two non-degenerate spatial modes (LP_{01}, LP_{11}) have achieved on-off gains typically below 10 dB, demonstrating the potential of this technology for next-generation optical communication systems [46, 104, 47, 41, 105, 106].

For configurations involving more than two non-degenerate spatial modes, theoretical studies have laid the basics [107, 108, 103, 109, 110]. These works present the fundamental principles of FM-DRA modeling [107, 108], and offer insights into the optimization of gain fluctuations across wavelength and modal domains using analytical [103] and machine learning approaches [109, 110]. Additionally, experimental work has demonstrated a hybrid configuration with FM-DRA and SM-EDFA [111].

Table 5.1 summarizes characteristics and performance metrics for various FM-DRA works. The first column in this table indicates the number of non-degenerate spatial modes (including degeneracy) used for signals, for example, 3M refers to spatial modes LP_{01}, LP_{11_a} and LP_{11_b}. From this table, some trends can be identified. FM-DRA amplifiers have the potential for use in both C and L bands. The predominant pump configuration is in the backward direction. When LP_{01}, $LP_{11_{a,b}}$, LP_{02} and $LP_{21_{a,b}}$ are available, the best pump configuration has been 70% pumping in LP_{21} and 30% in LP_{02}, regardless of the total available pump power budget. At the same time, some points are evident that require further research, such as the ideal number of pump wavelengths and their power distribution, as well as the advantages and disadvantages of using higher-order amplifiers compared to first-order ones. Higher-order pumping exploits interactions between wavelength pumps [5], including additional pumps at wavelengths one or more of the Raman gain bandwidth below the conventional first-order pumping approach [5, 47].

In [103], an analytical approach was used to optimize the pump profile of a 50 km FM-DRA supporting LP_{01}, LP_{11}, LP_{02}, and LP_{21} for signals in the wavelength range of 1525 – 1565 nm. Two optimized pump profiles were presented, each composed of 4 wavelengths (1420 nm, 1430 nm, 1450 nm, and 1465 nm) launched in backward direction into LP_{02} and LP_{21}. The total pumping power was (1) 1107 mW for a target on-off gain of 10 dB, achieving a gain ripple of 0.5 dB and DMG of 0.15 dB; and (2) 1665 mW for a target on-off gain of 15 dB, achieving a gain ripple of 0.8 dB and DMG of 0.2 dB.

Table 5.1: FM-DRA characterization reported from three to six signal modes.

FM-DRA	WDM channels	Length	Pumping profile		DMG	Gain ripple	Mean On-Off Gain	Effective NF
			Direction	Mode(s) & Wavelength(s) & Power				
3M-DRA [46]	(1550 – 1570 nm)	137 km	Backward	LP_{11} : 1455 nm(1250 mW)	0.5 dB	4 dB	8 dB	-1.5 dB
3M-DRA [104]	(1530 – 1565 nm)	70 km	Forward, Backward, bidirectional	$LP_{11_{a,b}}$: 1455nm(2000mW)	<2 dB	12 dB	17 dB	–
3M-DRA [47]	(1542 – 1558 nm)	70 km	Backward	$LP_{11_{a,b}}$: 1455nm(260mW), or $LP_{11_{a,b}}$: {1455nm(30mW), 1360nm(1290mW)},	0.4 dB	<1 dB	4 dB	-2 dB
3M-DRA [105]	16 (1530 – 1605 nm)	75 km	Backward	$LP_{11_{a,b}}$: {1425nm(161mW), 1452nm(128mW), 1465nm(27mW), 1495nm(188mW)}	<0.5dB	0.6 dB	4 dB	<-1 dB
3M-DRA [112]	8 (1542 – 1558 nm)	100 km	Backward	$LP_{11_{a,b}}$: {1455nm(75mW), 1360nm(1890mW)}	0.7 dB	1 dB	8 dB	<-2.5 dB
3M-DRA [106]	(1527 – 1608 nm)	54.3 km	Backward	$LP_{11_{a,b}}$: 12λs in the range of [1410.8 – 1502.7] nm, two lowest wavelengths with 160mW, the remaining 10 with 80mW	0.6 dB	2 dB	6 dB	–
4M-DRA [111]	8 (1530 – 1565 nm)	60 km	Forward Backward	LP_{02}: {1425nm, 1455nm} $LP_{21_{a,b}}$: {1420nm, 1435nm, 1460nm}, with 2000 mW total pump power	0.6 dB	0.7 dB	5.3 dB	-3 dB
6M-DRA [107]	–	–	–	LP_{21} : 0.696∗ Total pump power, LP_{02} : 0.304∗ Total pump power	0.13 dB	–	10 dB	–
6M-DRA [103]	50 (1525.2 – 1565 nm)	50 km	Backward	LP_{21}: {1420nm(190.81mW), 1430nm(171.31mW), 1450nm(258.48mW), 1465nm(150.57mW)}, LP_{02}: {1420nm(83.05mW), 1430nm(74.57mW), 1450nm(112.51mW), 1465nm(65.54mW)}	0.15 dB	0.5 dB	10 dB	–
6M-DRA [43]	15 (1530 – 1565 nm)	50 km	Backward	LP_{11} : 1455nm(100mW), LP_{21} : 1455nm(100mW)	2.5 dB	1.5 dB	8 dB	–
6M-DRA [109]	36 (1530 – 1565 nm)	70 km	Backward	5λs in the range of [1370 – 1485]nm, LP_{21} : (0.70∗ Total pump power), LP_{02} : (0.30∗ Total pump power)	0.3 dB	0.46 dB	14 dB	–
6M-DRA [110]	50 (1530 – 1625 nm)	70 km	Backward	8λs in the range of [1410 – 1520]nm, LP_{21} : (0.70∗ Total pump power), LP_{02} : (0.30∗ Total pump power)	0.6 dB	0.3 dB	15 dB	–

In [109], neural networks were used to optimize the pump profile for a 70 km second-order FM-DRA, supporting LP_{01}, LP_{11}, LP_{02}, and LP_{21} for signals in the wavelength range of $1530 - 1565$ nm. The pump profile was composed of five wavelengths selected from the range $1370 - 1485$ nm launched in a backward direction in LP_{02} and LP_{21}. This method achieved a maximum on-off gain of 12.5 dB with a gain flatness of 0.46 dB, a DMG of 0.3 dB, and a total pumping power budget of 3120 mW. Both studies, [103] and [109], indicated that approximately 70% of the total pump power should be injected in LP_{21}, with the remaining 30% in LP_{02}, and no pumps in modes LP_{01} and LP_{11}. However, none of the previous optimization works have presented a complete characterization in terms of gain, noise, OSNR, and pump efficiency of FM-DRA.

5.3 Mathematical Model of FM-DRA

The behavior of an FM-DRA, in the weak coupling regime, can be described by a nonlinear ordinary differential equation (Eq. (5.1)) that accounts for:

1. Interactions between signals and pumps under stimulated Raman scattering (SRS) effect;
2. Noise that adds to the amplified signal in such a similar way to the spontaneous emission that affects the performance of EDFAs.

The SRS effect transfers optical signal power from shorter wavelength channels to longer wavelength channels when the wavelength difference falls within the Raman gain bandwidth of 100 nm [4]. The mathematical model used in this work is based on the one presented in [47], which is valid for fist-order and second-order Raman amplification. This model has the following assumptions:

1. The coupling between modes with large propagation constant difference is negligible;
2. The transmission fiber has lengths of tens of kilometers; this lead to large mode dispersion, which results in random coupling processes that are independent for pumps and signals, and do not contribute to the amplification process;
3. Nonlinear propagation effects, such as FWM, XPM and SPM, are negligible. This assumption is valid since we will consider wavelength channels well separated in the C-band with power levels within the linear regime.

The power evolution of pumps or signals on spatial mode m and wavelength ν along z is mathematically expressed as follows [47]:

$$\begin{aligned} \frac{dP^{\pm}_{\nu,m}}{dz} &= \mp\alpha_{\nu,m}P^{\pm}_{\nu,m} \pm \sum_{n}\eta_{\nu,m,n}P^{\mp}_{\nu,n} \pm P^{\pm}_{\nu,m}\sum_{\mu>\nu}\sum_{n}\frac{g_{\mu,\nu}}{\Gamma}f_{m,n}(P^{+}_{\mu,n}+P^{-}_{\mu,n}) \\ &\pm h\nu\sum_{\mu>\nu}\sum_{n}g_{\mu,\nu}f_{m,n}(P^{+}_{\mu,n}+P^{-}_{\mu,n})W_{\mu,\nu}\Delta\nu \mp P^{\pm}_{\nu,m}\sum_{\mu<\nu}\sum_{n}\frac{\nu}{\mu}\frac{g_{\mu,\nu}}{\Gamma}f_{m,n}(P^{+}_{\mu,n}+P^{-}_{\mu,n}) \\ &\mp P^{\pm}_{\nu,m}\sum_{\mu<\nu}\sum_{n}\frac{\nu}{\mu}g_{\mu,\nu}f_{m,n}2h\mu W_{\nu,\mu}\Delta\mu \end{aligned} \tag{5.1}$$

where the sign "+" indicates forward propagation; the sign "−" indicates backward propagation; $P_{\nu,m}$ ($P_{\mu,n}$) is the optical power at frequency ν (μ) in mode m (n); $\alpha_{\nu,m}$ is the attenuation coefficient at frequency ν for mode m; $\eta_{\nu,m,n}$ is the Rayleigh-backscattering coefficient at frequency ν from mode n to mode m; $g_{\mu,\nu}$ is the Raman gain coefficient between frequencies μ and ν; $f_{m,n}$ is the intensity overlap integral between modes m and n; Γ is the polarization factor between the pump and signal; $W_{\mu,\nu}$ ($W_{\nu,\mu}$) is an auxiliary variable; $\Delta\nu$ ($\Delta\mu$) is the effective bandwidth at frequency ν (μ); and h is the Planck's constant. $W_{\mu,\nu} = [1 + (e^{(h(\mu-\nu)/kT)} - 1)^{-1}]$; where kT is the thermal energy at room temperature. Equation (5.1) aligns with the equations presented in [103, 109, 110].

The first term in Eq. (5.1) accounts for the fiber loss, the second term stands for Rayleigh-backscattering, the third and fifth terms account for the Raman-induced power transfer into and out of each frequency range, respectively, while the fourth and sixth terms include the noise that appears in the Raman amplification process which in turn depends on the effective bandwidth and the temperature of the Raman amplifier. This effective bandwidth is related to the width in which the noise is evaluated, i.e., the noise bin width. When Eq. (5.1) is applied to signals in conventional C-band, the fifth term represents the signal-to-signal Raman interactions, which is negligible when the wavelength separation within wavelengths in the C-band is smaller than the Raman gain bandwidth [46, 107, 43]. Conversely, when Eq. (5.1) is applied to pumps, the pump-to-pump Raman interactions can become significant. Depending on the separation between the pumps, some power from the short-wavelength pumps may be transferred to the long-wavelength pumps leading to Raman amplification of higher order. Since in this work are used wavelength pumps with spacing smaller than the Raman gain bandwidth, this interaction is negligible, resulting in first-order pumping.

In this work, it is assumed that the intensity overlap integral, $f_{m,n}$, is wavelength independent, and is defined similarly to Eq.3.10 (f_{mmpp}) without the normalization term of effective area, as follows [47]:

$$f_{m,n} = \frac{\iint_{-\infty}^{+\infty} I_m(x,y) I_n(x,y) \mathrm{d}x\mathrm{d}y}{\iint_{-\infty}^{+\infty} I_m(x,y) \mathrm{d}x\mathrm{d}y \iint_{-\infty}^{+\infty} I_n(x,y) \mathrm{d}x\mathrm{d}y}, \tag{5.2}$$

where $I_m(x,y)$ ($I_n(x,y)$) is the mode profile of spatial mode m (n). This parameter indicates the degree of spatial overlap between the two modes. Therefore, it has a very important role in the definition of the pumping modes, and consequently in the DMG. The $f_{m,n}$ is measured in units of m^{-2}, and is the inverse of the effective modal area.

5.3.1 Performance Metrics

To assess FM-DRA performance, several key metrics were employed to provide a comprehensive analysis. The chosen performance metrics were defined in Section 5.3.1 . Additional metrics, specific to FM-DRA, are defined as follows:

- The Raman **on-off gain** is one of the main performance parameters of interest in DRAs, it is defined as the increase in signal power at the amplifier output when the pumps are turned on [5, 47, 104]:

$$G_{on-off} = \frac{P_s^{on}(L)}{P_s^{off}(L)}, \tag{5.3}$$

where $P_s^{on}(L)$ and $P_s^{off}(L)$ are the signal power at the fiber output when the pumps are on and off, respectively.

- The parameter **effective noise figure** (NF_{eff}) [4, 5] is used to quantify the noise figure improvement of DRA. It is defined as the noise figure that a fictitious discrete amplifier would need when following a passive span to give the same noise performance as a DRA [5]. Figure 5.1 illustrates this concept. At the top, the actual system is shown, which is a fiber span using DRA with backward pumping. This system is characterized by the gain, G_{on-off}, and noise figure of the Raman-pumped fiber span, NF_{span}, which can take very large values [4]. At the bottom, the equivalent effective system is shown. It consists of a passive span with loss $\mathcal{L}$ followed by the fictitious pre-amplifier, the "effective amp", characterized by gain, G_{on-off}, and noise figure, NF_{eff}.

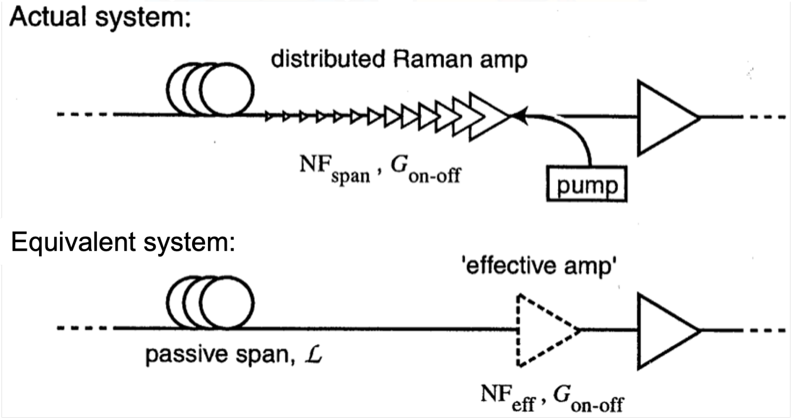

Figure 5.1: Equivalent effective system for DRA using backward pumping (Adapted from [5]).

The noise figure, NF_{span}, is defined by [5]:

$$NF_{span} = \frac{2P_{ASE}}{E_{ph}B_0G_{net}} + \frac{1}{G_{net}}, \tag{5.4}$$

where G_{net} is the net gain of the fiber amplifier defined as the ratio between the output and the input signal power, P_{ASE} is the amplified spontaneous emission (ASE) noise power measured in the noise bin bandwidth B_0; and E_{ph} is the signal photon energy. From Figure 5.1, NF_{span}, can also be expressed in terms of NF_{eff} as [5]:

$$NF_{span} = \mathcal{L} \cdot NF_{eff}, \tag{5.5}$$

where $\mathcal{L}$ is the loss of the passive span. In decibels (dB), the effective noise figure (NF_{eff}) is expressed as:

$$NF_{eff}\,[\text{dB}] = NF_{span}\,[\text{dB}] - \mathcal{L}\,[\text{dB}]. \tag{5.6}$$

This definition, demonstrates that NF_{eff} can even take negative values in the dB scale [4, 5]. This does not mean that the SNR at the output of the DRA is higher than at its input [5]. Instead, it reflects that the distributed gain counteracts fiber losses in the transmission fiber resulting in an improved OSNR, compared to scenarios where losses are compensated at the end of the fiber using EDFAs.

The effective NF, is defined in terms of the on-off gain, as follows [47]:

$$NF_{eff} = \frac{1}{G_{on-off}}\left(1 + \frac{P_{ASE}}{E_{ph}B_0}\right), \tag{5.7}$$

where the same definitions of Eq. (5.4) are used.

The interpretation of the effective noise figure becomes less straightforward when forward pumping is used compared to backward pumping because gain occurs at the opposite side of the span from the fictitious effective amplifier [5]. Nevertheless, the best NF_{span} is obtained when only forward pumping is used, and the span is pumped above transparency [5]. The reason is that the signal and ASE are both attenuated equally by the loss element [5]. This noise improvement is misleading because the maximum signal power in the fiber span has increased significantly [5]. This can increase signal distortions that result from Kerr and other signal nonlinearities, counteracting any benefits from reducing noise [5]. As a result, bidirectional pumping is positioned as the best trade-off between improving the SNR and reducing signal nonlinear distortions.

5.3.2 Genetic Algorithm to Optimize the Pumping Profile

The pumping profile must be carefully designed to achieve a flat on-off gain profile and low DMG. The flat gain per mode is obtained by selecting the appropriate number and value of wavelength locations for launching the pumps, while low DMG is achieved by tailoring the pump modes and pump powers. Therefore, optimizing the pumping profile involves considering these two dimensions. A commercial MATLAB® optimization toolbox [113] was used to program a GA to design the pumping profile. The GA was employed to minimize DMG while ensuring a flat gain. GAs have demonstrated effectiveness in optimizing the design of optical amplifiers in the context of FMF systems [78, 79, 21].

The GA was programmed to jointly select the wavelengths and powers for pumping, with the pumping modes fixed. The fitness function (FF) of the algorithm was defined as:

$$FF = \frac{\bar{G}}{\Delta G}, \tag{5.8}$$

where $\bar{G}$ is the mean on-off Raman gain; and ΔG represents the overall gain variation, computed by multiplying DMG and the gain flatness. This fitness function prioritizes pumping profiles with low gain variations and high on-off gains. The objective of the GA is to maximize this fitness function, thereby identifying an optimal combination of pumping wavelengths and powers.

The GA operation, is described in Algorithm 3, and summarized in the following steps:

- Step 1: To create a random initial population
  The first step of the GA is to create the initial population of size *Population size*. Each individual, denoted by a vector $\mathbf{g} = [\lambda_{p_1}, P_{p_1}, \lambda_{p_2}, P_{p_2}, \ldots \lambda_{p_n}, P_{p_n}]$, is generated by randomly selecting n pairs of pumping wavelengths and pumping powers from the predefined set $[\min(\lambda_{pump}), \max(\lambda_{pump})]$ and $[\min(P_{pump}), \max(P_{pump})]$, respectively. This step is represented in line 1 of Algorithm 3.

- Step 2: Individual evaluation
  Each individual in the initial population is evaluated with the fitness function (Eq. (5.8)); to do this, the FM-DRA mathematical model must be solved (Eq. (5.1)) and the on-off gain and the general gain variation must be calculated. Once all individuals in the population have been evaluated, the best individual, characterized by the maximum fitness value, is saved as a potential solution. This step is represented in lines 2 to 3 in Algorithm 3.
- Step 3: Generation and evaluation of new populations
  The third step of the GA is to construct a new population based on the actual one, in this step the processes of selection, crossover, and mutation are run. The GA uses the selection method `@selectionstochunif`, which maps each individual to a segment on a line, with the length of the segment proportional to the individual's FF value. The crossover method used was `@crossoverscattered`, which generates a random binary vector. Genes corresponding to 1s are inherited from the first parent, while those corresponding to 0s come from the second parent, combining to form a child. The mutation process employed `@mutationadaptfeasible`, which adaptively generates random directions based on the outcome of the previous generation (successful or unsuccessful). This mutation method selects a direction and step size that respect the problem's bounds. Then, the individuals' evaluation is repeated over this new population. Lines 5 to 11 in Algorithm 3 are representing this step.
- Step 4: Termination condition
  The fourth step of the GA is to check if the termination condition is met, this is either when the number of populations reaches the predefined maximum value ($MaxP$)- condition of the while loop of step 3- or when, the best individual is the same after 20 populations, this is the convergence condition verified in line 8 of Algorithm 3. The GA returns the best pumping profile based on the constructed populations.

Algorithm 3 Genetic Algorithm

```
Require: $Population\ size$, $[\min(\lambda_{pump}), \max(\lambda_{pump})]$, $[\min(P_{pump}), \max(P_{pump})]$, $MaxP$, $p_c$, $p_m$,
 1: Create the [$initial\ population$] of size $Population\ size$ based on the ranges of $\lambda_{pump}$ and $P_{pump}$
 2: Evaluate each individual in [$initial\ population$] with FF (Eq. (5.8))
 3: Save the best value of FF
 4: while $Actual\ population < MaxP$ do
 5:     Create a [$New\ Population$] based on $Actual\ population - 1$
 6:     Evaluate each individual in [$New\ Population$] with FF (Eq. (5.8))
 7:     Save the best value of FF in [$New\ Population$] and compare it with the previous best FF
 8:     if best FF $\rightarrow$ converges then
 9:         break
10:     end if
11: end while
        return Pumping profile with best FF
```

5.4 Simulation Results

This section provides a comprehensive evaluation of the designed pumping profile and the characterization of the FM-DRA. A simplified schematic of the physical configuration with backward pumping is presented in Figure 5.2. Numerical techniques were applied to solve Eq. (5.1) to numerically simulate the amplification process within a 70 km FM-DRA. The chosen fiber length corresponds to typical values used in FM-DRA design [104, 47, 109, 110]. Six co-propagating signal modes (LP_{01}, LP_{11_a}, LP_{11b}, LP_{02}, LP_{21_a}, and LP_{21b}) and three pumping modes (LP_{02}, LP_{21_a}, and LP_{21b}) were considered, with input parameters resumed in Table 5.2. The Raman gain coefficients were obtained using VPItransmissionMaker™ [99] software. The intensity overlaps integrals, assuming to be wavelength independent, are summarized in Table 5.3. In the simulations executed to show the results of this chapter, the SDM MUX and DEMUX, in Figure 5.2, were considered ideal, thus adding no penalty to system performance.

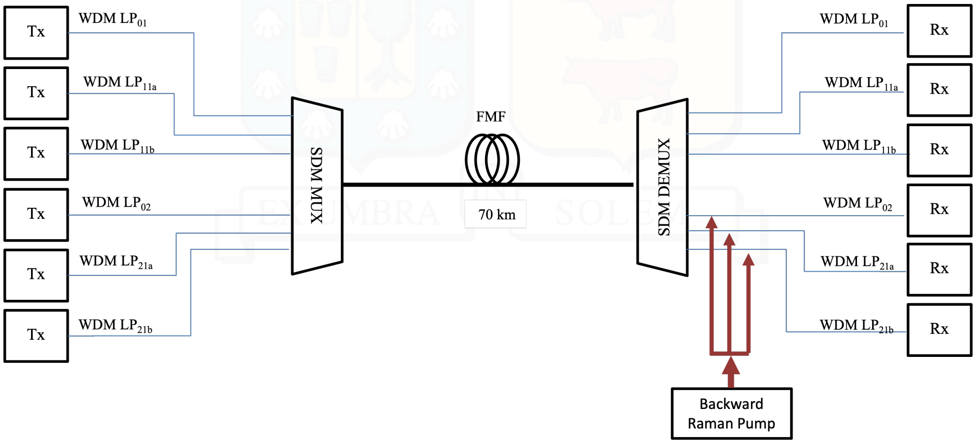

Figure 5.2: Schematic of a FM-DRA with backward pumping.

Table 5.2: Simulation parameters for FM-DRA characterization.

Parameter	**Value**
Radius [μm]	7.5
Core refractive index (n_1)	1.45
Cladding refractive index (n_2)	1.4403
Length [km]	70
Wavelength range operation (signal) [nm]	1530 – 1565 (C-band), 1530 – 1625 (C + L bands)
Number of signal wavelengths	9
Input power (per wavelength) [dBm]	-17
Pump direction	Backward, Forward or Bidirectional

Table 5.3: Intensity overlap integral in units $10^9/m^2$.

	LP_{01}	$LP_{11_{a,b}}$	LP_{02}	$LP_{21_{a,b}}$
LP_{01}	9.66	7.86	6.08	6.28
$LP_{11_{a,b}}$	7.86	9.19	5.15	6.55
LP_{02}	6.08	5.15	5.73	4.70
$LP_{21_{a,b}}$	6.28	6.55	4.70	7.61

5.4.1 Backward Pumping Profile

A GA to design the pumping profile was used, aiming to select the most effective combination of wavelength locations and their corresponding powers for injecting backward

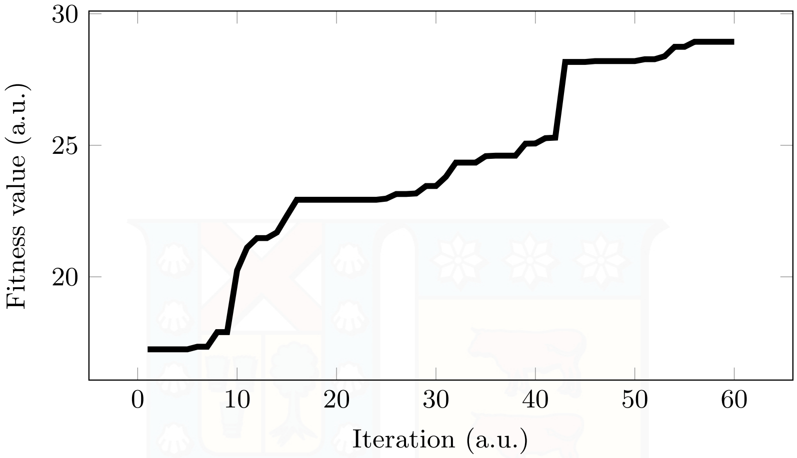

Figure 5.3: Genetic algorithm fitness function evolution for 60 generations for FM-DRA pumping profile design.

pumping into the FM-DRA. The wavelength search range was limited from 1427 nm to 1480 nm, focusing on amplifying signals in the conventional C-band. The pumping power search range was set between 20 mW to 400 mW, aligning with practical implementation constraints. Each population consisted of 60 individuals and 60 maximum number of populations. The fitness function (Eq. (5.8)) preserves the individuals with low gain variations and high gain averages. Figure 5.3 shows the evolution of the fitness value for 60 populations. After 44 populations the fitness function value does not experience a significant change. In this case, the GA stops because the maximum number of populations set was reached.

The optimal pumping profile obtained by the GA is composed of three wavelengths, 1431 nm, 1449 nm, and 1465 nm at spatial modes LP_{02}, LP_{21_a} and, LP_{21_b} with power combinations listed in Table 5.4.

Table 5.4: Optimal pump powers in units of mili-Wats (mW) **for an FM-DRA.**

Mode	**Wavelengths**		
	1431 nm	1449 nm	1465 nm
LP_{02}	85.13	26.45	167.45
LP_{21_a}	41.16	100.16	112.04
LP_{21_b}	191	23.68	280.86

The total pumping power of 1027.93 mW was distributed as follows: 27.14% in LP_{02}, 24.65% in LP_{21_a}, and 48.21% in LP_{21_b}. Consistently, it is observed that the largest proportion of the pumping budget is injected at 1465 nm. If the power in modes LP_{21_a} and LP_{21_b} are added up, our power distribution is similar to the solutions presented in [107, 103, 109, 110]. However, using different pump powers into the degenerated modes LP_{21_a} and LP_{21_b}, DMG between LP_{01}, $LP_{11_{a,b}}$, and LP_{21b} can be reduced, compared with previous works. Figure 5.4 illustrates the power evolution of signals (nine wavelengths per mode), and the optimized pumps along the 70 km FMF. The Raman gain effect is clearly observed at the end of the fiber.

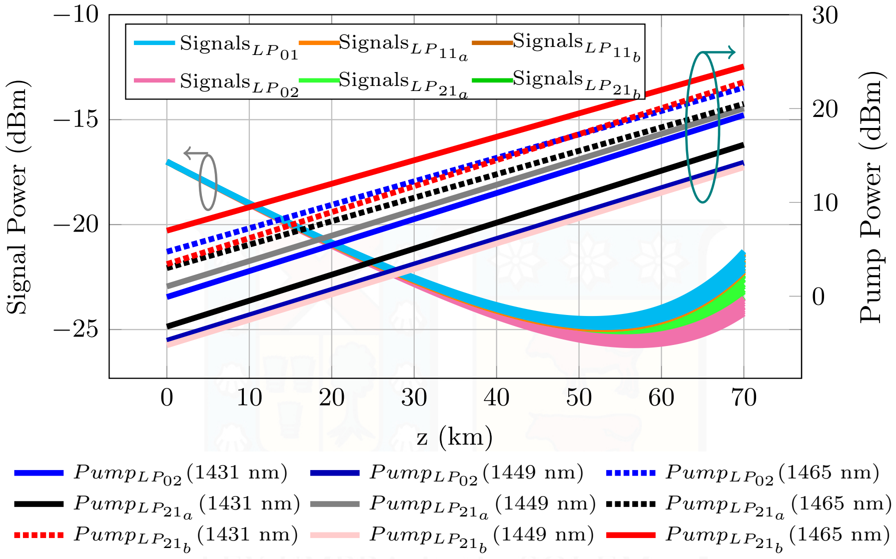

Figure 5.4: Signals and pumps power evolution along 70 km FMF.

5.4.2 FM-DRA Gain Characterization with Backward Pumping

Using the optimized backward pumping profile, the on-off gain and DMG as a function of wavelengths of an FM-DRA in the conventional C-band are presented in Figure 5.5. The on-off gain calculations were obtained using Eq. (5.3). The FM-DRA demonstrates a modal mean on-off gain exceeding 9.5 dB across the entire C-band, with a maximum DMG reaching 2.11 dB at 1539 nm, indicating the on-off gain difference between LP modes LP_{01} and LP_{02}. However, there is a DMG of 0.05 dB between modes LP_{01} and $LP_{11_{a,b}}$, and 0.3 dB between modes LP_{01} and LP_{21_b}, representing the smallest value reported to date for a system with six LP modes. For this gain profile, the flatness keeps the same for every LP mode, at a 0.90 dB value.

It was achieved only 9.5 dB mean gain due to the limited pump power, which is not enough to compensate for the span loss of 14 dB. Higher gains can be obtained by increasing the pump power budget, but at the expense of larger DMG and gain ripple. For instance, increasing the pump power budget by 50% (to a total of 1541.9 mW) the mean on-off gain raises to 14.33 dB. However, this also increases DMG to 3.2 dB and the gain ripple to 1.30 dB. This highlights the trade-off between higher on-off gain versus increased DMG and gain ripple, which must be carefully managed to avoid excessive penalties on the performance of the system. Higher gains can also be achieved using a hybrid configuration, combining FM-DRA + FM-EDFA. In this case, the FM-DRA serves as a pre-amplifier that provides a portion of the gain required to compensate for the span losses and largely determines the equivalent noise figure of the hybrid configuration, which is significantly lower than the noise figure of a FM-EDFA.

Figure 5.6 shows the noise characterization. ASE noise and effective NF were computed using a noise bin bandwidth of 12.5 GHz. It can be observed that the ASE noise curves and the on-off gain curves follow the same trend. The highest effective NF occurs at 1530 nm for all LP modes, with a peak value of 1.56 dB for LP_{02}. The maximum effective noise figure variation is 0.90 dB. To the best of our knowledge, this is the first noise

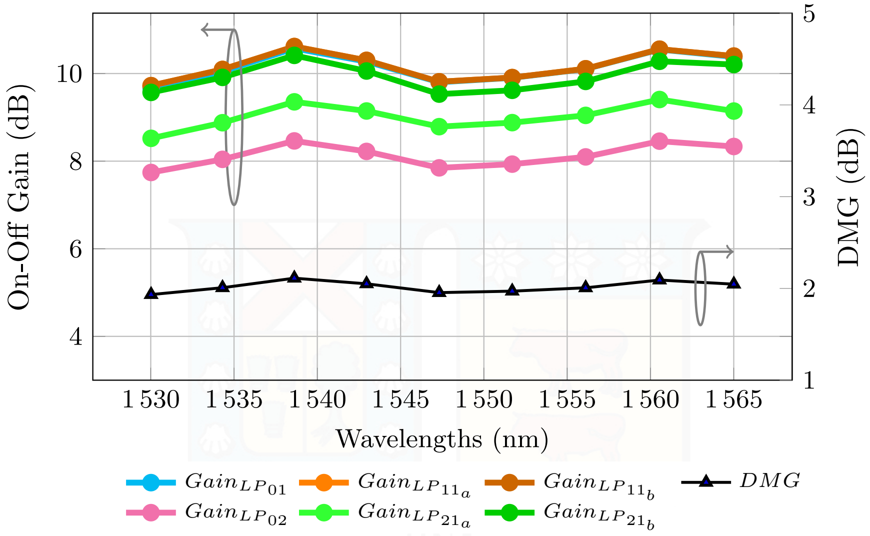

Figure 5.5: On-off Raman gain profile per mode and maximum DMG for a 6M-DRA using the optimized backward pumping profile.

characterization for a 6M-DRA, indicating good noise performance in conventional C-band. To illustrate the transmission capabilities, highlighting the system's performance due to its low noise levels, the OSNR at the end of the 70 km-long FMF is plotted in Figure 5.7. The plotted OSNR is mainly dominated by ASE noise, as the power values are within the linear regime and nonlinear effects are negligible. The modal OSNR variation is also plotted in Figure 5.7, with a maximum overall variation of 0.13 dB, and with an average OSNR of 25.2 dB.

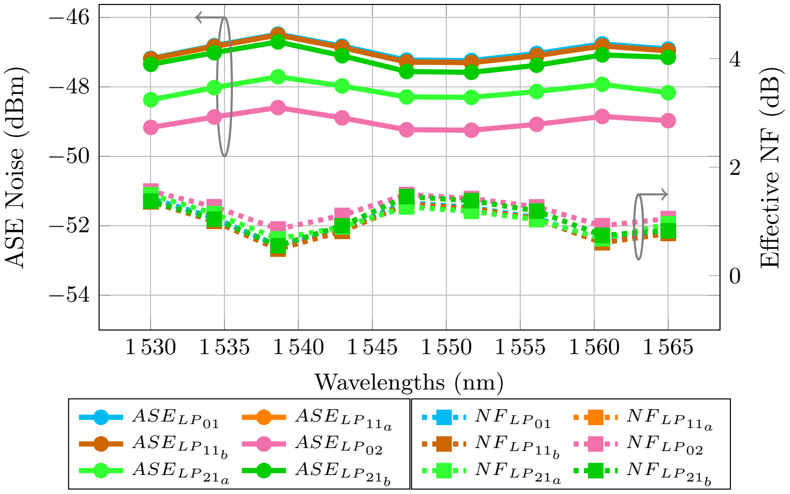

Figure 5.6: ASE noise and effective NF per mode for a 6M-DRA using the optimized backward pumping profile.

Another key performance metric for the 6M-DRA is pump efficiency, defined as the ratio between the mean on-off gain and the total pump power. For the 6M-DRA designed, this efficiency is 9.34 dB/W, representing a 3.4% improvement over the work by [103] and a 133% enhancement compared to [109].

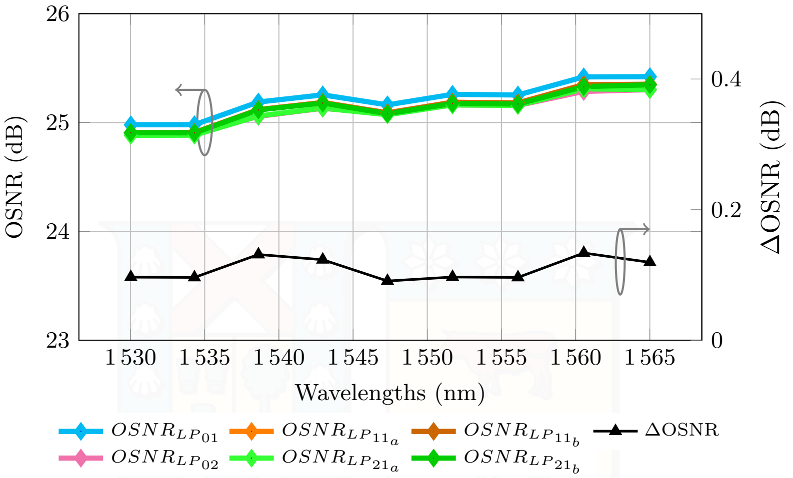

Figure 5.7: OSNR and OSNR variation (ΔOSNR) per mode for a 6M-DRA using the optimized backward pumping profile.

5.4.3 FM-DRA Gain Characterization with Forward Pumping

As well as in FM-EDFA, one of the degrees of freedom in FM-DRA design is the pump direction, which can be forward, backward, or bidirectional [104]. Backward pumping is commonly used for FM-Raman amplification [103, 46, 47, 106] since this configuration does not produce excessively high signal powers at the beginning of the fiber - which does happen in forward pumping - a condition that favors the generation of nonlinear distortions. However, using forward pumping, ASE noise power is reduced, compared to backward pumping. Figure 5.8, shows the schematic of the system with forward pumping, where signals and pumps co-propagate in the same direction. In this subsection, the gain characterization of an FM-DRA using forward pumping is presented.

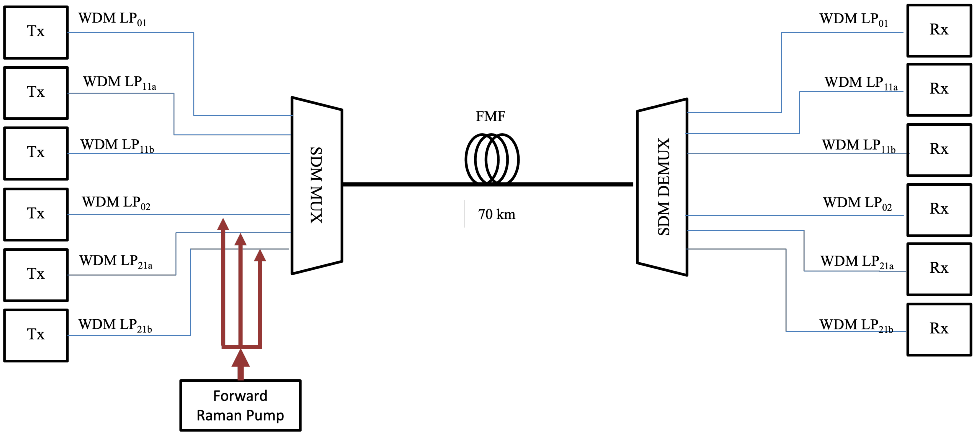

Figure 5.8: Schematic of a FM-DRA with forward pumping.

Using the same pump power budget designed for backward configuration, the on-off gain result is almost the same mean value of 9.5 dB with forward pumping, as can be seen in Figure 5.9, which shows the on-off gain with forward pumping configuration. Consequently, DMG is almost the same value of 2.11 dB using backward and forward pumping.

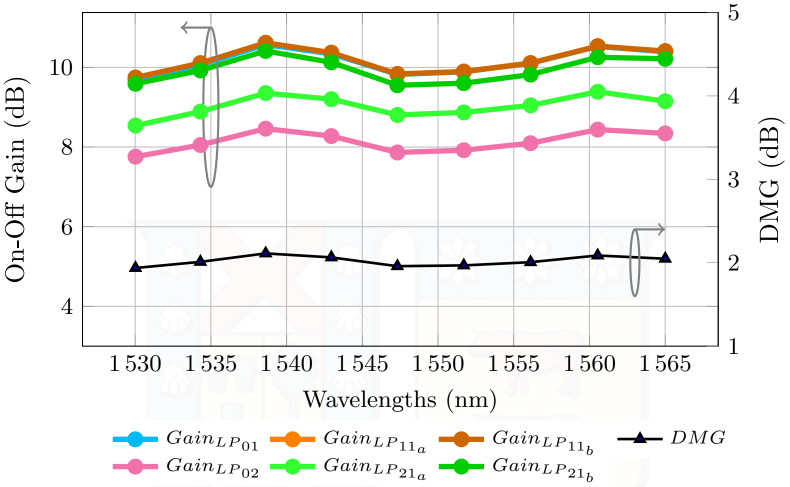

Figure 5.9: On-off Raman gain profile per mode and maximum DMG for a 6M-DRA using forward pumping.

Figure 5.10 shows the ASE noise and the effective NF using the forward pumping configuration. It is observed that lower ASE noise power and effective NF are obtained with the forward pumping, compared to backward pumping. Achieving a mean ASE noise value of −51.2 dB and maximum NF of −1.6 dB at 1530 nm for LP_{02}. In this configuration, the Raman gain is performed in the first section of the fiber length, the effective length, and then signal and ASE are attenuated by fiber losses in the umpumped section of the span, resulting in ASE noise power levels lower (compared to the backward configuration) at the end of the fiber span.

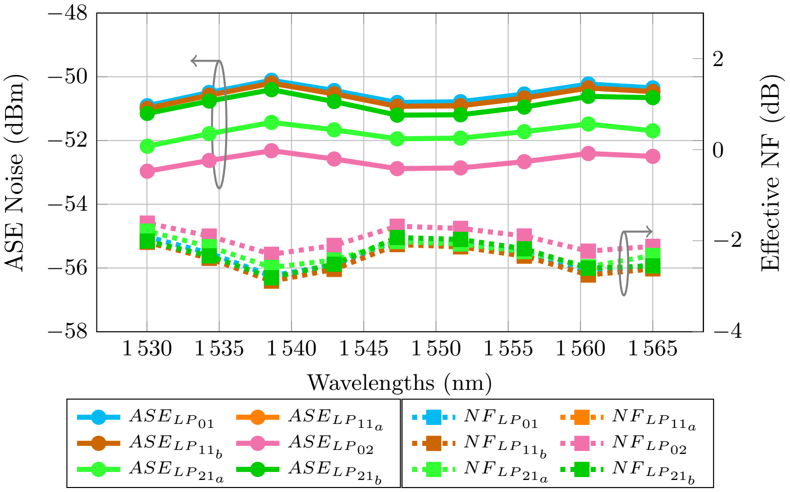

Figure 5.10: ASE noise and effective NF per mode for a 6M-DRA using forward pumping.

5.4.4 FM-DRA Gain Characterization with Bidirectional Pumping

Bidirectional pumping could offer the best trade-off between higher on-off gain with larger pump power budgets while maintaining a low effective NF, without significantly increasing the input power to the fiber span. Figure 5.11, shows the schematic of a system using bidirectional pumping. In this configuration, signals and forward Raman pumps co-propagate, while backward Raman pumps counter-propagate along the fiber. In this subsection, the gain characterization of an FM-DRA using bidirectional pumping is presented.

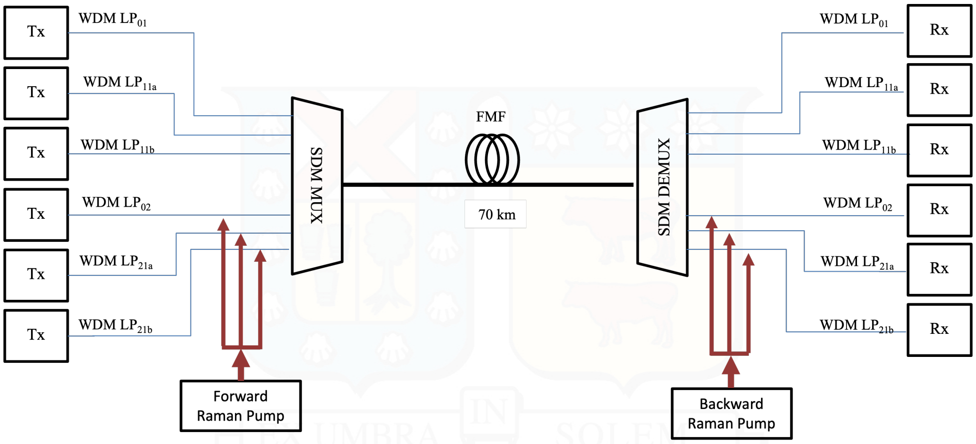

Figure 5.11: Schematic of a FM-DRA with bidirectional pumping.

The total pump power budget was equal to the one used in the backward configuration, that is 1027.93 mW. For the bidirectional pumping configuration, the pump powers were adjusted 30% of the total pump power launched in the forward and 70% launched in the backward direction, as is suggested in [104]. The mean on-off gain result was 9.5 dB, as can be seen in Figure 5.12. Comparing Figures 5.5, 5.9 and 5.12, the on-off gain result is the same in all three cases. Consequently, DMG is also the same value of 2.11 dB for the backward, forward, and bidirectional pumping directions.

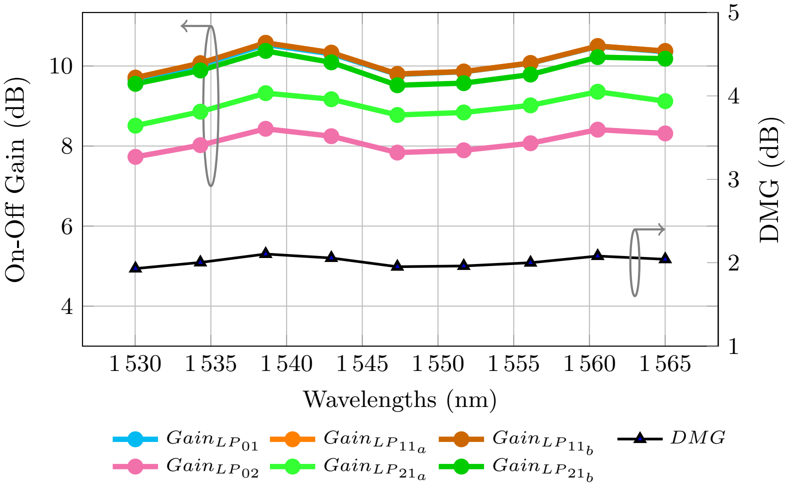

Figure 5.12: On-off Raman gain profile per mode and maximum DMG for a 6M-DRA using bidirectional pumping.

Figure 5.13 shows the ASE noise and the effective NF using bidirectional pumping. An ASE noise power with a mean value of −48.8 dB and maximum effective NF of 0.5 dB at 1530 nm for LP_{02}, are achieved. The latter is an intermediate value compared to backward and forward pumping without the effect of generating high powers at the beginning of the fiber span, which is the major drawback in the forward pumping configuration.

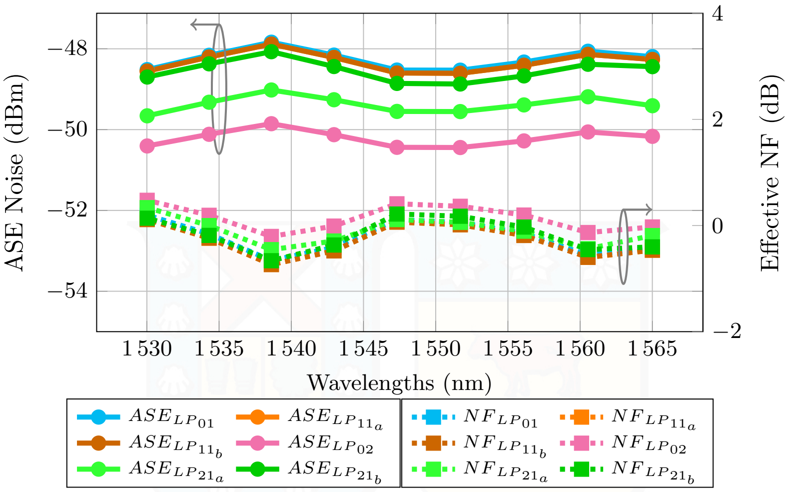

Figure 5.13: ASE noise and effective NF per mode for a 6M-DRA using bidirectional pumping.

5.4.5 FM-DRA Gain Characterization with Backward Pumping in C + L Bands

To fully take advantage of the well-known ultra-wide gain bandwidth of DRAs, the pumping profile design was extended to cover the C and L optical bands. To do this, the GA presented in Algorithm 3 was used to define the most effective combination of wavelength locations and their corresponding powers for injecting backward pumping into the FM-DRA.

The design of the pumping profile was carried out in two steps. First, Algorithm 3 was executed to determine the optimal pump profile for a system supporting only the LP_{01} mode. Second, the wavelengths obtained in the first step were reused in a subsequent execution of Algorithm 3 to find the corresponding power levels, thereby completing the pumping profile design for the 6M-DRA. This approach was adopted to simplify the optimization problem and reduce computational time.

In the first step, the wavelength search range was limited from 1427 nm to 1520 nm, focusing on amplifying 33 WDM signals equally spaced in the C and L optical bands (1530 nm to 1625 nm). By defining the pump wavelength range bellow the 100 nm of Raman gain bandwidth, the system is in the first-order pumping approach. The pumping power search range was set between 100 mW to 550 mW, while the number of wavelengths was fixed to six. Those values where selected based on a preliminary exploration aimed at achieving on-off gains equal or higher than 9.5 dB-the value obtained in the C-band FM-DRA desing- while maintaining a gain ripple below 1 dB. Each population in the GA consisted of 60 individuals, with a maximum of 60 populations. In this execution, the GA stops because the maximum number of populations set was reached.

The designed pumping profile obtained in the first step is composed of six pairs of wavelengths and powers: 1427 nm (278.125 mW), 1443 nm (131.98 mW), 1459 nm (124.41 mW), 1475 nm (191.80 mW), 1491 nm (146.88 mW), and 1520 nm (421.22 mW). Using this pumping profile a mean on-off gain of 11.61 dB and a gain ripple of 0.88 dB was achieved for LP_{01} mode.

Once the wavelengths have been identified, the second step is executed to complete the amplifier design. In this new execution of Algorithm 3, wavelengths are fixed for pumping modes (LP_{02}, LP_{21_a} and, LP_{21_b}) and the algorithm will find the powers preserving the distributions of the total power budget in 27.14% in LP_{02}, 24.65% in LP_{21_a}, and 48.21% in LP_{21_b}. Numerical simulations were programmed using MATLAB® and run on an Apple M1 Pro. This step required 1320050 seconds to complete, highlighting a significant computational time constraint.

The optimal pumping profile obtained by the GA is composed of wavelength and power combinations listed in Table 5.5.

Table 5.5: Optimal pump powers in units of mili-Wats (mW) **for C + L FM-DRA.**

Mode	**Wavelengths**					
	1427 nm	1443 nm	1459 nm	1475 nm	1491 nm	1520 nm
LP_{02}	147.43	62.48	64.12	98.79	73.63	221.32
LP_{21_a}	134.50	57.00	58.50	90.13	67.17	201.91
LP_{21_b}	263.05	111.49	114.41	176.27	131.37	394.89

The total pumping power budget is 2468.46 mW, distributed across the wavelengths as shown in Figure 5.14. Higher power levels are needed at the shortest and the longest wavelength pumps, because between those wavelengths the strongest Raman interaction occurs. Shorter wavelength signals, in the C-band, receive the Raman gain contribution from the shorter wavelength pumps. While, the longest wavelength pumps provides the Raman gain to the longest signal wavelengths, those covering the L-band.

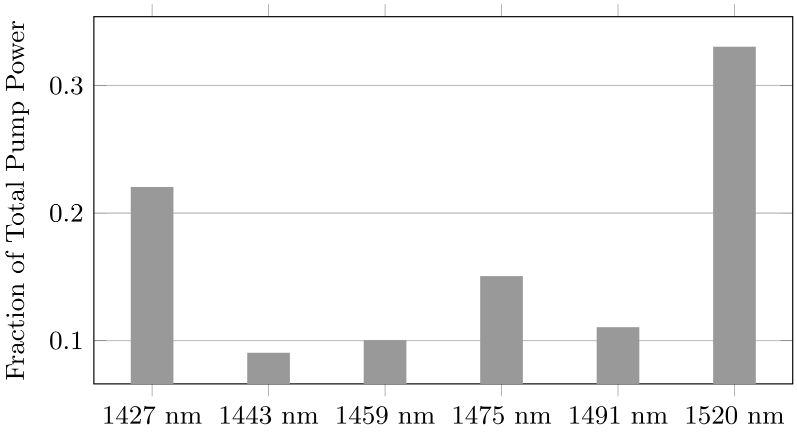

Figure 5.14: Distribution of the pump power budget by wavelengths for the designed FM-DRA for C + L bands.

Using the optimized backward pumping profile for signals in the C and L optical bands, the on-off gain and DMG as a function of wavelengths of the FM-DRA are presented in Figure 5.15. The on-off gain calculation was obtained using Eq. (5.3). The FM-DRA demonstrates a modal mean on-off gain exceeding 15.42 dB across the entire C and L bands, with a maximum DMG reaching 3.5 dB. For this gain profile, the highest gain ripple is 1.30 dB. By increasing the system capacity from C-band to C + L bands results in a 2.4× increase in the pump power budget, yielding a 5.92 dB improvement in mean on-off gain. However, this comes at the cost of a 1.39 dB increase in DMG and 0.4 dB in on-off gain flatness.

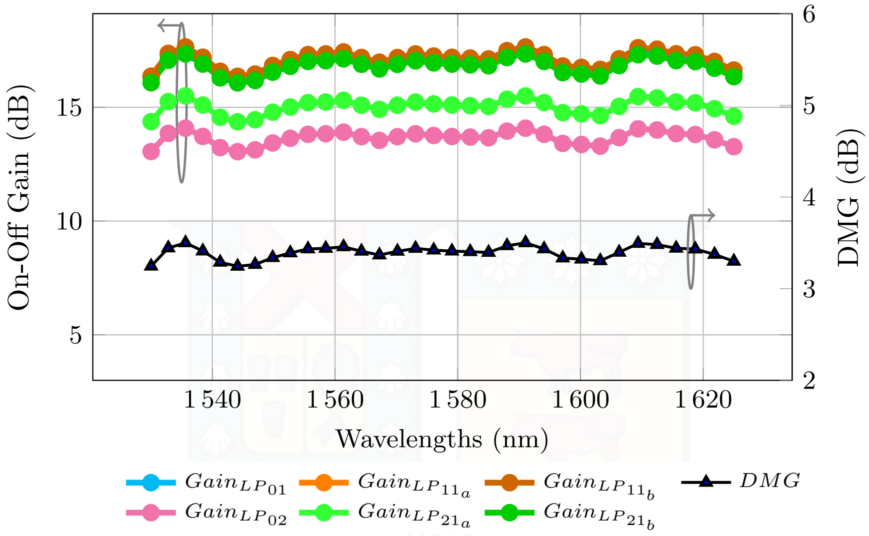

Figure 5.15: On-off Raman gain profile per LP mode and maximum DMG for a 6M-DRA using the optimized backward pumping profile for signals in the C + L bands.

Figure 5.16 shows the noise characterization of the designed FM-DRA for signals in C and L bands. ASE noise and effective NF were computed using a noise bin bandwidth of 12.5 GHz. The highest effective NF is 1.12 dB for LP_{02} and the maximum effective noise figure variation is 1.32 dB. Expanding the system capacity from the C-band to the C + L bands results in 5 dB higher ASE noise, preserving a similar effective NF, which can be explained by the increased on-off gain achieved in the extended system.

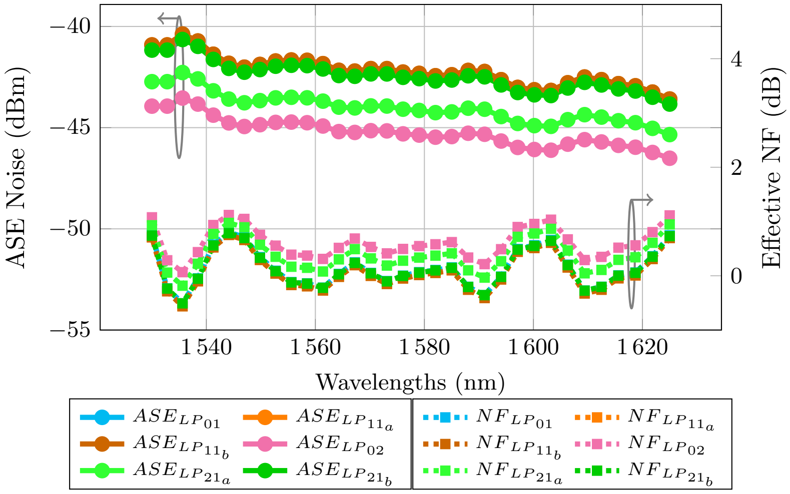

Figure 5.16: ASE noise and effective NF per mode for a 6M-DRA using the optimized backward pumping profile for signals in the C + L bands.

5.5 Conclusions

SDM networks with hundreds to thousands of kilometers in length, such as metro and long-haul networks, require amplification systems that compensate for losses in the optical fiber.

Among the optical amplification solutions for SDM systems based on FMF, FM-EDFAs (addressed in Chapter 4) and FM-DRA are promising solutions. This chapter has presented the basis of FM-DRA.

Optical amplification with FM-DRA uses the SRS effect to optical signal power from the shorter wavelength optical channels to be transferred to the longer wavelength optical channels whenever the wavelength difference is within the 100 nm Raman gain bandwidth. The main limitation of FM-DRAs is the unequal optical gain among the different wavelengths (resulting in gain ripple) and modes (resulting in DMG), which causes different WDM channels to be amplified with different gains in both dimensions. The pump profile must be designed in such a way as to achieve flat gains in the wavelength and spatial modal domains, this means tailoring the power at different wavelengths and modes.

In this chapter, numerical simulations were carried out to optimize the pumping profile for a 6M-DRA by using a genetic algorithm. The genetic algorithm was programmed to minimize the overall gain variation, i.e. DMG and gain ripple, while favoring high on-off gains. Low gain ripple is obtained by selecting the appropriate number and value of wavelength locations for launching the pumps, while low DMG is achieved by tailoring the pump modes and pump powers.

The mathematical model of FM-DRA was solved by the fourth-order Runge Kutta method within each population in the genetic algorithm execution. The output of the genetic algorithm is a pumping profile composed of wavelength locations and its powers, since from the FM-EDFA design - in Chapter 4- it was determined that when signals propagate in modes LP_{01}, $LP_{11_{a,b}}$, LP_{02}, and $LP_{21_{a,b}}$ the pumping modes that contribute to minimizing DMG are the LP_{02} and $LP_{21_{a,b}}$.

The genetic algorithm was applied to design the pumping profile for a FM-DRA supporting 9 WDM signal channels in the conventional C-band per LP mode, and 33 WDM signal channels in C + L bands per LP mode. Both designs where performed using backward pumping.

Simulation results shown that, for 9 WDM channels within C-band, per LP mode using 3 pumping modes in the backward direction in an FMF span of 70 km-length, a mean on-off gain of 9.60 dB, gain ripple less than 1 dB, DMG less than 2.11 dB, effective noise figure below 1.6 dB, OSNR greater than 24.9 dB, and pump efficiency of 9.34 dB/W are achieved. Additionally, using the designed pumping profile, the forward and bidirectional pumping configurations were analyzed. In terms of the on-off gain, the tree pumping configurations reach a similar value. The main difference between these three configurations is regarding the noise. The lowest ASE noise power and the lowest effective NF are obtained with the forward pumping configuration because the ASE noise power is more attenuated at the end of the fiber span - compared to the backward and bidirectional configurations-. However, in practice, backward pumping is preferred over forward pumping, since this configuration does not produce excessively high signal powers at the beginning of the fiber - which does happen in forward pumping - a condition that favors the generation of nonlinear distortions. Therefore, bidirectional pumping offers the best trade-off between on-off gain and low effective NF, without significantly increasing the input power to the fiber span.

Simulation results for high-capacity ultra-wideband systems, with signals in the C and L bands, shown a mean on-off gain of 15.42 dB, gain ripple less than 1.30 dB, DMG less than 3.5 dB, and effective noise figure below 1.12 dB. The power budget of this design is 2.4 times greater than the pumping profile designed for signals only in C-band.

FM-DRA presented in this chapter for signals in the C-band, offers limited on-off gain due to the limited pump power, which is not enough to compensate for the span loss. Higher gains can be obtained by increasing the pump power budget, but at the expense of larger DMG and gain ripple. As was shown in the C + L band case. Highlighting the trade-off between higher on-off gain versus increased DMG and gain ripple, which must be carefully managed to avoid excessive penalties on the performance of the system.

In the next chapter, the problem of resource allocation in FMF links will be addressed, proposing a heuristics aware of the physical layer impairments during propagation and amplification through the FMF link.

6

Resource Allocation in Few-Mode Networks

6.1 Introduction

SDM based on FMFs are one of the approaches addressing the eventual capacity depletion of current WDM systems. Compared to single-mode WDM systems, SDM-FMF systems experience additional impairments, such as differential mode delay and linear and nonlinear mode coupling [66], which were described in Chapter 3. Resource allocation algorithms aware of the physical layer impairments are required to make efficient use of the available resources. The introduction of the spatial dimension allows optical carriers to be transmitted using not only WDM channels, but also to be distributed in different spatial modes. In SDM optical networks, the resource allocation problem becomes the Routing, Spatial mode, and Spectrum Allocation problem, abbreviated with the acronym RSSA [3].

The RSSA problem consists of finding a route, a spatial mode and a portion of the spectrum available to attend a connection request from a user in an SDM-FMF network. Depending on the type of SDM fiber considered, the problem can take different names, for example, in the case of MCF it is called routing, spectrum and core llocation (RSCA) [54, 114, 115, 27]; in the case of FMF it is called routing, modulation format, mode group, and spectrum allocation (RMMSA) [116, 49, 55, 117, 22].

The transmission of spectral and spatial channels through the network requires an allocation of resources appropriate to the physical layer constraints of the underlying technology, such as the coupling between LP modes. Different types of modal coupling imply different levels of the quality of transmission in an FMF link, therefore, considering this constraint will have an impact on the resolution of the RSSA problem.

In this work, the weak and intermediate coupling regimes in FMF link propagation were studied. Under the weak coupling regime, resource allocation can be performed by considering each spatial mode as an independent optical path between transmitter and receiver, however, this approach requires higher complexity in the receiving MIMO DSP for the compensation of linear PLIs [49]. Under the intermediate coupling regime, the receiver complexity can be reduced by performing the allocation by mode groups [49]. This type of coupling gives rise to the mode group division multiplexing (MGDM) technology, where each mode group is composed of one or more LP modes. In this way, each mode group represents an independent optical path with reduced delay spread, and lower DSP complexity [49].

This chapter introduces resource allocation in SDM-FMF networks using MGDM technology. This chapter is structured as follows. Section 6.2 starts by presenting the state of the art in RMMSA assignment. Next, Section 6.3 outlines the network models used. Subsequently, Section 6.4 presents the proposed RMMSA algorithm with results reported in Section 6.5.

The work described in this chapter is based on work published in:

[22] **A. Lozada**, R. Olivares, D. Bórquez-Paredes, F. M. Ferreira, and A. Beghelli, “Few-Mode Amplification-Aware Resource Allocation in Mode-Group Division Multiplexing Systems,” in *2024 IEEE Latin-American Conference on Communications (LATINCOM)*, 2024, pp. 1-6.

6.2 Literature Review

Two methodologies have been presented in the literature for solving the RSSA problem [3]: optimization procedures and heuristics or metaheuristics methods. Optimization procedures produces globally optimal solutions, but they are of low scalability, i.e. they cannot provide optimal or even viable results in a reasonable computation time for practical network cases. While heuristic and metaheuristic methods represent a set of steps that can solve several large-scale problems relatively quickly. The disadvantage of this type of solution is that they do not have the guarantee of getting the optimum. Optimization procedures are compatible with network scenarios with static resource allocation. While heuristics are not restricted by the type of allocation, they are appropriate for scenarios with both dynamic and static allocation.

The first dynamic provisioning strategy for MGDM networks [116] considered the limitation of the transmission reach based on the end-to-end XT and the noise introduced by single-mode amplifiers. The physical layer was modeled using a simulation tool based on the Gaussian Noise Model [118], considering the XT induced during FMF propagation together with the XT due to the coupling efficiency introduced by the MMUX/MDMUX in addition with the ASE noise added by single-mode EDFAs. The MGDM-based provisioning presented in [116] first selects the transponders available in an optical path, giving preference to the ones with mode groups supporting exactly the requested bitrate. Then, the spectrum is assigned using the first-fit strategy. Connection requests are blocked if no transponder can be selected or spectrum is unavailable. Results showed MGDM reduces transponder complexity with respect to a full-MIMO approach while increasing network throughput.

The same provisioning strategy was used in [49] including different MGDM-compatible node architectures and considering state-of-the-art devices. Two node architectures were presented: the first architecture demultiplexes the spectrum and then switches mode groups; the second architecture first demultiplexes the mode groups and then switches the spectrum channels. The transmission reach used in this work is also based on the Gaussian Noise Model, as in [116], considering the ASE noise introduced by single-mode EDFAs, the signal distortion due to the Kerr nonlinear effects in WDM fiber propagation, and the inter-group XT, introduced as an additional source of Gaussian noise. Their results support the conclusion presented in [116] in a broader range of scenarios.

The provisioning algorithm in [116] was also used in a MIMO-free configuration architecture [55], with results showing the solution's viability as well as a blocking probability reduction compared with a single-mode approach. More recently, the provisioning algorithm proposed in [116] was compared to an MDGM solution using light trail (MGDM-LT) [117] in short and long link-length scenarios. Results showed that MGDM-LT offers the same reduction of MIMO complexity of [116] compared to a full-MIMO approach and that the spectrum occupation savings of MGDM-LT over [116] is 21% and 16% for the short-link- and the long-link scenarios, respectively. All previous studies are based on provisioning algorithms that have overlooked FMF optical amplification in the resource allocation problem and have not exploited the potential benefit of balancing the use of mode groups in the network performance. Few-mode amplification offers the advantage of physical integration, where a single device (single doped fibre and single laser diode pump) can amplify multiple modes [76]. However, it also presents limitations, such as the differential modal gain and the differential spectral gain, which were defined in Chapter 4.

6.3 Network Models

6.3.1 Physical Layer Model

In an SDM-FMF network using MGDM, a channel is constituted by a wavelength supporting a mode group, where mode groups are formed by LP modes with normalized propagation constants of similar value. In this work, as in [116, 49], mode groups are represented by lowercase letters, as shown in Figure 6.1: mode group (a) is composed of LP_{01}; mode group (b) is composed of LP_{11_a} and LP_{11_b}; and mode group (c) is composed of LP_{02}, LP_{21_a}, and LP_{21_b}.

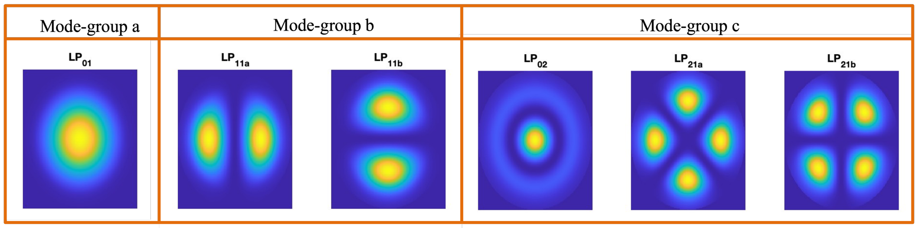

Figure 6.1: Organization of the considered LP modes in 3 mode groups.

Figure 6.2 shows a schematic of a link operating with MGDM technology for a system supporting 3 mode groups (MG). On the transmitter side, wavelength division multiplexed signals per mode group are generated. Thanks to mode group multiplexers/demultiplexers (MG MUXs/MG DEMUXs), mode groups can be added and drop at each network node, allowing mode group routing approach for each independent mode group. On the receiver side, LP modes within each mode group are separated with reduced DSP complexity compared to a non-mode group full-MIMO solution [116].

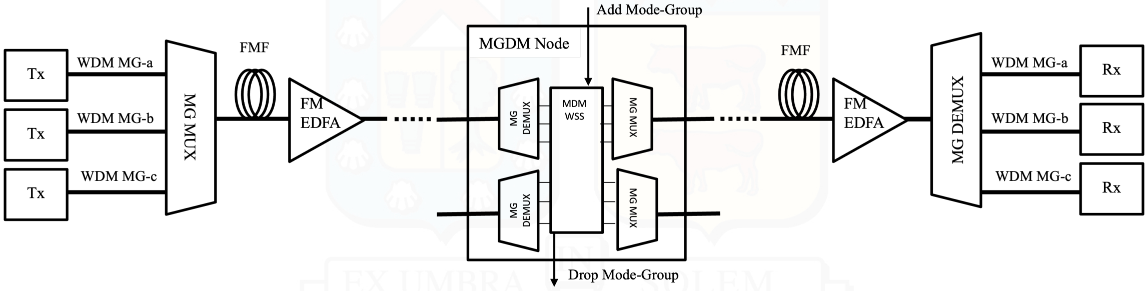

Figure 6.2: Schematic of a MGDM system with 3 mode groups (MG) over FMF.

In this chapter, an MGDM system with 3 mode groups was analyzed, as illustrated in Figure 6.2. In this configuration, coupling between the LP modes occurs in mode groups. Spatial modes in the same mode group exhibit strong coupling, while those in different mode groups exhibit weaker coupling. This is aligned with the intermediate coupling regime presented in Chapter 3. Additionally, the optical amplification approach was based on FM-EDFA, scheme presented in Chapter 4. Using this physical layer configuration, the optical reach of a wavelength within a mode group was calculated, considering a specific modulation format and quality-of-transmission constraints. This information was then used in a physical-layer-aware provisioning algorithm.

Table 6.1 shows the optical reach and the achievable bitrate by each combination of mode group and modulation format, assuming a bit error rate (BER) threshold of $4 \cdot 10^{-3}$ before Forward Error Correction. These optical reach values were calculated under a worst-case scenario, assuming that each mode group supports 81 wavelengths, for a full C-band occupation (1530 nm − 1565 nm). To determine the optical reach, the BER threshold is used to derive the minimum signal-to-noise ratio (SNR) threshold (SNR_{th}) for each modulation format under study. The mean SNR was then computed for every LP mode by: (a) modeling the propagation along the few-mode fiber using the physical layer model presented in Chapter 3 for the intermediate coupling-regime, with mean XT coupling of −35 dB; (b) using optical amplification based on the FM-EDFA configuration presented in Chapter 4. The LP mode with the lowest SNR determines the optical reach, given by the maximum distance that can be achieved by this mode such that its SNR is higher than SNR_{th}.

The bitrate reported in Table 6.1 can be achieved per wavelength per mode group: mode group *(a)* achieves the longest reach but offers the lowest bitrate; mode group *(b)* has a lower optical reach than mode group *(a)*, but doubles its bitrate; and mode group *(c)* has the shortest optical reach and the highest bitrate. As the number of LP modes comprising a mode group increases, the total capacity of the mode group scales proportionally relative to mode group *(a)*, which has the lowest capacity of 100 Gbps. This capacity increase arises

Table 6.1: Optical reach and bit rate per mode group for different modulation formats.

mode group $(a+b+c)$	**QPSK** (SNR_{th} = 10 dB)		**16-QAM** (SNR_{th} = 14 dB)		**64-QAM** (SNR_{th} = 21 dB)	
	Rate [Gbps]	Reach [km]	Rate [Gbps]	Reach [km]	Rate [Gbps]	Reach [km]
a (LP_{01})	100	2200	200	2100	300	900
b ($LP_{11a/b}$)	200	1300	400	1200	600	700
c ($LP_{02}, LP_{21a/b}$)	300	900	600	800	900	600

because, for the same wavelength, a bitrate of 100 Gbps can be transmitted for each LP mode within the mode group.

The different values for the optical reach and bitrate of the mode groups must be taken into account when designing efficient resource allocation algorithms. For instance, in the schematic network depicted in Figure 6.2, if a user requests a 100 Gbps connection, Table 6.1 indicates that this demand can be satisfied using BPSK, 16-QAM or 64-QAM as the modulation format, with mode group *a*, *b*, or *c*. However, the most resource-efficient choice is BPSK with mode group *a*, as it avoids the inefficient use of resources by aligning its capacity with the connection requests. This choice is evident since this pair (mode group, modulation format) are the only ones available to fulfill the connection request perfectly. However, what is the most resource-efficient choice when multiple mode groups and modulation format pairs could satisfy the connection request perfectly? For instance, consider connection requests of 200 Gbps, 300 Gbps, or 600 Gbps and that there is no optical reach limitation. To analyze this scenario, a novel algorithm was proposed and is detailed in Section 6.4.

6.3.2 Network and Traffic Models

The network topology is represented by graph $\mathcal{G} = (\mathcal{N}, \mathcal{L})$, with $\mathcal{N}$ the set of network nodes and $\mathcal{L}$ the set of unidirectional links, with N and L elements each. Nodes are equipped with transmitters able to select one modulation format from set $\mathcal{M}$. All links are equipped with the same capacity defined by the number of mode groups per wavelength and the number of wavelengths, with a fixed-grid approach. The capacity of each mode group is represented by the vector $\mathcal{S} = \{s_1, s_2, \dots s_W\}$ where the i-th element is equal to 1 if wavelength i is used and equal to 0 if available.

Connection request arrivals are modeled as a Poisson process, with an average arrival rate of λ. The holding time of each connection request follows an exponential distribution, with mean value $1/\mu$. The network traffic load is given by λ/μ [Erlang]. Connection requests are defined by the triplet (src, dst, r) where src and dst are the source and destination nodes, and r is the requested bitrate. The source and destination nodes of a request are uniformly distributed across the network nodes whilst the bitrate is also uniformly selected from set B.

6.4 The BANG Algorithm

To address the challenge of efficiently allocating resources in SDM-FMF networks with MGDM, a novel algorithm that exploits the **B**alanced **A**llocatio**N** of Mode **G**roups (BANG) was developed. This algorithm considers the diverse optical reach achievable by mode groups offered by different modulation formats to ensure optimal resource utilization. By balancing the use of mode groups, the proposed algorithm maximizes network performance, reducing the blocking probability compared to state-of-the-art provisionings.

BANG requires two off-line steps: (a) the calculation of the *k*-shortest paths between all node pairs, and (b) the computation of Table 6.1. BANG is described by the flow chart and pseudo-code shown in Figure 6.3 and Algorithm 4, respectively. Upon receiving a connection request (src, dst, r), the algorithm works as follows:

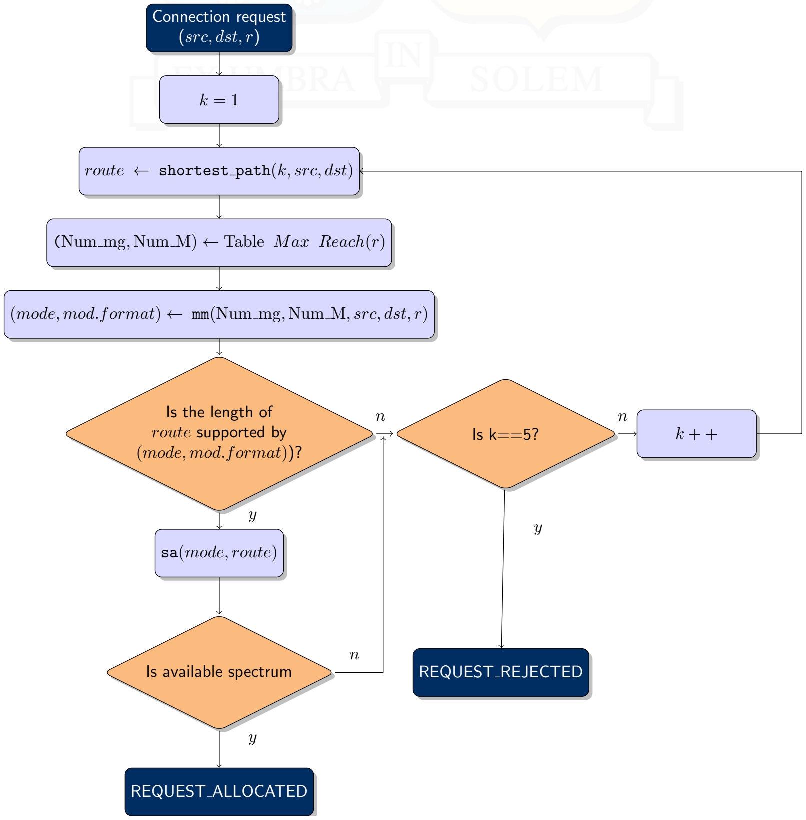

Figure 6.3: Flow chart of the RMMSA algorithm BANG.

- Step 1: Routing (function `shortest_path`)

  BANG selects the *k*-th shortest path between *src* and *dst* from a stored routing table. This step is represented in line 3 of Algorithm 4.

- Step 2: Modulation and Mode Group Allocation (function `mm`)

  BANG identifies and stores all pairs of mode groups and modulation formats that fit *r* perfectly (lines 4 and 5 of Algorithm 4, respectively). mode groups are stored in descending order, with the highest-order mode group in the first position. For example, considering Table 6.1, if r = 200 Gbps, then Num_mg = [b, a] and Num_M = [QPSK, 16 − QAM].

Function `mm` (line 7 of Algorithm 4) assigns the modulation format and the mode group to *mode*. To assign the modulation format the algorithm checks that the optical reach associated with the m-th pair (mode group, modulation format) is longer or equal to the length of *route*. Following the same example of $r = 200$ Gbps, BANG will first attempt the pair (b, QPSK) if the length of *route* is lower or equal to 1300 km. Otherwise, the pair (a, 16-QAM) will be attempted.

The balanced use of mode groups is achieved by prioritizing the use of higher-order modes: requests of high bitrate and short routes will be assigned mode groups (c) or (b), while requests of low bitrate and long routes will be assigned mode group (a). Note that, except for 100 Gbps, 400 Gbps and 900 Gbps, all bitrates available in Table 6.1 have two mode groups able to support them.

- Step 3: Spectrum Allocation (function `sa`)

  The function `sa` (line 8 of Algorithm 4) allocates the first available wavelength, starting from the lower part of the spectrum. The same mode group and wavelength must be allocated in all links in *route*. If resources are available, the request is assigned (line 9). Otherwise it is rejected (line 13).

Algorithm 4 BANG algorithm

```
 1: function RMMSA($src, dst, r$)
 2:     for $k = 0$; $k < 5$ ; $k + +$ do
 3:         $route$ ←shortest_path($k, src, dst$)
 4:         Num_mg ← Table 1($r$)
 5:         Num_M ← Table 1($r$)
 6:         for $m = 0$; $m <$ Num_M; $m + +$ do
 7:             $mode$ ← mm(Num_mg($m$), $src, dst, r$)
 8:             if sa($mode, route$) = $success$ then
 9:                 return REQUEST_ALLOCATED
10:             end if
11:         end for
12:     end for
13:     return REQUEST_REJECTED
14: end function
```

The algorithmic complexity is determined by the number of routes K, the number of mode groups MG, the number of modulation formats M, the maximum number of links in a route L, and the number of wavelengths in a link W. For each pre-calculated route, suitable mode groups and modulation formats must be identified. Then, for each modulation format, an attempt is made to allocate resources to the links of the selected route. Consequently, the algorithmic complexity is $O(K \cdot MG \cdot M \cdot L \cdot W)$. Usually, K, MG and M are limited to a few units irrespective of the network size. Hence, the complexity is reduced to $O(L \cdot W)$.

6.5 Simulation Results

The C++ event-driven simulator Flex Net Sim [119] was adapted to the MGDM scenario to evaluate the blocking probability of BANG in five networks of different sizes and connectivity. Flex Net Sim is a flexible optical networks simulator library used for testing resource assignment algorithms in the context of EON [119], and SDM networks [120].

Flex Net Sim returns metrics such as the blocking probability, the confidence interval, the percentage of use of the spectrum, and the CPU time consumption. In this work, it was used the blocking probability computed as the ratio between allocated and total requests. The main modification in this simulator was done in the allocator component by creating the algorithm for BANG.

The density (α) in a topology is defined as: $\alpha = L/N(N-1)$, where L and N are the number of unidirectional links and nodes, respectively. The network topologies evaluated-from the highest to the lowest density- were: *dfn-bwin* [121], *Eurocore* [24], *NSFNet* [24], *Abilene* [121], and *UKNet* [24]; showed in Figure 6.4 and with parameters summarized in Table 6.2 .

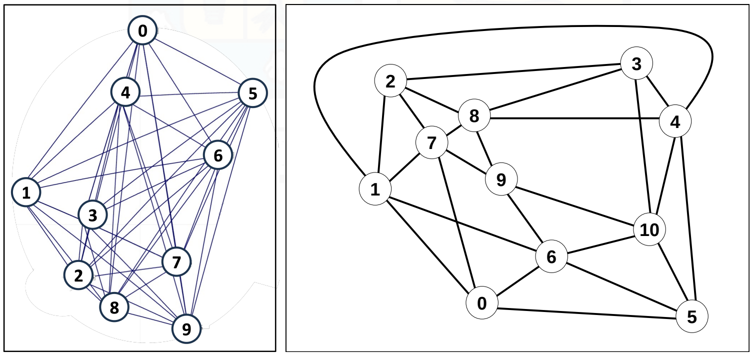

(a) dfn-bwin (b) Eurocore

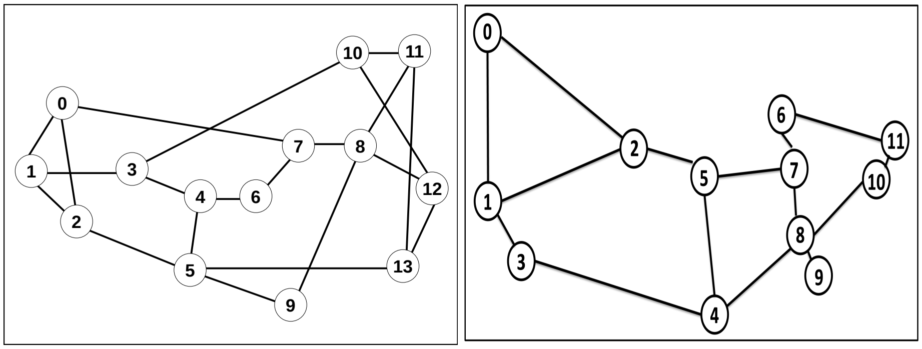

(c) NSFNet (d) Abilene

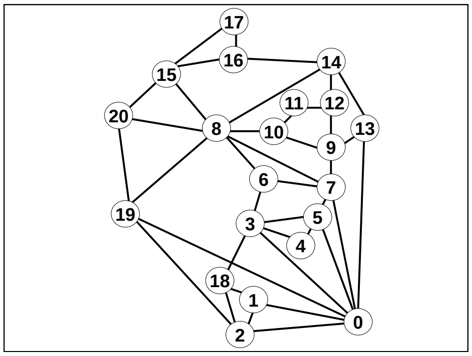

(e) UKNet

Figure 6.4: Topologies of (a) dfn-bwin, (b) Eurocore, (c) NSFNet, (d) Abilene, and (e) UKNet networks.

Table 6.2: Network topologies parameters.

Topology	N	L	α
dfn-bwin [121]	10	90	1
Eurocore [24]	11	50	0.45
NSFNet [24]	14	42	0.23
Abilene [121]	12	30	0.22
UKNet [24]	21	78	0.18

For fairness, each topology was scaled to the longest link of *UKNet*, so the focus will be on the impact of the structural properties of the networks rather than their geographic coverage on the blocking performance. The set of bitrates B, was defined as, B=$\{100, 200, 300, 400, 600\}$ Gbps; the pre-calculated shortest path was defined as $K = 5$; the set of modulation formats $\mathcal{M}$, was defined as, $\mathcal{M}$ = QPSK, 16 − QAM, 64 − QAM; the confidence interval was set to 0.95; and 10^6 connection requests per simulation run were generated.

As a way of comparison, the performance evaluation of a baseline algorithm based on the strategy presented in [116] is included. This allows BANG to be compared against the state-of-the-art. The baseline algorithm works as follows. Given the connection request (src, dst, r) it first selects a path between src and dst from the pre-calculated shortest routes. Then, a suitable modulation format and mode group, supporting a bitrate equal to (or higher than) r, are selected. The pair (modulation format, mode group) chosen must match the optical reach supported by that pair according to Table 6.1. Then, spectrum assignment is performed considering the first fit assignment. A connection request is blocked when no available spectrum satisfying the continuity constraint is present along the path between src and dst. As illustrated in Figure 6.5(a), BANG scans the optical reach table row by row, starting from the bottom and moving to the top. In contrast, the baseline does it column by column, from left to right, as shown in Figure 6.5(b). For example, for a connection request of r = 200 Gbps, with BANG the order to attempt to establish connections will be the pairs (b, QPSK), then (a, 16-QAM), if both fails then reject; while with the baseline algorithm, the order will be (b, QPSK), then (c, QPSK), followed by (a, 16-QAM), (b, 16-QAM), (c, 16-QAM), (a, 64-QAM), (b, 64-QAM), and finally (c, 64-QAM), if that fails then reject. By prioritizing mode groups with shorter optical reach, BANG enables greater allocation opportunities for longer routes and achieves a more balanced utilization of mode groups. In contrast, the baseline algorithm prioritizes mode groups with the longest optical reach, leading to quicker exhaustion of their resources.

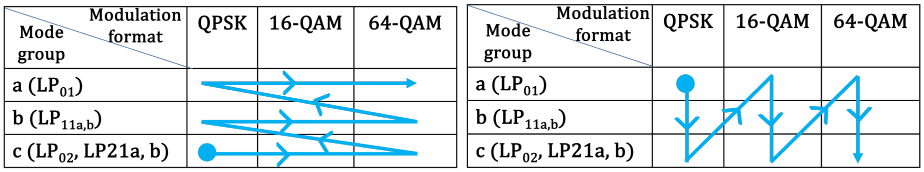

(a) BANG (b) Baseline

Figure 6.5: Search path in the optical reach table to assign the pair (mode group, modulation format) for (a) BANG and (b) the baseline algorithm.

Figures 6.6(a) to 6.10(a) show the blocking probability of BANG and the baseline for 5 topologies, ranging from the most connected (*dfn-bwin* network) to the least connected (*UKNet* network). Confidence intervals are shown for each simulation point. It can be observed that BANG outperforms the baseline for topologies with medium to high density, highlighting a better use of the network capacity with the balanced allocation of mode groups. Networks with density higher than 0.23 present higher improvement compared to the ones with lower density.

Figures 6.6(b) to 6.10(b) show the blocking probability contribution (i.e., blocking due to the lack of routes or spectrum satisfying the continuity constraint) for 5 networks: *dfn-bwin*, *Eurocore*, *NSFNet*, *Abilene*, and *UKNet*. The main source of blocking for baseline algorithm and BANG is due to spectrum unavailability since all topologies were scaled to reduce the impact of blocking due to reach. However, for the *NSFNet* network, this trend is broken as the average path length is larger compared to the rest of the networks, which is reflected in a similar contribution for the two main sources of blocking.

Table 6.3 presents the blocking probability (BP) improvement achieved by BANG compared to the baseline, calculated as $(1 - BP_{BANG}/BP_{base}).100\%$. Higher improvement is observed for lower traffic loads, with up to 100% of blocking probability reduction compared to the baseline in the *dfn-bwin* network for a traffic load of 3500 Erlang.

Table 6.3: Blocking Probability improvement with respect to baseline for highest connected topologies.

Traffic Load [Erlang]	**NSFNet**	**Eurocore**	**dfn-bwin**
2000	85%	–	–
2500	66%	–	–
3000	52%	98%	–
3500	30%	72%	100%
4000	14%	66%	70%
4500	7%	54%	73%
5000	4%	39%	64%
5500	2%	25%	59%

6.6 Conclusions

The introduction of SDM allows optical carriers to be transmitted using not only WDM channels but also to be distributed in different spatial modes. The transmission of spectral and spatial channels through the network requires an allocation of resources appropriate to the constraints of the underlying technology. Different types of modal coupling imply different levels of the quality of transmission in a link, therefore, considering this constraint will have an impact on the resolution of the RSSA problem.

This chapter explored resource allocation for MGDM-based FMF networks. Considering the physical layer model for the intermediate coupling regime, described in Chapter 3, and FM-EDFA-based optical amplification, described in Chapter 4. The maximum transmission reach for a 3-mode group SDM-FMF system with 81 wavelengths available per mode group, was computed. Those reaches were used as input for a novel algorithm for dynamic network provisioning in SDM-FMF systems under MGDM.

The proposed algorithm was named BANG, to represent the **B**alanced **A**llocatio**N** of

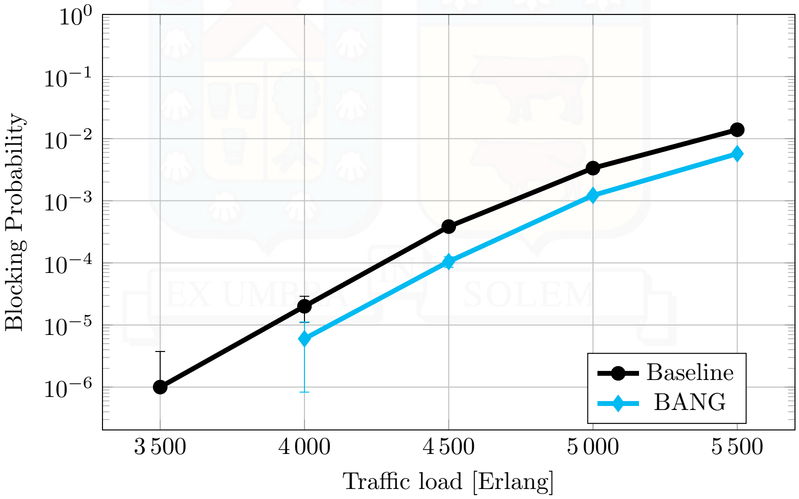

(a) Blocking probability vs. traffic load

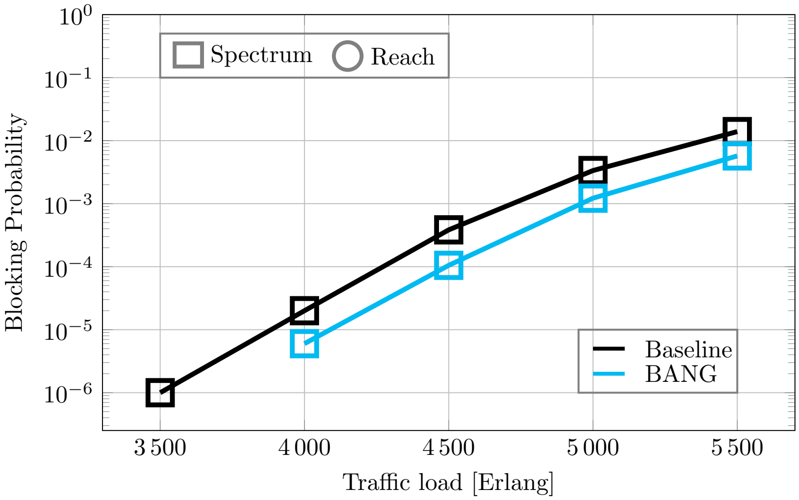

(b) Blocking probability contributions

Figure 6.6: (a) Blocking probability vs. traffic load and (b) Blocking probability contributions of dfn-bwin network.

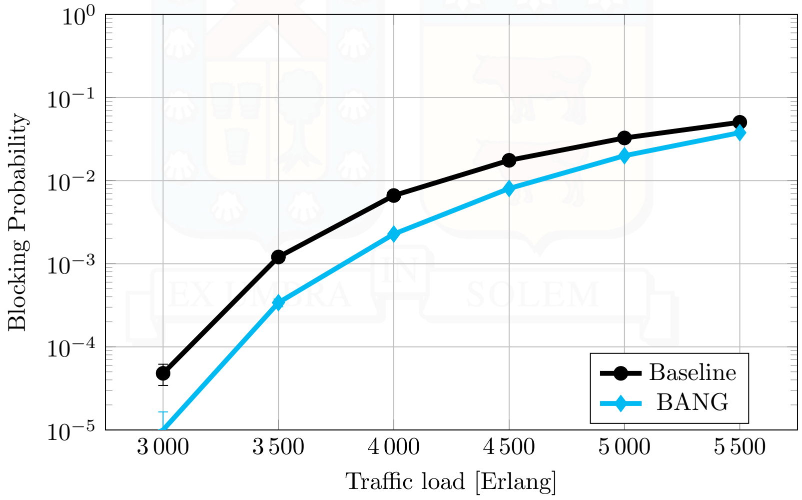

(a) Blocking probability vs. traffic load

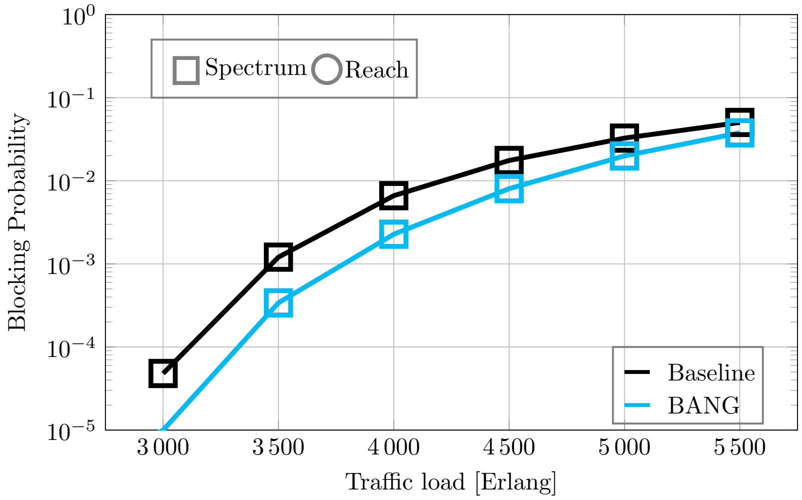

(b) Blocking probability contributions

Figure 6.7: (a) Blocking probability vs. traffic load and (b) Blocking probability contributions of Eurocore network.

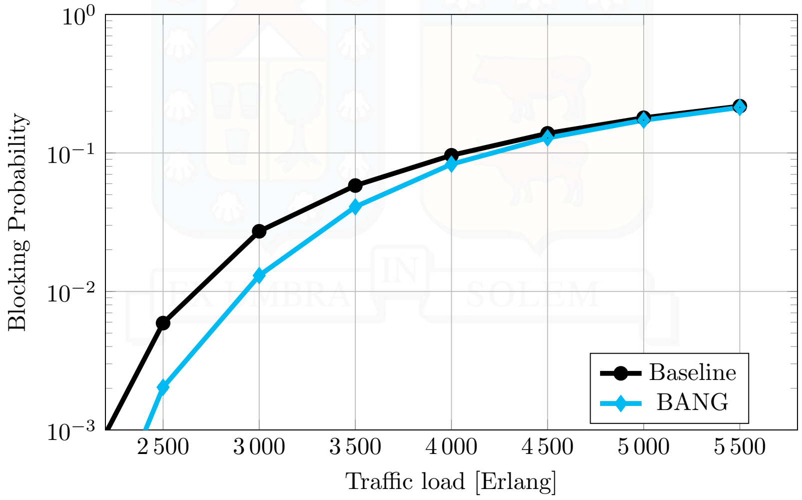

(a) Blocking probability vs. traffic load

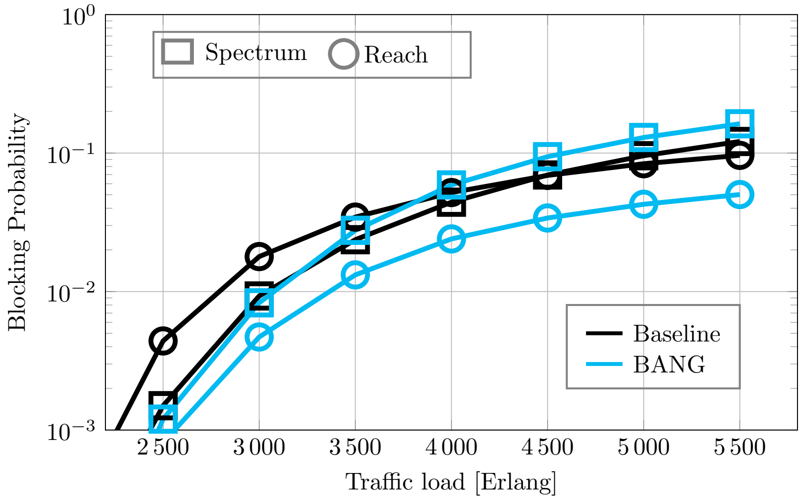

(b) Blocking probability contributions

Figure 6.8: (a) Blocking probability vs. traffic load and (b) Blocking probability contributions of NSFNet network.

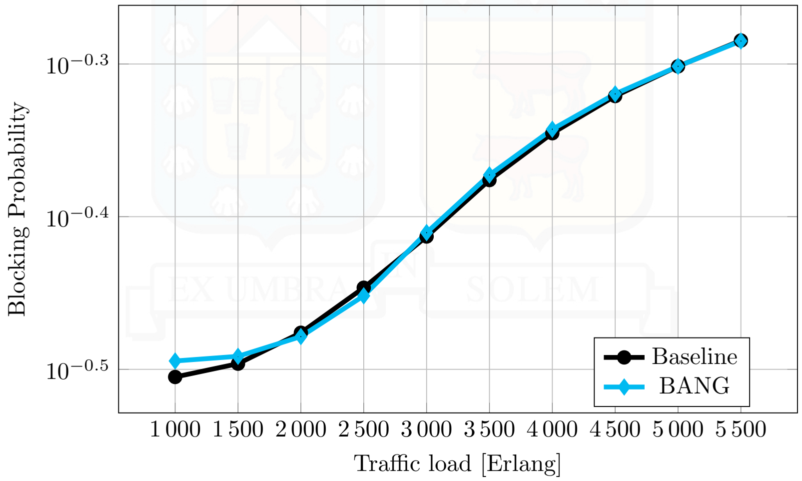

(a) Blocking probability vs. traffic load

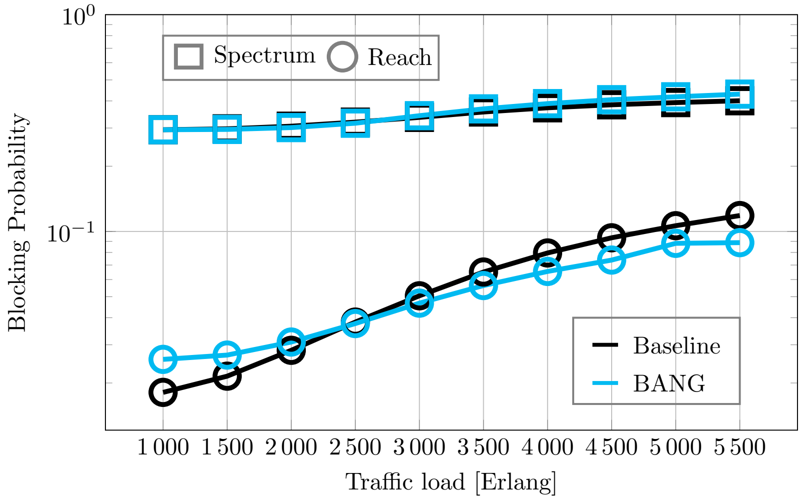

(b) Blocking probability contributions

Figure 6.9: (a) Blocking probability vs. traffic load and (b) Blocking probability contributions of Abilene network.

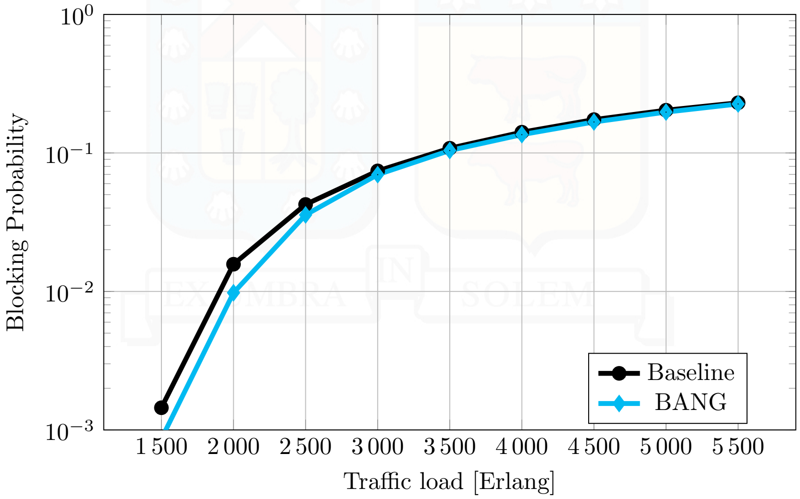

(a) Blocking probability vs. traffic load

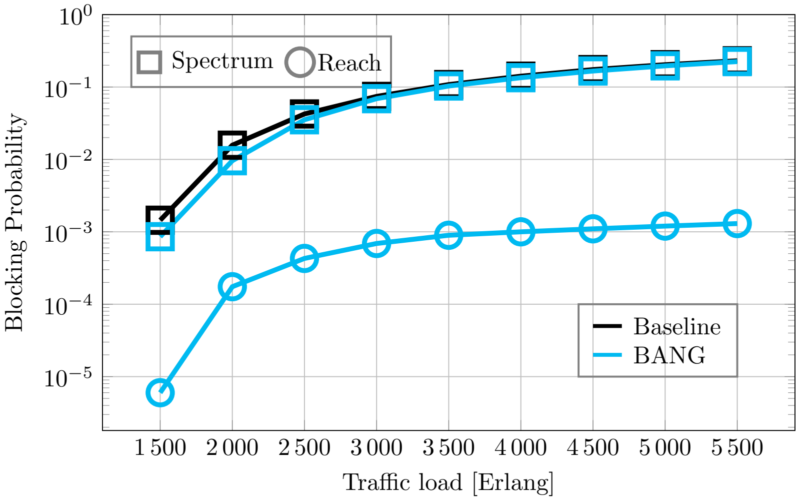

(b) Blocking probability contributions

Figure 6.10: (a) Blocking probability vs. traffic load and (b) Blocking probability contributions of UKNet network.

Mode **G**roups technique. Given a connection request (src, dst, r) BANG works as follows: (1) first selects a path between src and dst from the pre-calculated shortest routes; (2) Next, a suitable mode group and modulation format, supporting a bitrate equal to r, are selected; (3) Then, spectrum assignment is performed considering the first fit approach. The pair (mode group, modulation format) first attempts the allocation in mode groups of higher order (those with shorter optical reach), allowing for a more balanced use of mode groups. The blocking probability of BANG against a baseline based on a state-of-the-art algorithm with topologies dfn-bwin, Eurocore, NSFNet, Abilene and UKNet, was compared, using optical reach values that considered not only the propagation impairments in SDM-FMF networks, but also few-mode amplification. Simulation results show that, for well connected networks, our algorithm outperforms in 100 % the blocking performance of the baseline algorithm based on [116, 49, 55, 117]. The key to this improvement is the balanced allocation of mode groups.

7

Conclusions

This work investigated the performance of spatial division multiplexing systems based on few-mode fiber, SDM-FMF networks, addressing the central research question: How can the physical layer impairments of amplified SDM-FMF optical networks be effectively managed to mitigate their impact on transmission quality and resource allocation within these networks? By examining the impact of physical layer impairments (PLI) on the quality of transmission and optical amplification solutions, this research contributes to the understanding of SDM-FMF networks, for the next generation of optical communications systems.

The analysis began with a description of the PLI that degrade the signal performance. Attenuation, dispersion, crosstalk, mode-dependent loss, and differential mode delay are the main linear PLI. On the other hand, self-phase modulation, cross-phase modulation, four-wave mixing and stimulated Raman scattering are the main nonlinear PLI. Through numerical simulations under weak and intermediate coupling regimes, this study analyzed the SNR after transmission through FMF links.

In this work, SDM-FMF systems with six co-propagating signal modes (LP_{01}, LP_{11_a}, LP_{11b}, LP_{02}, LP_{21_a}, and LP_{21b}) were considered, each one supporting WDM signals even spaced to cover an optical band, such as the C-band (5 THz) or the L-band (10 THz).

Considering the same number of FMF spans and WDM signals per LP mode, under the weak coupling regime higher SNR is achieved compared to the intermediate coupling regime. However, metro and long-haul networks experience an intermediate coupling. This emphasizes the importance of having a rigorous mathematical model to estimate and optimize network performance for practical applications.

When signals operate with input powers within the linear range, the SNR is limited by the ASE noise generated by amplifiers. The ASE noise power is determined by the amplification scheme used. Two types of amplification solutions were addressed: lumped amplification using few-mode erbium-doped fiber amplifiers (FM-EDFA) and distributed amplification using few-mode distributed Raman amplifiers (FM-DRA).

The use of FMF amplifiers involves challenges related to the non-flatness—spatial and spectral—of the amplifier gain profiles. Therefore, optimization is necessary to achieve the lowest differential modal gain (DMG) in the spatial domain and the lowest differential spectral gain (DSG) in the spectral domain, which is also known as gain ripple. In this work, genetic algorithms were used to design optimized pumping profiles for FM-EDFA and FM-DRA.

The introduction of the Joint DMG-DSG Minimization Methodology was a significant step forward in optimizing pumping profiles and gain flattening filter design in two-stage FM-EDFAs. The simulation results demonstrated the potential of FM-EDFAs to maintain a high mean gain and reasonable noise figures within the C-band.

The optimization of pumping profiles through genetic algorithms for FM-DRA illustrated how tailored pumping profiles can mitigate gain ripple and DMG. Low gain ripple and DMG were achieved by selecting the appropriate number and value of wavelength locations and their pump powers. Operating with signals within the C-band, three directions were analyzed to launch the pump power: backward, forward, and bidirectional. In terms of the on-off gain, the three pumping configurations reach a similar value. The main difference between these three configurations is regarding the noise. The lowest ASE noise power and the lowest effective NF are obtained with the forward pumping configuration because the ASE noise power is attenuated through the fiber span, which is not the case with the backward and bidirectional configurations. However, in practice, backward pumping is preferred over forward pumping since this configuration does not produce excessively high signal powers at the beginning of the fiber - which does happen in forward pumping - a condition that favors the generation of nonlinear distortions. Therefore, bidirectional pumping offers the best trade-off between on-off gain and low effective NF, without significantly increasing the input power to the fiber span.

The spectral flexibility of FM-DRA allows the use of signals in any optical band with an appropriate selection of wavelengths and powers in the pumping profile. To extend operation to the C + L optical bands, the genetic algorithm was applied to design the pumping profile for this configuration. In this case, the number of pump wavelengths per pumping mode was double compared to operation in the C-band. Stimulated Raman scattering causes signals wavelengths transfer some power from the shortest to the longest wavelengths channels. Also, a similar interaction between pump wavelengths occurs. An increased pumping power budget was used compared to C-band operation, resulting in higher gains and greater ASE noise power, at the expense of larger DMG and gain ripple.

Applying an integrated physical layer model and an optimized amplifier configuration to estimate the transmission quality in FMF links allows designing algorithms that solve the resource allocation problem considering the limitations imposed by the physical layer. For network operators, it is important to estimate the transmission quality of the links in a rigorous manner since this way, the overestimation or underestimation of the effect of the PLI is avoided, which leads to inefficient use of resources or non-compliance with the service level agreement; both cases are unfavorable for the operation of the network.

An innovative solution for routing, spatial mode, and spectrum allocation (RSSA) was presented for MGDM-based SDM-FMF networks. The algorithm proposed was named BANG, to represent the **B**alanced **A**llocatio**N** of Mode **G**roups. Given a connection request (src, dst, r) BANG works as follows: (1) first, selects a path between src and dst from the pre-calculated shortest routes; (2) Next, a suitable mode group and modulation format, supporting a bitrate equal to r, are selected; (3) Then, spectrum assignment is performed considering first fit approach. The (mode group, modulation format) pair first attempts the allocation in mode groups of higher order (those with shorter optical reach), allowing for a more balanced use of mode groups. The blocking probability of BANG against a baseline based on a state-of-the-art algorithm in various scenarios was compared, using optical reach values that considered not only the propagation impairments in FMF networks, but also few-mode amplification. Simulation results show that, for well connected networks, our algorithm outperforms a significant reduction in blocking probability compared to existing algorithms. The success of BANG highlighted the importance of considering physical layer constraints in resource management, enabling efficient utilization of network resources, and supporting high-capacity transmission.

The evaluation of SDM-FMF systems presented in this work reveals that the performance of few-mode fiber networks is mainly limited by the interplay between amplification strategies and physical layer impairments. By optimizing amplification schemes and designing resource allocation algorithms aware of PLI, this research presented solutions for future developments in SDM-FMF systems that can effectively address the challenges posed by ever-increasing bandwidth demands.

Future Work

Moving forward, several avenues for future research will be addressed:

- **Integration of the Intermediate Coupling Regimen into Distributed Raman Amplification**

  The intermediate coupling regime is present in practical scenarios when the optical link length is higher than tens of kilometers. Consequently, it is required to include the coupling matrices in the mathematical model of FM-DRA. This inclusion could reduce the error between numerical simulations and experimental measurements.

- **Hybrid Amplification Techniques**

  Exploring hybrid amplification methodologies combining FM-DRA plus FM-EDFA could provide insights into optimizing performance under different operational scenarios, achieving enough gain to compensate for span losses with reduced noise figures.

- **Integration of Elastic Optical Networks**

  Flexible grids are one of the new paradigms to address the potential capacity crunch of existing WDM systems. It is required to explore this scenario, to determine the optical reach limitations and design new RSSA algorithms, to then make suggestions to networks operators on how convenient to increase the use of resources when the use of a flexible grid is available.

By addressing these challenges, future research can build upon the findings of this work, further advancing the field of optical communications and contributing to the development of next-generation SDM-FMF systems.

Bibliography

[1] TeleGeography, “Regional Overview Latin America Market Trends, Edition 2022,” Online, 2022, https://www2.telegeography.com/capacity-latam-2022.

[2] B. J. Puttnam, G. Rademacher, and R. S. Luís, “Space-division multiplexing for optical fiber communications,” *Optica*, vol. 8, no. 9, pp. 1186–1203, 2021.

[3] M. Klinkowski, P. Lechowicz, and K. Walkowiak, “Survey of resource allocation schemes and algorithms in spectrally-spatially flexible optical networking,” *Optical Switching and Networking*, vol. 27, pp. 58–78, 2018.

[4] G. Agrawal, *Fiber-Optic Communication Systems*, 4th ed. John Wiley & Sons, Inc., 2010.

[5] J. Bromage, “Raman amplification for fiber communications systems,” *Journal of Lightwave Technology*, vol. 22, no. 1, p. 79, 2004.

[6] W. Klaus, P. J. Winzer, and K. Nakajima, “The Role of Parallelism in the Evolution of Optical Fiber Communication Systems,” *Proceedings of the IEEE*, vol. 110, no. 11, pp. 1619–1654, 2022.

[7] A. Ellis, N. Suibhne, D. Saad, and D. Payne, “Communication networks beyond the capacity crunch,” *Philosophical Transactions of the Royal Society A: Mathematical, Physical and Engineering Sciences*, vol. 374, p. 20150191, 03 2016.

[8] G. P. Agrawal, “Optical communication: its history and recent progress,” in *Optics in Our Time*. Springer, Cham, 2016, pp. 177–199.

[9] N. Yoshikane and T. Tsuritani, “Recent progress in space-division multiplexing optical network technology,” in *2020 International Conference on Optical Network Design and Modeling (ONDM)*. IEEE, 2020, pp. 1–4.

[10] Í. Brasileiro, L. Costa, and A. Drummond, “A survey on challenges of Spatial Division Multiplexing enabled elastic optical networks,” *Optical Switching and Networking*, vol. 38, p. 100584, 2020.

[11] E. Virgillito, R. Sadeghi, A. Ferrari, A. Napoli, B. Correia, and V. Curri, “Network performance assessment with uniform and non-uniform nodes distribution in C+ L upgrades vs. fiber doubling SDM solutions,” in *2020 International Conference on Optical Network Design and Modeling (ONDM)*. IEEE, 2020, pp. 1–6.

[12] G. M. Saridis, D. Alexandropoulos, G. Zervas, and D. Simeonidou, "Survey and evaluation of space division multiplexing: From technologies to optical networks," *IEEE Communications Surveys & Tutorials*, vol. 17, no. 4, pp. 2136–2156, 2015.

[13] R. M. Kingsta and R. S. Selvakumari, "A review on coupled and uncoupled multicore fibers for future ultra-high capacity optical communication," *Optik*, vol. 199, p. 163341, 2019.

[14] K. Saitoh and S. Matsuo, "Multicore fiber technology," *Journal of Lightwave Technology*, vol. 34, no. 1, pp. 55–66, 2016.

[15] B. Shariati, A. Mastropaolo, N.-P. Diamantopoulos, J. M. Rivas-Moscoso, D. Klonidis, and I. Tomkos, "Physical-Layer-Aware Performance Evaluation of SDM Networks Based on SMF Bundles, MCFs, and FMFs," *Journal of Optical Communications and Networking*, vol. 10, no. 9, pp. 712–722, 2018.

[16] L. Zhang, J. Chen, E. Agrell, R. Lin, and L. Wosinska, "Enabling Technologies for Optical Data Center Networks: Spatial Division Multiplexing," *Journal of Lightwave Technology*, vol. 38, no. 1, pp. 18–30, 2020.

[17] F. M. Ferreira, "High Capacity Optical Transmission Systems Based on Mode Division Multiplexing," Ph.D. dissertation, Universidade de Coimbra, 2014.

[18] T. Mizuno, H. Takara, K. Shibahara, A. Sano, and Y. Miyamoto, "Dense space division multiplexed transmission over multicore and multimode fiber for long-haul transport systems," *Journal of Lightwave Technology*, vol. 34, no. 6, pp. 1484–1493, 2016.

[19] A. Lozada, F. Calderón, J. N. Kasaneva, D. Bórquez-Paredes, R. Olivares, A. Beghelli, N. Jara, A. Leiva, and G. Saavedra, "Impact of Amplification and Regeneration Schemes on the Blocking Performance and Energy Consumption of Wide-Area Elastic Optical Networks," *IEEE Access*, vol. 9, pp. 134 355–134 368, 2021.

[20] A. Lozada, R. Olivares, N. Jara, P. Morales, B. D. Feris, A. Leiva, G. Saavedra, and D. Bórquez-Paredes, "Performance evaluation of a two-stage few-mode EDFA for high-capacity SDM systems," *Optics Express*, vol. 32, no. 23, pp. 41 417–41 432, 2024.

[21] A. Lozada and R. Olivares, "Optimized Two-Stage Few-Mode Erbium Doped Fiber Amplifier," in *2023 SBMO/IEEE MTT-S International Microwave and Optoelectronics Conference (IMOC)*, 2023, pp. 316–318.

[22] A. Lozada, R. Olivares, D. Bórquez-Paredes, F. M. Ferreira, and A. Beghelli, "Few-Mode Amplification-Aware Resource Allocation in Mode-Group Division Multiplexing Systems," in *2024 IEEE Latin-American Conference on Communications (LATINCOM)*, 2024, pp. 1–6.

[23] F. I. Calderón, A. Lozada, D. Bórquez-Paredes, R. Olivares, E. J. Davalos, G. Saavedra, N. Jara, and A. Leiva, "BER-Adaptive RMLSA Algorithm for Wide-Area Flexible Optical Networks," *IEEE Access*, vol. 8, pp. 128 018–128 031, 2020.

[24] P. Morales, A. Lozada, D. Bórquez-Paredes, R. Olivares, G. Saavedra, A. Leiva, A. Beghelli, and N. Jara, "Improving the Performance of SDM-EON Through Demand Prioritization: A Comprehensive Analysis," *IEEE Access*, vol. 9, pp. 63 475–63 490, 2021.

[25] F. Calderón, A. Lozada, P. Morales, D. Bórquez-Paredes, N. Jara, R. Olivares, G. Saavedra, A. Beghelli, and A. Leiva, "Heuristic Approaches for Dynamic Provisioning in Multi-Band Elastic Optical Networks," *IEEE Communications Letters*, vol. 26, no. 2, pp. 379–383, 2022.

[26] D. Bórquez-Paredes, A. Beghelli, A. Leiva, N. Jara, A. Lozada, P. Morales, G. Saavedra, and R. Olivares, "Agent-based distributed protocol for resource discovery and allocation of virtual networks over elastic optical networks," *Journal of Optical Communications and Networking*, vol. 14, no. 8, pp. 667–679, 2022.

[27] J. Pinto-Ríos, F. Calderón, A. Leiva, G. Hermosilla, A. Beghelli, D. Bórquez-Paredes, A. Lozada, N. Jara, R. Olivares, and G. Saavedra, "Resource allocation in multicore elastic optical networks: a deep reinforcement learning approach," *Complexity*, vol. 2023, no. 1, p. 4140594, 2023.

[28] D. Bórquez-Paredes, F. Calderón, N. Jara, A. Leiva, A. Lozada, R. Olivares, and G. Saavedra, "3R Regeneration in Elastic Optical Networks and its Impact on the Network Quality of Service," in *2020 22nd International Conference on Transparent Optical Networks (ICTON)*, 2020, pp. 1–4.

[29] J. Bermúdez, A. Lozada, R. Olivares, and N. Jara, "Fragmentation-aware spectrum assignment strategies for elastic optical networks with static operation," in *2020 39th International Conference of the Chilean Computer Science Society (SCCC)*, 2020, pp. 1–8.

[30] D. Hernández, P. Morales, A. Lozada, R. Olivares, and N. Jara, "On sorting transmission demands in Elastic Optical Networks with Spatial-Division Multiplexing," in *2020 39th International Conference of the Chilean Computer Science Society (SCCC)*, 2020, pp. 1–8.

[31] P. Morales, P. Franco, A. Lozada, N. Jara, F. Calderón, J. Pinto-Ríos, and A. Leiva, "Multi-band Environments for Optical Reinforcement Learning Gym for Resource Allocation in Elastic Optical Networks," in *2021 International Conference on Optical Network Design and Modeling (ONDM)*, 2021, pp. 1–6.

[32] G. Rademacher and K. Petermann, "Nonlinear Gaussian noise model for multimode fibers with space-division multiplexing," *Journal of Lightwave Technology*, vol. 34, no. 9, pp. 2280–2287, 2016.

[33] C. Papapavlou, K. Paximadis, D. Uzunidis, and I. Tomkos, "Toward SDM-based submarine optical networks: a review of their evolution and upcoming trends," in *Telecom*, vol. 3, no. 2. MDPI, 2022, pp. 234–280.

[34] A. Muhammad, G. Zervas, and R. Forchheimer, "Resource allocation for space-division multiplexing: optical white box versus optical black box networking," *Journal of Lightwave Technology*, vol. 33, no. 23, pp. 4928–4941, 2015.

[35] S. Mumtaz, R.-J. Essiambre, and G. P. Agrawal, "Nonlinear Propagation in Multimode and Multicore Fibers: Generalization of the Manakov Equations," *Journal of Lightwave Technology*, vol. 31, no. 3, pp. 398–406, 2012.

[36] S. Matsuo, K. Takenaga, Y. Sasaki, Y. Amma, S. Saito, K. Saitoh, T. Matsui, K. Nakajima, T. Mizuno, H. Takara *et al.*, "High-spatial-multiplicity multicore fibers for future dense space-division-multiplexing systems," *Journal of Lightwave Technology*, vol. 34, no. 6, pp. 1464–1475, 2015.

[37] L. Bigot, G. Le Cocq, and Y. Quiquempois, "Few-mode erbium-doped fiber amplifiers: A review," *IEEE J Lightwave Technol*, vol. 33, no. 3, pp. 588–596, 2015.

[38] D. Jia, H. Zhang, Z. Ji, N. Bai, and G. Li, "Optical fiber amplifiers for space-division multiplexing," *Front Optoelectron*, vol. 5, no. 4, pp. 351–357, 2012.

[39] K. S. Abedin, M. F. Yan, T. F. Taunay, B. Zhu, E. M. Monberg, and D. J. DiGiovanni, "State-of-the-art multicore fiber amplifiers for space division multiplexing," *Opt Fiber Tech*, vol. 35, pp. 64–71, 2017.

[40] T. Qayoom, G. Qazi *et al.*, "Design, characterization and performance evaluation of few-mode edfa system with propagation up to six modes," *Optical and Quantum Electronics*, vol. 52, no. 10, pp. 1–19, 2020.

[41] J. Li, L. Wang, J. Du, S. Jiang, L. Ma, C. Cai, L. Zhu, A. Wang, M.-J. Li, H. Chen *et al.*, "Experimental demonstration of a few-mode Raman amplifier with a flat gain covering 1530–1605 nm," *Optics Letters*, vol. 43, no. 18, pp. 4530–4533, 2018.

[42] A. F. Herbster, "Few-Mode Erbium-Doped Fiber Amplifier Design Challenges for WDM Optical Networks," in *2019 SBFoton International Optics and Photonics Conference (SBFoton IOPC)*. IEEE, 2019, pp. 1–5.

[43] Y. Weng, T. Wang, and Z. Pan, "Optimization of mode-dependent gain efficiency based on intermodal Raman scattering for few-mode distributed Raman amplifier," in *CLEO: Science and Innovations*. Optica Publishing Group, 2016, pp. SW1P–5.

[44] U. C. de Moura, F. Da Ros, A. M. R. Brusin, A. Carena, and D. Zibar, "Experimental characterization of Raman amplifier optimization through inverse system design," *Journal of Lightwave Technology*, 2020.

[45] H. Ono, "Optical Amplification Technologies for Space Division Multiplexing," *NTT Technical Review*, vol. 15, no. 6, pp. 1–6, 2017.

[46] R. Ryf, A. Sierra, R.-J. Essiambre, S. Randel, A. Gnauck, C. Bolle, M. Esmaeelpour, P. Winzer, R. Delbue, P. Pupalaikise *et al.*, "Mode-equalized distributed Raman amplification in 137-km few-mode fiber," in *2011 37th European Conference and Exhibition on Optical Communication*. IEEE, 2011, pp. 1–3.

[47] J. Li, J. Du, L. Ma, M.-J. Li, K. Xu, and Z. He, "Second-order few-mode Raman amplifier for mode-division multiplexed optical communication systems," *Optics Express*, vol. 25, no. 2, pp. 810–820, 2017.

[48] D. M. Marom, P. D. Colbourne, A. D'errico, N. K. Fontaine, Y. Ikuma, R. Proietti, L. Zong, J. M. Rivas-Moscoso, and I. Tomkos, "Survey of photonic switching architectures and technologies in support of spatially and spectrally flexible optical

networking," *IEEE/OSA Journal of Optical Communications and Networking*, vol. 9, no. 1, pp. 1–26, 2017.

[49] P. Boffi, N. Sambo, P. Martelli, P. Parolari, A. Gatto, F. Cugini, and P. Castoldi, "Mode-Group Division Multiplexing: Transmission, Node Architecture, and Provisioning," *Journal of Lightwave Technology*, vol. 40, no. 8, pp. 2378–2389, 2022.

[50] F. Arpanaei, N. Ardalani, H. Beyranvand, and B. Shariati, "QoT-aware performance evaluation of spectrally–spatially flexible optical networks over FM-MCFs," *Journal of Optical Communications and Networking*, vol. 12, no. 8, pp. 288–300, 2020.

[51] R. J. Pandya, "Machine learning-oriented resource allocation in C+ L+ S bands extended SDM–EONs," *IET Communications*, vol. 14, no. 12, pp. 1957–1967, 2020.

[52] M. Klinkowski, P. Ksieniewicz, M. Jaworski, G. Zalewski, and K. Walkowiak, "Machine Learning Assisted Optimization of Dynamic Crosstalk-Aware Spectrally-Spatially Flexible Optical Networks," *Journal of Lightwave Technology*, vol. 38, no. 7, pp. 1625–1635, 2020.

[53] N. Jara, J. Salazar, and R. Vallejos, "A topology-based spectrum assignment solution for static elastic optical networks with ring topologies," *IEEE Access*, pp. 1–1, 2020.

[54] H. Liu, Q. Xiong, and Y. Chen, "Routing Core and Spectrum Allocation Algorithm for Inter-Core Crosstalk and Energy Efficiency in Space Division Multiplexing Elastic Optical Networks," *IEEE Access*, vol. 8, pp. 70 453–70 464, 2020.

[55] A. Gatto, P. Martelli, P. Parolari, N. Sambo, P. Castoldi, and P. Boffi, "Mode Group Division Multiplexing in 5 Mode-Group FMF Enabling MIMO-Free Solutions," *IEEE Photonics Technology Letters*, vol. 34, no. 21, pp. 1167–1170, 2022.

[56] A. Mirani, H. Beyranvand, and J. A. Salehi, "Analytical derivation of channel capacity in uncompensated optical space-division multiplexing systems," in *2017 Iran Workshop on Communication and Information Theory (IWCIT)*. IEEE, 2017, pp. 1–6.

[57] M. Hughes, "Fibre Mode Solver and Simulator," [Online], 2022, https://www.mathworks.com/matlabcentral/fileexchange/77497-fibre-mode-solver-and-simulator.

[58] B. Shariati, "Design, Monitoring, and Performance Evaluation of High Capacity Optical Networks," Ph.D. dissertation, Universitat Politécnica de Catalunya, Optical Communications Group, 2018.

[59] D. F. Semrau, "Physical Layer Modelling of Optical Fibre Communication Systems in the Nonlinear Regime," Ph.D. dissertation, University College London, 2020.

[60] C. Antonelli, M. Shtaif, and A. Mecozzi, "Modeling of Nonlinear Propagation in Space-Division Multiplexed Fiber-Optic Transmission," *Journal of Lightwave Technology*, vol. 34, no. 1, pp. 36–54, 2016.

[61] C. T. Politi, C. Matrakidis, and A. Stavdas, *A Tutorial on Physical-Layer Impairments in Optical Networks*, 02 2013, pp. 5–29.

[62] C. Saradhi and S. Subramaniam, "Physical Layer Impairment Aware Routing (PLIAR) In WDM Optical Networks: Issues and Challenges," *Communications Surveys & Tutorials, IEEE*, vol. 11, pp. 109 – 130, 01 2009.

[63] D. Semrau, R. I. Killey, and P. Bayvel, "The Gaussian Noise Model in the Presence of Inter-Channel Stimulated Raman Scattering," *Journal of Lightwave Technology*, vol. 36, no. 14, pp. 3046–3055, 2018.

[64] Y. Xie, L. Pei, J. Zheng, Q. Zhao, T. Ning, and J. Li, "Low-DMD and low-crosstalk few-mode multi-core fiber with air-trench/holes assisted graded-index profile," *Optics Communications*, p. 126155, 2020.

[65] T. Sakamoto, T. Mori, M. Wada, T. Yamamoto, and F. Yamamoto, "Coupled multi-core fiber design with low intercore differential mode delay for high-density space division multiplexing," *Journal of Lightwave Technology*, vol. 33, no. 6, pp. 1175–1181, 2014.

[66] F. M. Ferreira, C. S. Costa, S. Sygletos, and A. D. Ellis, "Semi-analytical modelling of linear mode coupling in few-mode fibers," *Journal of Lightwave Technology*, vol. 35, no. 18, pp. 4011–4022, 2017.

[67] A. Ellis, N. Mac Suibhne, F. G. Gunning, and S. Sygletos, "Expressions for the nonlinear transmission performance of multi-mode optical fiber," *Optics express*, vol. 21, no. 19, pp. 22 834–22 846, 2013.

[68] G. Rademacher, R. S. Luís, B. J. Puttnam, H. Furukawa, R. Maruyama, K. Aikawa, Y. Awaji, and N. Wada, "Investigation of Intermodal Four-Wave Mixing for Nonlinear Signal Processing in Few-Mode Fibers," *IEEE Photonics Technology Letters*, vol. 30, no. 17, pp. 1527–1530, 2018.

[69] R.-J. Essiambre, M. A. Mestre, R. Ryf, A. H. Gnauck, R. W. Tkach, A. R. Chraplyvy, Y. Sun, X. Jiang, and R. Lingle, "Experimental Observation of Inter-Modal Cross-Phase Modulation in Few-Mode Fibers," *IEEE Photonics Technology Letters*, vol. 25, no. 6, pp. 535–538, 2013.

[70] G. Agrawal, *Nonlinear Fiber Optics*, 3rd ed. Academic Press, 2001.

[71] L. G. Wright, Z. M. Ziegler, P. M. Lushnikov, Z. Zhu, M. A. Eftekhar, D. N. Christodoulides, and F. W. Wise, "Multimode Nonlinear Fiber Optics: Massively Parallel Numerical Solver, Tutorial, and Outlook," *IEEE Journal of Selected Topics in Quantum Electronics*, vol. 24, no. 3, pp. 1–16, 2018.

[72] G. Rademacher, R. S. Luís, B. J. Puttnam, R. Maruyama, K. Aikawa, Y. Awaji, H. Furukawa, K. Petermann, and N. Wada, "Investigation of Intermodal Nonlinear Signal Distortions in Few-Mode Fiber Transmission," *Journal of Lightwave Technology*, vol. 37, no. 4, pp. 1273–1279, 2019.

[73] A. E. Elfiqi, A. A. Ali, Z. A. El-Sahn, K. Kato, and H. M. Shalaby, "Theoretical analysis of long-haul systems adopting mode-division multiplexing," *Optics Communications*, vol. 445, pp. 10–18, 2019.

[74] W. Shieh and X. Chen, “Information Spectral Efficiency and Launch Power Density Limits Due to Fiber Nonlinearity for Coherent Optical OFDM Systems,” *IEEE Photonics Journal*, vol. 3, no. 2, pp. 158–173, 2011.

[75] F. Ferreira, S. Jansen, P. Monteiro, and H. Silva, “Nonlinear Semi-Analytical Model for Simulation of Few-Mode Fiber Transmission,” *IEEE Photonics Technology Letters*, vol. 24, no. 4, pp. 240–242, 2012.

[76] H. Guo, T. Li, F. Yan, G. Ren, W. Wang, X. Wang, Q. Qin, G. Wu, J. Gao, B. Wang *et al.*, “Few-Mode Erbium-Doped Fiber Amplifier With High Gain and Low Differential Modal Gain for Mode-Division-Multiplexed Systems,” *Journal of Lightwave Technology*, 2023.

[77] C. Yu, W. Ma, and G. Hu, “High-power, low noise, high gain few-mode fiber amplifier,” *Optics & Laser Technology*, vol. 169, p. 110008, 2024.

[78] Q. Kang, E.-L. Lim, F. P. Y. Jung, C. Baskiotis, S.-u. Alam, and D. J. Richardson, “Minimizing differential modal gain in cladding-pumped EDFAs supporting four and six mode groups,” *Optics express*, vol. 22, no. 18, pp. 21 499–21 507, 2014.

[79] G. Le Cocq, Y. Quiquempois, and L. Bigot, “Optimization algorithm applied to the design of few-mode erbium doped fiber amplifier for modal and spectral gain equalization,” *Journal of Lightwave Technology*, vol. 33, no. 1, pp. 100–108, 2015.

[80] T. Qayoom, G. Qazi *et al.*, “A comparative perspective on Differential Modal Gain reduction techniques for optimized few mode EDFA systems,” *Optik*, vol. 230, p. 166285, 2021.

[81] Q. Zhao, L. Pei, J. Tang, J. Wang, J. Zheng, J. Li, and T. Ning, “Design of few-mode erbium-doped fiber with a low differential modal gain and weak coupling based on layered doping,” *Applied Optics*, vol. 62, no. 6, pp. 1567–1574, 2023.

[82] S. Xu, W. Zhang, and Z. Qin, “Gain equalization for a six-mode-group Er-doped fiber amplifier,” *Optical and Quantum Electronics*, vol. 52, no. 1, pp. 1–14, 2020.

[83] J. Gao, F. Yan, G. Ren, H. Guo, B. Wang, G. Li, F. Zhu, H. Tan, and T. Feng, “Gain equalization for a few-mode erbium-doped fiber amplifier supporting eight spatial modes,” *Appl. Opt.*, vol. 62, no. 35, pp. 9274–9282, 2023.

[84] P.-O. Janvier, C. Matte-Breton, K. J.-J. Monga, L. Wang, L. Rusch, and S. LaRochelle, “Optimization criteria and design of few-mode erbium-doped fibers for cladding-pumped amplifiers,” *Optics Express*, vol. 31, no. 9, pp. 14 888–14 902, 2023.

[85] S. Jeurink and P. M. Krummrich, “Multimode EDFA with scalable mode selective gain control at 1480-nm pump wavelength,” *IEE Photon Technol Lett*, vol. 30, no. 9, pp. 849–852, 2018.

[86] N. Bai, E. Ip, T. Wang, and G. Li, “Multimode fiber amplifier with tunable modal gain using a reconfigurable multimode pump,” *Optics express*, vol. 19, no. 17, pp. 16 601–16 611, 2011.

[87] W. Xu, L. Pei, J. Wang, J. Zheng, Z. Li, T. Ning, L. Jing, and G. Ren, “Gain Characteristics of Few-Mode EDFA With Different Pump,” *IEEE Photonics Journal*, vol. 14, no. 5, pp. 1–7, 2022.

[88] E. Ip, R. Y. Gu, M.-J. Li, Y.-K. Huang, and J. Kahn, “Experimental demonstration of a gain-flattening filter for few-mode fiber based on a spatial light modulator,” in *Optical Fiber Communication Conference*. Optica Publishing Group, 2014, pp. Th4A–5.

[89] J. Zhu, Y. Yang, M. Zuo, Q. He, D. Ge, Z. Chen, Y. He, and J. Li, “Few-mode gain-flattening filter using LPFG in weakly-coupled double-cladding FMF,” *Journal of Lightwave Technology*, vol. 39, no. 13, pp. 4439–4446, 2021.

[90] Y. Zeng, C. Zhang, S. Zhang, Y. Fang, X. Huang, X. Zhang, J. Li, O. Xu, S. Fu, and Y. Qin, “All-fiber spatial and wavelength gain-flattening of few-mode EDFA via mode selective coupler,” *Optics & Laser Technology*, vol. 181, p. 111778, 2025.

[91] I. Rec, “G. 694.1: Spectral grids for WDM applications: DWDM frequency grid,” *International Telecommunication Union, ITU-T*, 2020.

[92] B. Belmahdi and K. Mazighi, “Implementation Efficiency of a Two-Stage EDFA Amplifier with an Inverted Trapezoidal Filter on Gain Flattening,” in *2022 7th International Conference on Image and Signal Processing and their Applications (ISPA)*. IEEE, 2022, pp. 1–6.

[93] Z. Zhang, Q. Zhao, N. Zhao, X. Li, and G. Li, “Bi-directionally-pumped few-mode EDFA,” in *Asia Communications and Photonics Conference*. Optica Publishing Group, 2014, pp. ATh3A–104.

[94] C. R. Giles and E. Desurvire, “Modeling Erbium-Doped Fiber Amplifiers,” *Journal of Lightwave Technology*, vol. 9, no. 2, pp. 271–283, 1991.

[95] A. Galvanauskas, “Mode-scalable fiber-based chirped pulse amplification systems,” *IEEE Journal of Selected Topics in Quantum Electronics*, vol. 7, no. 4, pp. 504–517, 2001.

[96] J. H. C. Júnior, F. L. Della Lucia, T. Sutili, D. A. A. Melloy, and R. C. Figueiredo, “Gradient-based Optimization for Unrepeatered Optical Systems,” in *2019 SBMO/IEEE MTT-S International Microwave and Optoelectronics Conference (IMOC)*, 2019, pp. 1–3.

[97] H. Friis, “Noise Figures of Radio Receivers,” *Proceedings of the IRE*, vol. 32, no. 7, pp. 419–422, 1944.

[98] R. E. Collin, *Foundations for microwave engineering*. IEEE Press, 2001.

[99] V. GmbH, “VPItransmissionMaker™ Optical Systems,” Berlin, Germany, 2023.

[100] Y. Jung, Q. Kang, J. K. Sahu, B. Corbett, J. O’Callagham, F. Poletti, S.-U. Alam, and D. J. Richardson, “Reconfigurable modal gain control of a few-mode EDFA supporting six spatial modes,” *IEEE Photonics Technology Letters*, vol. 26, no. 11, pp. 1100–1103, 2014.

[101] P. Poggiolini, A. Carena, V. Curri, G. Bosco, and F. Forghieri, “Analytical modeling of nonlinear propagation in uncompensated optical transmission links,” *IEEE Photonics technology letters*, vol. 23, no. 11, pp. 742–744, 2011.

[102] OpenROADM MSA, "OpenROADM MSA optical specifications v6.0," OpenROADM MSA, 2023. [Online]. Available: https://github.com/OpenROADM/OpenROADM_MSA_Public/wiki

[103] J. Zhou, "An analytical approach for gain optimization in multimode fiber Raman amplifiers," *Optics express*, vol. 22, no. 18, pp. 21 393–21 402, 2014.

[104] M. Esmaeelpour, R. Ryf, N. K. Fontaine, H. Chen, A. H. Gnauck, R.-J. Essiambre, J. Toulouse, Y. Sun, and R. Lingle, "Transmission over 1050-km few-mode fiber based on bidirectional distributed Raman amplification," *Journal of Lightwave Technology*, vol. 34, no. 8, pp. 1864–1871, 2016.

[105] J. Li, L. Wang, J. Du, Z. He, C. Cai, L. Zhu, A. Wang, and J. Wang, "C+ L band distributed few-mode Raman amplification with flattened gain for mode-division-multiplexed optical transmission over 75-km Few-mode fiber," in *Optical Fiber Communication Conference*. Optica Publishing Group, 2018, pp. W3D–2.

[106] G. Rademacher, R. S. Luis, B. J. Puttnam, J. C. A. Zacarias, R. Amezcua-Correa, K. Aikawa, Y. Awaji, and H. Furukawa, "Investigation of wideband distributed raman amplification in a few-mode fiber link," in *2022 Optical Fiber Communications Conference and Exhibition (OFC)*. IEEE, 2022, pp. 1–3.

[107] R. Ryf, R.-J. Essiambre, J. von Hoyningen-Huene, and P. Winzer, "Analysis of mode-dependent gain in Raman amplified few-mode fiber," in *Optical Fiber Communication Conference*. Optica Publishing Group, 2012, pp. OW1D–2.

[108] K. Rottwitt, K. Nielsen, S. M. Friis, and M. A. Castaneda, "Challenges in higher order mode Raman amplifiers," in *Optical Fiber Communication Conference*. Optica Publishing Group, 2015, pp. Tu3C–6.

[109] Y. Chen, J. Du, Y. Huang, K. Xu, and Z. He, "Intelligent gain flattening in wavelength and space domain for FMF Raman amplification by machine learning based inverse design," *Optics Express*, vol. 28, no. 8, pp. 11 911–11 920, 2020.

[110] G. Marcon, A. Galtarossa, L. Palmieri, and M. Santagiustina, "Model-aware deep learning method for Raman amplification in few-mode fibers," *Journal of Lightwave Technology*, vol. 39, no. 5, pp. 1371–1380, 2020.

[111] S. Huang, G. Qiao, Y. Gao, J. Cui, M. Zuo, Y. He, Z. Chen, J. Li *et al.*, "Experimental Investigation on Raman Amplification for Weakly-Coupled MDM Transmission," *Journal of Lightwave Technology*, 2023.

[112] J. Li, C. Cai, J. Du, S. Jiang, L. Ma, L. Wang, L. Zhu, A. Wang, M.-J. Li, H. Chen *et al.*, "Ultra-low-noise mode-division multiplexed WDM transmission over 100-km FMF based on a second-order few-mode Raman amplifier," *Journal of Lightwave Technology*, vol. 36, no. 16, pp. 3254–3260, 2018.

[113] T. M. Inc., "Optimization Toolbox version: 9.3 (R2022a)," Natick, Massachusetts, United States, 2022. [Online]. Available: https://www.mathworks.com

[114] P. M. Moura and N. L. Da Fonseca, "Routing, core, modulation level, and spectrum assignment based on image processing algorithms," *IEEE/OSA Journal of Optical Communications and Networking*, vol. 10, no. 12, pp. 947–958, 2018.

[115] H. Xuan, S. Wei, S. Guo, Y. Li, and Z. Xu, “Routing, spectrum and core assignment for multi-domain elastic optical networks with multi-core fibers,” *Optical Fiber Technology*, vol. 59, p. 102040, 2020.

[116] N. Sambo, P. Martelli, P. Parolari, A. Gatto, P. Castoldi, and P. Boffi, “Mode-group division multiplexing for provisioning in SDM networks,” in *2020 European Conference on Optical Communications (ECOC)*, 2020, pp. 1–4.

[117] Q. Zhang, Y. Yang, A. Gatto, and M. Tornatore, “Resource Allocation in Optical Networks with Mode Group Division Multiplexing and Light Trail,” in *Optical Fiber Communication Conference (OFC)*. Optica Publishing Group, 2023, pp. Tu2D–7.

[118] P. Martelli and P. Boffi, “Crosstalk-induced penalty in coherent space-division multiplexing transmission,” in *2018 20th International Conference on Transparent Optical Networks (ICTON)*, 2018, pp. 1–4.

[119] F. Falcón, G. España, and D. Bórquez-Paredes, “Flex Net Sim: A Lightly Manual,” 2021.

[120] M. Zitkovich, G. Saavedra, and D. Bórquez-Paredes, “Event-oriented simulation module for dynamic elastic optical networks with space division multiplexing,” in *SIMULTECH 2023 - Proceedings of the 13th International Conference on Simulation and Modeling Methodologies, Technologies and Applications*. Science and Technology Publications, Lda, 2023, pp. 295–302.

[121] S. Orlowski, M. Pióro, A. Tomaszewski, and R. Wessäly, “SNDlib 1.0–Survivable Network Design Library,” *Networks*, vol. 55, no. 3, pp. 276–286, 2010.

A

Journal Publication

Received August 20, 2021, accepted September 14, 2021, date of publication September 28, 2021, date of current version October 6, 2021.

Digital Object Identifier 10.1109/ACCESS.2021.3115998

Impact of Amplification and Regeneration Schemes on the Blocking Performance and Energy Consumption of Wide-Area Elastic Optical Networks

ASTRID LOZADA[1], **FELIPE CALDERÓN**[2], **JOSÉ NÚÑEZ KASANEVA**[3],
DANILO BÓRQUEZ-PAREDES[4], **RICARDO OLIVARES**[1], **ALEJANDRA BEGHELLI**[5],
NICOLÁS JARA[1], **(Member, IEEE), ARIEL LEIVA**[2], **(Member, IEEE),**
AND GABRIEL SAAVEDRA[3], **(Member, IEEE)**

[1]Department of Electronic Engineering, Universidad Técnica Federico Santa María, Valparaíso 2390123, Chile
[2]School of Electrical Engineering, Pontificia Universidad Católica de Valparaíso, Valparaíso 2362804, Chile
[3]Department of Electrical Engineering, Universidad de Concepción, Concepción 4070409, Chile
[4]Faculty of Engineering and Sciences, Universidad Adolfo Ibáñez, Santiago 7941169, Chile
[5]Department of Electronic and Electrical Engineering, University College London, London WC1E 7JE, U.K.

Corresponding author: Astrid Lozada (astrid.lozadav@sansano.usm.cl)

This work was supported in part by DI-PUCV 039.382/2021, in part by USM PI_LII_2020_74, in part by USM PIIC 007/2021, in part by the Agencia Nacional de Investigación y Desarrollo (ANID) Fondo Nacional de Desarrollo Científico y Tecnológico (FONDECYT) Iniciación 11190710, in part by ANID FONDECYT Iniciación 11201024, in part by ANID Doctorado Nacional/2021-21211075, and in part by ANID Magister Nacional/2021-22210736.

ABSTRACT This paper studies the physical layer's impact on the blocking probability and energy consumption of wide-area dynamic elastic optical networks (EONs). For this purpose, we consider five network configurations, each named with a network configuration identifier (NCI) from 1 to 5, for which the Routing, Modulation Level, and Spectrum Assignment (RMLSA) problem is solved. NCI 1-4 are transparent configurations based on all-EDFA, hybrid Raman/EDFA amplifiers (with different Raman gain ratio Γ_R), all-DFRA, and alternating span configuration (EDFA and DFRA). NCI 5 is a translucent configuration based on all-EDFA and 3R regenerators. We model the physical layer for every network configuration to determine the maximum achievable reach of optical signals. Employing simulation, we calculate the blocking probability and the energy consumption of the different network configurations. In terms of blocking, our results show that NCI 2 and 3 offer the lowest blocking probability, with at least 1 and 3 orders of magnitude of difference with respect to NCI 1 and 5 at high and low traffic loads, respectively. In terms of energy consumption, the best performing alternatives are the ones with the worst blocking (NCI 1), while NCI 3 exhibits the highest energy consumption with NCI 2 $\Gamma_R = 0.75$ following closely. This situation highlights a clear trade-off between blocking performance and energy cost that must be considered when designing a dynamic EON. Thus, we identify NCI 2 using $\Gamma_R = 0.25$ as a promising alternative to reduce the blocking probability significantly in wide-area dynamic EONs without a prohibitive increase in energy consumption.

INDEX TERMS Elastic optical networks, resource assignment, translucent configuration, transparent configuration.

I. INTRODUCTION

Elastic Optical Network (EON) architectures were proposed as a new paradigm to overcome the potential capacity crunch of legacy wavelength division multiplexing (WDM) networks [1], [2]. EONs divide the frequency spectrum into small slot units (Frequency Slot Units - FSU), usually of 12.5 or 6.25 GHz spectral width [3], which are flexibly allocated to the different traffic demands [4]. In this way, spectral resources are managed more efficiently than current fixed

The associate editor coordinating the review of this manuscript and approving it for publication was Bijoy Chand Chand Chatterjee.

grid WDM networks. When dynamically operated (connection requests are established on-demand and released after transmission [5]), EONs also have the potential of improving resource utilization in contrast to static operation (resources permanently allocated to each connection [6]). In this work, we focus on dynamic EON architectures.

One of the main tasks dynamic EON operators must solve is resource allocation. That is, finding a path, a modulation format suitable for the path length, and a portion of the optical spectrum on the path that meets the contiguity and continuity constraints, known as the Routing, Modulation Level, and Spectrum Assignment (RMLSA) problem [4]. Usually, the performance of RMLSA solutions for dynamic networks is contrasted in terms of the blocking ratio [6]. Thus, an RMLSA solution is better than another if it consistently exhibits a lower blocking ratio for different scenarios. In wide-area dynamic EON, there are two primary sources of blocking: a lack of capacity to establish connections and the inability to provide an acceptable quality-of-transmission (QoT) to the network connection, despite capacity availability [5], [7]–[9]. The former case arises when there are effectively no available slots to meet the requested bandwidth or having available slots these cannot be used due to spectrum fragmentation, which occurs when the available slots are isolated and they are neither continuous along the optical path nor contiguous on the spectrum domain [10], [11]. The latter case arises when the length of the route is such that the accumulation of physical layer impairments (PLI), such as amplified spontaneous emission (ASE) noise from optical amplifiers and nonlinear distortions from Kerr nonlinearity, degrade the signal-to-noise ratio (SNR) and thus, the bit-error-rate (BER), beyond acceptable limits. As in [9], we term these types of blocking as *capacity blocking* and *reach blocking*, respectively.

Standard approaches to solve the RMLSA problem establish end-to-end all-optical communication (i.e., transparent) relying only on erbium-doped fiber amplifiers (EDFAs) to compensate losses between source and destination nodes [5], [7], [8], [12]–[16]. In these cases, reach blocking has been the central problem in wide-area networks [5], [7]–[9]. This situation can be mitigated by increasing the maximum transmission reach of optical signals. Most alternatives include equipping the network with distributed fiber Raman amplifiers (DFRA) or hybrid Raman/EDFA fiber amplifiers (HFA) [17], and 3R (re-amplification, re-timing, and re-shaping) signal regeneration in some (or all) network nodes [9], [18]. There have been other proposals to extend optical transmission reach [19], [20], but they do not outperform the use of HFA [20], or may not be practical to implement [19].

Previous works studying amplification schemes and regeneration in optical networks have either focused on:

- 3R regenerators/HFA placement or assignment techniques for improving network performance or minimizing network cost [18]–[23],
- impact evaluation of different amplification schemes or 3R regeneration on the network performance, assuming a given placement technique [9], [24]–[27].

In the first case, strategies that selectively upgrade EDFA-based line optical amplifiers to HFA to reduce network cost (in terms of the required number of 3R regenerators) [20], [22] or blocking probability [19] have been proposed in fixed-grid WDM network scenarios. In EON scenarios, various algorithms have been proposed to solve the regenerator placement problem aiming to reduce power consumption [18] or reducing blocking probability [21]. Additionally, a solution for the regenerator assignment problem in dynamic EONs was proposed in [23], aiming to minimize the number of 3R regenerators and frequency slots used.

In the second case, previous studies demonstrate that the use of HFA reduces spectral occupancy (i.e., more connections can be accommodated with the same capacity) compared to pure EDFA in static EON architectures [24], [25]. In dynamic EON scenarios, it has been shown that the blocking probability can be decreased using 3R regenerators [9], [26]. However, the addition of regeneration devices exhibits diminishing returns in terms of blocking gain [27].

To the best of the authors' knowledge, previous research has not compared the performance of pure amplification schemes and the use of 3R regenerators in dynamic EON architectures. Neither have they evaluated the trade-off between the performance and cost of both cases. Such research can be beneficial for network operation and design by providing elements that help the decision-making related to what devices to deploy to increase optical reach in elastic optical networks.

In this work, we study the impact of using different amplification schemes and 3R regeneration on the blocking probability, energy consumption, and spectral and energy efficiency of dynamic EONs on two network configurations: transparent and translucent. The transparent network configuration used different amplification schemes (all-EDFA, HFA, or all-DFRA) without 3R regenerators, while the translucent one uses only 3R regenerators and EDFAs. The comparative study models the physical layer for all network configurations determining optical signals' maximum transmission reach. This information is then fed to an RMLSA algorithm operating in a dynamic scenario. As a case study, we quantify the network performance of the different configurations in the NSFNet and UKNet topologies.

The remainder of this paper is structured as follows: Section II describes the physical layer model used in this work. Next, Section III presents the methodology used to compare the different network configuration scenarios, which includes the performance metrics, the RMLSA algorithm and, the network simulator tool. Numerical results are then presented in Section IV. Finally, conclusions and remarks are provided in Section V.

II. PHYSICAL LAYER MODEL

This section describes the amplification and regeneration network configurations studied throughout this work and the model used to calculate the maximum achievable reach of optical signals.

A. NETWORK CONFIGURATIONS

We consider five different network configurations, each associated with a network configuration identifier (NCI). Configurations 1-4 correspond to transparent configurations, and configuration 5 is translucent.

a: TRANSPARENT CONFIGURATIONS

In transparent configurations, information is transmitted from source to destination entirely in the optical domain, implying that all intermediate operations, such as switching and amplification, are optical. Fig. 1 **(a)** shows a schematic of the transparent link configuration: the signal is optically transmitted through N spans with switching occurring at intermediate nodes if required. Each span is a segment (typically between 80 and 100 km long) made of standard single-mode fiber (SSMF) plus one amplification point. Although this figure only shows one switching point (OXC box in the middle of the two depicted spans), a signal can be switched at several points along the path or not switched at all if an optical fiber link directly connects the source and destination nodes. Optical amplification for one span can have one of the following configurations:

- *NCI* 1 (all-EDFA): at the end of each span an EDFA is placed to compensate for the losses, as shown in Fig. 1 **(b)**.
- *NCI* 2 (HFA): a Raman pump provides distributed Raman gain G_R, followed by an EDFA with gain G_E, recovering the residual loss. The total gain of the HFA is $G = G_R G_E$. This configuration is shown in Fig. 1 **(c)**, characterized by the Raman gain ratio (Γ_R) corresponding to the percentage of the total gain (in dB) compensated by the Raman amplifier. Note that the cases when $\Gamma_R = 0$ and $\Gamma_R = 1$ correspond to all-EDFA and all-DFRA, respectively.
- *NCI* 3 (all-DFRA): a Raman pump is used to provide gain in each span, as shown in Fig. 1 **(d)**.
- *NCI* 4 (alternating spans): one span uses EDFA and the one immediately after uses DFRA, as shown in Fig. 1 **(e)**.

b: TRANSLUCENT CONFIGURATION

In translucent communications, data is transmitted from source to destination using at least one optoelectronic conversion device. In our case, we use 3R regeneration devices for increasing the optical reach in intermediate nodes, as displayed in Fig. 2. Therefore, the fifth and last configuration is as follows:

- *NCI* 5 (translucent): the information transmitted from source to destination is regenerated in an intermediate node using a 3R regenerator equipped with optoelectronic conversion. As shown in Fig. 2, in this configuration, all-EDFA is used in each span.

The configurations selected for this study were chosen for the following reasons: NCI 1 because EDFA is the most used technology for the deployment of optical links [28], NCI 2 and 3 due to the benefits presented by Raman amplification in hybrid schemes and to a greater extent individually, in terms of noise accumulation [17], [29], NCI 4 as an intermediate alternative between NCI 1 and 3 with improved blocking rate without significant energy consumption increase, and NCI 5 with all-EDFA amplification in order to avoid combining two elements with high energy consumption and costs such as regenerators and DFRA [18]–[20].

B. OPTICAL TRANSMISSION REACH MODEL

We assumed that signals are degraded by ASE and nonlinear interference (NLI) noise to calculate the maximum distance achievable by any given modulation format. Other fiber impairments, such as chromatic and polarization mode dispersion, are assumed to be compensated for using digital signal processing [30]. Furthermore, we assume that all network components are carefully designed to avoid any additional sources of signal degradation.

We evaluate the signal QoT of each optical path in terms of its received SNR [30]:

$$SNR = \frac{P_{in}}{P_{ASE} + \psi_{NLI} P_{in}^3}, \tag{1}$$

where P_{in} is the input signal power, P_{ASE} is the ASE noise power over the signal bandwidth, and ψ_{NLI} is the NLI coefficient.

The total ASE noise at the receiver was calculated using [31]:

$$P_{ASE} = N_s F_{eq} h v \Delta_{ref} (G - 1), \tag{2}$$

where N_s is the number of spans, F_{eq} is the equivalent amplifier noise figure, h is Planck's constant, v is the carrier frequency, Δ_{ref} is the signal bandwidth and G is the amplifier gain.

For each amplifier configuration F_{eq} takes a different value. We denote by F_{EDFA}, F_{DFRA}, and F_{HFA} [32] the equivalent noise figure of the EDFA, DFRA, and HFA amplifiers, respectively. The right column of Table 1 shows the values used for F_{EDFA}, F_{DFRA} and F_{HFA}. F_{EDFA} is used in NCI 1 and NCI 5 for each span and in NCI 4 for spans using EDFA. F_{HFA} is used in NCI 2 for each span, depending on Γ_R value. F_{DFRA} is used in NCI 3 in each span and NCI 4 in spans using DFRA. In every network configuration (NCI 1 - 5), the amplifiers were set to compensate for the loss of one span and include a 2 dB of margin, thus $G = exp(\alpha L) \cdot 1.58$, where α is the fiber attenuation coefficient, and L is the span length. The values of α and L can be found in the left column of Table 1. Finally, for calculating the maximum distance achievable by optical signals, it is assumed that links are made of identical fiber spans.

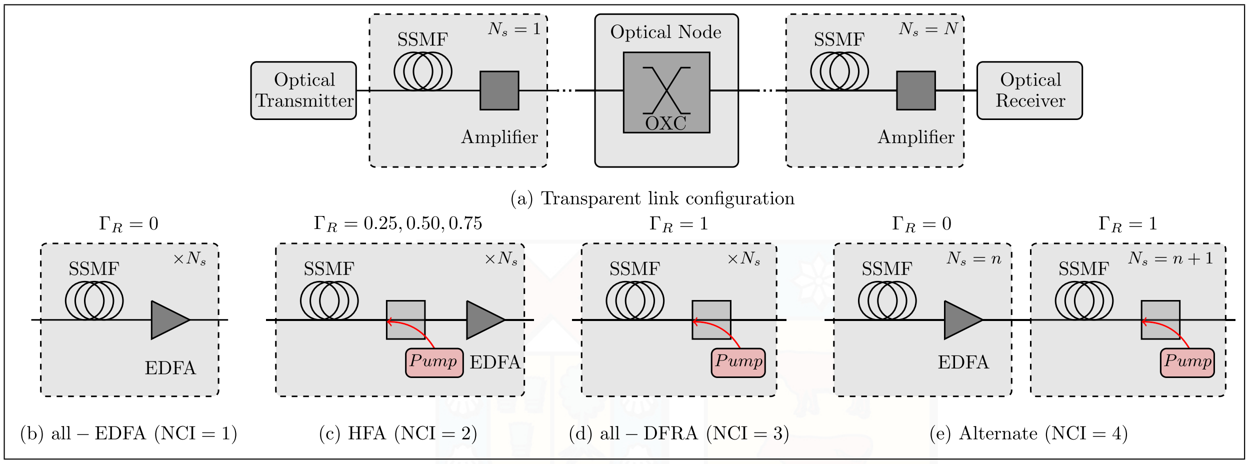

FIGURE 1. Transparent configuration. (a) Transparent link configuration. (b)-(e) Span configuration for different amplification configurations (NCI 1-4).

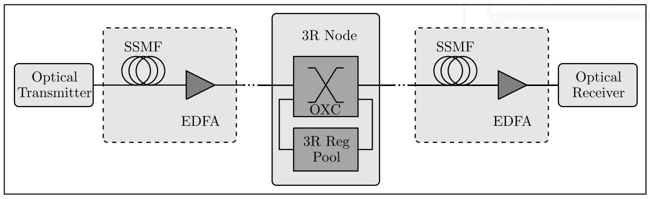

FIGURE 2. Translucent link configuration (NCI 5).

The NLI coefficient, ψ_{NLI}, is given by the product $N_s\psi_{NLI}^{1\ span}$ [30], [33] assuming incoherent NLI accumulation, where $\psi_{NLI}^{1\ span}$ is the NLI coefficient in a single span. The ψ_{NLI} coefficients were estimated using the conventional GN model [30] when EDFA amplification is used (NCI 1, 4 and 5) and a closed-form approximation from [29] for the configurations using HFA (NCI 2) and DFRA (NCI 3 and 4). The right column of Table 1 lists the value of ψ_{NLI} for 1 span for the different network configurations. We denote by $\psi_{NLI-EDFA}$, $\psi_{NLI-DFRA}$ and $\psi_{NLI-HFA}$ the NLI coefficients when EDFA, DFRA, and HFA amplification is used, respectively. The value $\psi_{NLI-EDFA}$ is used in each span in NCI 1 and NCI 5 and only in the spans using EDFAs in NCI 4. The value $\psi_{NLI-HFA}$ is used in each span in NCI 2, according to the value of Γ_R. Finally, the value $\psi_{NLI-DFRA}$ is used in each span in NCI 3, and in the spans using DFRA in NCI 4. Since the value of the NLI coefficient depends on the optical bandwidth used, the calculation of it considered a fully-loaded C-band with an optical bandwidth of 4 THz divided in 320 FSUs of 12.5 GHz each.

PM-QPSK, PM-16-QAM, and PM-64-QAM are the available modulation formats within the flexible transceivers, each with a target pre-FEC BER of $4.7 \cdot 10^{-3}$ using 6.25% overhead [34]. In this case, the bit rates allowed by each modulation format on an optical channel with a bandwidth of one FSU are 46, 92, and 140 Gb/s for PM-QPSK, PM-16-QAM and PM-64-QAM, respectively.

TABLE 1. Fiber and signal parameters for maximum achievable reach calculation for every NCI.

Fiber and signal parameters		*Amplifier parameters*	
		F_{EDFA}	5 dB
α	0.0507 Np/km	$F_{HFA-\Gamma_R=0.25}$	1.12 dB
α_p	0.0553 Np/km	$F_{HFA-\Gamma_R=0.50}$	-1.52 dB
β_2	-21.3 ps^{2}km^{-1}	$F_{HFA-\Gamma_R=0.75}$	-3.33 dB
γ	1.3 W^{-1}km^{-1}	F_{DFRA}	-4.71 dB
Δ_{ref}	12.5 GHz	g_R	0.4 W^{-1}km^{-1}
L	100 km	$\psi_{NLI-EDFA}^{1\ span}$	0.0097 mW^{-2}
v	193.5 THz	$\psi_{NLI-HFA(\Gamma_R=0.25)}^{1\ span}$	0.0105 mW^{-2}
R	12.5 GBaud	$\psi_{NLI-HFA(\Gamma_R=0.50)}^{1\ span}$	0.0106 mW^{-2}
BW	320 FSUs	$\psi_{NLI-HFA(\Gamma_R=0.75)}^{1\ span}$	0.0113 mW^{-2}
		$\psi_{NLI-DFRA}^{1\ span}$	0.0149 mW^{-2}

The maximum achievable reach (MAR) for each modulation format was defined as the maximum distance that the optical signal can be transmitted at optimum power before exceeding the target BER. Based on that target BER, the SNR thresholds for each modulation format were determined: 8.5, 15.5, and 21 dB for PM-QPSK, PM-16-QAM, and PM-64-QAM, respectively. The calculated MAR values for the available modulation formats are listed in Table 2. The values reported have been rounded down to the closest multiple of the span length. The MAR represents the distance constraint in the modulation level selection in the RMLSA algorithm. All fiber parameters used for the calculations of the maximum achievable reach used throughout this work are listed in Table 1 where parameters α_p, β_2, γ, R, and g_R are the pump attenuation coefficient, group velocity dispersion coefficient, nonlinear coefficient, symbol rate, and Raman gain coefficient, respectively.

III. METHODOLOGY

In this section, we describe the methodology used for the comparison of NCI 1-5, described in Section II. The network performance metrics are described in Subsection III-A (blocking probability, energy consumption, and spectral and

TABLE 2. **Maximum achievable reach (in km) for various modulation formats, using BER = $4.7 \cdot 10^{-3}$ and 320 FSUs optical bandwidth for every NCI.**

Modulation format	$NCI\ 1,5$ $\Gamma_R = 0$	$NCI\ 2$ $\Gamma_R = 0.25$	$NCI\ 2$ $\Gamma_R = 0.50$	$NCI\ 2$ $\Gamma_R = 0.75$	$NCI\ 3$ $\Gamma_R = 1$	$NCI\ 4$ *Alternate*
PM-QPSK	2900	5200	7800	10100	11400	4600
PM-16-QAM	500	1000	1500	2000	2200	800
PM-64-QAM	100	200	400	500	600	200

energy efficiency). The RMLSA algorithm and the simulation scenario are explained in subsections III-B and III-C, respectively.

A. PERFORMANCE METRICS

We define three performance metrics for evaluating all amplification/regeneration configurations on dynamic elastic optical networks.

1) BLOCKING PROBABILITY

The network must be designed so that the blocking probability does not exceed a threshold value. In wide-area elastic optical networks, a request can be blocked due to one of the following situations: First, lack of available resources (FSUs) on the selected path. Second, the selected route has enough FSUs to accommodate the request, but the optical signal cannot reach the destination since it does not meet the quality of transmission (QoT) required. We term these two blocking events as Capacity Blocking ($\mathcal{CB}$) and Reach Blocking ($\mathcal{RB}$), respectively.

Blocking events are recorded as follows. First, resource availability is checked. If resources are not available, the request is considered to be blocked due to the lack of capacity, and QoT is not evaluated. Once resource availability has been confirmed, QoT is evaluated. If the QoT requirements are not met, the request will be blocked and the event will be recorded as a reach blocking event. In this way, the overall blocking probability ($\mathcal{B}$) can be computed as the sum of these two blocking events:

$$\mathcal{B} = \mathcal{CB} + \mathcal{RB}. \qquad (3)$$

2) ENERGY CONSUMPTION

The main drawback of the network configurations used to extend the reach of an optical connection described in Section II is their high energy consumption, leading to a trade-off between blocking probability and energy consumption. This work analyzes the energy consumed by each NCI configuration considering the optical amplifiers in the transparent configurations and 3R regenerators and optical amplifiers in the translucent case. We assume that the energy consumed by network elements different from amplifiers and regenerators (e.g., optical transceivers and switches) remains constant during network operation.

The total energy consumed by a given network configuration, E_{NCI}, is the sum of the energy consumed by the amplifiers and the regenerators over the observation time:

$$E_{NCI} = \sum_{span} P^e_{AMP} T + \sum_{connection} P^e_{RGN} \tau, \qquad (4)$$

where the first term on the right side of the equation corresponds to the energy consumed by the optical amplifiers for a given NCI during the observation time T, and the second term is the energy consumed by all connections using a regeneration device.

In Eq. (4), P^e_{AMP} corresponds to the electrical power consumed by an optical amplifier, T is the cumulative work time, P^e_{RGN} is the electrical power consumed by a regenerator for a single connection, and τ is the holding time of the regenerated connection. Note that the amplifier power consumption is time-independent due to the fully loaded system assumption described in the physical layer model. The E_{NCI} value in Eq. (4) is expressed in Joules [J].

The power consumption of optical amplifiers depends on the network configuration selected. We use the model for HFA presented in [19], [35] which describes the behavior of all configurations studied herein. We calculate the power consumption of an optical amplifier for a single span using:

$$P^e_{AMP} = \frac{1}{\eta_{EDFA}} N_{ch} P_{ch} \left(1 - \frac{1}{G_E}\right) + \frac{N_R}{\eta_R} \frac{\ln(G_R)}{g_R L_{eff}}, \qquad (5)$$

where η_{EDFA} and η_R are the power conversion efficiency for EDFA and Raman amplifiers, respectively; N_{ch} and P_{ch} are the number and power for the channels amplified by the EDFA; and N_R, g_R, and L_{eff} are the Raman pump multiplicity, Raman gain coefficient, and effective amplification length, respectively. The first term on the right side of Eq. (5) corresponds to the electrical power required to pump the EDFA section with a G_E gain value. The second term is equivalent for the Raman amplifier with a gain G_R. In all-EDFA (NCI 1) and all-DFRA (NCI 3) configurations, the second and first terms of the right side of Eq. (5) are equal to 0, respectively.

The power consumption of 3R regenerator devices varies depending on the data rate of the regenerated signal. Here we assume that a regenerator consists of a variable bandwidth receiver and a transmitter in a back-to-back configuration. The model used to describe the electrical power consumption of a regenerator as a function of the bit rate [36]–[38] is as follows:

$$P^e_{RGN} = K_1 \times B_{sd} + K_2, \qquad (6)$$

where K_1 is a power scaling factor related to the transmission bit rate and the required DSP, B_{sd} is the bit rate of a connection request between nodes s and d, and K_2 is a constant consumed power related to the operation of the optical source and analog components. The values used for the constant values K_1 and K_2 depend on the studied transceiver, and different values are observed within the literature. The study from [36] is commonly used within the EON literature. In this case K_1 and K_2 correspond to 1.683 W/Gb/s and 91.3 W, respectively [36]–[40], representing a power consumption of 260 W for a 100 Gb/s transmission. However, these values correspond to a study from 2010 [40]. Thus the advances in transceiver manufacturing are not considered. We additionally consider a CFP digital coherent optical (DCO) transceiver, where K_1 and K_2 are equal to 0.105 W/Gb/s and 21.5 W [41], [42], respectively. That presents a maximum power consumption of just 32 W for 100 Gb/s transmission, eight times lower than the power consumption of devices from 2010.

3) SPECTRAL AND ENERGY EFFICIENCY

We study the efficiency of each network configuration using the network spectral efficiency (SE) and the energy efficiency (EE) metrics. Both metrics, SE and EE, are associated with the cost incurred to operate the network for a target throughput. SE indicates how well the spectral resources of the network are utilized and EE how much energy is required to operate the network.

SE is defined as the ratio between the total network throughput and the allocated spectrum during an observation period [43]. The network throughput is calculated as the sum of the bit rates of all established connections during the observation time T. The allocated spectrum is the sum of the required bandwidth for all connections.

$$SE = \frac{\sum_{\forall(s,d)} B_{sd} \cdot \tau}{\sum_{\forall(s,d)} \Delta f_{sd} \cdot \tau}, \tag{7}$$

where Δf_{sd} is the optical bandwidth in Hz allocated to connection (s, d), equal to the number of FSUs required by connection (s, d) multiplied by the spectral width of an FSU.

EE is the energy required to achieve a given network throughput during an observation time T. It is expressed in J/s, and it represents the energy-per-bit, a fundamental unit to measure energy efficiency in digital communications [44], [45]. It was calculated as follows:

$$EE = \frac{E_{NCI}}{\sum_{\forall(s,d)} B_{sd} \cdot \tau}, \tag{8}$$

where E_{NCI} is the energy consumption of amplifiers and regenerators of a given network configuration (Eq. (4)).

B. RMLSA ALGORITHM

The RMLSA algorithm used was presented in [9]. The algorithm establishes connections taking into account a given BER threshold. Fig. 3 shows a high-level description of the main steps executed by the RMLSA algorithm. In it, connection requests generated in transparent network configurations (NCI 1-4) are processed executing Stage A only, and connection requests generated in the translucent network configuration (NCI 5) are processed executing Stages A and B.

Upon receiving a connection request between nodes s and d with a bit rate of $B_{s,d}$, the algorithm attempts to establish a transparent connection (Stage A). The algorithm looks for available capacity in the candidate K shortest paths ($K - SP_{s,d}$) in increasing order of length. These routes have been previously calculated using the Dijkstra algorithm [46]. With each attempted route, the algorithm determines the modulation format that requires the lowest number of FSUs while having an optical reach greater than or equal to the length of the selected path. Next, the spectrum allocation is performed by executing the First-Fit (FF) algorithm, which exhibits a good trade-off between performance and computational complexity [9]. If the connection cannot be established after attempting all paths, the request is rejected (for NCI 1-4), or Stage B is activated to attempt to establish a translucent connection using one regenerator in the path (for NCI 5).

In Stage B, it is assumed that all network nodes are equipped with the same number of 3R regenerators and that they are used only if a connection request cannot reach the destination due to limited MAR or if the capacity on the path is not continuous or contiguous. The algorithm attempts to establish a translucent connection in one of the K shortest paths, in increasing order of length. In that case, the path is divided into two segments as described in [9], using the regenerator allocation algorithm based on the First Longest Reach Regenerator (FLR) policy [47]. If the node between both segments has at least one regenerator available, then the algorithm allocates resources for the first segment. If this allocation is successful, then the resource assignment for the second segment is attempted. It is assumed that the regeneration device can convert the modulation format and change the spectral position if required. If the connection between the nodes s and d cannot be established using these two segments in the candidate path, the algorithm attempts establishing the connection using a new pair of segments. This procedure is repeated until the connection can be established, or all segment combinations in the candidate path have been unsuccessful. If the translucent connection cannot be established in the shortest path, Stage B is re-started considering the following shortest path until every path in $K - SP_{s,d}$ has been evaluated. If none of these attempts is successful, then the connection request is finally rejected.

C. SIMULATION SCENARIO

The network performance was evaluated using an event-driven simulator built in C++. The operation of a flexible optical network was simulated considering as inputs: the network NCI, the network topology, the FSU capacity per link, the RMLSA algorithm, the number of regenerators per node, the set of bit rates and modulation formats supported by nodes, the optical reach table (MAR) of different network configurations and the number of FSUs required by different modulation formats and bit rates (Table 3). Table 4 lists the values of all the input data parameters used in the simulation.

Each event in the simulator represents a connection request or release. Each connection request is defined by a source-destination pair and a bit rate. All possible source-destination pairs generate traffic according to an ON-OFF traffic model, that assumes limited traffic sources, in which a maximum of one connection is established between each node pair at any time. That is, if successfully established, the connection is active during the ON time. During the ON period, the source

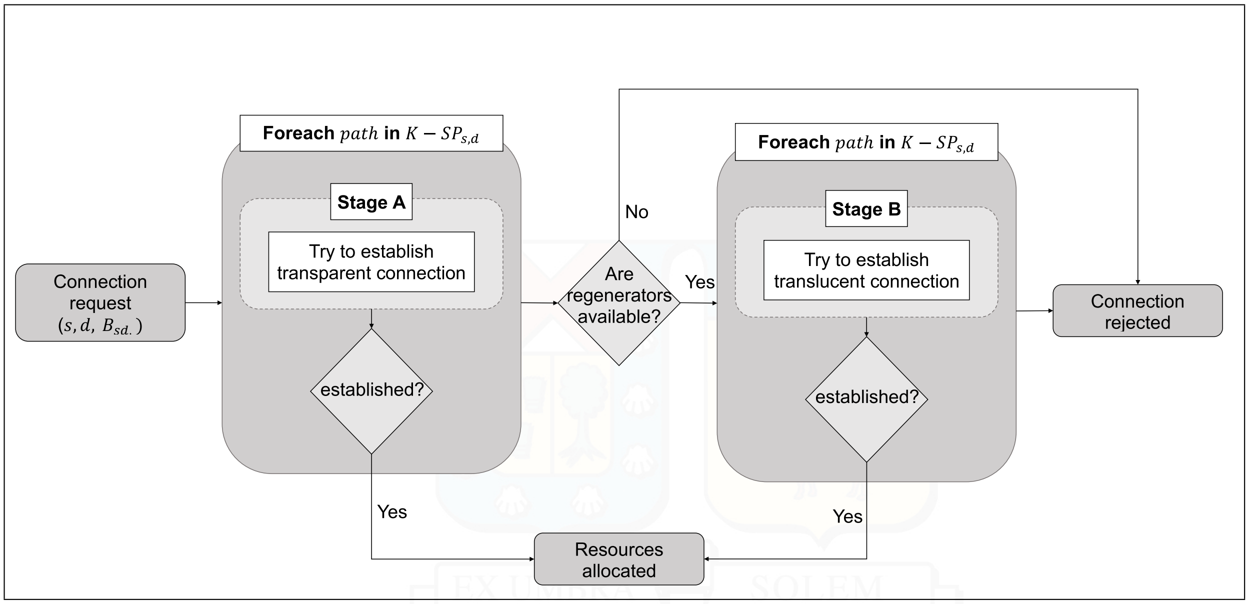

FIGURE 3. RMLSA flowchart.

transmits at the requested bit rate. After this time, a connection release event is generated, and the simulator releases the corresponding allocated resources. The connection is then inactive during the OFF time, after which a new connection request event for this specific source-destination pair is generated. Each time a new request event is generated, its bit rate is uniformly selected from the set of available bit rates listed in Table 4.

The ON and OFF periods are assumed to be exponentially distributed, with mean values denoted by τ and t_{OFF}, respectively. The network traffic load, denoted by ϱ, is given by:

$$\varrho = \frac{\tau}{\tau + t_{OFF}}. \tag{9}$$

For each value of traffic load studied, the simulator output data (number of connections established, number of connections rejected, and utilization of FSU and regenerators) is then used to calculate the blocking probability, the energy consumption, and the spectral and energy efficiency of each network configuration.

TABLE 3. Spectrum requirements in terms of FSUs for each bit rate and modulation format pair.

Modulation format	*Bit rate*				
	10 Gb/s	40 Gb/s	100 Gb/s	400 Gb/s	1000 Gb/s
PM-QPSK	1	2	4	16	40
PM-16-QAM	1	1	2	8	20
PM-64-QAM	1	1	2	6	14

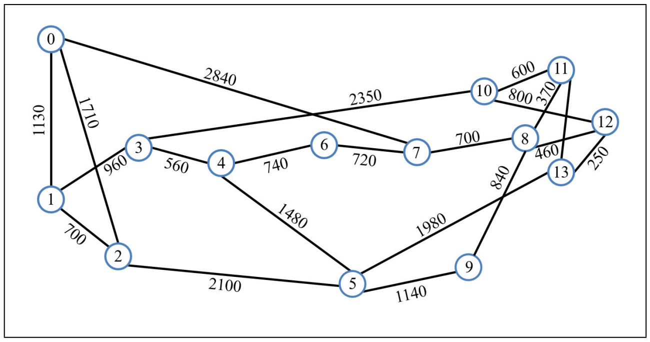

FIGURE 4. NSFNet network topology with the lengths of every optical link (in km).

IV. RESULTS

The performance of the different network configurations NCI 1-5 was evaluated employing simulation. We use Raman gains coefficient of 0.25, 0.50 and 0.75 for NCI 2 configuration, and 1, 3, 5, and 10 3R regenerators per node for NCI 5 scenario. Network simulations were run using the NSFNet topology, shown in Fig. 4. The values of the input data required for the network simulator are summarized in Table 4. For every network configuration, the blocking probability, the energy consumption, and the spectral and energy efficiency were evaluated. Additionally, simulations were carried out using the UKNet network topology with shorter links compared to NSFNet. UKNet presents a network diameter of 1000 km. Overall, the same trend in the results for NSFNet was observed in the UKNet. Due to space constraints, in this paper, we present the results obtained for the NFSNet topology only. Data supporting the results of both network topologies can be found in https://iro-team.gitlab.io/IA3R_ext.pdf.

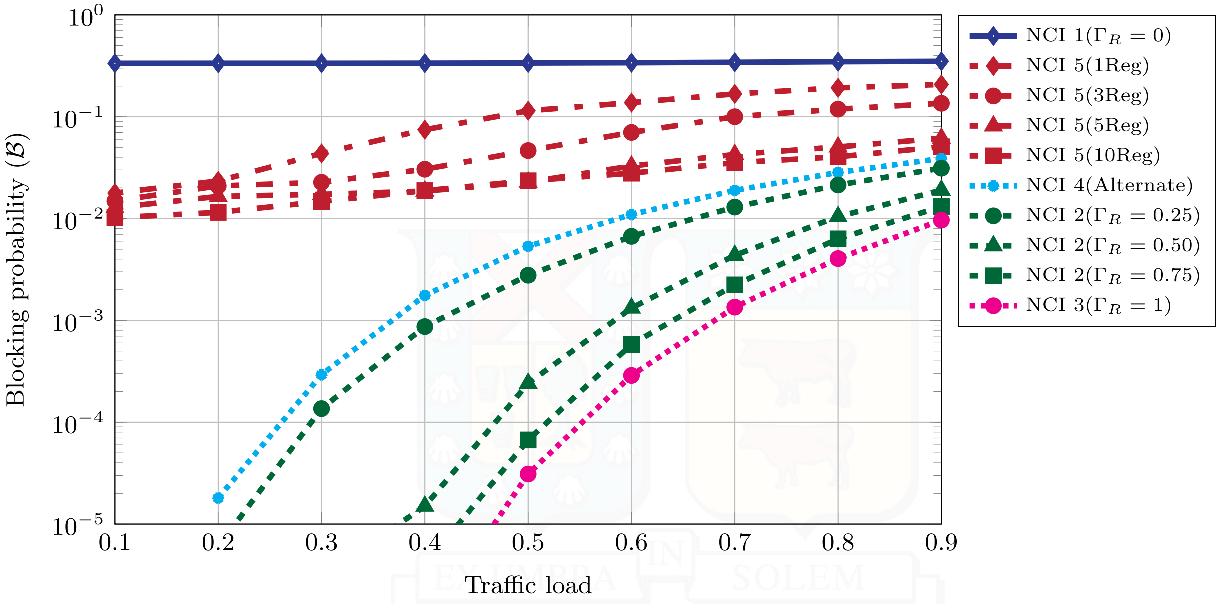

FIGURE 5. Blocking probability for the network for all network configurations.

TABLE 4. Simulation parameters.

Parameters	*Value*
Resource allocation algorithm	Fig. 3
Spectrum Requirements	Table 3
BER threshold	$4.7 \cdot 10^{-3}$
Topology	NSFNet (Fig. 4)
Number of connection requests	10^7
Traffic Load	0.1 – 0.9
Number of FSU by link	320
Bit rates [Gb/s]	10, 40, 100, 400 and 1000
Modulation Formats	PM-QPSK, PM-16-QAM, PM-64-QAM
MAR for all NCI	Table 2
Regeneration devices per node	1, 3, 5 and 10
T	1000 t.u
τ	1 t.u

A. BLOCKING PROBABILITY

Fig. 5 shows the network blocking probability for all the studied network configurations as a function of the traffic load.

NCI 1, based on all-EDFA amplification, exhibits the worst performance of the studied cases with an average blocking probability of $3.3 \cdot 10^{-1}$ for all traffic loads. The fact that the blocking does not change with the traffic load suggests that the main reason for blocked requests, in this case, is the limited reach offered by the modulation formats under consideration.

NCI 5 exhibits a lower blocking than NCI 1, despite having the same optical reach. The lower blocking of NCI 5 is achieved thanks to the use of 3R regenerators: some connections with limited optical reach (that would have been blocked in NCI 1) can still be established in NCI 5 by regenerating the signal at an intermediate node along the route. Besides, the better blocking performance of NCI 5 compared to NCI 1, is still worse than the remaining transparent schemes. It can be seen that although a higher number of regenerators reduces the blocking probability, the addition of more than three devices per node offers diminishing returns, and the improvement in the blocking ratio is marginal. For example, considering a traffic load of 0.3, increasing the number of regenerators per node from 3 to 10 only decreases the blocking probability from $3.0 \cdot 10^{-2}$ to $1.5 \cdot 10^{-2}$.

NCI 4, corresponding to the alternate span configuration, offers a reduced blocking probability than NCI 1 and NCI 5. For example, considering a traffic load of 0.3, the blocking probability using NCI 4 was $2.93 \cdot 10^{-4}$, almost three orders of magnitude less than NCI 1 and one order of magnitude lower than NCI 5 (average value of $2.45 \cdot 10^{-2}$). This behavior is obtained due to the increased reach for all modulation formats compared to NCI 1 and 5, as seen in Table 2.

NCI 2 and 3 present a significant improvement in the blocking probability compared to the other studied configurations. For NCI 2, 3 different Raman gain ratios (Γ_R) were studied: 0.25, 0.50 and 0.75. It can be seen that as Γ_R is increased, the blocking probability is reduced. For example, considering a traffic load of 0.3, a blocking probability of $1.36 \cdot 10^{-4}$, $3 \cdot 10^{-6}$, $4 \cdot 10^{-6}$ and $1 \cdot 10^{-6}$ was observed for a value Γ_R equal to 0.25, 0.50, 0.75 and 1, respectively. Two main reasons explain this behavior: Firstly, the increase in the MAR (see Table 2) reduces the number of connection requests blocked due to the inability to reach their destination; secondly, the extended MAR for all modulation formats allows the users to employ high order formats (that require a lower number of FSUs, as shown in Table 3) and thus, the blocking ratio is reduced due to increased spectrum availability.

Finally, we studied the source of blocking for all NCIs. Results are shown in Fig. 6. Each network configuration

3 bars are shown, corresponding (from left to right) to traffic loads of 0.3, 0.5, and 0.8, respectively. The main cause of blocking for NCI 1 is the limited MAR for all modulation formats for all studied traffic loads. Only at a traffic load of 0.8 capacity blocking is observed for NCI 1, with a value of $1.65 \cdot 10^{-2}$. On the contrary, lack of available capacity is the only cause of blocking for NCI 2, NCI 3, and NCI 4. Note that following the trend observed in Fig. 5, the blocking ratio increases with the traffic load. For NCI 2-4, the MAR is enough to establish every connection request independent of the traffic load. The blocking performance of NCI 5 is due to a mix of limited reach and capacity, but reach blocking dominates the performance. As the number of available regenerators increases, a decrease of reach blocking is observed for all traffic loads, as more connections can reach their destination using them. As reach blocking is reduced, an increment in capacity blocking is observed in NCI 5, when more connections are established in the network.

The difference in performance between the transparent (NCI 2-4) and translucent (NCI 5) solutions to improve the transmission reach is because a regenerator can only serve a single user at a time to extend its transmission reach. This situation means that only a limited number of connections can be established using regenerators, and other requests that cannot reach their destinations are blocked. On the other hand, NCI 2-4 offers lower noise accumulation across the entire available spectrum, improving the quality of service for all network users.

B. ENERGY CONSUMPTION

To evaluate the network's energy consumption, we evaluate the simulation after 1000 time units for every NCI under investigation for traffic loads of 0.3, 0.5, and 0.8. We define the duration of a single time unit as 1 second; thus, $T = 1000$ s and $\tau = 1$ s were used to evaluate the total energy consumption. As stated in Section III, only the energy consumed by the optical amplifiers and regenerators was considered for this analysis, assuming that the energy consumption of all other network elements in the different network configurations does not change. To evaluate the consumption of the amplifiers using Eq. (5) N_R was set as 2, conventionally used to pump the C-band, and power conversion efficiencies for EDFA (η_{EDFA}) and Raman (η_R) of 5% and 3% were assumed as in [35].

Fig. 7 shows the total energy consumed by amplifiers and regenerators for each network configuration, where Fig. 7 **(a)** shows the transparent cases (NCI 1-4) and Fig. 7 **(b)** shows the translucent cases (NCI 5). For NCI 1-4, the energy consumption is independent of the network's traffic load, as the amplifiers were assumed to provide gain over the entire available spectrum. NCI 1 exhibits the lowest energy consumption of 2.7 MJ due to the high power efficiency of EDFA amplifiers. NCI 2 and 3, representing scenarios with increased Raman gain ratio values, present a linear increase in consumed energy with values ranging from 5.7 to 14.1 MJ. NCI 4 exhibits an energy consumption of 9.2 MJ, comparable to NCI 2 with $\Gamma_R = 0.50$. The high energy consumption of NCI 4 arises from the spans amplified purely by the Raman amplifier. Note that this high energy consumption leads to a better blocking performance compared to NCI 1. However, it offers a higher blocking probability than any NCI 2 studied, as seen in Fig. 5.

For all network configurations using DFRA (NCI 2-4), the high energy consumption is related to the Raman gain coefficient of a single-mode fiber. As stimulated Raman scattering is a nonlinear effect, high power pumps are required to obtain signal amplification. Typically, Raman pump power can be as high as 500 mW, approximately an order of magnitude higher than EDFA pump power.

Finally, the total energy consumed by NCI 5 depends on the energy consumed by the EDFA amplifiers (same as NCI 1), the number of established connections using regenerators, and their bit rate.

In this configuration, we used two different transceiver models to evaluate the energy consumption of regenerators, as described in Section III. The blue bars in Fig. 7 **(b)** represent the energy consumption when the transceiver model from [36]–[38] is considered, called *Co-BVT* herein. This is the most common model used in previous work evaluating the energy consumption of regenerators and the values considered date from circa 2010. Additionally, the energy consumption of NCI 5 considering state-of-the-art values for the regenerator energy consumption, corresponding to CFP transceivers [41], [42] was studied, called *DCO* herein. The energy consumption of this type of regenerator is shown in red bars in Fig. 7 **(b)**. For a traffic load of 0.3, a low number of connections use the available regenerators. On increasing the number of regenerators per node from 1 to 10, no consumed energy addition is experienced, with a value of 3.6 MJ and 11 MJ for the Co-BVT and DCO transceiver models, respectively. For higher traffic loads, however, different energy consumption is observed when more regenerators are available. The consumed energy increases together with the traffic load and the number of available regenerators due to the higher number of connections using them. For a traffic load of 0.5, the consumed energy increased from 3.9 MJ to 6.1 MJ, and from 10.4 MJ to 22 MJ when 1 and 10 regenerators were available, considering the DCO and Co-BVT transceiver models, respectively.

Two main conclusions can be drawn from the energy consumption using regenerators. Firstly, the significant difference observed between the two transceiver models, which highlights the relevance of using state-of-the-art components, can greatly impact network operation costs. Secondly, the energy consumption only depends on the network traffic load in the translucent scenario, since in the transparent case, no additional equipment is needed at different traffic loads.

C. SPECTRAL AND ENERGY EFFICIENCY

Fig. 8 **(a)** shows the spectral efficiency (SE) achieved by the different network configurations for a traffic load equal to 0.3.

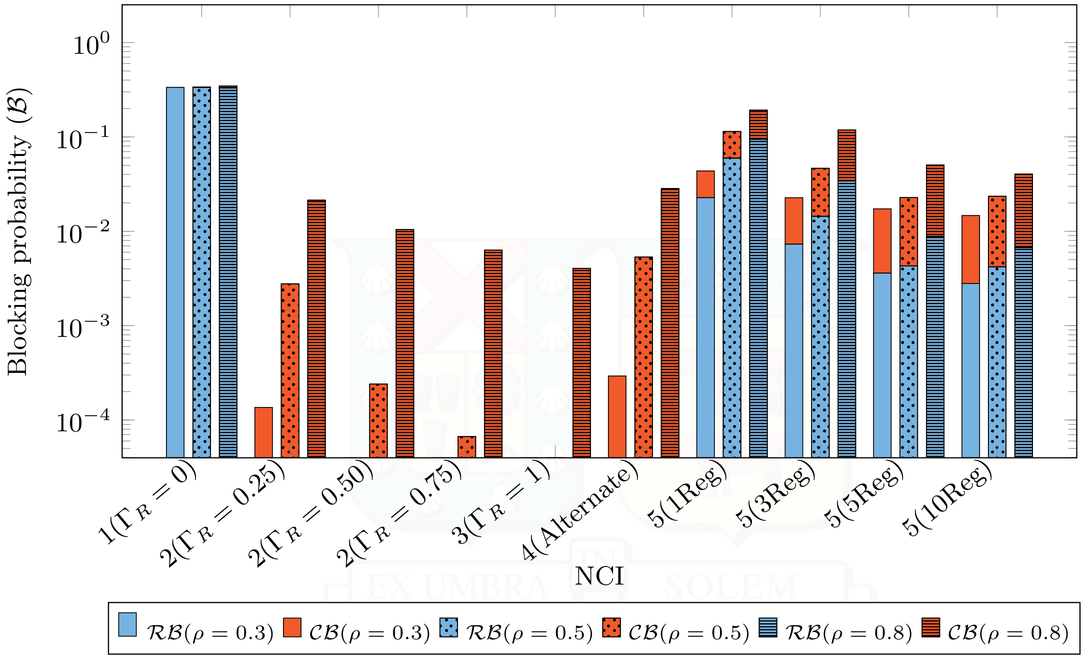

FIGURE 6. **Sources of blocking -reach blocking ($\mathcal{RB}$) and capacity blocking ($\mathcal{CB}$)- for every network configuration.**

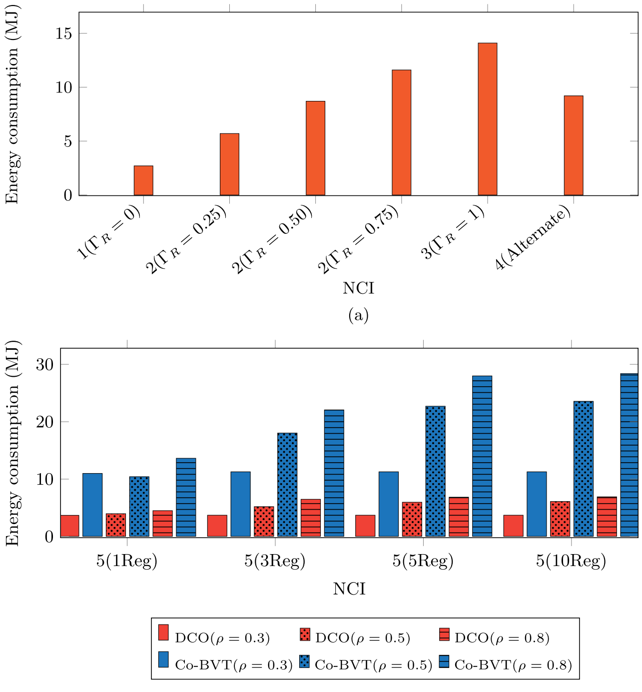

(a)

(b)

FIGURE 7. **Network energy consumption considering $T = 1000$ s.**

Among the transparent network configurations (NCI 1-4), NCI 1 presents the lowest SE, equal to 2.65 b/s/Hz. Compared to NCI 1, SE has increased in NCI 2, 3, and 4 thanks to Raman amplification. The higher the value of the factor Γ_R, the higher the observed SE (with NCI 4 achieving a spectral efficiency similar to NCI 2 with $\Gamma_R = 0.25$).

As shown in Fig. 8 **(b)**, this behavior occurs because the use of a higher Raman gain ratio allows for more efficient modulation formats, as PM-16-QAM and PM-64-QAM, to be used. For example, for NCI 1, only 8% of connections were established using PM-16-QAM, and the remaining 92% of them were established using PM-QPSK. Instead, in the case of NCI 3 ($\Gamma_R = 1$) 51%, 45% and 4% of the connections used PM-QPSK, PM-16-QAM and PM-64-QAM, respectively. These percentages explain the observed increase in the spectral efficiency of the network in NCI 3 compared to the NCI 1 shown in Fig. 8 **(a)**.

Notice that the maximum achievable SE is 3.2 b/s/Hz, which is lower than the SE achieved using QSPK over two polarizations. This value can be explained considering the requested bit rates used in the simulations, the available modulation formats, and the constraints of EONs that an established connection uses a minimum of 1 FSU. The simulated bit rate requests were 10, 40, 100, 400 and 1000 Gb/s. In particular, bit rates of 10, 40 Gb/s require less than a single FSU of optical bandwidth using the modulation formats under consideration, which reduces the overall SE as no other connections are established using the same FSU. Remark that, due to the uniform traffic distribution assumed in this work, 10 and 40 Gb/s represent 40% of the simulated connection requests.

For the translucent configuration (NCI 5), only a slight improvement compared to NCI 1 is observed. In this case, a SE of 2.675 b/s/Hz was obtained, 0.025 b/s/Hz higher than NCI 1. That is, the use of regenerators to increase the reach of a connection does not lead to a more significant usage of more efficient modulation formats, as shown in Fig. 8 **(b)**,

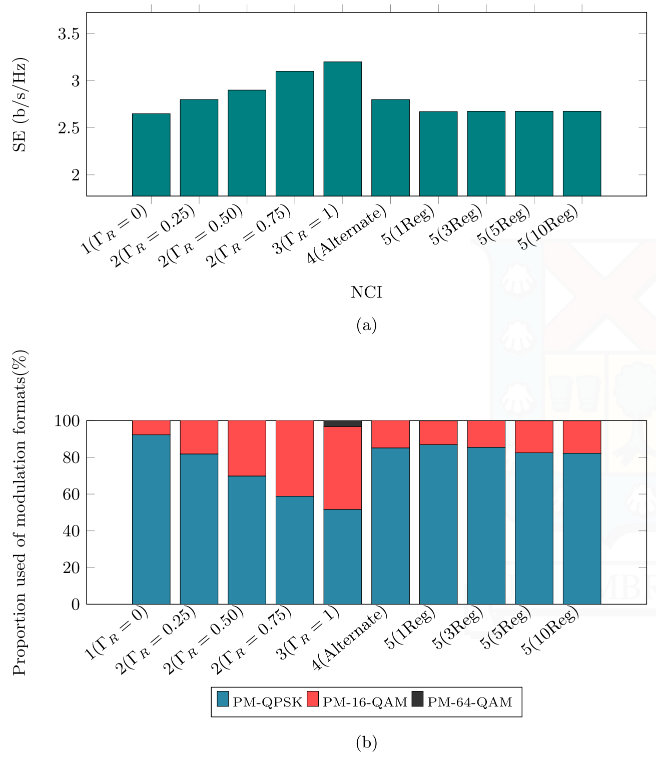

(a)

(b)

FIGURE 8. Spectral efficiency of the network for every NCI for a traffic load of 0.3.

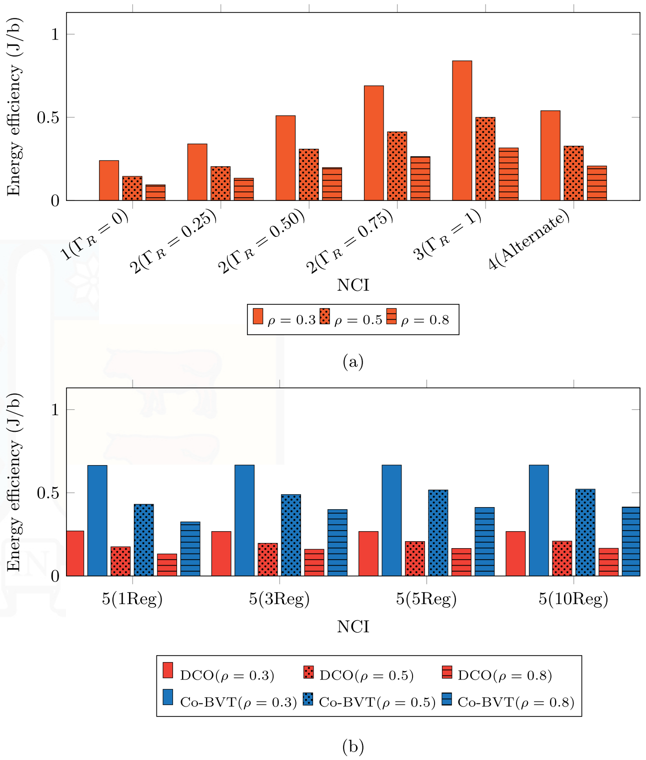

(a)

(b)

FIGURE 9. Energy efficiency of the network for every NCI.

where a maximum of 17% of PM-16-QAM connections is observed for NCI 5. This behavior is explained considering the limited number of regenerators per node, which translates into a maximum number of regenerated connections that can be established simultaneously. Thus, only a fraction of established connections could use modulation formats more efficiently than NCI 1. In particular, approximately 30 % of the established connections use regenerators, and only 30% of those connections can improve their SE using PM-16-QAM due to the reach limitations of the studied formats. The network SE obtained for traffic loads of 0.5 and 0.8 was similar to that shown in Fig. 8 **(a)** for a traffic load of 0.3. In particular, the same trend was observed when changing the NCI.

The energy efficiency of every network configuration is shown in Fig. 9 considering traffic loads of 0.3, 0.5, and 0.8. Fig. 9 **(a)** presents the energy efficiency for NCI 1-4, and Fig. 9 **(b)** for NCI 5. Similar to Fig.7 **(a)**, for NCI 1-4 a higher energy per bit is required as the Γ_R increases from 0 to 1 for all traffic loads. For every NCI, as the traffic load increases, the required energy per bit is reduced due to the greater throughput in the network. As the required energy for the transparent scenarios (NCI 1-4) is constant, the energy efficiency varies only according to the number of established connections.

Unlike amplifiers, regenerators only consume energy when they are operative. As seen in Fig. 7 **(b)**, both the traffic load and the number of available regenerators increase the overall energy consumption, and the number of established connections will determine the energy efficiency. For a traffic load of 0.3, we observe a constant energy per bit of 0.267 and 0.666 J/b for the DCO and Co-BVT, respectively. As the traffic load increments, the required energy per bit is reduced as a greater throughput is established in the network.

Noticeably, NCI 1 presents the best energy efficiency for all traffic loads. However, it offers the highest blocking probability. The use of regenerators (NCI 5) will strongly depend on the deployed technology, with the DCO transceiver offering a consumed energy per bit similar to NCI 1 (0.27 J/b). The Co-BVT presents a consumed energy per bit comparable to NCI 2 with $\Gamma_R = 0.5$, and the latter offers considerably lower blocking probabilities.

D. FINAL CONSIDERATION

The network configuration, in terms of the amplification and regeneration scheme selected, impacts the service performance parameters directly in the service level agreement for optical networks (O-SLA) [48] subscribed between a service provider and a subscriber, in particular the throughput. Since the network operator aims to reduce energy consumption while meeting the specified values of the O-SLA, the best amplification and regeneration scheme will be determined by the quality of service required by connections. For example, in a network serving high-throughput connections, NCI 3 would be the best choice. However, this is also the configuration with the highest energy consumption. Instead, connections with meager throughput requirements could be served with the lowest energy consumption NCI 1.

V. CONCLUSION

We have studied the impact of the physical layer implementation on the blocking probability and energy consumption of dynamic EONs, using two network topologies and considering transparent and translucent network configurations. The transparent configurations were all-EDFA, hybrid Raman-EDFA, all-DFRA, and alternating EDFA and DFRA spans, termed NCI 1-4. The translucent configuration, termed NCI 5, used all-EDFA amplification and a limited number of 3R regenerators in each node.

For NSFNet and UKNet topologies, the blocking probability of NCI 1 was the highest of the studied configurations, followed by NCI 5 and 4. NCI 2 and 3 offered the lowest blocking probability, which decreased as the Raman gain ratio (Γ_R) was increased. For NSFNet, the limited reach dominated the blocking in NCI 1 and 5 (reach blocking) of the available modulations formats, while for NCI 2, 3, and 4, the blocking was driven by lack of capacity (capacity blocking). On the other hand, for UKNet the blocking in all NCI is associated with capacity blocking; due to shorter routes there is no reach blocking, and more complex modulation formats are used. In general, as the blocking probability was reduced, all studied NCI improved their spectral efficiency using more complex modulation formats. For the two topologies, NCI 1 was shown to be the most efficient configuration in terms of energy consumption, while the total consumed energy increased linearly with the Γ_R for NCI 2 and 3. The energy consumption of NCI 4 was shown to be similar to NCI 2 with $\Gamma_R = 0.75$. The use of 3R regenerators in NCI 5 represented an increase in energy consumption relative to NCI 1. In the case of the UKNet, this behavior is observed for moderate to high traffic loads. For low traffic loads, 3R regenerators are not used at all. Furthermore, the technology used in the regenerators has a meaningful impact on the total consumed energy and the energy efficiency of the network. Finally, we identify NCI 2 with $\Gamma_R = 0.25$ as a promising alternative to reduce the blocking probability significantly in wide-area EONs, such as NSFNet, without a prohibitive increase in energy consumption, with a factor of 2.1, and energy efficiency, with a factor of 1.4, compared to NCI 1, as long as the O-SLA requirements are met. Notice that this recommendation is not based on financial considerations. We remark that the financial benefit-cost should inform the final decision made by a network operator of any alternative: an alternative will be feasible only if the financial benefit of decreasing the blocking ratio (due to increased revenue) compensates for the increased cost related to energy consumption.

The above-discussed results have been obtained under simplified models that impose some limitations on the work. Regarding the limitations of the physical layer model, Raman and hybrid amplifiers assume ideal depolarized pump sources and lossless coupling components, which might result in a lower equivalent noise figure than practical components. All network configurations (NCI 1-5) assume that the ASE noise is an Additive White Gaussian Noise process and do not consider wavelength-dependent noise and gain, which might lead to a different reach for every multiplexed channel. Other assumptions described in the manuscript include ideal network components and ideal compensation of linear impairments using digital signal processing. Despite all the mentioned limitations, a 2 dB margin for the amplifier gain in each network configuration was included to reduce the impact of the limitations mentioned herein.

In future work, we will extend our analysis to multiband and multicore transmission systems, two promising alternatives to enlarge the capacity of optical networks. In such systems, new physical impairments need to be considered (stimulated Raman scattering in multiband systems and intercore cross-talk in multicore fibers) that might affect the network performance. We will also focus on including the regenerator/HFA placement problem in the study.

REFERENCES

[1] O. Gerstel, M. Jinno, A. Lord, and S. J. B. Yoo, "Elastic optical networking: A new dawn for the optical layer?" *IEEE Commun. Mag.*, vol. 50, no. 2, pp. 12–20, Feb. 2012.

[2] H. Waldman, "The impending optical network capacity crunch," in *Proc. Int. Opt. Photon. Conf. (SBFoton IOPC)*, Oct. 2018, pp. 1–3.

[3] *Spectral Grids for WDM Applications: DWDM Frequency Grid*, document ITU-T G.694.1, Telecommunication Standardization Sector of ITU, Ginebra, Switzerland, 2012.

[4] B. Chatterjee and E. Oki, *Elastic Optical Networks: Fundamentals, Design, Control, and Management*. Boca Raton, FL, USA: CRC Press, 2020.

[5] A. Fontinele, I. Santos, J. N. Neto, D. R. Campelo, and A. Soares, "An efficient IA-RMLSA algorithm for transparent elastic optical networks," *Comput. Netw.*, vol. 118, pp. 1–14, May 2017.

[6] F. S. Abkenar and A. G. Rahbar, "Study and analysis of routing and spectrum allocation (RSA) and routing, modulation and spectrum allocation (RMSA) algorithms in elastic optical networks (EONs)," *Opt. Switching Netw.*, vol. 23, pp. 5–39, Jan. 2017.

[7] V. A. C. Vale and R. C. Almeida, "Power, routing, modulation level and spectrum assignment in all-optical and elastic networks," *Opt. Switching Netw.*, vol. 32, pp. 14–24, Apr. 2019.

[8] S. Araujo, A. Soares, A. Fontinele, D. R. Campelo, J. V. dos Reis, and E. Barbosa, "Circuit reallocation strategy aware of the physical layer effects for elastic optical networks," in *Proc. IEEE Symp. Comput. Commun. (ISCC)*, Jun. 2018, pp. 970–975.

[9] F. I. Calderón, A. Lozada, D. Bórquez-Paredes, R. Olivares, E. J. Davalos, G. Saavedra, N. Jara, and A. Leiva, "BER-adaptive RMLSA algorithm for wide-area flexible optical networks," *IEEE Access*, vol. 8, pp. 128018–128031, 2020.

[10] B. C. Chatterjee, N. Sarma, and E. Oki, "Routing and spectrum allocation in elastic optical networks: A tutorial," *IEEE Commun. Surveys Tuts.*, vol. 17, no. 3, pp. 1776–1800, Aug. 2015.

[11] B. C. Chatterjee, S. Ba, and E. Oki, "Fragmentation problems and management approaches in elastic optical networks: A survey," *IEEE Commun. Surveys Tuts.*, vol. 20, no. 1, pp. 183–210, 1st Quart., 2018.

[12] L. R. Costa, I. B. Brasileiro, and A. C. Drummond, "Low margin QoT-aware RMLSA with circuit invigoration in elastic optical networks," in *Proc. IEEE Global Commun. Conf. (GLOBECOM)*, Dec. 2020, pp. 1–6.

[13] X. Luo, Y. Zhao, X. Chen, L. Wang, M. Zhang, J. Zhang, Y. Ji, H. Wang, and T. Wang, "Manycast routing, modulation level and spectrum assignment over elastic optical networks," *Opt. Fiber Technol.*, vol. 36, pp. 317–326, Jul. 2017.

[14] B. Li and Y.-C. Kim, "Efficient routing and spectrum allocation considering QoT in elastic optical networks," in *Proc. 38th Int. Conf. Telecommun. Signal Process. (TSP)*, Jul. 2015, pp. 109–112.

[15] T. Hashimoto, K.-I. Baba, and S. Simojo, "A study on routing, modulation level, and spectrum allocation algorithms for elastic optical path networks," in *Proc. IEEE 3rd Int. Conf. Photon.*, Oct. 2012, pp. 395–399.

[16] M. Klinkowski, K. Walkowiak, and M. Jaworski, "Off-line algorithms for routing, modulation level, and spectrum assignment in elastic optical networks," in *Proc. 13th Int. Conf. Transparent Opt. Netw.*, Jun. 2011, pp. 1–6.

[17] W. S. Pelouch, "Raman amplification: An enabling technology for long-haul coherent transmission systems," *J. Lightw. Technol.*, vol. 34, no. 1, pp. 6–19, Jan. 1, 2016.

[18] A. Fallahpour, H. Beyranvand, S. A. Nezamalhosseini, and J. A. Salehi, "Energy efficient routing and spectrum assignment with regenerator placement in elastic optical networks," *J. Lightw. Technol.*, vol. 32, no. 10, pp. 2019–2027, May 2014.

[19] J. Pedro and N. Costa, "Optimized hybrid Raman/EDFA amplifier placement for DWDM mesh networks," *J. Lightw. Technol.*, vol. 36, no. 9, pp. 1552–1561, May 1, 2018.

[20] A. Ferrari, M. Cantono, A. Ahmad, and V. Curri, "Physical layer strategies to save lightpath regenerators," *IEEE/OSA J. Opt. Commun. Netw.*, vol. 10, no. 9, pp. 703–711, Sep. 2018.

[21] M. Aibin and K. Walkowiak, "Adaptive modulation and regenerator-aware dynamic routing algorithm in elastic optical networks," in *Proc. IEEE Int. Conf. Commun. (ICC)*, Jun. 2015, pp. 5138–5143.

[22] M. Cantono, A. Ferrari, U. Waheed, A. Ahmad, S. M. H. Zaidi, A. Bianco, and V. Curri, "Networking benefit of hybrid fiber amplification for lightpath regenerators saving," in *Proc. Opt. Fiber Commun. Conf.*, 2017, Paper W4F.7.

[23] E. F. da Silva, R. C. Almeida, H. A. Pereira, and D. A. R. Chaves, "Assessment of novel regenerator assignment strategies in dynamic translucent elastic optical networks," *Photonic Netw. Commun.*, vol. 39, no. 1, pp. 54–69, Feb. 2020.

[24] A. Ahmad, A. Bianco, H. Chouman, G. Marchetto, S. Tahir, and V. Curri, "Impact of fiber type and Raman pumping in NyWDM flexible-grid elastic optical networks," in *Proc. 18th Int. Conf. Transparent Opt. Netw. (ICTON)*, Jul. 2016, pp. 1–4.

[25] A. Ahmad, A. Bianco, V. Curri, G. Marchetto, and S. Tahir, "Raman pumping as an energy efficient solution for NyWDM flexible-grid elastic optical networks," *Int. J. Electr. Comput. Eng.*, vol. 7, no. 5, p. 2627, Oct. 2017.

[26] H.-C. Le, N. T. Dang, and N. Duc Nguyen, "Impact of optical regeneration on dynamic elastic optical networks," in *Proc. Int. Conf. Adv. Technol. Commun. (ATC)*, Oct. 2017, pp. 11–15.

[27] D. Borquez-Paredes, F. Calderon, N. Jara, A. Leiva, A. Lozada, R. Olivares, and G. Saavedra, "3R regeneration in elastic optical networks and its impact on the network quality of service," in *Proc. 22nd Int. Conf. Transparent Opt. Netw. (ICTON)*, Jul. 2020, pp. 1–4.

[28] G. P. Agrawal, "Optical communication: Its history and recent progress," in *Optics in Our Time*. Cham, Switzerland: Springer, 2016, pp. 177–199.

[29] D. Semrau, G. Saavedra, D. Lavery, R. I. Killey, and P. Bayvel, "A closed-form expression to evaluate nonlinear interference in Raman-amplified links," *J. Lightw. Technol.*, vol. 35, no. 19, pp. 4316–4328, Oct. 1, 2017.

[30] P. Poggiolini, G. Bosco, A. Carena, V. Curri, Y. Jiang, and F. Forghieri, "The GN-model of fiber non-linear propagation and its applications," *J. Lightw. Technol.*, vol. 32, no. 4, pp. 694–721, Feb. 15, 2014.

[31] V. Curri, A. Carena, P. Poggiolini, G. Bosco, and F. Forghieri, "Extension and validation of the GN model for non-linear interference to uncompensated links using Raman amplification," *Opt. Exp.*, vol. 21, no. 3, pp. 3308–3317, 2013.

[32] A. Mitra, D. Ives, A. Lord, P. Wright, and S. Kar, "Non-linear impairment modeling for flexgrid network and its application in offline network equipment upgrade strategy," in *Proc. Int. Conf. Opt. Netw. Design Modeling (ONDM)*, May 2015, pp. 57–62.

[33] D. Ives, P. Bayvel, and S. Savory, "Adapting transmitter power and modulation format to improve optical network performance utilizing the Gaussian noise model of nonlinear impairments," *J. Lightw. Technol.*, vol. 32, no. 21, pp. 3485–3494, Nov. 1, 2014.

[34] L. M. Zhang and F. R. Kschischang, "Staircase codes with 6% to 33% overhead," *J. Lightw. Technol.*, vol. 32, no. 10, pp. 1999–2002, May 15, 2014.

[35] L. Lundberg, P. A. Andrekson, and M. Karlsson, "Power consumption analysis of hybrid EDFA/Raman amplifiers in long-haul transmission systems," *J. Lightw. Technol.*, vol. 35, no. 11, pp. 2132–2142, Jun. 1, 2017.

[36] J. López, Y. Ye, V. López, F. Jiménez, R. Duque, and P. M. Krummrich, "On the energy efficiency of survivable optical transport networks with flexible-grid," in *Proc. Eur. Conf. Exhib. Opt. Commun.*, 2012, p. P5-05.

[37] J. Zhang, Y. Zhao, X. Yu, J. Zhang, M. Song, Y. Ji, and B. Mukherjee, "Energy-efficient traffic grooming in sliceable-transponder-equipped IP-over-elastic optical networks [Invited]," *J. Opt. Commun. Netw.*, vol. 7, no. 1, pp. A142–A152, 2015.

[38] G. A. Beletsioti, G. I. Papadimitriou, P. Nicopolitidis, E. Varvarigos, and S. Mavridopoulos, "A learning-automata-based congestion-aware scheme for energy-efficient elastic optical networks," *IEEE Access*, vol. 8, pp. 101978–101992, 2020.

[39] J. Halder, T. Acharya, M. Chatterjee, and U. Bhattacharya, "E-S-RSM-RSA: A novel energy and spectrum efficient regenerator aware multipath based survivable RSA in offline EON," *IEEE Trans. Green Commun. Netw.*, vol. 5, no. 3, pp. 1451–1466, Sep. 2021.

[40] J. M. H. Elmirghani, T. Klein, K. Hinton, T. E. H. El-Gorashi, A. Q. Lawey, and X. Dong, "GreenTouch GreenMeter core network power consumption models and results," in *Proc. IEEE Online Conf. Green Commun. (OnlineGreenComm)*, Nov. 2014, pp. 1–8.

[41] H. Zhang, B. Zhu, S. Park, C. Doerr, M. Aydinlik, J. Geyer, T. Pfau, G. Pendock, R. Aroca, F. Liu, and C. Rasmussen, "Real-time transmission of 16 Tb/s over 1020 km using 200 Gb/s CFP2-DCO," *Opt. Exp.*, vol. 26, no. 6, p. 6943, 2018.

[42] J. Geyer, C. Rasmussen, B. Shah, T. Nielsen, and M. Givehchi, "Power efficient coherent transceivers," in *Proc. 42nd Eur. Conf. Opt. Commun. (ECOC)*, 2016, pp. 1–3.

[43] P. J. Winzer, "High-spectral-efficiency optical modulation formats," *J. Lightw. Technol.*, vol. 30, no. 24, pp. 3824–3835, Dec. 15, 2012.

[44] R. S. Tucker, R. Parthiban, J. Baliga, K. Hinton, R. W. A. Ayre, and W. V. Sorin, "Evolution of WDM optical IP networks: A cost and energy perspective," *J. Lightw. Technol.*, vol. 27, no. 3, pp. 243–252, Feb. 1, 2009.

[45] R. S. Tucker, "Green optical communications—Part I: Energy limitations in transport," *IEEE J. Sel. Topics Quantum Electron.*, vol. 17, no. 2, pp. 245–260, Mar. 2011.

[46] D. Eppstein, "Finding the K shortest paths," *SIAM J. Comput.*, vol. 28, no. 2, pp. 652–673, 1999.

[47] Ì. Brasileiro, J. Valdemir, and A. Soares, "Regenerator assignment with circuit invigorating," *Opt. Switching Netw.*, vol. 34, pp. 58–66, Nov. 2019.

[48] W. Fawaz, B. Daheb, O. Audouin, M. Du-Pond, and G. Pujolle, "Service level agreement and provisioning in optical networks," *IEEE Commun. Mag.*, vol. 42, no. 1, pp. 36–43, Jan. 2004.

ASTRID LOZADA received the M.Sc. degree in electronic engineering from Universidad Técnica Federico Santa María (UTFSM), Chile, in 2020, where she is currently pursuing the Ph.D. degree in electronic engineering. Her research interests include fiber optic communication systems and nonlinear fiber effects.

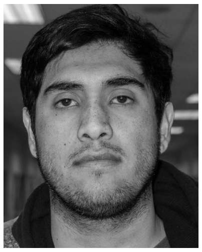

FELIPE CALDERÓN received the B.Sc. degree in electronic engineering from the Pontificia Universidad Católica de Valparaíso (PUCV), Chile, in 2020, where he is currently pursuing the M.Sc. degree in electrical engineering. His current interests include optical networking and machine learning.

JOSÉ NÚÑEZ KASANEVA received the B.Sc. degree in electrical engineering from the Universidad de Concepción (UDEC), Chile, in 2021, where he is currently pursuing the M.Sc. degree in electrical engineering. His current interests include elastic optical networks, optical network survivability, machine learning, and optimization.

DANILO BÓRQUEZ-PAREDES received the B.Eng. degree in telematics engineering from Universidad Técnica Federico Santa María (UTFSM), Valparaiso, Chile, in 2012, and the Ph.D. degree from Universidad Adolfo Ibañez, in September 2018. He also received the professional title in telematics engineering from UTFSM. He is currently a full-time Professor with the Faculty of Engineering and Sciences, Universidad Adolfo Ibañez. His research interests include the dynamic allocation of resources in flexible optical networks, network virtualization, graph theory, and optimization.

RICARDO OLIVARES received the B.Sc. degree in electronic engineering from Universidad Técnica Federico Santa María (UTFSM), Chile, in 1983, and the M.Sc. and D.Sc. degrees in electrical engineering from the Pontificia Universidade Católica do Rio de Janeiro, Brazil, in 1994 and 2001, respectively. He has been with the Department of Electronic Engineering, UTFSM, since 1986, where he is currently an Assistant Professor. His current interests include RF measurements, fiber optic communication systems, fiber optical sensors, and nonlinear fiber optics.

ALEJANDRA BEGHELLI received the B.Eng. degree in electronic engineering and the M.Sc. degree from Universidad Técnica Federico Santa María, Chile, in 1996 and 2001, respectively, and the Ph.D. degree from University College London (UCL), London, U.K. in 2006. She is currently a Lecturer with the Department of Electronic and Electrical Engineering, UCL. Her current research interests include dynamic resource allocation in optical networks, with an emphasis on the application of artificial intelligence techniques.

NICOLÁS JARA (Member, IEEE) received the B.Sc. and M.Sc. degrees in telematics engineering from Universidad Técnica Federico Santa María (UTFSM), Chile, in 2010, and the Ph.D. degree from the Université de Rennes I, France, in 2017, and UTFSM, in 2018. He is currently an Assistant Professor with the Department of Electronics, UTFSM. His current research interests include optical networks design, networks performability, and simulation techniques.

ARIEL LEIVA (Member, IEEE) received the B.Sc. degree in electronic engineering and the M.Sc. degree in electrical engineering from the Pontificia Universidad Católica de Valparaíso (PUCV), Chile, in 2003 and 2007, respectively, and the Ph.D. degree from Universidad Técnica Federico Santa María, Valparaiso, Chile, in 2013. He is currently a Lecturer with PUCV. His current interests include fiber optic communication systems and optical networking.

GABRIEL SAAVEDRA (Member, IEEE) received the B.Eng. degree in telecommunication engineering and the M.Sc. degree from the Universidad de Concepción, Chile, in 2013 and 2014, respectively, and the Ph.D. degree from University College London (UCL), London, U.K., in 2019. He is currently an Associate Professor with the Universidad de Concepción. His research interests include nonlinear fiber effects, nonlinear compensation methods, and digital signal processing for optical communications.

• • •

B

Journal Publication

Research Article Vol. 0, No. 0 / 00 00 0000 / *Optics Express* 1

Optics EXPRESS

Performance evaluation of a two-stage few-mode EDFA for high-capacity SDM systems

Astrid Lozada,[1,*] **Ricardo Olivares,**[1] **Nicolás Jara,**[1] **Patricia Morales,**[1] **Bárbara Dumas Feris,**[2] **Ariel Leiva,**[2] **Gabriel Saavedra,**[3] **and Danilo Bórquez-Paredes**[4]

[1] *Department of Electronic Engineering, Universidad Técnica Federico Santa María, Valparaíso, Chile*
[2] *School of Electrical Engineering, Pontificia Universidad Católica de Valparaíso, Valparaíso, Chile*
[3] *Department of Electrical Engineering, Universidad de Concepción, Concepción, Chile*
[4] *Faculty of Engineering and Sciences, Universidad Adolfo Ibáñez, Viña del Mar, Chile*
[*] *astrid.lozada@usm.cl*

Abstract: Space division multiplexing (SDM) systems using few-mode fibers (FMF) are essential for next-generation fiber optic communications. Optical amplifiers with low noise, minimal differential modal gain (DMG), and minimal differential spectral gain (DSG) are essential for these systems. In this work, we present a method to design and optimize a two-stage few-mode erbium-doped fiber amplifier (FM-EDFA) using a joint DMG-DSG minimization approach. This methodology involves the pumping profile design and the gain flattening filter design. Simulation results show the two-stage FM-EDFA achieves DMG and DSG below 2.8 dB and 0.42 dB, respectively, with an optical signal-to-noise ratio above 19 dB across the C-band, enabling a system capacity of 48.6 Tbps. This work reveals the effectiveness of this two-stage FM-EDFA for optical amplification in the context of SDM systems.

1. Introduction

Space division multiplexing (SDM) technology based on few-mode fiber (FMF) is an alternative to face the potential capacity crunch of current wavelength division multiplexing (WDM) networks [1]. This technology allows increasing the overall network throughput by using linearly polarized (LP) modes as independent spatial paths within the optical fiber core to transport information. To fully capitalize on the benefits offered by FMF transmission networks, including improved spatial efficiency and reduced power consumption, a rigorous design of all optical components within the network is necessary. This encloses elements such as optical amplifiers, switches, filters, (de) multiplexers, mode selectors, isolators, pump combiners, and various other components, ensuring a feasible system.

Designing and fabricating few-mode optical amplifiers is a challenging task. The main goal is to achieve high gain and low differential modal gain (DMG) between spatial modes [2]. Low DMG means that, a similar gain is obtained for all spatial modes available at a specific wavelength [3]. Besides that, it is also required to achieve a flat gain shape among all wavelengths per spatial mode, this metric, known as the differential spectral gain (DSG) [3], is referred to as the gain ripple in the context of single-mode systems. Furthermore, it is essential to maintain a low noise figure and high power efficiency.

In this work, we extend the investigation presented in a previous conference paper [4] where we focus on Few-Mode Erbium-Doped Fiber Amplifiers (FM-EDFAs). Here we present the methodology to jointly minimize DMG and DSG in a two-stage FM-EDFA. We used our methodology to design a 6M-EDFA, and then simulated a link to verify the amplifier performance in the potential real scenario. The main contributions of this paper are: (1) the methodology Joint DMG-DSG Minimization; (2) the first study of two-stage 6M-EDFA performance with a dense number of wavelengths in the conventional C-band; (3) the first study of a full-load link

#539087 https://doi.org/10.1364/OE.539087
Journal © 0000 Received 16 Aug 2024; revised 13 Oct 2024; accepted 15 Oct 2024; published 00 00 0000

composed of a chain of FMF span followed by a two-stage FM-EDFA. To achieve comprehensive coverage of the entire conventional C-band, we increase the number of WDM channels from 9 [4] to 81 per each spatial mode in an FMF system where optical amplification is achieved using two-stage 6M-EDFAs.

This paper is structured as follows: Section 2 presents a review of the literature. Then, Section 3 outlines the two-stage FM-EDFA design methodology joint DMG-DSG minimization. Subsequently, Section 4 presents the simulation results of the designed pumping and gain flattening filter (GFF) profiles, and the characterization of the two-stage FM-EDFA. Section 5 presents an analysis of the simulation results of a link composed of a cascade of the designed amplifier. Finally, Section 6 summarizes the concluding remarks.

2. Literature review

FM-EDFAs have been studied in the context of optical amplification for FMF systems [1–3,5]. Due to optical amplification performance depends on the fiber structure and the doping profile, researchers have focused on three approaches to improve FM-EDFA performance: tailoring the rare-earth doping profile [1,6–12]; tailoring the refractive-index profile [2,12,13]; and tailoring the pumping profile [4,14,15]. Another technique that improves the performance of FM-EDFA in terms of reducing DSG involves the use of gain flattening filters [4,13,16–18]. To fabricate GFF for FMF systems two approaches have been published in literature: one based on spatial light modulators [16] and the other one on long-period fiber grating [17].

All these techniques to improve FM-EDFA have been used individually or in combination to achieve the desired amplification performance as can be seen in Table 1 which summarizes characteristics and performance metrics for a variety of FM-EDFA works. To be comparable, Table 1 include works that have reported C-band operation in the range of 1530 to 1565 nm for signals over six LP modes (LP_{01}, $LP_{11_{a,b}}$, LP_{02}, and $LP_{21_{a,b}}$). From this table, some trends can be identified. The fiber refractive index profile has taken some configurations: step-index [1,4,6,15,18], double-cladding step-index [17], trench-assisted [2], and staircase index [12]. The pumping profile covers some degrees of freedom, for example, the pump can be injected into the core [2,4,7,8,15,17] or the cladding [1,6,12]; the pump can be launched into one or more spatial modes [2,4,7,8,15,17] with equal or different power and directions; and the optical fiber can be uniformly [4,8,15,17,18] or non-uniformly doped [2,6–9,12].

From Table 1, it can be observed that in terms of DMG, the best value is reported in [12], where it is proposed an optimization method to reduce DMG in FM-cladding pumped EDFAs. Regarding DSG, three works have reported results in the range between 0.38 to 0.6 dB [4,17,18]. These works have in common that they use GFF to obtain a low DSG. In [18], is proposed an FM-GFF based on mode selective couplers, in this case, the FM-GFF follows the FM-EDFA device. In [4], our previous work, we studied and examined the performance of a two-stage FM-EDFA, where we optimized the pumping profile and used a GFF in the middle of the amplifier to achieve improved performance. Finally, in [17] is proposed an FM-GFF based on cascaded long-period fiber grating using double cladding FMF, in this case, the FM-GFF is placed at the end of the FM-EDF. Note that, a dash in Table 1 represents that the information about the parameter presented in the column was not provided in the referenced study.

Most of the studies presented in Table 1 introduce methodologies for optimized amplifier design. In Refs. [2,6,8,12], either the refractive index or the doping profile of the fiber has been optimized to minimize DMG. Additionally, in [7], the doping profile was optimized to maximize gain and minimize the maximum DMG or DSG. Notably, few previous works [4,17,18] have jointly minimized DMG and DSG. In [4], our previous work, the pumping profile and the profile of a single GFF were optimized to flatten the gain spectrum across all modes and wavelengths. In [17] and [18], the design of the GFF was optimized based on a cascade of 15 long-period fiber gratings for a double cladding FMF, and a cascade of 5 mode selective couplers, respectively.

Table 1. FM-EDFA papers reported over six-signal modes and C-band (1530-1565 nm) operation

FM-EDFA	Index profile	WDM channels	Pumping profile				DMG	DSG	Mean Gain	NF
			Type	Direction	Power	Doping				
6M-EDFA [6]	Step-index	15	Cladding	Forward	2.5 W	Multilayered	<1 dB	–	24.8 dB	5.3 dB
6M-EDFA [7]	–	4	Core	–	LP_{01} (100 mW), LP_{02} (100 mW)	Micro-structure	2.3 dB	2.3 dB	18.8 dB	–
6M-EDFA [8]	–	–	Core	–	LP_{01}(264.94 mW), LP_{02} (500 mW), and LP_{21} (500 mW)	Uniform	2 dB	–	–	–
	–	–	Core	–	LP_{01} (600 mW)	Multi-well ion	2.5 dB	–	–	–
6M-EDFA [17]	Double-cladding	–	Core	–	LP_{02} (200 mW)	Uniform	0.6 dB	0.6 dB	20 dB	–
6M-EDFA [15]	Step-index	8	Core	–	LP_{01} (400 mW or 800 mW)	Uniform	10 dB	2.5 dB	–	–
			Core	–	LP_{01} and LP_{11} (400 mW or 800 mW)	Uniform	10 dB	5 dB	–	–
6M-EDFA [2]	Trench-assisted	8	Core	Forward	LP_{01} (400 mW)	Multilayer	1.945 dB	2.562 dB	25 dB	4 dB
6M-EDFA [12]	Staircase index	36	Cladding	-	20 W	Double-ring	0.18 dB	<4 dB	23.7 dB	4.08 dB
6M-EDFA [4]	Step-index	9	Core	Forward	LP_{02} (200 mW), LP_{21_a} (225 mW), and LP_{21_b} (235 mW)	Uniform	<3dB	0.53 dB	17 dB	4.66 dB
6M-EYDFA [1]	Step-index	7	Cladding	Forward (1st stage) and Backward (2nd stage)	0.8 W (1st stage) and 8 W (2nd stage)	Ytterbium co-doping	3 dB	4 dB	40 dB	7 dB
6M-EDFA [18]	Step-index	–	Core	Forward	LP_{01} (600 mW)	Uniform	0.38	0.38	21	–

The studies outlined in Table 1 limited the number of WDM channels between 4 [7] to 36 [12]. However, conventional C-band has the potential to allow until 320 WDM channels, using a separation between adjacent channels of 12.5 GHz [19]. To harness the full capabilities of FMF systems for practical applications, and to meet the demands of increased data capacity while ensuring the reliability and efficiency of FMF networks, it becomes necessary to explore the entire spectrum of the C-band. Consequently, FM-EDFA must exhibit robust performance under these conditions. To the best of our knowledge, none of the studies presented in Table 1, have validated the adaptability of their designs to accommodate a higher number of WDM channels or use in a link composed of several spans.

3. Joint DMG-DSG minimization methodology

We present a diagram of our methodology in Fig. 1. This methodology begins with defining the physical configuration of the two-stage FM-EDFA as the input; an example of this is presented in subsection 3.1. Next, a genetic algorithm (GA) is applied to design the pumping profile (subsection 3.2) in conjunction with an iterative algorithm to design the GFF profile (subsection 3.3). The output is a pumping and GFF profile that jointly minimizes DMG and DSG. Joint minimization of DMG and DSG is accomplished in two steps: DMG is minimized by tailoring the pumping profile, and DSG is minimized by adjusting the GFF profile.

The following subsections detail each step in the joint DMG-DSG minimization methodology. We conclude this section with the definition of the performance metrics used to evaluate and characterize the two-stage FM-EDFA.

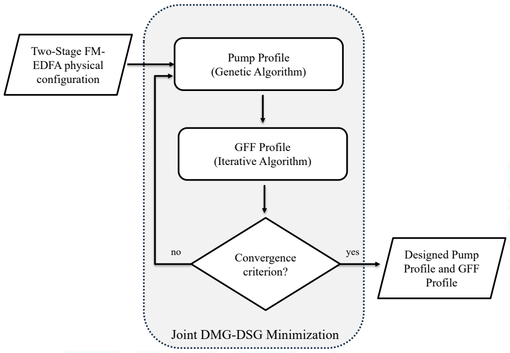

Fig. 1. Schematic of the Joint DMG-DSG Minimization methodology

3.1. Two-stage FM-EDFA configuration

The two-stage FM-EDFA modeled in this study is illustrated in Fig. 2. This configuration, previously explored in FM-EDFA research [4] with favorable results, involves injecting WDM channels into the first erbium-doped few-mode fiber (ED-FMF) stage through a Wavelength-Selective WDM Coupler (WSC$_1$). Signal amplification is achieved using 980 *nm* forward multimode pumping. WSCs are considered to have high isolation between the signal and pump ports, so that any unwanted interference between the signals and the pumps can be neglected. A GFF, an ASE filter, and an optical isolator (ISO) are strategically positioned between two ED-FMF equal sections, as in [4,13,20], referred to as *Stage 1* and *Stage 2*. *Stage 1* has the major contribution to the total gain and noise figure of the two-stage FM-EDFA, while *Stage 2* provides the additional gain necessary to achieve an output gain profile as flat as possible. The GFF is designed to flatten the gain curve across the wavelength range for each spatial mode, consequently, the bandwidth of the filter is around 4 THz. The ASE filter, which is a bandpass filter, is introduced to only pass the wavelengths of interest and eliminate the propagation of the forward-traveling Amplified Spontaneous Emission (ASE) noise. In practice, the ASE filter and the GFF can be implemented in a single filter. The ISO is incorporated to suppress backward-traveling ASE originating in *Stage 2* of the amplifier. *Stage 2* is then fed by the flattened WDM signals and residual pumping from the first stage, facilitated through a third WSC$_3$.

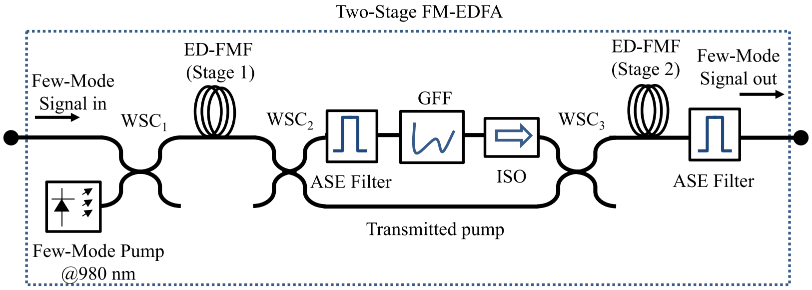

Fig. 2. Configuration of the two-stage FM-EDFA.

3.2. Pumping profile design

The pumping profile for an FM-EDFA should define the type, pump direction, pump wavelength(s), pump mode(s), pump power(s), and doping profile. In this work, we assumed a core pumping type in the forward direction at 980 nm with a uniform doping profile. This wavelength and pump direction were selected based on the performance it has shown for amplifying the first LP modes [13,14]. As is also the case in single-mode EDFAs, where higher pumping efficiency is shown due to a larger absorption cross-section at 980 nm compared to 1480 nm, and low noise figure with forward pumping [21]. To complete the design of the pumping profile, which involves the selection of the pumping mode(s) and its power, we employed a GA. GAs have demonstrated effectiveness in improving various aspects of FM-EDFA designs, including the selection of parameters such as the doping profile in a multilayer configuration [2,6,7,10], the refractive index profile in a trench-assisted configuration [13], and the pumping profile itself [4]. In this work, we refine the GA originally introduced in [4] to design the pumping profile for the specific demands of C-band full-channel occupation. The fitness function (*FF*) employed to evaluate individuals within each population is detailed as follows:

$$FF = \sum_{\lambda_s=1530\text{nm}}^{1565\text{nm}} \frac{G_{ave}(\lambda_s)}{DMG(\lambda_s)}, \tag{1}$$

where G_{ave} denotes the average modal gain at λ_s and $DMG(\lambda_s)$ is the maximum DMG at wavelength λ_s. The objective of the GA presented in Algorithm 1 is to maximize the fitness function, selecting a proper combination between pumping modes and pumping powers. In the GA, each individual is represented by a vector $\mathbf{g}$ of size $2p$, where p denotes the number of pumping modes. Each pair of genes within this vector represents a specific pumping mode along with its corresponding power. As an example, for 3 pumping modes, $\mathbf{g} = [0, 0.100, 1, 0.100, 2, 0.100]$. This individual represents a pumping profile composed of 3 LP modes, identified with different integer numbers $(0, 1, 2)$, each one with equal power of 0.100 W.

Algorithm 1. Genetic Algorithm

```
Require: $I$, $p$, mode and power range, $MaxP$, $p_c$, $p_m$, $P = 0$.
 1: if $P == 0$ then
 2:     for $i = 0 : i++ : I - 1$ do
 3:         Create $\mathbf{g}_i$ of size $2p$
 4:         $[GFF]$ = GFF_Algorithm
 5:         $[Gain, DMG] = \text{EDFA}_{\text{calc}}(\mathbf{g}_i, GFF)$
 6:         $FF_i(Gain, DMG)$
 7:     end for
 8:     Save the best $\mathbf{g}$ $(\max(FF))$
 9: end if
10: $P = P + 1$
11: while $P <= MaxP - 1$ do
12:     $[New\ population] = \mathbb{S} \rightarrow \mathbb{X}(p_c) \rightarrow \mathbb{M}(p_m)$
13:     Repeat 4 to 6 $\forall\ \mathbf{g} \in New\ population$
14:     Save the best $\mathbf{g}$ $(\max(FF))$ and compare it with the previous best $\max(FF)$
15:     if best $\max(FF) \rightarrow$ converges then
16:         break
17:     end if
18:     $P = P + 1$
19: end while
        return Pumping profile: $\mathbf{g}(\max(FF))$
```

The GA operation, described in Algorithm 1, can be summarized in the next four steps:

- Step 1: To generate a starting population of size *I*

The first step of the GA is to build a starting population of size I, which is composed of a number I of individuals $\mathbf{g}$. Each $\mathbf{g}$ is generated by randomly selecting p pumping modes and p pumping powers from a predefined set of searching ranges for each variable. This step is represented in line 3 of Algorithm 1.

- Step 2: Individual evaluation

  The second step of the GA performs the following actions for each individual in the population: (1) Determine the GFF profile using Algorithm 2; (2) To solve the set of coupled Eq. (2)–(4) with the GFF at the midstage of the amplifier, refereed as function $\text{EDFA}_{\text{calc}}$ in Algorithm 1; (3) To calculate the fitness function. Once all individuals in the population have been evaluated, the best individual, characterized by the maximum fitness value, is saved as a potential solution. This step is represented from lines 1 to 9 in Algorithm 1.

- Step 3: Generation of new populations

  The third step of the GA is to construct a new population based on the previous one, in this step the processes of selection ($\mathbb{S}$) using the tournament approach, crossover ($\mathbb{X}$) with probability p_c, and mutation ($\mathbb{M}$) with probability p_m are applied. Then, the individuals' evaluation is repeated over this new population. Lines 12 to 14 in Algorithm 1 are representing this step.

- Step 4: Termination condition

  The fourth step of the GA is to check if the termination condition is met, this is either when the number of populations (P) reaches the predefined maximum value ($MaxP$)- condition of the while loop of step 3- or when, after 25 successive populations, the best individual is the same, this is the convergence condition verified in line 15 of Algorithm 1. The GA returns the best pumping profile based on the constructed populations.

Algorithm 2. Gain Flattening Filter Algorithm

```
Require: $Filter_{in},\ Fit,\ P_{target}, MaxIt.$
$i = 1$;
$GFF(i)$ initialized with ones
while ( $P <\ P_{target}$) $or$ ($i <= MaxIt$) do
    $Filter_{out} = Filter_{in} * GFF(i)$
    $EDFA_{out}(i) = EDFA_{calc}(Filter_{out})$
    $GFF(i+1) = GFF(i) -\ Fit(EDFA_{out}(i) - \min(EDFA_{out}(i)))$
    $P = \max(EDFA_{out}(i)) - \min(EDFA_{out}(i))$
    $i = i + 1$
end while
    return GFF profile: $GFF(i\text{-}1)$
```

The algorithmic complexity is determined by the population size I, i.e., the number of individuals per generation, the maximum number of generations $MaxP$, the number of signaling and pumping wavelengths Λ_s and Λ_p, respectively, and the number of LP modes M. For each individual per generation, the mathematical model for the two-stage FM-EDFA is solved going through all Λ_s and Λ_p for all M modes to compute de fitness function of that individual. Consequently, the algorithmic complexity is $O(I \cdot MaxP \cdot \Lambda_s \cdot \Lambda_p \cdot M)$. The fitness function evaluations dominate the overall complexity and scales with the product of population size and number of generations.

3.2.1. Mathematical model of FM-EDFA

The behavior of an FM-EDFA can be described through a set of coupled differential equations. These equations model the dynamics of optical power propagation for the signal, pump, and ASE noise within the amplifier [3]. It is also required to model the Erbium population densities between energy levels to describe the amplification process. The mathematical model used here, is the multimode case of the model suggested by Giles and Desurvire [22], which has been extensively used to describe the optical amplification process in single mode EDFA. This model has the following assumptions [15]: (1) At 980 nm pump wavelength, the model is approximately a quasi-three-level system, and the excited state absorption is ignored; (2) The concentration of Erbium ions is uniformly distributed along the longitudinal direction of the fiber.

The coupled equations representing power on spatial signal mode ($P_{s,i}$), spatial pump mode ($P_{p,j}$), and ASE ($P_{ASE,i}$) are mathematically expressed as follows [3,5,13]:

$$\frac{dP_{s,i}}{dz} = P_{s,i} \iint \Gamma_{s,i}(r,\phi)[N_2(r,\phi)\sigma_{es,i} - N_1(r,\phi)\sigma_{as,i}]dA - \sum_{k=1}^{m_s} d_{s,i\rightarrow k}[P_{s,i} - P_{s,k}], \tag{2}$$

$$\frac{dP^{\pm}_{p,j}}{dz} = P^{\pm}_{p,j} \iint \Gamma_{p,j}(r,\phi)\, N_1(r,\phi)\sigma_{ap,j}\, dA - \sum_{k=1}^{m_p} d_{p,j\rightarrow k}[P^{\pm}_{p,j} - P^{\pm}_{p,k}], \tag{3}$$

$$\begin{aligned}\frac{dP^{\pm}_{ASE,i}}{dz} &= P^{\pm}_{ASE,i} \iint \Gamma_{ASE,i}(r,\phi)[N_2(r,\phi)\sigma_{eASE,i} + N_1(r,\phi)\sigma_{aASE,i}]dA \\ &\cdots + 2\sigma_{eASE,i} h\nu_{ASE,i}\Delta\nu_{ASE,i} \iint N_2(r,\phi)\Gamma_{ASE,i}(r,\phi)dA - \sum_{k=1}^{m_s} d_{s,i\rightarrow k}[P^{\pm}_{ASE,i} - P^{\pm}_{ASE,k}],\end{aligned} \tag{4}$$

where subscripts s and p indicate the signal and pump wavelengths, respectively. ASE refers to the central wavelength of a spectral slot of width $\Delta\nu_{ASE}$ (noise bin) that result from decomposing the total spectrum of frequencies of interest of the amplifier. The ASE subscript will run through all the spectral positions of the amplifier bandwidth, while s will only refer to those where the signals are located. Therefore, ASE and s may or may not assume the same values, depending on whether or not they refer to the same spectral position. Subscripts i, and j indicate the i-th signal mode and j-th pump mode. $\Gamma_{s/p}(r,\phi)$ is the normalized intensity profile of the i-th signal or j-th pump mode; $N_1(r,\phi)$ and $N_2(r,\phi)$ are the population densities of Erbium atoms in the lower and upper levels; $\sigma_{es(p),i}$ and $\sigma_{as(p),i}$ are the emission and absorption cross sections at the i-th signal (pump) mode at the wavelength of the signal (pump) $\lambda_{s(p)}$; h is the Planck's constant; $\nu_{s,i}$ is the frequency of the i-th signal mode at the wavelength λ_s; $\Delta\nu_{s,i}$ is the equivalent amplifying bandwidth; and $d_{s(p),i\rightarrow k}$'s [23] are coupling coefficients between signal modes i and k at wavelength $s(p)$ and computed as a function of the difference between the propagation constants of modes i and k. $d_{s(p),i\rightarrow k}$ represents a fraction of the i-th mode power scattered into the k-th mode [23].

The total doping concentration N_0, is given by [5]: $N_0(r,\phi) = N_1(r,\phi) + N_2(r,\phi)$. The rate equations for the population densities are as follows:

$$N_1(r,\phi) = \frac{\frac{1}{\tau} + W^{e}_{(s,ASE)}}{\frac{1}{\tau} + W^{(e,a)}_{(s,ASE)} + W^{a}_{p}} N_0(r,\phi), \tag{5}$$

$$N_2(r,\phi) = \frac{W^{a}_{(s,ASE)} + W^{a}_{p}}{\frac{1}{\tau} + W^{(e,a)}_{(s,ASE)} + W^{a}_{p}} N_0(r,\phi), \tag{6}$$

we use the auxiliary variables $W^{e(a)}_{(s,ASE)}$, $W^{(e,a)}_{(s,ASE)}$, and W^{a}_{p} to calculate $N_1(r,\phi)$ and $N_2(r,\phi)$. These are defined as follows:

$$W^{e(a)}_{(s,ASE)} = \sum_{s=\lambda_{s_1}}^{\lambda_s} \sum_{i=1}^{m_s} \frac{[P_{s,i} + P_{ASE,i}]\sigma_{e(a)s,i}\Gamma_{s,i}(r,\phi)}{h\nu_{s,i}}, \tag{7}$$

$$W^{(e,a)}_{(s,ASE)} = \sum_{s=\lambda_{s_1}}^{\lambda_s} \sum_{i=1}^{m_s} \frac{[P_{s,i} + P_{ASE,i}](\sigma_{es,i} + \sigma_{as,i})\Gamma_{s,i}(r,\phi)}{h\nu_{s,i}}, \tag{8}$$

$$W^{a}_{p} = \sum_{p=\lambda_{p_1}}^{\lambda_p} \sum_{j=1}^{m_p} \frac{P_{p,j}\sigma_{ap,j}\Gamma_{p,j}(r,\phi)}{h\nu_{p,i}}, \tag{9}$$

where τ is the spontaneous emission lifetime for the excited state, $m_{s(p)}$ is the total number of guided modes for signal (pump), and $\lambda_{s(p)}$ is the total number of wavelengths for signal (pump). To calculate the gain and noise figure of the FM-EDFA Eq. (2)–(9) must be solved.

3.3. Gain-flattening filter (GFF)

To design the GFF profile, we programmed an iterative algorithm based on the gradient-descent optimization approach [7,24]. The pseudo-code is presented in Algorithm 2. This algorithm requires the following inputs: $Filter_{in}$ which is related to the signal and noise power obtained by solving Eq. (2) and Eq. (4) in the midstage of the EDFA, the filter adaptation step (ΔFit), the power variation goal (ΔP_{target}), and the maximum number of iterations ($MaxIt$). Parameters ΔFit, ΔP_{target}, and $MaxIt$ should be selected according to the target performance and the computation constraints. The output of the algorithm is the GFF profile, represented by a set of coefficients ranging from 0 to 1 associated with the signal wavelengths.

In the first iteration ($i = 1$), the GFF profile is initialized with ones, this way, it does not have a flattening effect over the output signals of the first stage of the FM-EDFA. To determine the new set of coefficients ($GFF(i + 1)$), the input signal and the average output signal of the second stage of the FM-EDFA are required, these are represented by $Filter_{out}$ and $EDFA_{out}$ in Algorithm 2. The function $EDFA_{calc}$ solves the set of differential coupled Eq. (2) to Eq. (4) and returns the mean power of the output signal. The coefficients of the GFF profile for the next iteration are adjusted using the product between ΔFit and the difference between the mean signal output and its minimum value. This relationship allows the adaptation of the filter transfer function, aiming to achieve reduced power variations (ΔP) and the desired flattening effect, consequently decreasing DSG per mode.

The parameter ΔFit is fixed to a constant value within the range of $[0 - 1]$. On one hand, a value closer to 0 results in gradual changes to the GFF profile in each iteration, requiring a higher iteration count to meet the $\Delta Ptarget$ condition. On the other hand, a value closer to 1 induces rapid changes to the GFF profile, potentially compromising the achievement of $\Delta Ptarget$. Therefore, selecting an optimal ΔFit requires a sensitivity analysis to evaluate its impact on the overall process. The iterative algorithm ends either when the current ΔP is lower than ΔP_{target} or when the iteration count reaches $MaxIt$.

3.4. Performance metrics

To evaluate the performance of the two-stage FM-EDFA, we employed various key metrics to provide a comprehensive analysis. The chosen performance metrics verify the effectiveness of the amplifier in maintaining low noise and flat gain distribution handling multiple WDM signals. These metrics are crucial for optimal performance in practical applications. We define these metrics as follows:

- The **gain** in the signal at wavelength s and at a mode i is:

$$G(s, i) = \frac{P_{s,i}(z)}{P_{s,i}(0)}, \tag{10}$$

where $P_{s,i}(z)$ is obtained using Eq. (2) at any position z.

- Although the **total NF** strongly depends on NF of the first stage, it is also degraded by the GFF and the second stage of the amplifier. Total NF in the signal at wavelength s and at a mode i is [25,26]:

$$NF_{s,i}^{total} = NF_{s,i}^{stage_1} + \frac{NF_s^{GFF} - 1}{G_{s,i}^{stage_1}} + \frac{NF_{s,i}^{stage_2} - 1}{G_s^{GFF}.G_{s,i}^{stage_1}}, \tag{11}$$

where $NF_{s,i}^{stage_x}$ is the noise figure of the first stage of the amplifier, NF_s^{GFF} is the noise figure of the GFF computed as the inverse of the gain flattening filter coefficients, $NF_{s,i}^{stage_2}$ is the noise figure of the second stage of the amplifier, and $G_{s,i}^{stage_x}$ is the gain of the stage of the amplifier indicated by the superscript $stage_x$. Subscripts s and i indicate the wavelength and the LP mode, respectively.

- The **DMG** parameter is the differential gain in the modal domain for a fixed wavelength s, it is defined as [3]:

$$DMG(s) = \max\{|G(s, i) - G(s, j)|\}, \tag{12}$$

where at wavelength s $i \neq j$ for all i and j spatial modes.

- The **DSG** parameter is the differential gain in the wavelength domain for one spatial mode i, it is defined as [3]:

$$DSG(i) = \max\{G(s, i)\} - \min\{G(s', i)\}, \tag{13}$$

where $s \neq s'$ for the spatial mode i.

4. Results and discussion

This section provides a comprehensive evaluation of the joint DMG-DSG minimization methodology employed for designing the pumping profile and the GFF profile, along with a detailed characterization of the two-stage FM-EDFA. We applied numerical techniques to solve Eq. (2) - Eq. (4) to simulate the amplification process within the FM-EDFA. We considered six co-propagating signal modes (LP_{01}, LP_{11_a}, LP_{11b}, LP_{02}, LP_{21_a}, and LP_{21b}), with input parameters resumed in Table 2. The total length of the amplifier was optimized by numerical simulation to achieve the highest possible gain, taking into account the available pump power levels. The length of the doped fiber of *Stage 1* and *Stage 2* is half of the value reported in Table 2. The emission and absorption coefficients for the Erbium-doped fiber were obtained from the software VPItransmissionMaker™ [27]. We used a coupling coefficient, $d_{s(p),i \to k}$, with a mean value of the order of μm^{-1}, consequently, its impact on amplifier performance is small.

4.1. Pumping and GFF profiles

We used Algorithm 1 to design the pumping profile, aiming to select the most effective combination of LP modes and their corresponding powers for injecting forward pumping into the first stage of the amplifier. For the pumping mode search range, we limited our selection to the first eight LP modes that best match the intensity profile distribution of the signal modes (LP_{01}, $LP_{11_{a,b}}$, LP_{02}, $LP_{21_{a,b}}$, and $LP_{12a,b}$). Additionally, the pumping power search range was set between 200 mW

Table 2. Simulation parameters

Step-index ED-FMF		**Signal**		**Pump**	
Radius [μm]	12	Wavelength range operation [nm]	1530 – 1565 (C-band)	Pump wavelength [nm]	980
Core refractive index (n_1)	1.45	Number of wavelengths	81	Pump direction	Forward
Numerical aperture	0.1	Input power (per wavelength) [dBm]	−25		
Uniform doping concentration [$(N)\,m^{-3}$]	$1 \cdot 10^{24}$				
Length [m]	30				
Photon lifetime [ms]	10				

and 300 mW. Each population consisted of 80 individuals, and for subsequent populations, we used the tournament method for selection, and crossover and mutation probabilities were set to 0.90 and 0.10, respectively. Numerical simulations were programmed in C++ and run on an Apple M1 Pro, with time costs of 432000 s. The fitness function preserves the individuals with high gain average and lower DMG. Figure 3(a) shows the evolution of the fitness value for 60 populations. After 21 populations the fitness function value does not experience a significant change. The optimal individual, extracted from the 46-th population, is composed of the pumping profile: LP_{02}(295 mW), LP_{21a}(295 mW) and, LP_{21b}(285 mW). The resultant optimized pumping profile is explained by the mode field distribution of each mode and its capabilities to amplify the LP signal modes. The two-stage FM-EDFA with this pumping profile, exhibits the best combination between high mean gain and low DGM.

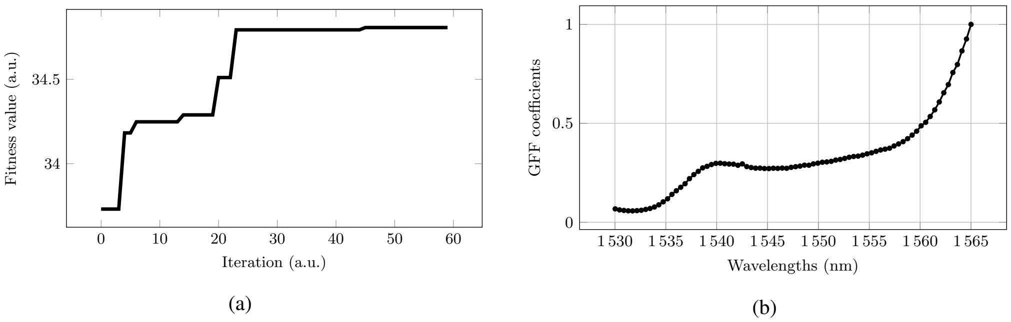

(a)

(b)

Fig. 3. (a) Genetic algorithm fitness function evolution for 60 generations. (b) GFF profile for gain flattening in a 6M-EDFA.

We set the predefined parameters required for designing the GFF to 0.6 for the filter adaptation step (ΔFit) and 0.3 dB for the power variation goal (ΔP_{target}). These specific values were carefully chosen to obtain the lowest DSG when the optimized pumping profile was used. The resulting GFF profile is illustrated in Fig. 3(b). Lower coefficients are allocated to wavelengths requiring a more pronounced flattening effect, while higher coefficients correspond to wavelengths where a lower flattening effect is necessary. This tailored profile grants the efficiency of the GFF in achieving the flattened gain profile across the wavelength spectrum.

Figure 4 illustrates two cases of study: one without using the gain flattening filter (w/o GFF - dotted lines) and the other with its application (wGFF - solid lines). The comparison is drawn for both the best (LP_{01}) and the worst (LP_{02}) spatial modes, with similar trends observed across other modes. The effectiveness of the GFF is measured by the parameter DSG (Eq. (13)), where a lower

DSG means a flatter gain profile. In the absence of the GFF, the maximum DSG reaches 9.17 dB for the LP_{01} mode. Conversely, with the implementation of the GFF, the DSG is improved, reaching a value of 0.54 dB. There is an unavoidable cost in terms of gain reduction when the GFF is applied. For this cost not to impact communication efficiency in practical applications, it must be included in the power budget of the initial design of the amplifier, to compensate for link losses adequately. Despite this, the loss in modal mean gain is only 2.26 dB, which is offset by a substantial improvement in flatness, reducing from 9 dB to 0.54 dB. The reduction in DSG highlights the substantial benefit of applying the GFF, resulting in a flat gain profile. When comparing our DSG results with previous work (Table 1), we obtained a DSG similar to the best-reported values ([4,17,18]) while our system capacity is 9 times greater compared to [4].

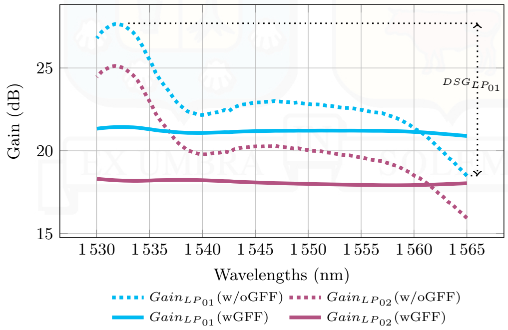

Fig. 4. Gain for modes LP_{01} and LP_{02} using the GFF (wGFF - solid lines) and without using it (w/oGFF - dotted lines).

4.2. FM-EDFA gain characterization

Using the designed pumping profile and the GFF from the preceding subsection, the gain and DMG as a function of wavelengths in the two-stage FM-EDFA, are presented in Fig. 5(a). The calculations for gain and DMG were obtained from Eq. (10) and Eq. (12), respectively. The FM-EDFA demonstrates a mean gain exceeding 18 dB per mode across the entire C-band, with the maximum DMG reaching 3.58 dB at 1530 nm. Considering the DMG values reported in Table 1 for FM-EDFA configurations with the same conditions of refractive index, pumping type, and doping profile, our amplifier has better performance than [17], in addition to being the only one tested under the full channel load scenario. Works with refractive indices and/or doping profiles more complex and, consequently, more expensive, obtain better results in terms of DMG.

Regarding the noise, we computed NF using Eq. (11), and the results are shown in Fig. 5(b). The highest NF is observed at 1530 nm reaching 5.83 dB and the lowest value (4.43 dB) at 1535 nm for LP_{21b}. This represents a noise figure variation of 1.40 dB for the worst case. Nonetheless, the resultant mean NF produced by the two-stage FM-EDFA remains within the range of 5 dB, aligning with the desirable noise performance across the entire C-band spectrum for EDFA amplifiers.

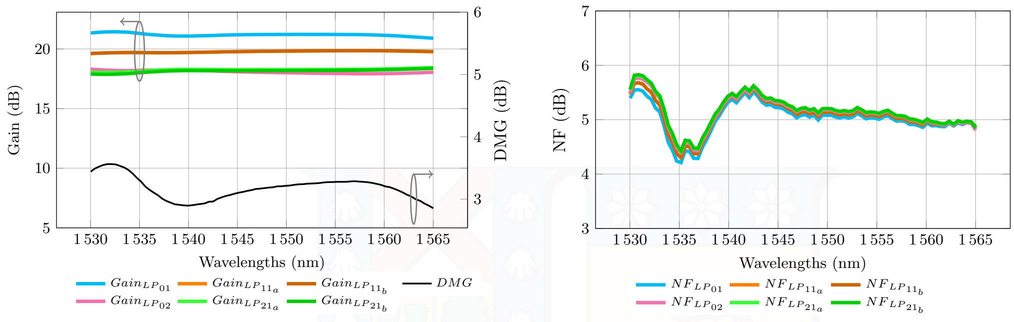

(a)

(b)

Fig. 5. (a) Gain per mode and maximum DMG and (b) Noise figure per mode, for a two-stage 6M-EDFA using a GFF and the designed pumping scheme.

5. Cascade of FM-EDFA in an FMF link

In this section, the two-stage FM-EDFA designed in the previous section is employed in an FMF link, composed of a cascade of these amplifiers. Designing the amplifier across a broad spectrum of wavelengths enables us to simulate and analyze its behavior under the transmission scenario with a full channel load in the conventional C-band.

The FMF system is composed of 4 spans of 100 km each. Following each span, a two-stage FM-EDFA is placed. For the transmission modeling part we solved numerically the Manakov equation for FMF in the weak-coupling regime [28] with the the split-step Fourier method. The parameters used in this part of the simulation are equal to those used in [28] and shown in Table 3. The injected power per wavelength per mode is equal to −5 dBm.

Table 3. Step-index FMF parameters: differential modal group delay (DMGD), dispersion (D), effective mode area (A_{eff}), attenuation coefficient (α), and nonlinear coefficient (γ).

	DMGD [ns/km]	D [ps/(km − nm)]	A_{eff} [μm^2]	α [dB/km]	γ [(W.km)$^{-1}$]
LP_{01}	0	25	80	0.2	1.4
$LP_{11_{a,b}}$	6.5	27.3	76		
LP_{02}	9.9	−2.3	83		
$LP_{21_{a,b}}$	12	20.8	86		

Figure 6 presents the output signal power of each FM-EDFA throughout the FMF link. The input signal at the first amplifier is uniform for all LP modes and wavelengths, as we assume that the attenuation coefficient is the same for all LP modes in the wavelength range of signals. The first amplifier satisfies the input power condition for the designed FM-EDFA, resulting in amplified signals with the gains reported in Fig. 5 and the corresponding DMG. However, as signals progress through successive spans, the signal power becomes non-uniform due to DMG, leading to power variations for each subsequent FM-EDFA.

On one hand, mode LP_{01} achieves the highest gain, with a mean value of 21.24 dB in the first span, effectively compensating for all losses due to the attenuation coefficient of the fiber, estimated to be 20 dB per span, resulting in higher input power to the successive amplifiers in the link and a maximum mean gain variation of 0.65 dB along the link. On the other hand, LP_{02} achieves a mean gain of 18.12 dB in the first span, failing to fully compensate for the losses associated with the attenuation coefficient of the fiber, resulting in lower input power to the following amplifiers in the link. This is also valid for mode $LP_{21_{a,b}}$, with a mean gain of 18.25 dB

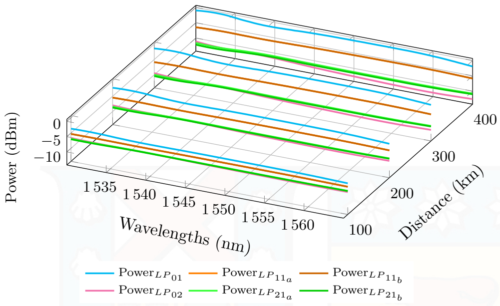

Fig. 6. Output signal power of successive FM-EDFAs in an FMF system composed of 4 spans.

in the first span. The maximum mean gain variation for LP modes LP_{02} and $LP21_{a,b}$ is 0.20 dB and 0.24 dB, respectively. The mean gain achieved by the signal over modes $LP_{11_{a,b}}$ is close to 20 dB span after span, resulting in minimal power variations and a maximum mean gain variation of 0.3 dB.

The signal power for modes LP_{01}, LP_{02}, and $LP21_{a,b}$ at the output of the FM-EDFAs deviates from the initial value of −5 dBm. However, there are ways to control this range of variation in the output power. For example, we could periodically correct the powers of the input signals to the amplifier or tailor the pumping profile.

Figure 7(a) presents the DMG evolution throughout the FMF link. The upper line in the plot is equal to the one presented in Fig. 5, as the first FM-EDFA satisfies the input power condition for the designed FM-EDFA. Note that, as the signal progresses through the spans DMG decreases while signal power dispersion at the FM-EDFA output increases. This inverse relationship can be explained by the gain definition and the power evolutions shown in Fig. 6. The gain is a relation between output and input power to the amplifier, the maximum difference between output and input powers (maximum gain) occurs in the first amplifier because of the uniform launched powers. As the signal power evolves along the link, the power variations between spans become smaller. Consequently, the gain variation compared to the previous span also decreases, leading to a lower DMG.

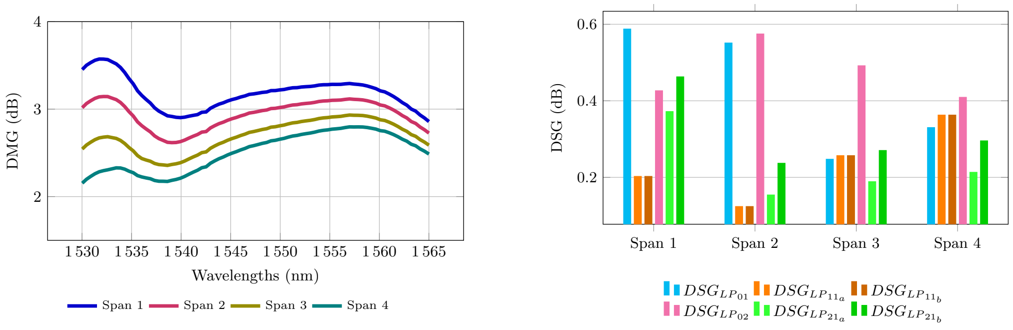

(a)

(b)

Fig. 7. (a) DMG, and (b) DSG per span in an FMF system composed of 4 spans.

Figure 7(b) presents the DSG evolution throughout the FMF link. The first amplifier reaches the highest DSG value for mode LP_{01}. The designed GFF demonstrates effectiveness in maintaining

DSG values below 0.6 dB after successive spans, thanks to the fact that the GFF coefficients were designed from the average modal gain, which remains close to 19 dB for the entire link.

In Fig. 7(a) it is also observed a shift of the maximum DMG from lower wavelengths in the first span to higher wavelengths in the last span. This phenomenon is due to the GFF, lower wavelengths are more attenuated than higher wavelengths (see Fig. 3(b)). If LP_{01} and LP_{02} are looked at in detail -as these LP modes dictate the DMG- after the first span, the signal power is relatively higher for lower wavelengths than for the higher ones. After successive spans, this trend is preserved but reduced for LP_{01} and pronounced for LP_{02}, this leads to a shift in DMG from 1530 nm in the initial span to 1557 nm after the fourth span.

The last FM-EDFA exhibits the gain presented in Fig. 8(a), with a mean gain of 19 dB and achieving a maximum DMG of 2.8 at 1557 nm. These are better results compared to the ones obtained for the first amplifier, this is due to the gain reduction of the mode LP_{01}. In terms of DSG, it is not degraded after 4 spans, in fact, it is improved, and the final value is under 0.42 dB.

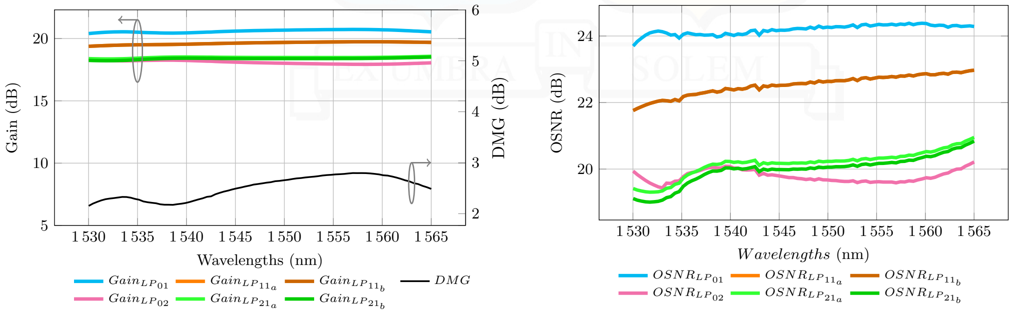

(a) (b)

Fig. 8. (a) Gain per mode and DMG, and (b) OSNR out per mode, achieved by the last FM-EDFA in a 400 km FMF link.

We also evaluate the performance of our FMF system in terms of the Optical Signal-to-Noise Ratio (OSNR) [29]. In our particular case, we operate with input power within the linear regime, where the OSNR is primarily limited by ASE noise, while nonlinear effects are negligible. The OSNR at the output of the last FM-EDFA is shown in Fig. 8(b). The highest OSNR is achieved by mode LP_{01} and the lowest by LP_{02}, aligning with the gain performance reported in Fig. 8(a). The differential OSNR between the best and worst LP modes reaches a maximum of 5.5 dB at 1533 nm. Nevertheless, in the wavelength range of 1535 to 1565 nm, the OSNR is close to or higher than 20 dB with a differential OSNR of 5 dB. Furthermore, spectral variations of OSNR are observed for each LP mode, with the highest value for LP_{21_b} with 1.90 dB and the lowest for LP_{01} with 0.71 dB. This variability is related with the use of the GFF over the signals and noise power for reducing the DSG. These results verify the effectiveness of the proposed two-stage FM-EDFA to meet the compensation of losses in spans of 100 km length, preserving low DMG and DSG for FMF systems. At the same time, the OSNR values obtained at the end of the FMF link fulfill the requirements for bit rates of 100 Gbps [30], which would allow a system capacity of 48.6 Tbps.

6. Conclusions

In this study, we designed a two-stage FM-EDFA using the proposed Joint DMG-DSG Minimization methodology. With a uniform doping profile and the transmission of 81 WDM channels per 6 LP modes, in combination with the designed multipumping profile and a GFF strategically placed at the midstage of the amplifier, the resulting performance metrics demonstrated good effectiveness. Specifically, the two-stage FM-EDFA exhibits a mean gain of 18 dB, DMG below

4 dB, DSG lower than 0.6 dB, and a NF under 6 dB. The incorporation of the GFF results in a remarkably flat gain profile for all the spatial modes.

Moreover, we also modeled an FMF link composed of 4 spans of equal length, using the designed amplifier for compensating losses after each span. DMG and DSG along the cascade of FM-EDFA within the link are not degraded compared to the results of the designed amplifier. We achieved a modal OSNR higher than 19.2 dB for the wavelength range between 1530 to 1565 nm, corresponding to a potential system capacity of 48.6 Tbps. These favorable performances position the amplifier as highly promising for the implementation in long-haul FMF systems. Our methodology with the union of strategies such as the use of GFF and the design of the multipumping profile put in evidence the potential of the proposed two-stage FM-EDFA for next-generation optical communication networks.

Funding. Agencia Nacional de Investigación y Desarrollo (ANID Doctorado Nacional/2021-21211075, Fondecyt Iniciación 11220650, Fondecyt Regular 1231826, Fondecyt Regular 1241362); Universidad Técnica Federico Santa María (USM PI_LIR_24_21, USM PI_LII_24_15). Q1

Disclosures. The authors declare no conflicts of interest.

Data availability. Data underlying the results presented in this paper are not publicly available at this time but may be obtained from the authors upon reasonable request.

References

1. C. Yu, W. Ma, and G. Hu, "High-power, low noise, high gain few-mode fiber amplifier," Opt. Laser Technol. **169**, 110008 (2024).
2. H. Guo, T. Li, F. Yan, *et al.*, "Few-Mode Erbium-Doped Fiber Amplifier With High Gain and Low Differential Modal Gain for Mode-Division-Multiplexed Systems," J. Lightwave Technol. **41**(21), 6657–6663 (2023).
3. L. Bigot, G. Le Cocq, and Y. Quiquempois, "Few-mode erbium-doped fiber amplifiers: A review," J. Lightwave Technol. **33**(3), 588–596 (2015).
4. A. Lozada and R. Olivares, "Optimized Two-Stage Few-Mode Erbium Doped Fiber Amplifier," in *2023 SBMO/IEEE MTT-S International Microwave and Optoelectronics Conference (IMOC)*, (2023), pp. 316–318.
5. D. Jia, H. Zhang, Z. Ji, *et al.*, "Optical fiber amplifiers for space-division multiplexing," Front. Optoelectron. **5**(4), 351–357 (2012).
6. Q. Kang, E.-L. Lim, F. P. Y. Jung, *et al.*, "Minimizing differential modal gain in cladding-pumped EDFAs supporting four and six mode groups," Opt. Express **22**(18), 21499–21507 (2014).
7. G. Le Cocq, Y. Quiquempois, and L. Bigot, "Optimization algorithm applied to the design of few-mode erbium doped fiber amplifier for modal and spectral gain equalization," J. Lightwave Technol. **33**(1), 100–108 (2015).
8. T. Qayoom, G. Qazi, H. Najeeb-ud-din, *et al.*, "A comparative perspective on Differential Modal Gain reduction techniques for optimized few mode EDFA systems," Optik **230**, 166285 (2021).
9. Q. Zhao, L. Pei, J. Tang, *et al.*, "Design of few-mode erbium-doped fiber with a low differential modal gain and weak coupling based on layered doping," Appl. Opt. **62**(6), 1567–1574 (2023).
10. S. Xu, W. Zhang, and Z. Qin, "Gain equalization for a six-mode-group Er-doped fiber amplifier," Opt. Quantum Electron. **52**(1), 20 (2020).
11. J. Gao, F. Yan, G. Ren, *et al.*, "Gain equalization for a few-mode erbium-doped fiber amplifier supporting eight spatial modes," Appl. Opt. **62**(35), 9274–9282 (2023).
12. P.-O. Janvier, C. Matte-Breton, K. J.-J. Monga, *et al.*, "Optimization criteria and design of few-mode erbium-doped fibers for cladding-pumped amplifiers," Opt. Express **31**(9), 14888–14902 (2023).
13. S. Jeurink and P. M. Krummrich, "Multimode EDFA with scalable mode selective gain control at 1480-nm pump wavelength," IEEE Photonics Technol. Lett. **30**(9), 849–852 (2018).
14. N. Bai, E. Ip, T. Wang, *et al.*, "Multimode fiber amplifier with tunable modal gain using a reconfigurable multimode pump," Opt. Express **19**(17), 16601–16611 (2011).
15. W. Xu, L. Pei, J. Wang, *et al.*, "Gain Characteristics of Few-Mode EDFA With Different Pump," IEEE Photonics J. **14**(5), 1–7 (2022).
16. E. Ip, R. Y. Gu, M.-J. Li, *et al.*, "Experimental demonstration of a gain-flattening filter for few-mode fiber based on a spatial light modulator," in *Optical Fiber Communication Conference*, (Optica Publishing Group, 2014), pp. Th4A–5.
17. J. Zhu, Y. Yang, M. Zuo, *et al.*, "Few-mode gain-flattening filter using LPFG in weakly-coupled double-cladding FMF," J. Lightwave Technol. **39**(13), 4439–4446 (2021).
18. Y. Zeng, C. Zhang, S. Zhang, *et al.*, "All-fiber spatial and wavelength gain-flattening of few-mode EDFA via mode selective coupler," Opt. Laser Technol. **181**, 111778 (2025).
19. I. Rec, "G. 694.1: Spectral grids for WDM applications: DWDM frequency grid," International Telecommunication Union, ITU-T (2020).

20. B. Belmahdi and K. Mazighi, “Implementation Efficiency of a Two-Stage EDFA Amplifier with an Inverted Trapezoidal Filter on Gain Flattening,” in *2022 7th International Conference on Image and Signal Processing and their Applications (ISPA)*, (IEEE, 2022), pp. 1–6.
21. Z. Zhang, Q. Zhao, N. Zhao, *et al.*, “Bi-directionally-pumped few-mode EDFA,” in *Asia Communications and Photonics Conference*, (Optica Publishing Group, 2014), pp. ATh3A–104.
22. C. R. Giles and E. Desurvire, “Modeling Erbium-Doped Fiber Amplifiers,” J. Lightwave Technol. **9**(2), 271–283 (1991).
23. A. Galvanauskas, “Mode-scalable fiber-based chirped pulse amplification systems,” IEEE J. Sel. Top. Quantum Electron. **7**(4), 504–517 (2001).
24. J. H. C. Júnior, F. L. Della Lucia, T. Sutili, *et al.*, “Gradient-based Optimization for Unrepeatered Optical Systems,” in *2019 SBMO/IEEE MTT-S International Microwave and Optoelectronics Conference (IMOC)*, (2019), pp. 1–3.
25. H. Friis, “Noise Figures of Radio Receivers,” Proc. IRE **32**(7), 419–422 (1944).
26. R. E. Collin, *Foundations for microwave engineering* (IEEE Press, 2001).
27. V. GmbH, “VPItransmissionMaker$^{\mathrm{TM}}$ Optical Systems,” (2023).
28. S. Mumtaz, R.-J. Essiambre, and G. P. Agrawal, “Nonlinear propagation in multimode and multicore fibers: generalization of the Manakov equations,” J. Lightwave Technol. **31**(3), 398–406 (2012).
29. P. Poggiolini, A. Carena, V. Curri, *et al.*, “Analytical modeling of nonlinear propagation in uncompensated optical transmission links,” IEEE Photonics Technol. Lett. **23**(11), 742–744 (2011).
30. OpenROADM MSA, “OpenROADM MSA optical specifications v6.0,” Online (2023).